



University
of Glasgow

Niven, Andrew James (1988) An experimental investigation into the influence of trailing-edge separation on an aerofoil's dynamic stall performance. PhD thesis.

<http://theses.gla.ac.uk/5380/>

Copyright and moral rights for this thesis are retained by the author

A copy can be downloaded for personal non-commercial research or study, without prior permission or charge

This thesis cannot be reproduced or quoted extensively from without first obtaining permission in writing from the Author

The content must not be changed in any way or sold commercially in any format or medium without the formal permission of the Author

When referring to this work, full bibliographic details including the author, title, awarding institution and date of the thesis must be given.

AN EXPERIMENTAL INVESTIGATION INTO THE INFLUENCE
OF TRAILING-EDGE SEPARATION ON AN AEROFOIL'S
DYNAMIC STALL PERFORMANCE

By

Andrew James Niven

B.Sc., University of Glasgow, 1983

Submitted to the Department of Aerospace Engineering
for the degree of
Doctor of Philosophy

University of Glasgow

© A. J. Niven, 1988

In Memory of My Father

TABLE OF CONTENTS

Page

Acknowledgements	viii
Declaration	ix
Abstract	x
Nomenclature	xii

CH.1 INTRODUCTION

1.1 Helicopter Rotor Environment	1
1.2 Steady-State Stall Characteristics	2
1.3 Unsteady Stall Characteristics	4
1.3.1 Dynamic Stall	4
1.3.2 The Unsteady Boundary Layer	6
1.3.3 Vortex Initiation Mechanisms	8
1.3.4 Unsteady Stall Classification	10
1.3.5 Dynamic Stall Prediction Techniques	11
1.4 Present Work	14
1.4.1 Objectives	14
1.4.2 Outline of Dissertation	15

CH.2 EXPERIMENTAL APPARATUS

2.1 Introduction	17
2.2 Description of Apparatus	17
2.2.1 Wind Tunnel	17
2.2.2 Pitch Drive Mechanism	18
2.2.3 Data Acquisition and Control System	19
2.2.4 Pressure Instrumentation	21

2.2.5 Hot-Film Equipment	22
2.3 Test Procedure	23
2.4 Data Presentation	24
CH.3 TEST AEROFOIL	
3.1 Introduction	25
3.2 Choice of Donor Aerofoil	27
3.3 Type of Modification	28
3.4 Structural Design of the NACA 23012(A) Aerofoil	35
3.5 Conclusions	39
CH.4 FLOW VISUALISATION	
4.1 Introduction	40
4.2 Flow Visualisation Technique	41
4.3 Oil-Flow Characteristics of the NACA 23012 Aerofoil	42
4.4 Oil-Flow Characteristics of Two Modified NACA 23012 Aerofoils	44
4.4.1 The NACA 23012(M1)	44
4.4.2 The NACA 23012(A)	45
4.5 Discussion	46
4.6 Conclusions	48
CH.5 STEADY AERODYNAMIC BEHAVIOUR	
5.1 Introduction	49
5.2 Verification of the Aerofoil Modification Technique	50
5.3 Comparison of Separation Characteristics	52

5.4 Comparison of Aerodynamic Behaviour	54
5.5 Conclusions	57

**CH.6 AERODYNAMIC BEHAVIOUR IN OSCILLATORY PITCH
CONDITIONS**

6.1 Introduction	59
6.2 Degree of Stall	61
6.2.1 Background	61
6.2.2 No Stall	61
6.2.3 Dynamic Stall Onset	62
6.2.4 Light Stall	63
6.2.5 Deep Stall	64
6.2.6 Effect of Pitch Rate	66
6.3 Effect of Trailing-Edge Separation on Vortex Initiation	68
6.3.1 Background	68
6.3.2 Pressure-Time Histories	68
6.3.3 Effect of Trailing-Edge Separation	71
6.4 Critical Angle Calculation	72
6.4.1 Background	72
6.4.2 Critical Angle Calculation	73
6.5 Pitch Damping Boundaries	74
6.5.1 Background	74
6.5.2 Derivation of the Damping Factor	75
6.5.3 Effect of Stall Penetration on the Damping Factor	77
6.6 Conclusions	79

CH.7 AERODYNAMIC BEHAVIOUR IN CONSTANT PITCH

CONDITIONS

7.1 Introduction	81
7.2 Ramp Aerodynamic Characteristics	83
7.3 Comparison with Oscillatory Data	87
7.3.1 Qualitative Results	87
7.3.2 Effect of Pitch Rate	88
7.4 Dynamic Stall Event Timing	89
7.4.1 Definition of Timing Marks	89
7.4.2 Formation of Time Delays	91
7.5 Calculation of Time Delays	94
7.5.1 Stall Onset	94
7.5.2 Post-Stall Characteristics	97
7.6 Conclusions	98

CH.8 HOT-FILM ANEMOMETRY

8.1 Introduction	100
8.2 The Hot-Film Anemometer	101
8.3 Steady-State Results	102
8.3.1 Boundary-Layer Characteristics	102
8.3.2 Flow Separation Estimation	104
8.4 Ramp Test Results	106
8.4.1 Flow Reversal Characteristics	106
8.4.2 Vortex Initiation	108
8.4.3 Time Delay Calculation	110
8.4.4 The Unsteady Laminar Separation Bubble	111
8.5 Oscillatory Test Results	112
8.5.1 Flow Reversal Characteristics	112
8.5.2 Time Delay Calculation	113

8.5.3 Comparison with other Data Sources	115
8.6 The Unsteady Stall Progression	115
8.7 Conclusions	117

CH.9 SUMMARY OF CONCLUSIONS AND RECOMMENDATIONS

FOR FURTHER WORK

9.1 Introduction	118
9.2 Aerofoil Modification Procedure	118
9.3 Conclusions from Oscillatory Tests	119
9.4 Conclusions from Ramp Tests	122
9.5 Conclusions from Hot-Film Tests	123
9.6 Further Work	124

APPENDIX A

The Effect of Pitch Rate on the Dynamic Stall of a Modified NACA 23012 Aerofoil and Comparison with the Unmodified Case.	126
---	-----

REFERENCES

FIGURES

TABLES

ACKNOWLEDGEMENTS

The author wishes to express his sincere gratitude to Dr. R.A.McD. Galbraith for his supervision, assistance and advice throughout the duration of this work. His optimism, confidence and patience were greatly appreciated. The author wishes to express his thanks to Prof. B. E. Richards for his support and encouragement.

The assistance and friendship of the following people at the University of Glasgow is also gratefully acknowledged:

Mr. R. Gordon, Mr. A. Smedley, Mr. R. Gilmour, Mr. J. Kitching, Mr. D. Perrins, Mr. D. Whitelaw, Mrs. E. Leitch, Mrs. E. Murray-Smith.

A special mention is due to Mr. B. Stockley whose company was always welcome, and his willingness to share his knowledge greatly appreciated. The author also wishes to thank Mr. L. Seto, Dr. M. Vezza, Dr. F. Coton and Dr. A. Kokkalis for their companionship and the many rewarding discussions on aerodynamics. The advice of Mr. T. Beddoes (Westland Helicopters plc) and Mr. P. Wilby (R.A.E., Farnborough) was also appreciated.

The financial support of the Science and Engineering Research Council and Westland Helicopters plc via an SERC CASE award No. 8051/3408, and the Royal Aircraft Establishment under MOD agreement 2048/026 XR/STR is gratefully acknowledged.

Finally, the author wishes to express his loving gratitude to his mother for her kind understanding and support, to his sister for proof reading the text, and to his fiancée, Miss Aileen Fulton, for her patience and immense optimism.

Declaration page not scanned
at the request of the
University

ABSTRACT

The influence of trailing-edge separation on the dynamic stall characteristics of a typical rotor section is at present unclear. Although previous research has given a fundamental understanding of the unsteady stall process, the variety of aerofoils tested has made it difficult to isolate the effect of trailing-edge separation. Further investigation into this field may be carried out by testing two similar aerofoils which differ only in their trailing-edge separation characteristics. The early part of the work concentrated on the development of a numerical method whereby the theoretical pressure gradient over the trailing-edge upper surface of a given aerofoil may be modified to either enhance or reduce such separation. Since previous work at the University of Glasgow had included a detailed unsteady aerodynamic study of a NACA 23012 aerofoil, this was the appropriate profile for modification. The above technique was applied to this aerofoil with the objective of modifying the geometry in such a manner that would retain the leading-edge pressure distribution whilst forcing an earlier and more gradual trailing-edge separation growth. The subsequently designed aerofoil, designated the NACA 23012(A), was shown to display an enhancement of the trailing-edge separation characteristics via both boundary-layer calculations and oil-flow visualisation tests.

On comparison with unsteady data previously collected for the NACA 23012, several systematic methods of estimating the

effects of trailing-edge separation on the dynamic stall process are presented. During oscillatory tests the NACA 23012(A) displayed a more stable damping characteristic which was attributed to the enhanced trailing-edge separation producing an earlier pitching-moment break. Based on the analysis of pressure-time histories obtained during ramp tests, it was deduced that a consequence of significant trailing-edge separation was to delay the initiation of the dynamic stall vortex. Detailed analysis of hot-film data led to the conclusion that aerofoils which display a tendency to stall in steady conditions, via separation growth from the trailing-edge, will experience vortex initiation by the breakdown of a thin layer of reversed flow travelling upstream beneath a stable shear layer which remains in close proximity to the aerofoil's surface contour.

NOMENCLATURE

c	<i>aerofoil chord, m</i>
C_l	<i>lift coefficient</i>
C_m	<i>quarter-chord pitching moment</i>
C_n	<i>normal force coefficient</i>
C_p	<i>pressure coefficient</i>
C_t	<i>tangential force coefficient</i>
f	<i>non-dimensional chord, x/c</i>
k	<i>reduced frequency, $\omega c/2U_\infty$</i>
k_1	<i>reduced pitch rate, $\dot{\alpha} \pi c/360U_\infty$</i>
M, M_∞	<i>freestream Mach number</i>
p	<i>pressure, N/m^2</i>
R, Re, R_c	<i>Reynolds number</i>
s	<i>distance along aerofoil surface, m</i>
t	<i>time, s</i>
t_n	<i>non-dimensional time, tU_∞/c</i>
u	<i>streamwise velocity within boundary layer, m/s</i>
U_e	<i>velocity at outer-edge of boundary layer, m/s</i>
U_∞	<i>freestream velocity, m/s</i>
x	<i>chordwise distance, m</i>
α	<i>angle of incidence, deg</i>
$\dot{\alpha}$	<i>pitch rate, degs/s</i>
Δ	<i>increment</i>
ρ	<i>density, Kg/m^3</i>
τ	<i>non-dimensional time delay, $U_\infty \Delta t/c$</i>
ω	<i>angular frequency, rad/sec</i>

subscripts

a	<i>amplitude</i>
c	<i>critical value</i>
DS	<i>dynamic stall value</i>
i	<i>dynamic stall criterion</i>
m	<i>mean value</i>
mv	<i>vortex inception value based on pitching-moment response</i>
max	<i>maximum value</i>
o	<i>zero lift value</i>
pv	<i>vortex inception value based on pressure history response</i>
ss	<i>static stall value</i>
v	<i>vortex inception value</i>

CHAPTER 1

INTRODUCTION

1.1 Helicopter Rotor Environment

The unsteady aerodynamics of rotary-winged aircraft presents a fascinating, yet formidable, challenge to the fluid dynamics researcher. The consequences of the unsteadiness in rotor aerodynamics, illustrated in Figure 1.1, are clearly evident in practically every aspect of rotorcraft technology. A major portion of the helicopter flight boundary is determined by excessive control loads. These arise from a form of stall flutter on the retreating blade which involves the interaction of unsteady separation phenomena with the blade torsion degree of freedom. Dynamic effects on aerofoil stall are of sufficient magnitude to influence the choice of both section geometry and structural dynamic characteristics of the rotor blade.

The diversity in the requirements of aerofoils suitable for helicopter rotor blades chiefly stem from the particular environment in which they operate. Consequently, the designer, when confronted with the problem of either selecting the most suitable blade aerofoil section from a

catalogue, or attempting to develop new profiles, must seek a compromise between often conflicting requirements. Dadone (1978) indicated that early rotor blade development programmes, such as Davenport and Front (1966), used the steady-state lift, drag and moment characteristics as aerofoil optimisation criteria, since little was known about the effects of the unsteady rotor environment on these parameters. Therefore, a knowledge of an aerofoil's steady-state performance should contribute to a better judgement of the possibilities, as well as the limitations, regarding rotorcraft performance gains which can be achieved through the application of the most suitable blade aerofoil section. Also, it would be reasonable to speculate that the manner by which a particular unsteady separation phenomenon was triggered may depend on the aerofoil's steady-state stall mechanism. Therefore, a short review of steady-state separation behaviour is presented in the following section.

1.2 Steady-State Stall Characteristics

In 1929, the National Advisory Committee for Aeronautics (NACA) began studying the aerodynamic characteristics of a systematic series of aerofoils in an effort to find the geometries that were best suited for specific purposes. Since then, much data has been collected and a fundamental understanding of the dependence of static stall on aerofoil geometry has been obtained. Figure 1.2 illustrates the esteemed, and frequently referenced, correlation of aerofoil stalling characteristics, with Reynolds number and leading-

edge geometry, carried out by Gault (1957). Four types of static stall were recognised:

- (1) **Short-bubble (or leading-edge) stall.** This type of stall is related to the formation of a laminar separation bubble immediately downstream of the leading-edge suction peak. Increasing the incidence causes the laminar separation point to move forward to a region of increasing surface curvature and eventually turbulent reattachment fails to take place causing the bubble to 'burst'. Van den Berg (1980) illustrated an alternative cause of leading-edge stall which involves the abrupt 'reseparation' of the turbulent boundary layer immediately downstream of the bubble reattachment point.
- (2) **Long-bubble (or thin-aerofoil) stall.** This type of stall is associated with the formation of a 'long bubble', in which the turbulent reattachment point moves rearward with increasing incidence. When this point reaches the trailing edge the bubble bursts and stall is attained.
- (3) **Trailing-edge stall.** This type of stall is caused by the turbulent separation point moving progressively forward from the trailing edge as the incidence is increased. At maximum lift the flow is separated over approximately 50% of the aerofoils upper surface

(4) **Combined (or mixed) stall.** This type of stall displays characteristics which are a combination of short-bubble and trailing-edge separation behaviour.

Figure 1.3 summarises the contemporary understanding of the various steady-state separation characteristics, and the manner in which they are related to the aerofoil's geometry and freestream condition.

1.3 Unsteady Stall Characteristics

1.3.1 Dynamic Stall

It was noticed in the Sixties (e.g., Harris and Pruyn, 1967) that the boundaries of rotor stall in forward flight were more favourable than those predicted on the basis of static two-dimensional data. It appeared that differences in aerofoil characteristics, resulting from unsteady aerodynamic phenomena, may have been responsible for the discrepancies. The importance of these phenomena to the understanding, and analysis, of blade aeroelastic problems provided an additional incentive for experimental and analytical studies of unsteady flow. Early experimental studies emphasised application to the retreating blade stall of the helicopter rotor that occurs in high speed forward flight. Consequently, measurements were typically made of the unsteady airloads during sinusoidal pitching oscillations characteristic of the retreating blade. Liiva et al (1968) represents one of the first efforts directed exclusively toward specific unsteady

aerodynamic problems of blade aerofoil sections. The result of this work, and of the many subsequent oscillatory experiments that followed (e.g., Ham, 1968, McCroskey and Fisher, 1972), was the general observation of a distinctive aerodynamic behaviour which became known as 'dynamic stall'.

The phenomenon of dynamic stall on aerofoils in unsteady flow environments has been studied for many years, both as an important practical problem and as a challenging fundamental one. Over the last twenty years it has been established that a predominant feature of dynamic stall is the shedding of a strong vortex from the leading-edge region. This vortex passes over the upper surface of the aerofoil, distorting the chordwise pressure distribution and producing transient forces and moments that are fundamentally different from their static stall counterparts. The contemporary understanding of the dynamic stall process is illustrated in Figure 1.4, and the behaviour is a direct consequence of the aerofoil being pitched through the static stall incidence at some significant rate.

If the reduced frequency, amplitude, and maximum incidence are sufficiently high, the vortex shedding is well defined and the qualitative aerodynamic loadings are relatively independent of aerofoil geometry, Reynolds number, and type of motion. This limiting case is designated 'deep dynamic stall'. Under the less severe conditions, which are more common in helicopter applications, the vortex shedding is less well defined. The origin, strength, and transient

development of the vortex appear to depend on all the parameters listed in Table 1.1. This case is known as 'light dynamic stall'.

1.3.2 The Unsteady Boundary Layer

The ability to understand fundamentally, and predict, the unsteady boundary-layer behaviour, over the aerofoil's upper surface, is a necessary starting point for a dynamic stall analysis, since the various unsteady phenomena must originate from the response of the surrounding shear layers to the imposed conditions. It has been recognised for some time, that the boundary layer remains attached to the aerofoil surface at higher angles of incidence under unsteady conditions than could be obtained under static conditions. Carta (1973) suggested that the phase lag and attenuation of the inviscid pressure distribution might be significant enough to explain the delay of the dynamic stall onset. McCroskey (1973) showed that this postulation was essentially valid, although it was clear that other mechanisms were involved in the stall delay. Scruggs *et al* (1974) illustrated, via a numerical boundary-layer scheme, that unsteadiness in both the potential flow and viscous regions contribute to the delay of flow-reversal onset. However, it was stressed that their analysis did not suggest that dynamic stall occurred simply as the result of the forward movement of the turbulent flow reversal point. What was shown was that the effects of time-dependence permit the turbulent boundary layer to remain in a non-reversed (and non-separated) condition during

dynamic overshoot. McCroskey and Philippe (1975) illustrated that the response of an unsteady boundary layer was governed by the relative magnitude of the temporal and spatial velocity gradients. Figure 1.5 illustrates their calculations of the loci of laminar and turbulent flow reversal on an oscillating NACA 0012. As the static stall incidence is approached, the spatial gradients overwhelm the unsteady derivatives in the leading-edge region, where laminar separation occurs, and therefore any observed hysteresis will be due to the phase lag in the velocity at the outer edge of the boundary layer. However, as the turbulent boundary layer approaches separation at the trailing edge, the unsteady derivatives are of comparable magnitude with the spatial gradients, and therefore the aerofoil motion has a considerable influence on the onset of flow reversal. On comparison with experimental data, McCroskey and Philippe concluded that the main deficiency of the employed boundary-layer method was its inability to indicate a possible mechanism of formation and shedding of the dynamic stall vortex. This deficiency is also apparent when consideration is given to similar work by Scruggs et al (1974) and Cebeci and Carr (1981).

Although not specific to oscillatory aerofoil flow conditions, an interesting parallel line of research, concerning experimental measurements on unsteady turbulent boundary layers, is reviewed by Carr (1981). In many of these experiments the metric surface is a flat plate or one wall of the wind tunnel. Unsteadiness is frequently introduced by

oscillating vanes or shutters located either upstream, or downstream, of the test section. Using this technique, Simpson *et al* (1981) observed that, near the wall, between the viscous sublayer and the semi-logarithmic region, unexpected phase shifts of the velocity and turbulence oscillations occurred. Parikh *et al* (1981) observed that if the applied adverse pressure gradient was varied at a significant frequency, the shear layer thickness remained frozen even though flow reversals were indicated near the wall. During a series of wind tunnel experiments on a NACA 0012 aerofoil, Covert and Lorber (1984) observed that the interior of the turbulent boundary layer was strongly affected by unsteadiness in the freestream flow. Similar observations, by other researchers, have led to the generally accepted opinion that flow reversal and separation are distinct boundary-layer phenomena in unsteady flows. Simpson *et al* (1981) noted that turbulent separation must mean either the entire process of shear-layer departure from the aerofoil contour, or the complete breakdown of the classical boundary-layer concept.

1.3.3 Vortex Initiation Mechanisms

A particular characteristic that strongly influences the dynamic stall behaviour, especially in the light-stall regime, is the nature of the initial boundary-layer separation that precedes vortex formation. The work of McCroskey *et al* (1976) represents one of the first experimental investigations, via hot-wire anemometers, into

the nature of the boundary layer prior to, and the mechanism by which, vortex shedding occurs. Four boundary-layer phenomena were identified as possible vortex inception mechanisms:

- (1) The bursting of the laminar separation bubble.
- (2) Abrupt breakdown of the turbulent flow immediately downstream of the laminar separation bubble.
- (3) The arrival, at the leading-edge region, of a thin stratum of reversed flow travelling forward from the trailing edge. This behaviour was described as a 'tongue of reversed flow', since it was found that no upper-surface pressure divergence was observed, indicating possible boundary-layer separation.
- (4) The appearance of transonic flow near the leading edge ($M_\infty > 0.2$).

The mechanism that first succeeds in triggering vortex shedding will depend on the parameters listed in Table 1.1. A detailed review of these vortex inception mechanisms is given by Young (1981).

1.3.4 Unsteady Stall Classification

McCroskey et al (1980) combined the initial boundary-layer disturbance, preceding vortex inception, with the subsequent direction of propagation, either upstream or downstream, to generate the following unsteady stall types:

- (1) **Leading-edge stall**; bursting of the laminar separation bubble.
- (2) **Abrupt trailing-edge stall**; a turbulent reseparation propagating upstream from behind the laminar separation bubble.
- (3) **Trailing-edge stall**; tongue of reversed flow moving upstream from the trailing-edge.
- (4) **Mixed stall**; a combination of (1) and (3) OR a modified version of (2) in which the disturbance travels both upstream and downstream from the 25% chord region.

When considering the inability of numerical boundary-layer methods to indicate a possible vortex formation mechanism, McCroskey (1975) commented that, because of this constraint, "the boundary-layer approximation will probably have to be abandoned". However, if the amount of flow reversal, indicated by the computational method, is used in conjunction with the above experimentally-obtained vortex trigger

mechanisms, then the possibility exists, that, for a given aerofoil, the type of unsteady stall may be predicted.

Although impressive progress has been made in the recognition of vortex initiation mechanisms, no unique correlation of unsteady stall type with the parameters listed in Table 1.1 exists. As with static stall characteristics, a detailed knowledge of the dependence of dynamic stall on aerofoil geometry would be extremely useful. In order to achieve this knowledge, a large amount of unsteady experimental research will be required to obtain a detailed understanding of the dynamic stall process.

1.3.5 Dynamic Stall Prediction Techniques

Several approaches have been taken in the past to predict and analyse dynamic stall using various modelling techniques. In general, these methods invoke certain assumptions and are therefore often tailored to model specific stall regime features. Excellent reviews of the current predictive schemes are given by Beddoes (1980), McCroskey (1981), Johnson (1986) and Ericsson and Reding (1988). However, to complete the present discussion, a summary is now presented which indicates some of the deficiencies associated with each model.

Generally, each model can be classified according to the prediction technique used:

(1) Discrete Potential Vortex Approach.

- (i) Does not model viscous effects.
- (ii) Cannot predict vortex initiation point.

(2) Zonal (or Viscous-Inviscid) Methods.

Two subsets exist:

- (a) Uncoupled -
 - (i) No interaction between viscous and inviscid regions, Therefore only models light stall regime.
 - (ii) No indication of possible vortex trigger mechanism.
- (b) Coupled -
 - (i) Assumptions made about unsteady wake geometry.
 - (ii) Does not account for thin layer of reversed flow near wall.
 - (iii) Vortex shedding not modelled.

(3) Navier-Stokes Calculations.

- (i) Problems with unsteady turbulence modelling.
- (ii) Large computational times.

(4) Empirical Correlation Techniques.

- (i) Relies heavily on unsteady wind tunnel data and a knowledge of the factors which affect dynamic stall.
- (ii) Does not contribute to the detailed understanding of the dynamic stall process.

The helicopter industry has developed several engineering prediction techniques, based on empirical correlations of wind tunnel data, allowing the effects of dynamic stall to be included in helicopter flow calculations. These methods seek to correlate the appropriate force and moment data as functions of the numerous parameters that govern the dynamic stall process. A common aspect of these empirical techniques is that these correlations are used as corrections to steady-state aerofoil data, so that the geometrical, Reynolds number, and Mach number effects are included only insofar as they determine the static characteristics. However, this assumes an aerofoil's unsteady behaviour will display a similar dependence on these parameters as was observed in the steady state.

A particular class of empirical model assumes that each dynamic stall event is governed by a separate universal dimensionless time constant of the form $\tau = U_{\infty} \Delta t / c$, regardless of the time history of the motion. A notable model adopting this approach was presented by Beddoes (1975) and is illustrated in Figure 1.6. A detailed discussion of the stall progression and associated time delay calculations particular to this method, is presented in Chapter 7. Further research by Beddoes (1978) illustrated that, for particular aerofoils at low Mach number ($M_{\infty} < 0.35$), the prediction of dynamic stall onset was influenced by the presence of trailing-edge separation. Therefore, a detailed knowledge of this effect would be beneficial. At present the only practical means of determining an aerofoil's unsteady separation

characteristics, and studying their dependence on the parameters mentioned above, is via a series of unsteady wind tunnel experiments.

1.4 Present Work

1.4.1 Objectives

Clearly, empirical modelling relies heavily on unsteady wind tunnel data and a knowledge of the factors which affect dynamic stall. One such factor is the influence of trailing-edge separation on the sequential timing of the dynamic stall process. Therefore, to investigate this aspect the objectives of the present work were as follows:

- (1) to select an aerofoil, typical of current helicopter rotor profiles, which exhibited a stall by the mechanism of trailing-edge separation at low Mach number. For future clarity this profile will be referred to as the 'basic' or 'donor' aerofoil.
- (2) to modify the selected aerofoil in such a manner that would retain the leading-edge pressure distribution whilst forcing an earlier and more gradual trailing-edge separation growth.
- (3) to test the modified aerofoil under unsteady conditions and, by comparison with existing experimental data for the basic profile, provide preliminary information into

the effects of trailing-edge separation on the dynamic stall process. If both aerofoils were tested in the same wind tunnel, under similar conditions, then any observed differences in dynamic stall performance may be directly attributed to the change in trailing-edge separation characteristics.

1.4.2 Outline of Dissertation

The chapters of the dissertation are organised in a manner which represents the sequence of events adopted to accomplish the stated objectives of the research project.

Chapter 2 describes a test facility, previously developed at the University of Glasgow by Leishman (1984), and designed for the investigation of dynamic stall. Chapter 3 describes the selection of the donor aerofoil section, subsequent modification to enhance the trailing-edge separation characteristics, and the structural design and construction of a fully instrumented (i.e., pressure transducers and hot-film gauges) wind tunnel model possessing the required section geometry. Chapter 4 details an experimental investigation into the applicability of the modification procedure via the technique of oil-flow visualisation. Chapter 5 presents the results from a series of steady-state tests on the instrumented modified aerofoil. Chapter 6 presents the unsteady aerodynamic forces obtained for the modified aerofoil during various oscillatory tests. On comparison with similar wind tunnel data previously collected

for the donor aerofoil, several systematic methods of estimating the effects of trailing-edge separation on the dynamic stall process are presented. Chapter 7 describes the unsteady aerodynamic forces obtained during a series of ramp tests designed to study the sequential timing of dynamic stall. An analysis of the pressure data relevant to empirical modelling techniques is presented. Chapter 8 details a hot-film investigation into the type of unsteady boundary-layer separation characteristics associated with both the donor and modified aerofoils. Finally, Chapter 9 summarises the work of the previous Chapters, and highlights the main conclusions concerning the effects of trailing-edge separation on the dynamic stall process. Appendix A contains an intermediate overview of the research work as published in Vertica (1987).

CHAPTER 2

EXPERIMENTAL APPARATUS

2.1 Introduction

Since October 1980, the Department of Aeronautics and Fluid Mechanics at the University of Glasgow has been developing a facility to experimentally investigate the low speed dynamic stall characteristics of current and projected helicopter rotor aerofoils. A detailed description of the design and development of the facility is documented by Leishman (1984). The present investigation utilises this dynamic stall test rig and therefore, for completeness, a brief description of the experimental apparatus is given below.

2.2 Description of Apparatus

2.2.1 Wind Tunnel

The Glasgow University 'Handley Page' wind tunnel, illustrated in Figure 2.1, is a low speed closed-return type with a 1.61 x 2.13m octagonal working section. As shown in Figure 2.2, the test aerofoil, of chord length 0.55m and span

1.61m, was mounted vertically within the working section. The model was pivoted about the quarter chord position on two tubular steel shafts connected to the main support via two self-aligning bearings (the model weight being carried by a single thrust bearing on the top beam). The aerofoil was constructed of a glass-fibre skin filled with balsa wood and mounted on a hollow aluminium spar; a detailed description of the structural design is presented in Chapter 3.

2.2.2 Pitch Drive Mechanism

Angular displacement of the aerofoil was obtained using a linear hydraulic actuator and crank mechanism. The actuator was mounted horizontally below the wind tunnel working section, with the crank rigidly connected to a tubular extension of the aerofoil's internal spar. The actuator was a UNIDYNE 907/1 type with a normal dynamic thrust of 6.1 KN operated from a supply pressure of 7 MNm⁻². A MOOG 76 series 450 servo valve was used via a UNIDYNE servo controller unit. A suitable feedback signal for the controller was provided by a precision linear angular displacement transducer.

2.2.3 Data Acquisition and Control System

The data acquisition unit was a DEC MINC-11 microcomputer, configured with an LSI-11/23 16-bit microprocessor and four standard laboratory modules which included:

- (1) A combined A/D converter module and 16 single-ended channel multiplexer. This was a successive approximation type which converted the instantaneous value of a voltage applied to one of its inputs into a 12-bit binary value. Conversion time was approximately 30 μ s, but multiplexer settling time, channel selection, and transfer of data from the A/D converter register to memory increased the conversion time to 44 μ s.
- (2) A multiplexer module, of 16 single-ended channels. This increased the number of channels that could be sampled to a total of 32.
- (3) A real-time clock module, with two Schmitt triggers. This was used as a time-base generator to accurately set the sampling frequency. The desired overflow value of the counter was determined from the frequency of oscillation at run time, with the constraint that 128 sample sweeps be obtained during each cycle. One of the Schmitt triggers was used for data sampling initiation and counter start, by setting the trigger voltage to that from the angular displacement transducer corresponding to a particular angle of incidence.

(4) A D/A converter module which housed four independent 12-bit D/A converters. This was used to power the angular displacement transducer and provide a signal to the actuator controller.

The input signal to the actuator controller allowing incrementation of the aerofoil's angle of incidence during the static test was provided under software control by one of the four D/A converters mentioned above. This was possible because sufficient time between sampling was available and, during the sampling, the incidence was fixed. The two activities were separate and carried out sequentially. However this was not the case for the unsteady tests where sampling and model motion were required simultaneously. The input signal for the oscillatory tests was, therefore, provided by an IEEE controlled FARNELL DSG2 synthesised function generator, the amplitude and frequency of which was set via the minicomputer at the start of each test condition. The ramp function generator comprised of a PET microcomputer interfaced with an 8-bit D/A converter which transformed the digital outputs of the PET into analogue form for command input to the controller. In built in the D/A converter was a scaler to provide manual adjustment of the maximum desired voltage output when all the digital inputs were high, thus ensuring that the maximum resolution of 255 increments was achieved. The parallel I/O part of the PET was configured as output lines by software and used to communicate with the D/A converter. A ramp signal was obtained by incrementing the PET's output lines sequentially from 0000 0000 to 1111 1111,

while the desired delay between increments was generated by a software counter.

The path of data flow and system layout is illustrated diagrammatically in Figure 2.3. The main test control programs were written in FORTRAN 4, and were designed to prompt the user for specific run information before calling a specialised sub-program, written in MACRO 11 assembly language, to control the A/D conversion sequence. The timing and control of the A/D converter and associated circuitry were performed by the processor, but channel selection, data transfer and data management were done under software control which optimised the conversion code for the specific task.

2.2.4 Pressure Instrumentation

The chordwise surface pressure distribution was measured using thirty ultra-miniature silicon strain-gauge pressure transducers (ENTRAN EPI-080-5 and KULITE LSQ-57) installed just below the surface of the aerofoil's centre section. The transducers were of sealed-gauge type with one side of the pressure-sensitive diaphragm sealed to a reference pressure during manufacture. Each transducer was fitted with a temperature compensation module, which minimised the change of zero offset and sensitivity with temperature. The location of the transducers on the aerofoil are shown in Figure 2.4. The low voltage outputs from the thirty pressure transducers were suitably amplified and conditioned in a bank of differential amplifiers before passing to a sample and hold

unit to overcome the time skew problems associated with sequential analogue multiplexing and A/D conversion.

The dynamic pressure in the wind-tunnel working section was determined by a pitot-static probe mounted on the tunnel sidewall approximately one chord length upstream of the aerofoil's leading edge. This probe was connected to a FURNESS MDC FC 012 micromanometer which, in addition to the digital display of the dynamic pressure in mm H₂O, provided a differential voltage output to the data acquisition system.

2.2.5 Hot-Film Equipment

An examination of the aerofoil's upper surface boundary-layer shear stress characteristics was carried out via 12 DANTEC hot-film probes. These sensors were operated in the constant temperature mode by twelve CTA bridges designed and built at the University of Glasgow. The output from each CTA bridge was interfaced with an SE-LABS SE2100 MULTI-CHANNEL ULTRA-VIOLET RECORDER via an individual voltage attenuator consisting of a series and parallel resistor chosen, in conjunction with the source impedance, to obtain the correct galvanometer damping and sensitivity for optimum performance. As indicated in Figure 2.4, each hot-film was positioned opposite a particular pressure transducer orifice and staggered in the spanwise direction to avoid operation in the wake of an upstream gauge. No calibration was performed on the CTA signals, as the objective of the present work was

only to investigate the qualitative behaviour of the boundary layer under steady and unsteady conditions.

2.3 Test Procedure

Due to the thermal characteristics of the tunnel and the problem of pressure transducer drift, a precise sequence had to be followed before initiating a test. Prior to any series of tests, the tunnel was run for approximately 20-25 minutes to achieve thermal stability at around 28°C, allowing the pressure transducers to be brought into a temperature range where the offset drift compensation units were most effective. Before each individual test, the tunnel was shut down and the air flow allowed to cease before the transducer offsets were logged. Immediately after this logging, the appropriate data acquisition routine was initiated whilst the tunnel was brought up to speed and thence data gathered as per the software prompts.

The static data presented in Chapter 5 were obtained during continuous running of the tunnel whilst the aerofoil's angle of incidence was first incremented, from around -2.0°, in discrete steps of approximately 0.5° through a 30° change, and then decremented in a similar manner. After each incidence change, a delay of a few seconds took place before the data were sampled. One hundred sample sweeps of each transducer were taken and averaged at each incidence. For each unsteady test condition, ten cycles of oscillatory data were recorded, whilst, to maintain similar data management

and storage, five cycles were collected for ramp runs (i.e., data sampling was carried out during both ramp-up and hold, this being equivalent to two oscillatory cycles). If, on completion of a test, the overall change in air temperature was less than 2°C, further runs could proceed. However, if the temperature change exceeded 2°C, the tunnel was shut down and offsets re-logged. This procedure minimised the effect of thermal offsets on the transducers.

2.4 Data Presentation

All data collected by the data acquisition routines were stored in unformatted form on disc and magnetic tape. A data reduction program was used to convert the cycles of raw data into averaged or unaveraged non-dimensional pressure coefficients by applying offsets, gain, calibration, etc., to the raw data. These coefficients were transferred to a DEC VAX 750, where details were stored on the University of Glasgow Aerofoil Database, as described by Leitch and Galbraith (1987). A further library of programs is available for the presentation of the data in this form. During the processing of unsteady data, no account was taken of tunnel interference effects, these being treated as unknown. To facilitate a direct comparison with the unsteady tests, static data was also left uncorrected.

CHAPTER 3

TEST AEROFOIL

3.1 Introduction

During the autogyro era of rotary-wing flight it was quickly realised that the use of aerofoils with high aerodynamic pitching moments led to extreme blade twisting and high control loads. These experiences led to a period of almost exclusive use of low pitching-moment symmetrical aerofoils. The later development of stiffer blades and irreversible control systems allowed the use of aerofoils promising a significant aerodynamic improvement over the symmetrical section. Possibly the most significant advance in rotor aerofoil design was the introduction of leading-edge camber. This particular geometrical arrangement was found to produce a high maximum lift coefficient and, even though a negative zero-lift pitching moment was induced, this was seen as a desirable rotor characteristic. For example, rotor performance would be improved by exchanging the blade section from the NACA 0012 to the NACA 23012. A notable optimisation of leading-edge camber and radius was carried out on the NACA 23012 aerofoil by Davenport and Front (1966) which resulted in the Boeing-Vertol VR profiles. Later aerofoil designs

regulated the magnitude of the negative pitching moment by reflexing the trailing edge, either as an integral part of the geometry or as an add-on trim tab. Although this arrangement has been shown to be detrimental to both the maximum lift and drag divergence characteristics (Dadone, 1978), it is still incorporated into new aerofoil designs, especially those dedicated for use in the inboard region of the rotor blade.

Whilst considering existing steady two-dimensional aerofoil test data, Prouty (1975) indicated that the most significant steady aerodynamic characteristics were related to a few key geometrical parameters e.g., Figure 1.3. A subsequent review of current rotor aerofoil optimisation methods by Dadone (1978) extended a similar analysis into the unsteady stall regime by examining the relationship between static stall and aerodynamic damping. He concluded that the only aerofoil design constraint with any direct bearing on the unsteady aerodynamic performance was one that required the static stall to be gradual at Mach numbers between 0.3 and 0.4. McCroskey *et al* (1980) studied the dynamic stall characteristics of eight aerofoils. Their results provided a unique comparison of the effects of section geometry in a simulated rotor environment. However, each aerofoil simultaneously varied in thickness, camber and leading-edge radius, hampering any independent attribution of one particular geometrical difference on the final dynamic stall response. Similar investigations were performed by Wilby (1980 & 1984) in which RAE/ARA unsteady test data were

examined, and an attempt to quantify the effect of specific section geometrical parameters on dynamic stall was made.

Although there has been considerable advancement in the understanding of the effect of section geometry on dynamic stall, there is still a clear need for further experimental investigations in order to expand existing data bases. The present chapter considers the selection and modification of a particular aerofoil that, when tested under unsteady conditions, will, on comparison with existing experimental data for the original section, provide preliminary information into the effects of trailing-edge separation on the dynamic stall process.

3.2 Choice of Donor Aerofoil

The NACA 23012 aerofoil represents a typical helicopter rotor profile which utilises the effects of leading-edge camber to increase its overall aerodynamic performance. For many years this aerofoil has been the subject of many aerodynamic tests, and the subsequent accumulation of data is well documented within the literature (e.g., Abbott and von Donhoff, 1959, Miley, 1982). One dominating feature of this aerofoil is its unusual stalling characteristics. On the basis of its abrupt lift collapse one might have expected a leading-edge stall. However, as predicted by Gault (1957), this aerofoil should exhibit a trailing-edge type stall. This apparent contradiction was found to be due to a rapid growth of trailing-edge separation at a critical incidence of 14.2°

(Leishman, 1984). Prouty (1975) suggested that this characteristic could actually be considered to be one of a "very good aerofoil which achieves its maximum lift coefficient by maintaining attached flow at both the leading and trailing edges longer than other aerofoils. However, when the flow does separate, the resultant stall is abrupt".

Over the past few years the NACA 23012 aerofoil has been the subject of intensive aerodynamic testing at the University of Glasgow (e.g., Leishman, 1984, Seto and Galbraith, 1984). This has allowed a reasonable picture of its unsteady stalling characteristics to be obtained and thus it satisfied all the requirements for the selection as the donor aerofoil.

3.3 Type of Modification

The generally accepted dependency of aerodynamic characteristics on section geometry then suggests that only a small profile modification to the NACA 23012 aerofoil may significantly alter its sensitive stalling behaviour. As previously mentioned, a useful modification to this aerofoil would be one which retained the leading-edge conditions whilst forcing an earlier and more gradual trailing-edge separation growth. It is well known (Chang, 1976) that a region of adverse pressure gradient will, if persistent enough, cause a boundary layer to separate. It follows from this that in order to increase the probability of boundary-layer separation within a given region, one should increase the applied adverse pressure gradient. Therefore, a

modification to the separation characteristics of the NACA 23012 may be achieved by a specified alteration to the existing adverse pressure gradient over the rear upper surface.

To permit an assessment into the applicability of an existing theoretical aerofoil design technique, it was decided that an attempt to quantify the type of modification in terms of the theoretical upper surface pressure distribution, rather than an heuristic geometrical alteration to the section, should be made. This requirement led to an aerofoil design technique which, as illustrated in Figure 3.1, comprised of four algorithms:

- (1) A 'forward' potential flow panel method (Leishman and Galbraith, 1985) replaced the aerofoil contour by an inscribed polygon on which was placed a variable strength vortex distribution. The strength of this distribution was calculated using the boundary conditions of surface flow tangency and Kutta trailing-edge flow. This algorithm was used to calculate the inviscid pressure distribution about the donor aerofoil.
- (2) A procedure by which this pressure distribution could be methodically modified.
- (3) An 'inverse' potential flow panel method (Veza, 1986). This procedure was used to generate the coordinates of an aerofoil possessing the modified pressure distribution.

The inverse algorithm simply took the donor aerofoil geometry and adjusted the influence coefficients of the panel matrix to satisfy the new pressure distribution. The process was iterative and, for small modifications in pressure gradient, converged well.

- (4) A boundary-layer calculation to determine the success of the modification by indicating the relative change in trailing-edge separation as compared to that predicted for the donor aerofoil. This procedure was adapted, for use at the University of Glasgow, from an algorithm given by Moran (1984). The calculation used Thwaites method for the laminar region and Heads method for the turbulent region. Transition was set to occur at the point of minimum pressure during which the shape factor became 1.5 and turbulent separation was indicated when a value of 2.8 was reached. Unlike Dutt and Srekanth (1980) this algorithm was not integrated with the inverse panel method as it was felt that its ability to predict boundary-layer thickness and separation position was insufficient.

Although algorithms (1) and (3) were already available at the University of Glasgow, a procedure for modifying the pressure gradient had to be developed. The pressure gradient over an arbitrary body moving through a fluid can be calculated using the relationship:

$$\frac{1}{\rho} \frac{dp}{ds} = -Ue \frac{dUe}{ds} \quad (3.1)$$

Equation (3.1) can be easily converted into the following form, suitable for a panel method (see Figure 3.2):

$$\left[\frac{1}{\rho} \frac{dp}{ds} \right]_{ic} = \frac{\gamma_{i+1}^2 - \gamma_i^2}{2L_i} \quad (3.2)$$

where γ_i and γ_{i+1} are the vortex strengths at the panel corner points and L_i the panel length.

The procedure used to modify the pressure gradient was essentially a curve fitting routine conforming to three boundary conditions. If, for instance, the pressure gradient between a point x_{nc} and the trailing-edge was to be altered, then the following three boundary conditions would apply: at x_{nc} both magnitude and gradient must match the donor aerofoil's pressure gradient distribution, and at the trailing edge the magnitude must equal a specified value. Once the type of modification was chosen, the new vorticity distribution could be calculated and input into the inverse panel program. This was carried out from x_{nc} towards the trailing edge using the following form of equation 3.2:

$$\gamma_i^2 = \gamma_{i+1}^2 - 2L_i \left[\frac{1}{\rho} \frac{dp}{ds} \right]_{ic}^m \quad (3.3)$$

where m indicates the modified value of pressure gradient.

This obviously gave a different value of γ_i than the original, and therefore to satisfy the Kutta condition γ_{N+1} had to be altered accordingly. During modification, all

vortices, except γ_1 to γ_{nc} inclusive and γ_{N+1} , were held constant at their original values. A consequence of this criterion was, that for a large modification the following error conditions would occur:

- (1) The right-hand side of Equation 3.3 would become negative before the trailing edge was reached.
- (2) A noticeable discontinuity in pressure gradient over the Nth panel would appear.

Therefore, in order to achieve a sensible distribution of vorticity, and hence a reasonably designed profile, only small alterations in pressure gradient were implemented. Several forms of modification curve were examined, and it was concluded that the 'best fit' was achieved by the use of a conic parabola. In terms of pressure gradient this had the following form:

$$\left[\left[\frac{1}{\rho} \frac{dp}{ds} \right]^m - a \right]^2 = 4A \left[\frac{x}{c} - b \right]^2 \quad (3.4)$$

where (a,b) is the vertex position.

If the stalling characteristics of the NACA 23012 were to be altered, then the pressure gradient at the critical incidence of 14.2° would be an ideal basis on which to quantify the modification. Figure 3.3 illustrates this particular condition, complete with two subsequent modifications designed to increase the severity of the donor pressure

gradient. When input into the inverse panel program, the pressure gradient curve labelled MOD1 gave rise to the aerofoil illustrated in Figure 3.4, subsequently designated the NACA 23012(M1). It is interesting to note that this particular profile has a slight reflex trailing edge which was discovered to be a consequence of holding the lower surface vortices constant. However, as discussed in Section 3.1, this could easily represent a typical inboard rotor blade profile, and therefore was not seen as detrimental to the present experiment.

The results obtained from the boundary-layer algorithm, illustrated in Figure 3.5, indicated the NACA 23012(M1) aerofoil to display an enhanced separation characteristic which implied the pressure gradient modification procedure was an adequate method of profile alteration. To facilitate a more thorough investigation into the modified aerofoil's steady-state boundary-layer separation characteristics, the technique of oil-flow visualisation was adopted. The main requirement for this particular procedure was a simply-constructed model possessing an aerodynamically smooth surface (Section 3.4), and was therefore ideal for the current application. Although a full presentation of the oil-flow experiments is given in Chapter 4, selected results are illustrated here to maintain the logic of the present discussion. As illustrated in Figures 3.5 and 3.6, the results obtained, for the NACA 23012(M1), from both the boundary-layer program and the oil-flow tests suggested that the modification to the original trailing-edge separation

characteristics, displayed by the NACA 23012, was relatively small. It has been shown within the literature, that unsteady conditions can suppress the effects of trailing-edge separation. Therefore, in a dynamic situation, any small differences in separation characteristics, between two aerofoils could easily be obscured. Based on this previous experience, it was decided that a second modification to the NACA 23012 should be implemented. The subsequent pressure gradient alteration, labelled MOD2 in Figure 3.3, gave rise to the NACA 23012(A) aerofoil illustrated in Figure 3.7, whose coordinates are listed in Table 3.1. It is interesting to note that during the iterative procedure, adopted by the inverse panel method, an abrupt discontinuity at the trailing edge appeared. This is a typically encountered problem when applying a potential flow panel method to an aerofoil with a cusped or thin trailing edge. Under these circumstances, the influence coefficient matrix tends to become ill-conditioned. In Figure 3.8 a comparison between the theoretical pressure distribution over the NACA 23012(A) and the NACA 23012, at an incidence of 14.2° , is illustrated.

Both the boundary-layer program and the oil-flow experiments showed the NACA 23012(A) to have a substantially enhanced trailing-edge separation growth (see Figures 3.4 & 3.5). It is interesting to note that although the boundary-layer prediction and the oil-flow results do not agree in absolute value, they do display a similar relative difference between all three aerofoils. The steady-state separation growth displayed by the NACA 23012(A) was assumed to be sufficient

to influence the aerofoil's unsteady stall performance, and therefore it was decided that a fully instrumented wind tunnel model of this aerofoil should be designed and constructed.

3.4 Structural Design of the NACA 23012(A)

In general, the type and construction of a wind tunnel model are dictated by the tunnel in which it is to be tested and the type of test to be implemented. In most situations the criterion for model strength is one based on deflection rather than yield load limits (Pope, 1954). To satisfy this requirement the final model design should possess both high rigidity in torsion and flexure. Equivalent importance must be given to those structural aspects which depend on the type of test i.e., model accuracy, instrument accessibility and maintenance. Also, though perhaps not a strict design criterion, is the problem of handling the model during installation and removal. This requirement can be alleviated by keeping the model weight to a minimum. However, this may be found to be in conflict with the high rigidity requirement, and hence the final model design may become quite complex. A possible wind tunnel model specification may comprise of the following requirements:

- (1) The estimation of the aerodynamic and inertia loads likely to be encountered during the test.

(2) The calculation of steady-state and aeroelastic structural deflections

(3) The estimation of any relevant natural frequencies.

It was anticipated that the present investigation into the effects of a modification in trailing-edge geometry would be a precursor to a series of similar experiments requiring equally dedicated wind tunnel models. To comply with this requirement a facility to manufacture aerofoil models of arbitrary section was developed, at the University of Glasgow, utilising a wax moulding process. In general, the construction method consisted of the following steps:

(1) Construction of a female half-mould (either upper or lower surface) from progressive cutting of a wax block.

(2) Fabrication, at the desired position within the mould, of any particular sections of the model surface required to be removable in order to access internal instrumentation.

(3) Lay-up of a continuous spanwise glass-fibre/resin skin. This was achieved by over-laying the previously constructed removable panels, positioned in the mould at the required locations, with the fibre mix, thus allowing them to lie flush with the external surface without breaking the structural continuity of the main load bearing skin.

(4) Interior construction with a suitable filler material e.g., balsa or foam, etc. This part of the design must allow for the possible insertion of a spar and instrument wiring.

This procedure was then repeated for the remaining half-model before final bonding was implemented. A distinct advantage offered by this method was the ability to construct a simple glass-fibre/balsa model (i.e., no internal instrumentation or spar) quickly and accurately. This facility was extensively used for the construction of aerofoil models dedicated to oil-flow experiments.

Once the oil-flow tests had been completed it was decided that useful structural information, relevant to any future model design, could be obtained by a series of three experiments consisting of the following:

(1) The calculation of the torsional stiffness of the basic glass-fibre/balsa model. This was achieved by the construction of a test rig designed to twist the model with a known torque whilst monitoring the resulting torsional deflection. For a given applied torque the twist was measured at three spanwise positions, thus allowing for the calculation of both the torsional stiffness (K_{θ}) and rigidity (GJ) (see Figure 3.9). This information was then used to generate the design requirements for an internal spar.

- (2) The establishment of the centre of gravity by simultaneous suspension of the model and a plumb-bob from various points and locating the point of intersection of the resulting plumb-lines
- (3) The calculation of the moment of inertia about the 1/4 chord by means of a physical pendulum test.

Using the aforementioned wind tunnel model design criteria, the final structural composition of the NACA 23012(A) was completed and is illustrated in Figure 3.10. The aerofoil model contained a removable centre-span instrument pod and a hollow Aluminium spar (see Figure 3.11) designed to keep the weight at a minimum without reducing torsional rigidity. A summary of the structural design is given in Table 3.2 in which the structural deflection calculations were based on previously obtained unsteady aerodynamic data on the NACA 23012 aerofoil.

As mentioned earlier, instrument accessibility is an important aspect of any wind tunnel model design. In this particular model, the instrument pod housed thirty miniature silicon strain-gauge pressure transducers. Due to their small size (2mm diameter) and delicate wiring each transducer was mounted inside a perspex block which was vented to the atmosphere via a short length of 0.8mm bore PVC tubing. As illustrated in Figure 3.12, the position of this tube was varied to accommodate for the higher density of transducers at the leading edge. Each perspex block was then located in

the pod using an elastometric sealant, and the resulting wiring passed through an internally embedded 6mm bore PVC tube. This arrangement greatly assisted the initial insertion and later servicing of each transducer.

3.5 Conclusions

A method enabling the generation of a geometrical alteration to a standard aerofoil, allowing a modification in its static stall separation characteristics, has been developed. This method utilised a theoretical aerofoil design technique which quantified the geometrical difference in terms of a modification to the inviscid pressure gradient. The NACA 23012 aerofoil was successfully modified in such a manner that would enhance the trailing-edge separation characteristics whilst retaining the leading-edge pressure distribution; the subsequent aerofoil was designated the NACA 23012(A). The comparison of the unsteady performance of this aerofoil with that of the NACA 23012 should provide preliminary information about the effects of trailing-edge separation on the dynamic stall process.

CHAPTER 4

FLOW VISUALISATION

4.1 Introduction

An aerofoil's boundary-layer characteristics may be studied by coating its surface with a thin layer of oil which, under the action of the local wall shear stress, indicates the surface streamline (Chang, 1976). Since a separation line is generally an envelope of surface streamlines it can be visualised by this technique. Before assessing any measured pressure distributions it is often desirable to have a knowledge of the extent and form of any three-dimensional flow effects. This is of particular importance for, in the presence of induced-flow conditions, the pressure transducers may not lie within a region of nominally two-dimensional flow. The aim of this section of work was to investigate the flow development and degree of separation over two derivatives of the NACA 23012 aerofoil designed by the inverse technique described in Chapter 3. By establishing the amount of trailing-edge separation over each aerofoil, an insight into the applicability of the inverse aerofoil technique was obtained. The oil-flow visualisation technique

represented an easy and effective method of achieving this investigation

4.2 Flow Visualisation Technique

The oil-film technique, adopted for this series of tests, consisted of smearing the aerofoil's upper surface with a petroleum-based lubricating oil containing a suspension of fluorescent additive. When illuminated by ultra-violet light, the resulting mixture fluoresced and, after 'exposing' the coated aerofoil to the required airflow, the resulting pattern was recorded on black and white film. Good photographic contrast was obtained by removing the ultra-violet light by means of a yellow filter. The exposing of the oil consisted of setting the aerofoil incidence and then raising the airspeed from zero to the test value. As was pointed out by Gregory *et al* (1970), the static stall is a function of incidence and Reynolds number, as well as the direction in which these parameters are varied, since there may be a difference in the corresponding movements of separation and reattachment fronts. Thus, for the current tests, the separated flow present during flow acceleration, to the test velocity, could have been, to some extent, suppressed and modified by the acceleration itself. In order to study these effects a series of slow ramp tests was carried out, the results of which will be discussed Section 4.5.

Development of the flow pattern was allowed to proceed until either no further modification was likely or, in regions of oil accumulations, gravitational effects began to cause major distortion. To observe the aerofoil's overall stall development, a series of oil-flow patterns were obtained for a range of incidence values. Each resulting pattern was then photographed, producing a standard method of documenting the stall. An estimation of the separation point was then made by direct measurement from the photograph. Although an error of $\pm 3\%$ was assigned to these assessments, it was unknown to what extent the oil influenced the final separation point.

Unfortunately, due to structural considerations, the aerofoil had to be mounted vertically within the wind tunnel and therefore, in regions of weak shear stress, the effect of gravity gave a downward bias to the oil flow. This occasionally led to difficulty in interpreting the final 'developed' flow pattern, especially in the region of the tunnel roof. As well as supplying information about the extent of trailing-edge separation, the final oil-flow pattern also indicated the position of the laminar separation bubble and the nature of any corner flow.

4.3 Oil-Flow Characteristics of the NACA 23012 Aerofoil

A series of oil-flow tests were carried out, on the NACA 23012 at 1.5×10^6 Reynolds number, by Seto *et al* (1984), and for a complete visual comparison with the modified NACA 23012 aerofoils their photographic results are presented in Figure

4.1. A summary of their conclusions concerning the stall development is as follows:

- (1) The aerofoil exhibited a rapid trailing-edge stall characteristic.
- (2) The degree of flow three-dimensionality depended on the amount of trailing-edge separation present. Above an incidence of 14.0° , two distinct vortices formed at the outer span positions.
- (3) The trailing-edge separation front became irregular and unsteady as the stall progressed.
- (4) There was no indication of separation at the aerofoil/tunnel junction prior to the establishment of three-dimensional flow.
- (5) That it was unlikely that three-dimensional flow developments would be of significance prior to the attainment of maximum lift.

Further observations of the stall development on the NACA 23012 are discussed by Leishman (1984).

4.4 Oil-Flow Characteristics of Two Modified NACA 23012

Aerofoils

4.4.1 The NACA 23012(M1)

As mentioned in Chapter 3, two aerofoils were derived from the NACA 23012 using the inverse technique. The decision to design the second modification was based on the following oil-flow results obtained for the NACA 23012(M1).

Figure 4.2 shows the flow development on the NACA 23012(M1) obtained for various angles of incidence at a Reynolds number of 1.5×10^6 . Up to an angle of 11.4° the flow was essentially two-dimensional, and it was observed that the boundary layer underwent a laminar to turbulent transition which moved towards the leading edge with increasing incidence. At 12.5° the boundary layer began to separate asymmetrically from the trailing edge, with a tendency towards a larger separated region over the lower half span. For angles greater than 13.0° this asymmetry became significant and the three-dimensional flow increased. Two 'stall induced' vortices developed on the upper surface at 15.7° causing the flow pattern to become symmetrical with respect to the mid-span. Angles of incidence greater than 15.7° had stable symmetrical separation fronts, and the vortex pair was still present at 20.0° where 90% of the flow was fully separated.

The overall flow behaviour indicated that the NACA 23012(M1) had an enhanced trailing-edge turbulent boundary-layer stall

characteristic when compared to the basic NACA 23012 aerofoil (Figure 4.3). However, the change was relatively small and under dynamic conditions, where significant separation suppression may occur, its influence on the final outcome was doubtful. It was due to this reasoning that a second modification of the NACA 23012 was implemented.

4.4.2 The NACA 23012(A)

The flow development on the NACA 23012(A), not unexpectedly, demonstrated many similarities with that of both NACA 23012 and NACA 23012(M1) aerofoils. Figure 4.4 shows the results obtained for various angles of incidence at a constant Reynolds number of 1.5×10^6 .

At 10.0° , trailing-edge separation was initiated and, as the angle of incidence was increased, the separation front moved towards the leading edge with a high degree of flow two-dimensionality. For angles above 13.0° the separation front developed the familiar reverse 'S' pattern indicating a more prominent lower span separation. Approximately 60% of the aerofoil's upper surface area became separated at 15.3° and a stall induced vortex pair became apparent. However, unlike the NACA 23012 and 23012(M1) aerofoils, there was a change in vortex structure at 17.0° . The flow pattern became symmetrical, with the upper and lower span separated regions becoming equal in size. Since the NACA 23012(A) was designed to have a more prominent adverse pressure gradient over the rear upper surface, the local velocities, and hence surface

shear stresses, should be expected to be less than those found over both the NACA 23012 and NACA 23012(M1) aerofoils. Figure 4.5 clearly shows the oil flow, over the rear 25% of each aerofoil, becoming progressively more gravity biased. This suggested that, for each subsequent modification, this region was being subjected to an increasingly more intense adverse pressure gradient.

As expected, the overall flow behaviour indicated that the NACA 23012(A) had a trailing-edge turbulent boundary-layer stall. The measured separation points, as inferred by the oil-flow results, are illustrated in Figure 4.6 and they clearly indicate an enhanced trailing-edge stall. To complete the oil-flow investigation, tests were also carried out at Reynolds numbers of 1.0×10^6 and 1.85×10^6 , the results of which are also indicated on Figure 4.6, and it is interesting to note that they imply no significant change in the separation movement.

4.5 Discussion

Figure 4.7 illustrates a typical oil-flow test result and summarises the main flow components associated with any two-dimensional wind tunnel test. The following discussion considers these flow phenomena and suggests possible reasons for their existence. It is well known (Schlichting, 1979) that the boundary-layer flow approaching the stagnation zone of an obstacle separates and forms an unstable vortex sheet, which rolls up in a "horseshoe-like manner". Bippes and Turk

(1981) showed that, at high angles of incidence, the interference of the 'horseshoe vortex' and the separated region on the aerofoil prevented symmetrical flow conditions. It was further suggested that the result of this interference was the formation of an additional vortex, on the aerofoil's upper surface, near the tunnel wall. If this flow phenomenon is coupled with a minor tunnel flow imbalance then a highly asymmetrical flow separation will result. It was noted by Gregory *et al* (1970) that the spanwise flow variations appeared to be affected by the aerofoil profile and aspect ratio. The present oil-flow results appeared to demonstrate a similar dependence of flow three-dimensionality on aerofoil profile. A possible explanation of this phenomenon is, that the aerofoil's pressure distribution may have influenced the nature of the interference between the horseshoe vortex and the separated region.

As was suggested in Section 4.2, the region of separated flow may have been modified by the flow acceleration as the tunnel airspeed was raised to the required test value. This effect was studied by means of a series of slow ramp tests in which the angle of incidence was uniformly increased from zero to the test value after the tunnel airspeed had been set. Any difference in observed flow pattern was attributed to the elimination of the tunnel airspeed acceleration. Figure 4.8 shows that, for various angles of incidence, no significant change in flow pattern or separation point was indicated. However, this may have been due to the lack of sensitivity of the oil to subtle changes in the separated region.

4.6 Conclusions

The technique of oil-flow visualisation was successfully employed to verify the steady-state stalling characteristics of two modified NACA 23012 aerofoil sections designed by an inverse aerofoil design technique. When compared to the 'donor' NACA 23012 aerofoil, the second modification was found to have a greatly enhanced trailing-edge separation. This difference was assumed to be sufficient to influence the aerofoil's unsteady stall performance.

CHAPTER 5

STEADY AERODYNAMIC BEHAVIOUR

5.1 Introduction

Chapter 3 described a theoretical technique enabling the controlled modification of a given aerofoil's static stall separation characteristics by means of a particular geometrical alteration. The method developed was applied to the NACA 23012 aerofoil and a derivative, the NACA 23012(A), was designed which was predicted to have an earlier and more gradual trailing-edge separation growth. In order to assess the applicability of the aerofoil design technique, simply constructed wind tunnel models were tested using the oil-flow visualisation technique. Chapter 4 dealt with results from these tests, and some of the problems associated with the assessment of a given aerofoil's trailing-edge separation characteristics using this technique. Based on these results a fully instrumented wind tunnel model of the NACA 23012(A) aerofoil was constructed.

The present chapter describes the results of a series of static tests on both the NACA 23012 and 23012(A) aerofoils. Although static tests were carried out over a variety of

Reynolds numbers, comparison between the aerodynamic behaviour of the two test aerofoils was restricted to 1.5×10^6 , which corresponded to a Mach number of 0.11. These data were used to assess the applicability of the aerofoil design technique, investigate the change in trailing-edge separation characteristics, and to preface the unsteady pressure data presented in Chapters 6, 7 and 8. Wind tunnel wall corrections were not applied to the presented data.

5.2 Verification of the Aerofoil Modification Technique

In order to check the response of the thirty pressure transducers, a comparison with potential theory was carried out. Utilising the panel method, described in Chapter 3, theoretical pressure distributions were obtained for various angles of incidence. However, there are three possible reasons why the theoretical and experimental distributions should not coincide exactly.

- (1) Wind tunnel interference, associated with the circulation around the aerofoil, induces a curvature into the flow, modifying the aerofoil's incidence and camber (Rogers, 1959). This effect may vary slightly with each specific test section since the outcome depends on the aerofoil's own aerodynamic characteristics.
- (2) The influence of the boundary-layer will globally modify the aerofoil's pressure distribution in such a manner as

to cause the experimental values to differ from those given by potential flow.

- (3) A direct consequence of the test equipment and test conditions i.e., inappropriate distribution of transducers around the aerofoil contour, incorrect gain values, inadequate compensation from variations in tunnel air temperature, etc.

Figure 5.1 shows the comparisons between theoretical predictions and experimental results for both the NACA 23012 and 23012(A) aerofoils. Each transducer output is shown to be indicating the correct order of magnitude in pressure, and therefore the data acquisition system was considered to be functioning correctly.

Chapter 3 described a method by which the NACA 23012 aerofoil was modified to produce an aerofoil whose rear upper surface geometry induced an adverse pressure gradient of increased severity. This method relied entirely on potential flow theory and did not include any modifications due to viscous interactions. It was therefore interesting to compare the theoretical difference in pressure distribution between the two test aerofoils with those obtained from the wind tunnel tests. Figure 5.2 shows that the test data follow the predicted trend very well. However, a noticeable difference between the theory and the test data was that the predicted difference in suction peaks was not realised. On inspection of the NACA 23012 aerofoil, it became evident that its

leading-edge geometry and surface finish was not of the same high quality as the NACA 23012(A). This effect would reduce the suction peak on the NACA 23012 aerofoil. Further support of this was given by the further downstream position of the laminar separation bubble (illustrated in Figure 5.2) on the NACA 23012(A) indicating a longer laminar boundary layer, which would accompany the superior leading-edge finish. This was also indicated during a series of hot-film tests described in Chapter 8. After further consideration of the similar suction peaks, it was concluded that this feature would not be detrimental, as one of the criteria used in the aerofoil modification procedure was the retention of the flow conditions at the leading edge between the NACA 23012 and 23012(A) aerofoils.

5.3 Comparison of Separation Characteristics

Figures 5.3 and 5.4 display selected pressure distributions obtained during typical static tests on the two test aerofoils. At the higher incidence values, a series of separation points was deduced from the extent of the constant pressure region resulting from the wake formation over the upper surface of the aerofoil. However, obtaining the exact incidence above which fully attached flow could not be sustained was found to be difficult, since the trailing-edge pressure gradient became small at this condition. Figure 5.5 compares the estimated separation loci for both the NACA 23012 and 23012(A) aerofoils. Although the 23012(A) displayed an enhanced separation characteristic, it did not realise the

full modification indicated by the oil-flow visualisation tests (c.f., Figure 4.6). However, Figure 5.6 indicates that good agreement with the oil-flow results was obtained, in trend rather than absolute magnitude, and that, for the 23012(A), there was little dependency of flow separation on Reynolds number.

In agreement with the well recognised correlation by Gault (1957) both the NACA 23012 and 23012(A) aerofoils exhibited trailing-edge stall types (Figure 1.2). It is interesting to note that, although the abrupt trailing-edge separation characteristics of the NACA 23012 were delayed slightly, giving the NACA 23012(A) an initially slower rate of growth, the separation point still travelled rapidly forward between 60% and 25% chord. Separation stabilisation was achieved, for both aerofoils, at the 15% chord with attached flow remaining over the leading edge, until final collapse occurred with the bursting of the laminar separation bubble. Figure 5.7 illustrates three-dimensional representations of the chordwise pressure distributions and summarises the separation/re-attachment characteristics of the two test aerofoils. In general, during the downstroke phase of the test, the aerodynamic coefficients displayed both a larger amount of unsteadiness and occasionally a different course to that obtained for increasing incidence. The three-dimensional pressure plots clearly show both the unsteady behaviour at the leading edge, and the delay in the return to attached flow conditions. This is, of course, the familiar

characteristic of stall hysteresis, and is commonly found during most static tests.

Figure 5.8 displays the response of the local chordwise pressure coefficient, found over the upper surface of the NACA 23012(A), as a function of incidence and serves to illustrate the sequences of flow separation and reattachment over the aerofoil chord. The mild progressive pressure divergence may be attributed to the localised thickening of the boundary layer, followed by separation and wake formation. The analysis of individual pressure responses, as a function of time, will be shown later to be extremely valuable when studying the timing of the various aerodynamic events found during unsteady aerofoil experiments.

5.4 Comparison of Aerodynamic Behaviour

Generally, when discussing an aerofoil's aerodynamic behaviour, the lift parameters usually considered to be of most importance are the maximum lift coefficient, the lift-curve slope, and the zero-lift incidence. Similarly, important pitching-moment parameters are the magnitude at zero-lift and at $dC_m/d\alpha = 0$, just prior to stall.

Figure 5.9 compares the normal force coefficient and the pitching moment behaviour of the two test aerofoils from which the following results were obtained.

NACA 23012(A)

Zero lift incidence (α_0) = 1.3°
(potential flow value = 1.5°)
Cm at α_0 = 0.05
C_{Dmax} = 1.31
Stall incidence (α_{st}) = 13.6°
Cm at α_{st} = 0.06

NACA 23012

Zero lift incidence (α_0) = -1.2°
(potential flow value = -1.2°)
Cm at α_0 = -0.03
C_{Dmax} = 1.43
Stall incidence (α_{st}) = 14.2°
Cm at α_{st} = 0.00

Although an aerofoil's aerodynamic behaviour is inseparably related to its geometry, and the subsequent response of the boundary layer, the following discussion is divided into the three areas to assist the comparison between the two test aerofoils.

- (1) **Effect of the reflex trailing-edge;** As illustrated in Figure 5.4, the reflex trailing edge induces regions of pressure and suction on the upper and lower surfaces respectively. This 'inverted aerodynamic loading' has two predominant effects: the induction of a positive zero-lift incidence, and a positive pre-stall pitching moment.
- (2) **Effect of trailing-edge separation behaviour;** It has been shown that the enhanced separation characteristics displayed by the NACA 23012(A) were attributed to the increase in adverse pressure gradient over the rear upper surface. This behaviour induces a rounding of the normal force peak, a reduction in the stall incidence, and a lower maximum attainable lift.
- (3) **Effect of viscous interaction;** The effect of the boundary layer is to modify the aerofoil's global velocity field, which can be thought of as a modification to the profile to incorporate the displacement thickness. Abbott and v. Doenhoff (1959) showed, from both theory and experiment, that the zero-lift incidence is controlled by the camber, whilst the thickness distribution influences the lift-curve slope. It may be noticed that the NACA 23012(A)

displays a non-linear lift-curve behaviour. It is postulated here, that the effect of the reflex trailing edge, at moderate incidence values, was to induce the formation of a thick turbulent boundary layer over this region. This would have the effect of modifying the distribution of both thickness and camber. If the effective camber was increased, the zero-lift incidence would decrease, whilst the changing thickness distribution would modify the lift-curve slope. If the non-linear lift curve was the result of some form of viscous interaction, then its characteristic may change with Reynolds number. Figure 5.10 illustrates the aerodynamic behaviour of the NACA 23012(A) at a Reynolds number of 2.0×10^6 , and it may be noticed that the lift-curve slope now displays a greater linearity.

5.5 Conclusions

Based on static data recorded for the NACA 23012 and 23012(A) aerofoils at a Reynolds number of 1.5×10^6 , the following conclusions were made:

- (1) The theoretical aerofoil design technique, described in Chapter 3, can be used to advise the aerodynamicist of a change in profile geometry which would fulfil the design requirements.
- (2) Wind tunnel experiments have indicated that the effect of viscous interactions modify the predicted difference

between the basic aerofoil and its modified counterpart. This suggests that the inclusion of viscous/inviscid interactions within the aerofoil design procedure would be useful.

- (3) The objective, set in Chapter 3, of modifying a selected aerofoil in such a manner that would retain the leading-edge pressure distribution whilst forcing an earlier and more gradual trailing-edge separation growth has been, on the whole, achieved.
- (4) The unsteady testing of the NACA 23012(A), and comparison with the NACA 23012, should provide preliminary information into the effects of trailing-edge separation on the dynamic stall process.

CHAPTER 6

AERODYNAMIC BEHAVIOUR IN OSCILLATORY PITCH CONDITIONS

6.1 Introduction

As demonstrated in Chapter 1, a fundamental understanding of the dependence of static stall on aerofoil geometry has been obtained. The ability to categorise an aerofoil's geometry and steady-state separation characteristics from the sole interpretation of its variation in lift with incidence was shown to be possible. However, although a significant understanding of the dynamic stall process has been achieved, little is known about the specific effect of aerofoil geometry. In the past decade numerous new aerofoil designs (Dadone, 1978) have been used in an attempt to improve the stall characteristics of rotors without compromising advancing blade performance. McCroskey *et al* (1980) noted that almost none of these new aerofoils had been designed with dynamic stall considerations in mind, and few of them had been wind tunnel tested under unsteady conditions.

In general then, this has led to two main objectives being set by researchers in the unsteady stall field.

- (1) To create databases, specific to different wind tunnels, from which the basic dynamic stall characteristics of a series of representative helicopter rotor aerofoils can be compared. These collections of data are extremely useful to the helicopter industry, which has concentrated on the development of semi-empirical models of dynamic stall.
- (2) To investigate the type of unsteady stall and boundary-layer separation characteristics associated with each profile, since this can be expected to be crucial in correlating the differences between different sections, and in estimating the dynamic stall behaviour of new aerofoils in the future.

The present work attempts to satisfy both of these objectives by conducting both analysis of the aerodynamic forces (Chapters 5, 6 and 7) and of the boundary-layer response via pressure-time histories and hot-film signals (Chapter 8). The present chapter describes the results obtained during a series of oscillatory tests on the NACA 23012 and 23012(A) aerofoils at a Reynolds number of 1.5×10^6 and a Mach number of 0.11. All the oscillatory tests on the NACA 23012 aerofoil were carried out by Leishman (1984), whose work should be consulted if detailed information concerning his analysis is required.

6.2 Degree of Stall

6.2.1 Background

To facilitate a meaningful qualitative description of an aerofoil's unsteady aerodynamic characteristics, the behaviour of the pitching moment may be used as a criterion to indicate the degree of stall for a given set of oscillation parameters. McCroskey et al (1980) used this method to create four stall regimes which were used to describe, and compare, the unsteady response of a series of aerofoils. The evolution of these different types of stall behaviour become apparent when, for a given oscillation frequency and amplitude, the effects of a variation in mean angle are considered. For the present discussion a variation in mean angle, at a fixed reduced frequency of 0.10 and an amplitude of 10.0° , will be used to illustrate the four stall regimes.

6.2.2 No Stall

Figure 6.1 shows that, for a mean angle of 4.0° , the maximum angle of attack is of a similar magnitude to the static stall incidence and the boundary layer remains largely attached throughout the cycle. This flow can be approximated by classical inviscid theory and it will be illustrated later that this is especially true for the pitch damping.

6.2.3 Dynamic Stall Onset

This regime is the unsteady counterpart, for helicopter applications, to operating a fixed wing on the verge of static stall. It represents a measure of the maximum useful lift that a given aerofoil can deliver if drag-rise and moment stall are to be avoided. The nature of the unsteady airloads is a direct consequence of the unsteady effects on the aerofoil's boundary-layer separation characteristics and therefore can be expected to be largely dependent on its geometry. Although an aerofoil's geometry heavily dominates its static stall behaviour, McCroskey *et al* (1980) found that the static, or quasi-static (i.e low reduced frequencies), stall characteristics were not necessarily a reliable guide to the dynamic stall onset characteristics. In fact, they found that, for this particular regime, all their test aerofoils stalled by the mechanism of trailing-edge separation, for reduced frequencies from 0.10 down to 0.01, irrespective of the static stall behaviour. The present tests also showed that, under the aforementioned conditions, both the NACA 23012 and NACA 23012(A) aerofoils displayed trailing-edge separation characteristics similar to those observed under steady conditions. However, since in the present experiments, the static stall behaviour of both test aerofoils is of the trailing-edge type, it is difficult to augment McCroskey's findings.

In Section 6.4, a method, devised by Wilby (1984), of calculating the angle of incidence at which dynamic stall

onset is inevitable, called the 'critical angle', is presented. However, for the current discussion, a mean angle of 6.0° serves as a good illustration of the differences in dynamic stall onset between the NACA 23012(A) and NACA 23012 aerofoils. Figures 6.2 and 6.3 show the NACA 23012(A) to exhibit a slight drop in pitching moment, at the beginning of the downstroke, which suggested a local increase in rear loading that would accompany a rear separation with reattachment. Indeed, the three-dimensional pressure plot clearly supported this interpretation. This is not surprising since, as will be shown later, the NACA 23012(A) has just exceeded its critical angle, whilst the NACA 23012 has not.

6.2.4 Light Stall

The common aspect of light stall data is that it represents a transition from a static stall type behaviour, which can vary significantly from one aerofoil to another, to the deep stall (Section 6.2.5) regime, where the behaviour is dominated by the dynamic stall vortex. This condition, where the vortex shedding phenomenon is less well defined, has been noted as being that which is most common to the helicopter rotor. McCroskey et al (1980) noted that the origin, strength, and transient development of the vortex appeared to be dependent on all the parameters listed in Table 1.1. The airloads typically exhibit significant amounts of hysteresis and, as will be shown in Section 6.5, negative aerodynamic damping is more likely to occur than in deep stall.

Figures 6.4 and 6.5 show that, when the mean angle is increased from 6.0 to 8.0 degrees, both test aerofoils display the characteristics of light stall. The three-dimensional plot indicates that, when compared to the NACA 23012, the trailing-edge separation on the NACA 23012(A) had been significantly enhanced and the associated drop in pitching moment was less abrupt. Although a significant negative pitching moment had been induced, the resultant flow field appeared to resemble a coalescing of the dynamic stall vortex with the trailing-edge separation to create a more diffuse pressure wave. This interpretation was supported by the lack of any vortex induced perturbations in the normal force coefficient. In general then, the main difference between the two test aerofoils was that, although both displayed similar magnitudes in their airloads, the NACA 23012(A) approached these values in a less abrupt manner.

6.2.5 Deep Stall

As discussed in Chapter 1, numerous experiments have shown that dynamic stall is characterised by the shedding of a discrete vortex, whose convection over the aerofoil's upper surface induces a highly unsteady pressure field. If the reduced frequency and maximum incidence are sufficiently high, the vortex shedding phenomenon is well defined, the unsteady fluctuations in airloads are very large, and the qualitative results are relatively independent of aerofoil shape, Reynolds number and type of motion. This case is commonly known as the 'deep stall' regime.

When the mean angle is set to 10.0° , Figures 6.6 and 6.7 indicate that both the test aerofoils have entered the deep stall regime. The principal differences are very similar to those for the light stall regime, these being, the NACA 23012(A) having a more prominent trailing-edge separation, weaker vortex shedding and a slightly less abrupt approach to the maximum values of the airloads. Increasing the mean angle to 15.0° introduces two more events in the dynamic stall process:

- (1) The collapse of the leading-edge suction peak. The commencement of this event appeared to occur after the initiation of the dynamic stall vortex, and complete suction collapse only became apparent when the vortex strength had become significant. This series of events is illustrated in the three-dimensional plot of Figure 6.8. The apparent conclusion from these observations is that the leading-edge laminar separation bubble had no direct involvement with the initial formation of the dynamic stall vortex. This aspect was also noticed by McCroskey *et al* (1980), and will be discussed more fully in Section 6.3. It is interesting to note that the suction collapse, on the NACA 23012, induced a small pressure wave which originated close to the leading edge (see Figure 6.8(b)). This phenomenon indicated the possible presence of a weak 'suction collapse' vortex which, at approximately 50% chord, coalesced with the dynamic stall vortex (see also Section 6.3.2).

(2) The appearance of secondary vortex shedding. The generation of this secondary vortex appeared to be dependent on the strength of the initial dynamic stall vortex. Figure 6.9 supports this interpretation, since when the mean angle was increased to 20.0° , the secondary vortex became as strong as the dynamic stall vortex. Seto and Galbraith (1985) noted that when the dynamic stall vortex left the trailing edge there was a subsequent inrush of air over the upper surface. Combining this with the above observations, it is reasonable to postulate that it is this inrush which initiates the secondary vortex. Since both shed vortices have nearly identical characteristics, the above postulation may allude to the possibility that a similar initiation mechanism, involving a region of reversed flow, exists for the dynamic stall vortex.

6.2.6 Effect of Pitch Rate

Comparison between the three-dimensional pressure plots of Figures 6.2, 6.10, and 6.11 reveals that, during the light stall regime, the amount of trailing-edge separation present within the cycle was dependent on the imposed reduced frequency. This observation is in agreement with Leishman (1984) who also noticed that, for conditions under which the static stall incidence was exceeded by a small margin and slight separation was indicated, the separation could generally be suppressed by increasing the reduced frequency.

For a given set of oscillation parameters, it can be shown, that the maximum value of pitch rate is related to both frequency and amplitude in the following manner:

$$\dot{\alpha}_{max} = 2\pi f \alpha_a$$

The implication of the above discussion is that the amount of trailing-edge separation is controlled by the magnitude of the imposed pitch rate. Especially important to the stall onset is the magnitude of the pitch rate as the aerofoil passes through static stall incidence. The subsequent development of the stall is controlled by both the maximum incidence, attained during the motion, and, if the forcing function is periodic, the time spent above the static stall angle. McCroskey *et al* (1980) similarly found that, when considering the differences between test runs in the deep stall regime, the amplitude and reduced frequency were less important than the absolute value of incidence and its rate of change on the upstroke. They also suggested that the dynamic stall events proceeded on a time scale of $U_\infty t/c$ rather than ωt .

6.3 The Effect of Trailing-Edge Separation on Vortex Initiation

6.3.1 Background

A critical problem in modelling dynamic stall is the determination of the vortex initiation incidence. The value at which this event occurs identifies the transition from an extended static stall type behaviour, which will depend on the aerofoil profile, to a flow-field dominated by the development of the dynamic stall vortex. Therefore, when considering the development of a complete dynamic stall model, its dependence on both aerofoil profile and oscillatory forcing parameters will need to be realised.

6.3.2 Pressure-Time Histories

Chapter 1 introduced the idea that the dynamic stall vortex development could be inferred from the aerofoil's unsteady lift, drag and pitching-moment characteristics. However, it would be reasonable to postulate that the formation of a localised protuberance within the boundary layer would be immediately indicated by the response of the local pressure coefficient, and that the integrated values (i.e., the airloads) would 'de-sensitise' the inception point. Therefore, it would be prudent to develop a functional method of displaying the response of an aerofoil's local chordwise pressure coefficient to a variation in either time or incidence. Such a method was first suggested by Carta (1974)

and utilised by McCroskey *et al* (1980) to illustrate an aerofoil's unsteady boundary-layer separation characteristics. When considering the interpretation of each individual pressure trace the following points should be noted:

- (1) A mild progressive pressure divergence may be attributed to the localised thickening of the boundary layer, followed by separation and wake formation. This behaviour was normally found at the trailing edge.
- (2) An abrupt change in pressure coefficient may be used to locate the chordwise origin of the vortex inception and monitor its translation across the aerofoil's upper surface.

Over the last decade, it has been observed that the nature of the initial boundary-layer separation, that precedes vortex inception, strongly influences an aerofoil's dynamic stall behaviour, especially in the light stall regime. Based on the aforementioned pressure-time histories, the relative phasing between vortex initiation and trailing-edge separation can be used to generate the following unsteady stall types:

- (1) **Leading-edge stall**; the vortex forms at the leading edge (i.e., forward of the 5% chord position) before the trailing-edge pressure diverges.

- (2) **Trailing-edge stall**; a distinct trailing-edge pressure divergence precedes the vortex initiation, now generally at the 20-30% chord position.
- (3) **Mixed stall**; either trailing-edge pressure divergence preceding leading-edge vortex shedding at the 5% chord OR the formation of the vortex at approximately the 20-30% chord position followed by leading-edge suction collapse and trailing-edge pressure divergence.

Figure 6.12 illustrates two pressure-time histories, obtained by McCroskey *et al* (1980), for the NLR-7 and AMES-01 aerofoils undergoing an oscillatory test of 15.0° mean angle, 10.0° amplitude and 0.10 reduced frequency. In this reference, the NLR-7 aerofoil was categorised as displaying a trailing-edge stall behaviour, whilst the AMES-01 aerofoil was classified as mixed stall (graphically indicated by the shaded regions in the figure). Following the above criteria, Figures 6.13 and 6.14 show that whilst the NACA 23012(A) displays the features of a trailing-edge stall type, the NACA 23012 tends towards those of a mixed stall.

In agreement with the three-dimensional pressure plot (see Section 6.2.5) the pressure-time history for the NACA 23012 also indicated the possible existence of a weak suction-collapse vortex. This vortex, which apparently travelled at a slightly higher velocity than the dynamic stall vortex, caused the two to coalesce at approximately 50% chord.

6.3.3 Effect of Trailing-Edge Separation

Using the aforementioned analysis, an attempt at visualising the boundary layer was made. Figures 6.15 and 6.16 illustrate the postulated deep stall boundary-layer response prior to, and during, vortex formation. Based on the comparative analysis of the individual pressure-time traces, obtained from both aerofoils, the following observations were made:

- (1) The vortex inception point, displayed by the NACA 23012(A), appeared to originate further downstream. When combined with similar observations made by McCroskey *et al* (1976), on the ONERA Cambré profile, this characteristic may be tentatively attributed to those aerofoils whose unsteady stall type may be termed as trailing-edge.
- (2) The trailing-edge separation, as indicated on the NACA 23012(A) by divergences in pressure rearward of the 76% chord, appeared to be unsuppressed.
- (3) For both aerofoils the collapse in leading-edge suction occurred after the initiation of the vortex (see also Section 6.2.5)

Concentrating on the pressure response at the 27% chord, Figure 6.15 shows the NACA 23012(A) to display a reversal in local pressure-time gradient prior to the abrupt vortex induced divergence. This drop in suction suggested that a

region of separated flow, further downstream, had formed and was modifying the aerofoil's surface velocity distribution. Indeed, these turning points had accompanied a substantial rise in suction at the trailing edge, which strongly suggested wake formation.

The analysis of individual pressure responses, as a function of time, will be shown in Chapter 7 to be extremely valuable when studying the timing of the various aerodynamic events found during the dynamic stall process. Although the pressure-time histories locate the position of vortex inception and indicate the subsequent stall development, they supply little information about the detailed fluid mechanics of the actual process. However, it will be shown in Chapter 8 that this can be largely overcome by correlation of the pressure responses with a series of hot-film experiments.

6.4 Critical Angle Calculation

6.4.1 Background

Whilst considering the problem of assessing an aerofoil's dynamic stall performance, by virtue of its low Mach number (i.e. $M = 0.3$) steady-state maximum lift, Wilby (1980) reasoned that, since retreating blade stall was dynamic in nature, this parameter was not necessarily of high importance. He noted that, as shown previously, the limit to rotor thrust was the large and sudden change in the pitching moment which led to high blade torsional loads. Wilby

concluded that to attain high values of rotor thrust a blade section that can reach large values of incidence, in oscillatory conditions, without involving large changes in pitching moment would be beneficial.

6.4.2 Critical Angle Calculation

Figures 6.17 and 6.18 show the aerodynamic loads obtained for the NACA 23012(A) and 23012 aerofoils respectively during oscillatory tests at an amplitude of 8.0° and a reduced frequency of 0.10. The mean angle for these cycles was progressively increased allowing both test aerofoils to be taken from unstalled to highly stalled conditions. The resulting aerodynamic loads allowed the maximum deviation in pitching moment, from its pre-stall single loop, to be calculated and plotted against the maximum attained incidence in the cycle. Figure 6.19 shows the results obtained for both 8.0 and 10.0° amplitude. The intercept with the incidence axis gives the maximum value that each aerofoil can attain before there will be a break in the pitching moment. This value is known as the 'critical angle', and is the unsteady counterpart, for a typical full scale rotor, to operating a fixed wing on the verge of static stall. It is therefore a useful quantity when assessing an aerofoil's suitability as a rotor section. For aerofoils intended for use on helicopter rotor blades, it is the difference between the critical angle and the zero-lift incidence that is important.

The following data were obtained from static and oscillatory tests:

	$\alpha_o = 1.3^\circ$	
NACA 23012(A)	$\alpha_{ms} = 13.6^\circ$	giving $(\alpha_c - \alpha_o) = 14.3^\circ$
	$\alpha_c = 15.6^\circ$	
	$\alpha_o = -1.2^\circ$	
NACA 23012	$\alpha_{ms} = 14.2^\circ$	giving $(\alpha_c - \alpha_o) = 17.4^\circ$
	$\alpha_c = 16.6^\circ$	

Since the leading-edge pressure distributions of both test aerofoils were similar, the lower critical angle exhibited by the NACA 23012(A) aerofoil must have been caused by the trailing-edge separation aggravated by the more severe rear pressure gradient. When coupled with the positive zero-lift angle, due to the reflex trailing edge, the NACA 23012(A) displays a reduced performance in the unsteady regime.

6.5 Pitch Damping Boundaries

6.5.1 Background

The existence of excessive blade torsional loads feeding into the control system of a helicopter has long been recognised as a prime rotor limitation. These high control loads result from an aeroelastic self-excited pitching motion precipitated by repeated submersion of a large portion of the blade into and out of stall. This phenomenon is commonly known as 'stall

flutter', and results from the high angles of incidence required to maintain proper lateral trim requirements. Fortunately, Tarzanin (1972) noted that, in forward flight, blade stall, and the corresponding torsional loads, occurred for only a fraction of the rotor cycle, and therefore the phenomenon did not become divergent. However, when considering the magnitude of the torsional loads, it is reasonable to assume that the rotor blade profile, and its behaviour under a stall flutter situation, would be of prime importance.

6.5.2 Derivation of the Damping Factor

When considering the unsteady response of an aerofoil, the area enclosed within the pitching-moment versus incidence curve, and the sense of transcription, have an important physical significance. The net work done by the aerofoil on the surrounding airstream is proportional to the integral:

$$C_w = \oint C_m d\alpha$$

This integral, known as the 'work coefficient', is proportional to the area enclosed by the curve and is positive for an anticlockwise circuit. If the pitching-moment response contains a substantial area in a clockwise sense, the contribution of that area is negative and it represents an energy extraction from the airstream by the aerofoil. Net energy extraction in the cycle (negative damping) implies that the rotor blade oscillation, in which it occurred, would

tend to increase in amplitude and the blade would begin to flutter. It is therefore obvious that an aerofoil's stall flutter response is fundamentally dependent on its dynamic stall characteristics and thus can be investigated by identical oscillatory tests. When considering the value of the work coefficient, obtained from wind tunnel tests, it is convenient to convert it to the following form:

$$\delta = -C_w / \pi \alpha_m^2$$

which is known as the 'two-dimensional aerodynamic damping coefficient'. Liiva (1968) illustrated that, for a sinusoidal oscillation about the quarter chord, the theoretical work coefficient and two-dimensional aerodynamic damping coefficient were:

$$C_w = -\frac{1}{2} \pi^2 k \alpha_m^2$$

and

$$\delta_T = \pi k / 2$$

The latter of these two equations is frequently used to non-dimensionalise its experimental counterpart to form a grouping commonly known as the 'damping factor' i.e δ / δ_T .

6.5.3 Effect of Stall Penetration on the Damping Factor

It was shown in Section 6.2 that variations in the oscillation forcing parameters cause the events, which constitute dynamic stall, to shift around the cycle and produce significant changes in aerodynamic loadings. Concentrating on the pitching-moment response, Figures 6.2 and 6.4 show that initial penetration of stall (dynamic stall onset) introduced a clockwise loop which enlarged with increasing mean angle (light stall regime). Further excursions into the deep stall regime, illustrated by Figure 6.8, produced a pitching-moment break which was sufficiently early in the cycle to allow its maximum value to be achieved whilst the angle of incidence was still increasing. This introduced a secondary loop in the anticlockwise sense which helped reinstate positive damping.

Figure 6.20(a) summarises the damping response of the two test aerofoils as they progress through the four stall regimes. A closer examination of this particular data set gave rise to the following observations concerning the NACA 23012(A) aerofoil:

- (1) An earlier departure from the potential flow damping was apparent. Comparison of the three-dimensional pressure plots with those for the NACA 23012 revealed that this was due to an earlier trailing-edge separation.

(2) When compared to the NACA 23012 a more stable characteristic was displayed which was also attributed to an enhanced trailing-edge separation producing an earlier pitching-moment break. This observation was in agreement with Dadone (1978) who noted that, for reduced frequencies up to 0.12, positive damping was commonly associated with gradual static stall whilst negative damping was typical of abrupt static stall.

Figure 6.20(b) illustrates similar damping responses obtained during the specific oscillatory tests required to calculate an aerofoil's critical angle. It clearly shows that, while the NACA 23012(A) remained positively damped over the entire test range, the NACA 23012 became unstable when its critical angle was only exceeded by approximately 1.0° . Figure 6.21 presents the aerodynamic damping coefficient data in an identical manner to that of Carta (1967). For mean angles less than 10.0° , the deviation from the potential flow value indicates the amount of flow separation present within the cycle. In this format, it clearly illustrates the dominating role of reduced frequency on separation suppression.

6.6 Conclusions

Based on oscillatory data recorded for the NACA 23012 and 23012(A) aerofoils at a Reynolds number of 1.5×10^6 , the following conclusions were made:

- (1) The enhanced trailing-edge separation characteristic of the NACA 23012(A), observed during static tests, was carried through to the unsteady regime.
- (2) Although the two test aerofoils displayed similar magnitudes in the aerodynamic loadings, the NACA 23012(A) approached these values in a less abrupt manner.
- (3) The amount of trailing-edge separation, found during the oscillatory cycle, was controlled by the magnitude of the imposed pitch rate.
- (4) The leading-edge laminar separation bubble had no direct involvement in the initial formation of the dynamic stall vortex.
- (5) The vortex inception point, displayed by aerofoils whose unsteady stall type is termed as trailing edge, lies further downstream.
- (6) In terms of the difference between the critical angle and the zero-lift incidence, aerofoils that display trailing-

edge stall may have a reduced aerodynamic performance in the unsteady regime.

- (7) The NACA 23012(A) displayed a more stable damping characteristic which was attributed to the enhanced trailing-edge separation producing an earlier pitching moment break. In general, positive damping is commonly associated with gradual static stall, whilst negative damping is typical of abrupt static stall.

CHAPTER 7

AERODYNAMIC BEHAVIOUR IN CONSTANT PITCH CONDITIONS

7.1 Introduction

In Chapter 1, it was shown that the aerodynamic effect of rapidly pitching an aerofoil beyond its steady-state stall incidence has been studied by numerous investigators. Most of this work emphasised application to the retreating blade stall encountered by the helicopter rotor blade during high speed forward flight. Consequently, measurements were typically made of the unsteady aerodynamic loadings during sinusoidal pitching oscillations characteristic of the cyclic variation in incidence imposed on the rotor blade (Chapter 6). However, associated with oscillatory aerofoil wind tunnel tests is the necessity of acquiring a large data set required to cover, with reasonable resolution, all the conditions of interest (i.e., variations of amplitude, frequency, mean angle, Reynolds number, and Mach number). Also, the inherent non-linear nature of the aerofoil motion introduces difficulties when analysing individual various aspects of the stall process.

Chapter 6 showed that, for a given set of oscillation parameters, the maximum pitch rate, imposed during the cycle, was dependent on both the frequency and amplitude of the motion. It was further suggested, that the amount of trailing-edge separation, present within the cycle, was controlled by the magnitude of the imposed pitch rate. Based on this observation, it would be reasonable to speculate that the entire dynamic stall process may also be dominated by the magnitude of the instantaneous pitch rate. Especially important to the stall onset, is the magnitude of the pitch rate as the aerofoil passes through the static stall incidence (Section 7.3.2). The subsequent development of the stall is controlled by both the maximum incidence, attained during the motion, and, if the forcing function is periodic, the time spent above the static stall angle. In an attempt to clarify this effect, it would be prudent to consider a series of constant pitch rate displacements (i.e., ramp tests). If dynamic stall is governed by a fundamental aerodynamic process, dependent mainly on pitch rate, then a series of ramp tests should allow the sequential timing and manner of stall to be deduced and documented. The resulting decomposition of the stall process into a series of non-dimensional 'time delays' is of great value to the developers of predictive codes employing predominantly empirical procedures.

Recently (Lang and Francis, 1985), a more direct application of ramp tests has developed following the interest in using the lift and drag augmentations, that occur during dynamic

stall, to improve combat aircraft manoeuvrability. Such manoeuvres typically involve a rapid controlled pitching of the aircraft to a very high angle of incidence at low to moderate Mach numbers.

The present chapter describes the results obtained during a series of ramp tests on the NACA 23012 and 23012(A) aerofoils, at a Reynolds number of 1.5×10^6 , and cover a range of pitch rates from 0 to 330 °/sec. Although the original ramp testing of the NACA 23012 was carried out by Seto and Galbraith (1985), their data have been separately analysed by the author to facilitate a uniform comparison with the NACA 23012(A) aerofoil.

7.2 Ramp Aerodynamic Characteristics

Figures 7.1 and 7.2 illustrate selected ramp tests chosen to illustrate the effect of pitch rate on the stall development of the two test aerofoils. The immediate observation, from these data, is the dependence of the separation characteristics on the imposed angular velocity. Increasing the pitch rate induces the separation to transform from a static type behaviour to a deep stall characteristic, similar to that displayed by the oscillatory tests. Furthermore, comparing the three-dimensional pressure plots of Figure 7.1(c) with 6.9 illustrates the high qualitative agreement in dynamic separation behaviour for both ramp and oscillatory tests. Clearly a similar vortex shedding phenomenon is common

to both motions and, as Figure 7.3 displays, its effect on the aerodynamic coefficients is substantial.

As for the oscillatory tests, pressure-time histories can be used to categorise an aerofoil's unsteady boundary-layer response to the ramp input. Figures 7.4 and 7.5 show the NACA 23012(A) to display the features of a trailing-edge stall type, whilst the NACA 23012 tends towards those of a mixed stall. It is interesting to note that this result is identical to that found for the oscillatory tests, and this aspect will be discussed later in Section 7.3.

Seto and Galbraith (1985) observed that the vortex initiation was associated with a local pressure divergence in the region of the 20-35% chord. They argued that the presence or absence of this phenomenon, together with the behaviour of the leading-edge suction at 0.5% chord, may be used to indicate the type of flow separation present. In a manner similar to that presented by Seto and Galbraith, Figures 7.6 and 7.7 illustrate the behaviour of the pressure coefficient at the 34% chord for various values of reduced pitch rate. Their analysis of the NACA 23012 data divided the aerofoil's unsteady separation response into two phases: 'quasi-static' and 'dynamic', with a transition occurring at a reduced pitch rate of 0.0037. However, Figure 7.6 shows that the present analysis has revealed a third phase, designated 'quasi-dynamic', where, as indicated in Figure 7.10, the dynamic stall vortex is only of sufficient strength to induce the partial collapse in suction at the 0.5% chord.

The author is of the opinion that this apportioning the stall phases more logically, allowing the quasi-static behaviour to be free of any vortex shedding. Following these criteria, Figure 7.7 implies the NACA 23012(A) aerofoil to have an extended quasi-dynamic regime, with full dynamic stall not developing until the reduced pitch rate exceeds 0.0055.

As previously discussed in Chapter 6, the reversal in local pressure-time gradient, displayed at the 34% chord, indicated that a region of separated flow, further downstream, had formed and was modifying the aerofoil's velocity distribution. Therefore, the response of the 34% chord transducer may be used to imply the presence or absence of any significant trailing-edge separation. A generally accepted fact is that, during unsteady motion, the amount of trailing-edge separation within the cycle is controlled by the magnitude of the imposed pitch rate. Figure 7.6 indicates that, for the NACA 23012, significant separation suppression existed for reduced pitch rates above 0.011. However, Figure 7.7 implies that, for the illustrated range, this behaviour is not displayed by the NACA 23012(A) and is evidence of its enhanced separation characteristics.

It is clear, from the above discussion, that three salient locations for pressure history analysis are, at the leading and trailing edges, and in the vicinity of the 30% chord position. Focusing on these responses, Figure 7.8 implies that the vortex initiation was prior to the leading-edge suction collapse and, although not presented here, this was

found to be common for both test aerofoils at all relevant reduced frequencies. This particular phasing of events indicates the limited role of the leading-edge pressure distribution as an indicator of the region of local boundary-layer breakdown which precedes vortex formation. In fact, as Figures 7.9 and 7.10 show, although the manner of leading-edge response changes from a partial collapse during quasi-dynamic stall, to complete collapse during dynamic stall, the peak suction and its associated incidence continue to increase with increasing reduced pitch rate. It might be expected that the continual rise in peak velocity, and the implied increasing severity of the adverse pressure gradient, imposed on the local boundary layer, would eventually cause the vortex inception point to move towards the leading edge. However, the results, obtained for both test aerofoils, indicated that this trend did not occur, and that the vortex initiation point remained in the vicinity of the 30% chord.

It is interesting to compare the results illustrated in Figure 7.11 to those obtained by Wilby (1984), where a levelling off of both peak suction and its associated incidence was observed at a reduced pitch rate of approximately 0.01. Wilby suggested that a possible interpretation of his data was that, for low pitch rates the stall vortex was triggered by a rear separation, which was progressively suppressed as the angular velocity was increased. This allowed greater values of incidence, and higher suction peaks, to be attained before stall onset occurred. At high pitch rates, the rear separation was

sufficiently suppressed for the leading-edge pressure distribution to become the stall trigger. However, it must be appreciated that these data were obtained under a test condition of $Re = 2.8 \times 10^6$ and $M_\infty = 0.3$, and as such, the local Mach number at the leading edge was in the critical region of 0.85 to 1.05, thus allowing the development of strong compressibility effects. The present low speed tests were taken at a Mach number of 0.11 which, even at the highest pitch rate of 330 °/sec, only induced a local Mach number at the leading edge of approximately 0.5. The difference in these findings, therefore, indicate a possible effect of freestream Mach number on the role of the leading edge as a stall trigger.

7.3 Comparison With Oscillatory Data

7.3.1 Qualitative Results

If dynamic stall is governed by a specific boundary-layer response to the imposed pitch rate, then comparisons between ramp and oscillatory data should provide an insight into this phenomenon. The near linear portion of the oscillatory test should adequately span the aerofoil's static stall incidence, and the maximum attainable incidence should be large enough to ensure deep dynamic stall. In order that the comparison is valid, the stall process would need to be similar in the manner of onset and development. Chapter 6 introduced the use of pressure-time histories to illustrate an aerofoil's unsteady boundary-layer separation characteristics. It was

also shown that the analysis of individual transducer pressure traces may be used to locate the chordwise origin of the vortex inception, and monitor its subsequent translation across the aerofoil's upper surface. Figure 7.12 summarises the unsteady separation characteristics of the two test aerofoils undergoing both ramp and oscillatory variations in incidence. The pitch rate of the near linear portion of the oscillatory cycle was chosen to equate that achieved during the ramp test (≈ 150 °/sec). It can be seen that, for each test aerofoil, good qualitative agreement exists between the separation characteristics observed during each test condition. Galbraith *et al* (1986) suggested that, once initiated, an aerofoil's deep dynamic stall development was governed by a freestream dependent process and, therefore, similar observations for different motions could be made. The pressure wave, normally associated with vortex movement, may be highlighted by the use of pressure coefficient contour plots. In this format the vortex appears as a ridge, and Figure 7.13 illustrates that the gross features of the dynamic stall development are common for both types of motion.

7.3.2 Effect of Pitch Rate

Common to all the available literature on dynamic stall is the observation that unsteady effects are enhanced with increasing rate of change of aerofoil incidence. As discussed in Chapter 1, the boundary layer is particularly sensitive to pitch rate, and this is reflected in the response of

individual transducer pressure-time histories. If this is true, then, providing equal pitch rates are imposed, the boundary-layer response should be similar for different types of motion. Figures 7.14 and 7.15 compare the responses from three transducers obtained, for both test aerofoils, during oscillatory and ramp tests in which the pitch rate was approximately 150 °/sec. It can be seen that the stall onset (indicated by the abrupt pressure divergence at the 34% chord), vortex strength, trailing-edge separation characteristics, and the leading-edge suction response are all essentially independent of motion type. These pressure responses manifest themselves in the aerodynamic loadings and, Figure 7.16 illustrates the high qualitative agreement between the ramp and the upstroke of the oscillatory test.

The apparent conclusion from the aforementioned analysis is that, providing the aerofoil motion allows deep stall development, the dynamic stall process is governed by the magnitude of the pitch rate through the static stall incidence.

7.4 Dynamic Stall Event Timing

7.4.1 Definition of Timing Marks

Chapter 1 introduced the generally accepted qualitative description of the dynamic stall phenomenon, which involved an explanation of the distinctive aerodynamic loadings observed, by virtue of the division of the process into

several particular phases of flow development (Figure 1.4). The manner of the stall inception, and subsequent vortex translation, represent an important phase change from a flow dependency on the aerofoil state to that of the freestream, where the associated wake will be insensitive to the detailed aerofoil shape and motion. This process can be described as a transformation from a streamlined flow to that of a bluff body. The passage of the dynamic stall vortex over the aerofoil surface manifests itself in the aerodynamic loadings, and therefore, the time histories of the appropriate coefficients may be used as an indicator of the average development time. However, the formation of a localised protuberance within the boundary layer would be immediately indicated by the response of the local pressure coefficient, and therefore an assessment of the non-dimensional time delays, associated with the stall process, can be achieved by the isolation of well defined timing marks on particular chordal pressure histories. Figure 7.4 indicated vortex inception to occur in the region of the 30% chord, and hence stall onset was assumed to have begun when the pressure coefficient at the 34% chord abruptly diverged. From the three-dimensional representation of the upper surface pressure, it may be observed that there is a prominent peak in the trailing-edge pressure history. This, as discussed by Seto and Galbraith (1985), was taken to be the point at which the vortex broke away from the trailing edge, and the subsequent inrush of fluid into the low pressure region. This peak was assumed to be representative of stall completion. The association of the distinct stall

events with a common time scale, incorporating the effects of parameter variations (i.e., aerofoil, motion type, etc), would be most beneficial when attempting to model dynamic stall via an empirical approach.

7.4.2 Formation of Time Delays

Throughout the available literature relevant to dynamic stall, the non-dimensional pitch rate parameter, $\dot{\alpha}c/U_\infty$, seems to be the most important factor in determining the increase of the dynamic stall incidence above the static stall value. The essential requirement of an empirical dynamic stall model is to predict the dynamic stall delay, $(\alpha_{ds} - \alpha_{ss})$, and, based on the above argument, it is logical to assume as a first approximation:

$$\alpha_{ds} - \alpha_{ss} = f(\dot{\alpha}c/U_\infty)$$

When considering a practical method for the prediction of unsteady aerodynamic loadings for helicopter rotors, Beddoes (1975) adopted a statistical analysis of some 300 specific test cases exhibiting similar dynamic stall characteristics (e.g., Liiva et al, 1968). The fundamental physical principle for the model assumes that, once initiated, the stall and recovery processes unfold within a set non-dimensional time scale i.e., $t_n = tU_\infty/c$. For a particular test, the angle of incidence, α_1 , which delimits static behaviour is determined by the break in pitching moment. When the local value of incidence exceeds α_1 , the onset of separation is assumed to

be delayed for a finite period of time, τ_1 , during which the aerodynamic response is an extension of the attached flow behaviour. If this time delay is exceeded, vortex shedding is triggered, and after a further period of time, τ_2 , during which the vortex traverses the chord, it passes free of the trailing edge. In this interval, lift is generated by the vortex, and the overall level maintained equivalent to that for the fully attached flow, but the centre of pressure moves aft as a function of both angle of incidence and time. Figure 1.6 illustrates the sequence of events and associated behaviour of lift and pitching moment. The calculated values of these time delays did not appear to be sensitive to pitch rate, and were found to be:

$$\tau_1 = 2.44 \pm 0.49 \text{ and } \tau_2 = 5.41 \pm 0.61$$

Further research by Beddoes (1978) showed that the steady flow pitching-moment break criterion led to a premature prediction of dynamic stall for some aerofoils at low Mach number ($M_\infty < 0.35$). Beddoes concluded that this was due to the effect of trailing-edge separation, and that the criterion of static pitching-moment break was inadequate for the dynamic case. He argued that the suppression of trailing-edge separation, under dynamic conditions, would allow the usage of the leading-edge pressure distribution as a criterion for static delimitation. This method allowed the time dependent local velocity distribution to be calculated for unsteady attached flow conditions. The subsequent information was used to predict the initiation of the dynamic stall process by

comparison with a limiting value of leading-edge velocity given by the correlation of Evans and Mort (1959). Application of the new criterion gave a reduction in τ_1 to a value of approximately 2.0.

It is obvious, from the above discussion, that a fundamental aspect of an empirical time delay model is the selection of the event, and associated incidence, that signifies the delimitation of the static stall behaviour (hereby designated the dynamic stall criterion). However, following the selection of a particular dynamic stall event (i.e., vortex inception), the choice of whether or not to reference it to a unique static stall feature remains optional. For example, consider a ramp test whose start incidence is α_0 , dynamic stall criterion, α_1 , and vortex inception, α_v . Then the non-dimensional time delay for vortex inception, referred to α_1 , is:

$$\tau = \Delta t U_\infty / c = (\alpha_v - \alpha_1) / (\dot{\alpha} c / U_\infty)$$

Assuming, as Beddoes (1975) found, the time delays were independent of pitch rate, a linear regression calculation, using α_v as the dependent variable and $\dot{\alpha} c / U_\infty$ as the independent, would need to be constrained to pass through α_1 before the calculated gradient of the line can be equated to the time delay.

If, however, the observed relationship between α_v and $\dot{\alpha}c/U_\infty$ is non-linear, then one of the following conclusions may apply:

- (1) The time delay is a function of the pitch rate.
- (2) The choice of dynamic stall criterion was incorrect.

To alleviate this problem the linear regression calculation may be unconstrained, and the calculated intercept with the incidence axis attributed to the critical value of static delimitation. Although this method was adopted during the present analysis, Section 7.5 illustrates the problem of attributing this particular value of incidence to a meaningful static stall event.

7.5 Calculation of Time Delays

7.5.1 Stall Onset

From the ramp data, collected for the two test aerofoils, the variation of pitching-moment break (indicating vortex inception) with pitch rate was obtained for each profile. Subsequent analysis followed that given by Wilby (1980), in which a definition of the pitching-moment break was taken as the angle of incidence, α_{mv} , for which the value of the coefficient had fallen by 0.05 below its maximum value. Plotting these values against the non-dimensional pitch rate parameter, $\dot{\alpha}c/U_\infty$, and calculating the resultant slope gave a

value for non-dimensional time delay associated with vortex shedding. It is apparent, from Figure 7.17, that the variation of α_{mv} , does not possess a unique linear dependence on the pitch rate parameter throughout the full range of pitch rates. However, in conformation with those data obtained by Wilby (1980), it was inferred that a linear relationship existed for values of pitch rate parameter less than 2.0. The results from this analysis imply that the earlier vortex initiation, displayed by the NACA 23012(A), had been triggered by the enhanced trailing-edge separation characteristics. However, as previously mentioned, Beddoes (1978) concluded that, for aerofoils displaying prominent trailing-edge separation, the use of a pitching-moment break, to indicate stall onset, may be inadequate. Therefore, an alternative method of defining vortex inception, from the pressure histories at particular chord positions, was implemented, the results of which are discussed in the following text.

If the divergence of the 34% chord pressure history can be used to indicate vortex inception, then its response may also supply information about the effect of trailing-edge separation on the stall onset. Figure 7.18 shows the NACA 23012(A) to display a reversal in local pressure-time gradient prior to the abrupt vortex induced divergence. This drop in suction suggested that a region of separated flow further downstream, had formed and was modifying the aerofoil's surface velocity distribution. Indeed, this turning point was accompanied by a substantial rise in

suction at the trailing edge, which strongly suggested the formation of a wake behind the aerofoil. The NACA 23012 displayed neither of these characteristics, and therefore presumably very little, if any, trailing-edge separation had occurred prior to vortex inception. The delay in pressure divergence, displayed by the NACA 23012(A), is significant, since it suggests that a possible effect of enhanced trailing-edge separation is to suppress vortex initiation. This particular observation is significant, since it contradicts the previous time delay calculation based on the pitching-moment break. To further investigate this conflict, pressure-time histories were analysed, and the incidence at which the earliest abrupt vortex induced divergence, within the region of 20-40% chord, was noted. This incidence, designated α_{pv} , was used in an identical time delay calculation to the pitching-moment break. Figure 7.19 illustrates the results of this analysis, which, with respect to the NACA 23012, now imply the NACA 23012(A) to have a delay in vortex initiation. It is interesting to note that for each test aerofoil the implied value of static delimitation, illustrated by the intercept with the incidence axis in Figure 7.19, is approximately 1.5° greater than the static stall angle, obtained from the steady-state tests described in Chapter 5. The significance of this intercept is at present unclear and, although not presented here, warrants further investigation. Assuming that the pressure history divergence gave a correct indication of vortex inception, Figure 7.20 may help to resolve the contradiction between the two aforementioned time delay calculations. The implication

is that, a 0.05 reduction in pitching moment for the NACA 23012(A) was caused by the presence of trailing-edge separation, whilst for the NACA 23012 this response was due to the presence of the dynamic stall vortex.

7.5.2 Post-Stall Characteristics

Figure 7.21 illustrates that a periodic vortex shedding was induced subsequent to the aerofoil developing a region of fully separated flow over the upper surface. The observed periodic fluctuations in trailing-edge pressure were found to be approximately that for a Von Karman vortex street shed by a circular cylinder, having a diameter equal to the vertical projection of the aerofoil chord. As discussed by Schlichting (1979), a cylinder will generate a vortex street at a Strouhal number of 0.21 for Reynolds numbers less than 10^6 , and at 0.27 for values greater than 3×10^6 . No regular vortex street will be formed when the aerofoil is between these limits. The Reynolds number of a cylinder equivalent to the test aerofoil, at an incidence of 40° , is approximately 10^6 which, since this is a value near the boundary where periodic shedding would cease, may explain the decay in shed vortex strength with time. However, the averaging process, used during data reduction, will also contribute to the elimination of any out-of-phase phenomena.

7.6 Conclusions

Based on ramp data recorded for the NACA 23012 and 23012(A) aerofoils at a Reynolds number of 1.5×10^6 , the following conclusions were made:

- (1) The nature of the upper surface separation was dependent on the imposed angular velocity. Increasing the pitch rate induced the separation to transform from a static type behaviour to a deep stall characteristic, dominated by the presence of a shed vortex. The enhanced trailing-edge separation characteristics, of the NACA 23012(A) aerofoil, caused an increase in the pitch rate at which weak vortex shedding first appeared.
- (2) The amount of trailing-edge separation, found during a particular ramp test, was modified by the magnitude of the imposed pitch rate. For the NACA 23012 significant separation suppression existed for reduced pitch rates above 0.01. This behaviour was not observed for the NACA 23012(A), and was accepted as evidence, that the enhanced trailing-edge separation characteristics, observed during static tests, were carried through to the unsteady regime.
- (3) Based on the qualitative comparisons between ramp and oscillatory data it was possible to conclude, that the dynamic stall process was governed by a specific boundary-layer response to the magnitude of the pitch

rate, imposed by the forcing function. Especially important to the stall onset point was the value subjected to the aerofoil as it passed through the static stall incidence.

- (4) The leading-edge laminar separation bubble had no direct involvement with the initial formation of the dynamic stall vortex.
- (5) On comparison of the present ramp data with those obtained by Wilby (1984), a possible effect of freestream Mach number on the appearance of the leading-edge pressure distribution as the stall trigger was implied.
- (6) The deduction of the sequential timing and manner of the stall process was shown to be effectively accomplished by the use of ramp test data.
- (7) The method adopted to define vortex inception was shown to be critical when attempting a calculation of the non-dimensional time delay associated with this event. Based on the analysis of pressure histories, at particular chord positions, it was deduced that a consequence of significant trailing-edge separation was to delay the initiation of the dynamic stall vortex.

CHAPTER 8

HOT FILM ANEMOMETRY

8.1 Introduction

In Chapter 6 it was shown that the pressure-time histories could be used to locate and monitor the development of the dynamic stall vortex. However, this form of analysis supplied little information about the fundamental fluid mechanics of the process. It is well known that static stall mechanisms are derived from combinations of separation phenomena at the aerofoil's leading and trailing edges. It would therefore be reasonable to assume that a similar picture may emerge when considering an aerofoil's dynamic stall characteristics. A major component of dynamic stall is the overshoot of the static stall incidence which, as discussed in Chapter 1, implies the existence of a time delay induced by the unsteady response of both the potential flow and the aerofoil's boundary layer.

Numerous oscillatory aerofoil tests involving either hydrogen bubbles in water (McAlister and Carr, 1978) or oil-smoke in air (Robinson and Luttges, 1983) have attempted to visualise the unsteady boundary layer during the dynamic stall process.

Although these experiments are extremely valuable their application is restricted by the low Reynolds number required to achieve successful visualisation. This Chapter describes the results obtained from a series of hot-film experiments which allowed an investigation into the boundary-layer characteristics at a Reynolds number of 1.5×10^6 .

8.2 The Hot-Film Anemometer

A standard method of investigating the surface shear stress distribution, associated with a boundary-layer flow, is the use of hot-film probes. This equipment can determine the boundary-layer transition, flow reversal and separation characteristics over a large Reynolds number range. Although the hot-film is a powerful sensor, its design and construction gives rise to the following problematic characteristics:

- (1) For single element gauges, forward and reversed flow can not be directly distinguished. However, since the output of the probe is related directly to the wall shear stress, when flow reversal occurs, the instantaneous value of skin friction passes through zero, which results in a local minimum in the resultant signal.
- (2) Meier *et al* (1981) noted that in the region of vanishing wall shear stress, the hot-film became insensitive to the surrounding flow conditions. McCroskey *et al* (1976) showed that this feature was caused by heat loss to the

substrate of the gauge which had the effect of causing the minimum value of the hot-film signal to decrease slowly with time.

- (3) Subjective decisions are required in order to isolate salient features of the flow behaviour. McCroskey *et al* (1982) commented that the "evaluation of hot wire data is very subjective, and presents a formidable analytical task".

These effects can make the interpretation of the signal difficult. Whenever possible, error bands, associated with each hot-film signal, were estimated and these are indicated on the relevant figures.

8.3 Steady-State Results

8.3.1 Boundary-Layer Characteristics

Figures 8.1 and 8.2 illustrate typical sets of ultra-violet oscillograph traces obtained during static tests on the two test aerofoils. The vertical scale on the trace represents the uncalibrated boundary-layer surface shear stress, whilst the horizontal axis depicts time. The angle of incidence was also recorded and is illustrated by a series of 'steps'. It should be noted that in order to conveniently accommodate the twelve hot-film output signals on the UV paper, the four trailing-edge traces were inverted. Appropriate to each chordwise gauge, the estimated points of transition, flow

reversal, and separation are marked on the resulting output trace.

When the hot-film was within the laminar region the output signal contained, as expected, very little noise indicating that no boundary-layer turbulence was present. The progressive drop in output followed by an abrupt increase can be interpreted as a transition from laminar to turbulent flow. This characteristic demonstrates the low wall shear stress of the laminar region and, when used in conjunction with the oil-flow visualisation results (Chapter 4), indicates the possible presence of a leading-edge laminar separation bubble.

In contrast to the laminar region, the signal from the 90% gauge shows the high noise generated by the turbulent boundary layer. As a result of this turbulent component being superimposed on the mean response, the instantaneous value of the signal reaches zero before flow reversal of the ensemble averaged flow has occurred. This observation is in agreement with Kline *et al* (1981) who noted that two-dimensional turbulent flow detachment was not a single event but a transition from attached to detached flow. For a turbulent boundary-layer, zero wall shear stress is created by the averaging to zero of strong unsteady motions of opposite sign, and therefore full detachment occurs over a zone. However, forward of the 48% chord position, separation occurred in a different manner, apparently involving a

shorter transition time to detached flow, and weaker post-detachment flow reversal.

8.3.2 Flow Separation Estimation

Figure 8.3(a) shows the estimated static separation loci for both the NACA 23012(A) and 23012 aerofoils. Although the NACA 23012(A) displayed an enhanced separation characteristic, Figure 8.3(b) indicates that it did not realise the full modification inferred by the oil-flow visualisation tests. However, this figure also displays two 'pre-separation' points of low wall shear stress, as indicated by the trailing-edge hot-films, and these correlate much closer with the oil-flow results. The implication is therefore, that in regions of low wall shear stress, the accumulation of oil promotes boundary-layer separation. Since estimations of flow separation from oil-flow tests are commonly hampered by oil accumulations, gravitational effects and three-dimensional flow, it is not surprising that the correlation with the hot-film gauges is poor.

As previously discussed in Chapter 6, separation estimations can be achieved by the analysis of the instantaneous chordwise pressure distributions. Figure 8.3(c) shows that, for incidence values less than 17.0° , good agreement exists between the estimated separation points from both hot-film and pressure distribution data. The consideration of the reattachment loci, as indicated by the hot-films and pressure

distributions (Figure 8.3(d)) led to the following interesting observations:

- (1) Both aerofoils displayed similar reattachment characteristics.
- (2) For incidences above 18.0° , both aerofoils displayed an approximate 3.0° difference between separation and reattachment.
- (3) For incidences below 15.0° , the NACA 23012 still displayed a small difference, whilst the NACA 23012(A) did not.
- (4) Leishman (1984) commented that, for the NACA 23012, the correlation between hot-film reattachment and oil-flow separation was much closer. However, on consideration of the experimental error limits associated with each method of separation estimation, this observation was difficult to substantiate; the data obtained for the NACA 23012(A) did not support this observation. Although the subjective nature of both hot-film and oil-flow analysis combined with Leishmans limited number of gauges (only three) would probably explain this difference of opinion.

In agreement with the oil-flow results, Figure 8.4(a) demonstrates that, for the NACA 23012(A), there was little dependency of flow separation on Reynolds number. Figure

8.4(b) also shows a similar trend for the NACA 23012 aerofoil.

8.4 Ramp Test Results

8.4.1 Flow Reversal Characteristics

Figures 8.5 and 8.6 illustrate typical hot-film data obtained during ramp tests on the two test aerofoils. Following the same rules as for the steady tests, the estimated points of average zero wall shear stress are indicated for each chordwise station. During each ramp test, five cycles of hot-film data were logged. These data were then visually compared, in a qualitative manner, and a 'representative' cycle was selected for final detailed analysis. As previously mentioned, hot-film data evaluation presents a formidable task, and the above procedure was adopted to reduce analysis time. Unfortunately this left a large amount of data unanalysed , and, more importantly, the final results may not accurately represent the aerofoil's average unsteady boundary-layer response to a particular test condition.

When considering the characteristics of an unsteady boundary layer, it must be remembered (Chapter 1) that flow reversal and separation are generally distinct phenomena. Flow reversal refers to conditions in the inner part of the boundary layer, adjacent to the aerofoil surface, and its onset corresponds to the vanishing of the local wall shear stress. Separation, on the other hand, refers to the

detachment of the outer flow from the aerofoil contour, and the subsequent breakdown of the classical boundary-layer equations. Figure 8.7, therefore, compares the zero skin friction loci for both of the test aerofoils undergoing an identical series of ramp tests of increasing pitch rate. These data display a distinct delay in the movement of the flow reversal point with increasing pitch rate. Scruggs *et al* (1974) commented that any delay in the flow reversal onset could be regarded as an estimate of the delay in dynamic stall onset.

Figure 8.8 illustrates the chordwise pressure distributions, for an equivalent series of ramp tests, at selected instantaneous incidence values equal to those indicated by flow reversal at the 90% chord hot-film. For pitch rates greater than 4.8 °/s the pressure distributions for the NACA 23012 do not indicate separation at the 90% chord despite the existence of flow reversals. Even when the estimated angular error band for the hot-film traces was accounted for, this general observation was still apparent. As discussed in Chapter 1, the flow in the interior of the turbulent boundary layer is strongly affected by unsteady effects. In a particular series of unsteady turbulent boundary layer experiments, Parikh *et al* (1981) observed that if the applied unsteady pressure gradient was varied at a significant frequency, the boundary-layer thickness remained frozen even though flow reversals were indicated. This behaviour is in contrast to that of a steady boundary layer, where a large thickening of the shear layer occurs as flow reversal is

approached. The present experimental results support this observation since they indicate that regions of zero average wall shear stress, and weak flow reversals, can exist without boundary-layer separation. However, although the trailing-edge pressure gradient is very low, the chordwise pressure distributions for the NACA 23012(A) may be indicating that the onset of flow reversal and separation are in closer agreement. The implication then, is that if the external adverse pressure gradient is strong enough the unsteady boundary layer will separate and a small wake will form behind the aerofoil.

8.4.2 Vortex Initiation

Figure 8.9 illustrates the chordwise pressure distributions, obtained during a ramp test of 100 °/s pitch rate, at incidence values chosen to coincide with those indicating flow reversal at the 34% chord hot-film. The NACA 23012 pressure data clearly indicate that boundary-layer separation had not occurred despite the deep penetration of flow reversal towards the leading edge (c.f., Figure 8.6). However the NACA 23012(A) pressure data now positively indicate flow separation and although not coincident with the point of flow reversal the possibility of the formation of a wake behind the aerofoil now exists (c.f., Figure 8.5).

Whilst studying the deep dynamic stall characteristics of the NACA 0012 aerofoil, McCroskey et al (1976) noted that a region of highly disturbed boundary-layer flow progressed

upstream, with increasing incidence, to the vicinity of the 30% chord. This behaviour was described as a 'tongue of reversed flow', since it was found that no upper surface pressure divergence, indicating possible boundary-layer separation, was observed. Water tunnel experiments by McAlister and Carr (1978) also found that, prior to vortex formation, a region of reversed flow momentarily appeared over the entire upper surface without any appreciable disturbance to the viscous-inviscid boundary. Figures 8.9(b) and 8.9(d) display the pressure distributions at an incidence of 1.6° above that for which flow reversal was indicated at the 34% hot-film. At these incidence values, both test aerofoils developed a region of discontinuous pressure gradient between the 20 to 50 percent chord (marked 'P' in the figure). It was generally observed that this region developed into the well known vortex induced pressure protuberance, whose appearance correlated with the pressure divergence at the 34% chord location (see also Chapter 7). McCroskey *et al* (1980) observed that, for aerofoils displaying a trailing-edge type static stall, unsteady moment stall was preceded by a movement of flow reversal in a thin layer at the bottom of the boundary layer. When this flow reversal point reached the leading-edge region, the boundary layer broke down and a vortex formed at the 30% chord position. The present data support this observation that, for aerofoils which display a steady-state stall mechanism via abrupt or gradual trailing-edge separation, vortex initiation occurs after the appearance of flow reversal at approximately 30% chord.

8.4.3 Time Delay Calculation

Assuming that the dynamic stall vortex is initiated after the flow reversal point has reached the 34% chord, a series of ramp tests of increasing pitch rate can be used to calculate a time delay similar to that developed in Chapter 7. Figure 8.10 shows the angle of incidence at which the point of flow reversal reached the 34% hot-film, plotted as a function of the pitch rate parameter. A linear regression calculation on these data points gave the following results:

- (1) The NACA 23012(A) had a higher time delay than the NACA 23012. This was attributed to the slower movement of the flow reversal point over its upper surface.
- (2) The value of each intercept was approximately equal to the incidence at which flow reversal reached the 34% chord during a static test.

Both the pressure distributions and the pressure divergence at the 34% chord indicate that there was a finite time between the arrival of flow reversal at the 34% chord and the formation of the dynamic stall vortex. This extra time delay may be dependent on the magnitude of the adverse pressure gradients ahead of the 34% chord i.e., when a certain value of pressure gradient is acquired, the local boundary layer, in the region of the zero shear stress point, breaks away from the aerofoil contour and forms the dynamic stall vortex, which subsequently feeds from the reversed flow moving

upstream from the trailing edge. Figures 8.5 and 8.6 indicate large increases of reversed flow, signifying the formation of the dynamic stall vortex. A well known effect of trailing-edge separation is the reduction of the leading-edge suction peak. It is postulated here, that, during the aforementioned unsteady motion, this effect will relieve the leading-edge pressure gradients, allowing a delay in boundary-layer breakdown and subsequent vortex formation.

Figure 8.11 summarises the theoretical results obtained by Scruggs *et al* (1974), in which an unsteady potential flow and unsteady boundary-layer calculation was utilised to investigate the effect of pitch rate on the behaviour of the flow reversal point. Although these data were for the NACA 0012 aerofoil at a Reynolds number of 1×10^6 , they have predicted the general trend of the present experimental data. Whilst considering the time delay, associated with dynamic stall overshoot, Scruggs examined the predicted arrival of the flow reversal point at the 50% chord. Figure 8.11(b) reproduces his theoretical results and compares them with the current flow reversal data obtained from the 48% chord hot-film. The correlation in trend is seen to be very high.

8.4.4 The Unsteady Laminar Separation Bubble

Brief mention should be made in this Chapter on the attempts to relate the onset of dynamic stall to the bursting of the leading-edge separation bubble e.g., the work of Johnson and Ham (1972). The bubble characteristics were modelled in such

a way that unsteady potential flow effects delay its bursting, which was the mechanism presumed to precipitate the dynamic stall process. The present results indicate that, at least for trailing-edge stall aerofoils, bubble bursting was not involved in the formation of the dynamic stall vortex. Similar results obtained by McCroskey et al (1980) also indicated that for many types of aerofoils, bubble bursting was not the correct mechanism for dynamic stall onset.

8.5 Oscillatory Test Results

8.5.1 Flow Reversal Characteristics

Figures 8.12 and 8.13 illustrate sample hot-film UV records, for both test aerofoils, obtained during an oscillatory test of 10° mean angle, 10° amplitude and 0.10 reduced frequency. As mentioned previously, each flow reversal locus was obtained from the analysis of one individual cycle and therefore may not accurately represent the aerofoil's average unsteady boundary-layer response to a particular test condition. For selected tests, two or three cycles were analysed and, in general, the agreement in flow reversal over the rear of the aerofoil was good. However, as shown in Figure 8.13, differences were occasionally observed in the leading-edge region. Figures 8.14 and 8.15 demonstrate the effect of reduced frequency on the flow reversal loci for two oscillatory tests of 10° mean angle and amplitudes of 8° and 10° respectively. The dominant effect is, as expected, very similar to that of increasing pitch rate. These data

reinforce the observation that, for locations greater than the 50% chord, the NACA 23012(A) displayed a tendency to reach the condition of zero wall shear stress before the NACA 23012. Figure 8.16 illustrates the chordwise pressure distributions that accompany the hot-film tests above. These data, which show distinct similarities to the ramp data, highlight the difference between flow reversal and separation during unsteady flow conditions. They also show that the dynamic stall vortex is not due to the bursting of the leading-edge bubble, but is initiated after flow reversal reaches the 34% chord position.

8.5.2 Time Delay Calculation.

When considering vortex initiation during an oscillatory test, the non-linear variation in pitch rate throughout the cycle complicates aerofoil performance comparison. Referring to the results obtained from the ramp tests in Chapter 7, Figure 7.19 can be used, in conjunction with the maximum pitch rate experienced during the oscillatory test, to estimate the incidence at which the dynamic stall vortex would be initiated. For an oscillatory test of $10^\circ + 10^\circ \sin \omega t$ at 0.1 reduced frequency, the NACA 23012 ramp data indicated that vortex initiation would occur at the maximum incidence. However, although a similar calculation for the NACA 23012(A) suggested that vortex initiation would not occur unless the maximum incidence was increased by 1.0° , Figure 8.16 indicates that both aerofoils displayed vortex formation (marked 'V' in the figure) at the maximum oscillatory

incidence. Based on these observations, two possible conclusions exist:

- (1) The decreasing pitch rate encountered by the aerofoil, as the maximum incidence was approached, induced premature initiation of the dynamic stall vortex.
- (2) That there must exist a critical incidence, lower than the vortex initiation value, which, if exceeded makes vortex formation inevitable. This observation is very similar to that of Wilby (1980) who, as described in Chapter 6, suggested that for an oscillatory motion there existed a critical angle which, if exceeded, would produce an unavoidable break in pitching moment.

As for the ramp data, a time delay calculation based on the arrival of flow reversal at the 34% hot-film can be achieved. However, as discussed above, if the maximum oscillatory incidence is too low, then vortex shedding will be constrained to occur at this point, and any differences between the two test aerofoils will be obscured. This explanation may account for the similar time delays indicated in Figure 8.17.

8.5.3 Comparison with Other Data Sources

A major contribution to the experimental investigation into unsteady boundary-layer characteristics, during oscillatory wind tunnel tests, has been made by McCroskey *et al* (1982). This document described the techniques developed for analysis and evaluation of hot-film and hot-wire signals, offered some interpretations of the results, and tabulated all the cases in which flow reversal was observed. Figure 8.18 compares the results obtained for two aerofoils which displayed similar geometric differences to the present test aerofoils. These data show a very similar trend to the present test results described above. It is interesting to note that for increasing Mach number both the VR-7 and FX-098 aerofoils show a transition from a trailing-edge to a leading-edge stall. The implication is that the present observations, of a trailing-edge vortex initiation, will also be restricted to the low Mach number regime.

8.6 The Unsteady Stall Progression

The following series of events concern the formation of the primary vortex, associated with an aerofoil undergoing deep dynamic stall, whose steady-state stall mechanism is via separation growth from the trailing-edge.

- (1) Aerofoil exceeds static stall incidence; the boundary layer remains attached, and thus induces a linear

extrapolation of the aerofoil's steady-state aerodynamic behaviour.

- (2) A thin stratum of reversed flow develops in the wall region of the boundary layer; the resulting shear layer remains in close proximity to the aerofoil surface contour. However, as the preceding discussion has indicated, if the geometry of the aerofoil induces the formation of large adverse pressure gradients over the trailing-edge region, a small amount of separation, and subsequent wake formation, will occur.
- (3) The thin layer of reversed flow penetrates to the 30% chord region; the local boundary layer breaks down and the dynamic stall vortex is initiated. As this vortex begins to grow the magnitude of the reversed flow at the aerofoil surface increases. Separation at the trailing edge may now become prominent.
- (4) Vortex assisted flow reversals reach the leading edge; if the incidence is still increasing, the laminar separation bubble will burst causing the suction peak to collapse.

8.7 Conclusions

Based on unsteady hot-film data recorded for the NACA 23012 and 23012(A) aerofoils, at a Reynolds number of 1.5×10^6 , the following conclusions can be made:

- (1) The present work has shown that hot-film data can be of great benefit to the understanding of the behaviour of the boundary layer under unsteady conditions.
- (2) When considering an aerofoil's dynamic stall separation characteristics, hot-film analysis is capable of distinguishing between vortex initiation mechanisms originating from the aerofoil's leading or trailing edge.
- (3) Aerofoils that display a tendency to stall, in steady conditions, via separation growth from the trailing edge will experience vortex initiation by the breakdown of a thin layer of reversed flow travelling upstream beneath a stable shear layer, which remains in close proximity to the aerofoil's surface contour.
- (4) The actual fluid mechanics of the boundary-layer breakdown and subsequent vortex formation are still unknown. However, it is postulated that the main effect of trailing-edge separation is to alleviate the conditions which trigger this phenomenon.

CHAPTER 9

SUMMARY OF CONCLUSIONS

AND

RECOMMENDATIONS FOR FURTHER WORK

9.1 Introduction

The objectives of the present work, stated in Chapter 1, have, on the whole, been fulfilled. The manner in which these objectives were accomplished allowed the investigation into various associated aspects of aerodynamics i.e., validation of an inverse aerofoil design technique, the ability of oil-flow visualisation to indicate an aerofoil's trailing-edge separation characteristics, etc. The following summary of the observations, made during the present research, attempts to highlight these aspects.

9.2 Aerofoil Modification Procedure

The theoretical aerofoil design technique, described in Chapter 3, can be used to advise the aerodynamicist of a change in profile geometry which would fulfil the design requirements. This technique was applied to the NACA 23012 aerofoil with the objective of modifying the geometry in such

a manner that would retain the leading-edge pressure distribution whilst forcing an earlier and more gradual trailing-edge separation growth. The subsequently designed aerofoil, designated the NACA 23012(A), was shown to display an enhancement of the trailing-edge separation characteristics via both boundary-layer calculations and oil-flow visualisation tests. However, the steady-state chordwise pressure measurements, discussed in Chapter 5 indicated that the effect of viscous interactions reduced the predicted difference between the basic aerofoil and its modified counterpart. This suggested that the inclusion of viscous/inviscid interactions within the aerofoil design procedure would be useful.

9.3 Conclusions from Oscillatory Tests

Chapter 6 presented the unsteady aerodynamic forces obtained, for the NACA 23012(A), from various oscillatory tests at a Reynolds number of 1.5×10^6 . On comparison with similar wind tunnel data previously collected for the NACA 23012, several systematic methods of estimating the effects of trailing-edge separation on the dynamic stall process were presented. Generally, it was observed that the enhanced trailing-edge separation characteristic of the NACA 23012(A), displayed during static tests, was carried through to the unsteady regime. The amount of trailing-edge separation, found during a particular oscillatory cycle, was controlled by the magnitude of the imposed pitch rate. Especially important to the stall onset point was the value subjected to the aerofoil

as it passed through the static stall incidence. The subsequent development of the stall was controlled by both the maximum incidence, attained during the motion, and, if the forcing function is periodic, the time spent above the static stall angle.

The maximum oscillatory incidence to which an aerofoil can be forced whilst maintaining fully attached flow is known as the critical angle, and identifies the dynamic stall onset regime. This value is the unsteady counterpart, for helicopter applications, to operating a fixed wing on the verge of static stall. For aerofoils intended for use as rotor blades, it is the difference between the critical angle and the zero-lift incidence that is important. When compared to the NACA 23012, the present results indicated the NACA 23012(A) to have a lower critical angle which, when coupled with the positive zero-lift incidence due to the reflex trailing edge, gave the aerofoil a reduced performance in the unsteady regime. During the light stall regime, the flow separation characteristics over the NACA 23012(A) appeared to resemble a coalescing of the dynamic stall vortex with the flow separation at the trailing edge. Although the resulting pressure wave was more diffuse than that observed for the NACA 23012, the more prominent separation at the trailing-edge induced a significant negative pitching moment. Analysis of three-dimensional upper surface plots revealed the NACA 23012(A) to display weaker vortex shedding during deep dynamic stall. However, the relative magnitudes of the leading-edge suction, vortex strength and trailing-edge

separation induced similar values of negative pitching moment as the NACA 23012.

The present results indicate that, at least for aerofoils whose steady-state stall mechanism is via trailing-edge separation, bursting of the laminar separation bubble had no direct involvement in the initial formation of the dynamic stall vortex. The deterioration of the leading-edge suction peak appeared to occur after the initiation of the dynamic stall vortex, and complete collapse only became apparent when the vortex strength had become significant. It was observed, that the suction collapse, on the NACA 23012, induced a small downstream travelling pressure wave which, at approximately 50% chord, coalesced with the dynamic stall vortex. This weak vortex shedding may have been associated with the bursting of the laminar separation bubble.

Consideration was given to the possible rotor blade response under a stall flutter condition by examination of the pitch damping characteristics of both test aerofoils under various oscillatory cases. The NACA 23012(A) displayed a more stable damping characteristic which was attributed to the enhanced trailing-edge separation producing an earlier pitching moment break. In general, positive damping is commonly associated with gradual static stall, whilst negative damping is typical of abrupt static stall.

9.4 Conclusions from Ramp Tests

Based on the qualitative comparisons between ramp and oscillatory data it was concluded in Chapter 7, that the dynamic stall process was governed by a specific boundary-layer response to the magnitude of the pitch rate imposed by the forcing function. The ramp tests were used to investigate the sequential timing and manner of the dynamic stall process. The resulting decomposition of the stall process into a series of non-dimensional time delays is of great value to the developers of predictive codes employing a predominantly empirical procedure. It was observed that increasing the pitch rate induced the separation to transform from a static type behaviour to a deep stall characteristic, dominated by the presence of a shed vortex. The enhanced trailing-edge separation characteristics, of the NACA 23012(A) aerofoil, caused an increase in the pitch rate at which weak vortex shedding first appears.

The method adopted to define vortex inception was shown to be critical when attempting a calculation of the non-dimensional time delay associated with this event. Based on the analysis of pressure histories, at particular chord positions, it was deduced that a consequence of significant trailing-edge separation was to delay the initiation of the dynamic stall vortex. Figure 9.1 summarises the difference in steady-state separation characteristics, between the two test aerofoils, and illustrates the subsequent effect this has on the timing of vortex inception under dynamic conditions.

On comparison of the present ramp data with those obtained by Wilby (1984), a possible effect of freestream Mach number on the appearance of the leading-edge pressure distribution as the stall trigger was implied.

9.5 Conclusions from Hot-film Tests

An essential objective recognised by most researchers in the dynamic stall field is the investigation of the type of unsteady stall and boundary-layer separation characteristics associated with various aerofoils. It is these examinations which are expected to be crucial in correlating the difference between different sections, and in estimating the dynamic stall behaviour of new aerofoils in the future. The present work, described in Chapter 8, attempted to satisfy this objective by conducting an examination of the aerofoil's upper surface boundary-layer shear stress characteristics via twelve hot-film gauges. Detailed analysis of the subsequent data led to the conclusion that aerofoils which display a tendency to stall in steady conditions, via separation growth from the trailing-edge, will experience vortex initiation by the breakdown of a thin layer of reversed flow travelling upstream beneath a stable shear layer which remains in close proximity to the aerofoil's surface contour. Although the actual fluid mechanics of the boundary-layer breakdown and subsequent vortex formation are still unknown, it is postulated that the main effect of trailing-edge separation is to alleviate the conditions which trigger this phenomenon.

9.6 Further Work

At present the theoretical aerofoil design technique relies on the user having a prior knowledge of how the boundary layer will respond to a prescribed pressure distribution. The inclusion of viscous/inviscid interactions within the design procedure would not only remove this necessity, but also increase the accuracy of the predicted pressure distribution.

As with static stall characteristics, a detailed knowledge of the dependence of the dynamic stall process on aerofoil geometry will only be acquired via a large amount of unsteady experimental research involving various aerofoils possessing specific geometrical properties. A future modification to the NACA 23012 aerofoil could be one which reduces the leading-edge radius, in an attempt to promote stall due to bubble bursting. The comparison of this aerofoil's unsteady behaviour with the present data may supply much needed information concerning the dependence of vortex initiation mechanisms on the static stall characteristics. For each aerofoil tested under unsteady conditions, the nature of the initial boundary-layer separation that precedes vortex formation must be identified. This could be accomplished by detailed analysis of hot-film data obtained for a wide range of test cases. Also, it would be useful to have corresponding measurements of the boundary-layer thickness, perhaps by the use of hot-wires displaced from the aerofoil surface. The ability to fundamentally understand an aerofoil's unsteady boundary-layer behaviour is a necessary starting point for

any dynamic stall analysis, since the various unsteady phenomena must originate from the response of the surrounding shear layers to the imposed conditions.

THE EFFECT OF PITCH RATE ON THE DYNAMIC STALL OF A MODIFIED NACA 23012 AEROFOIL AND COMPARISON WITH THE UNMODIFIED CASE*

ANDREW J. NIVEN and RODERICK A. MCD. GALBRAITH
University of Glasgow, Glasgow, G12 8QQ, U.K.

(Submitted October 1986)

Abstract—An investigation into the effects of trailing-edge separation on dynamic stall was carried out by modifying and re-testing a NACA 23012 aerofoil. An enhancement in rear separation was obtained by modifying the trailing-edge geometry. To maintain similar flow conditions at the leading-edge, the original aerofoil geometry within this area was left unaltered. The paper presents data obtained from oscillatory and ramp tests and shows the modified aerofoil to have an earlier dynamic stall initiation. It is suggested that this initiation was triggered, at the lower angle of incidence, by the enhanced rear separation.

NOMENCLATURE

c = Aerofoil chord (m)	α = Pitch rate ($^{\circ}/s$)
C_m = Quarter-chord pitching moment	α_b = Incidence at which $\Delta C_m = 0.05$
C_n = Normal force coefficient	α_c = Critical angle of incidence
C_p = Pressure coefficient	α_{st} = Static stall angle (at C_n collapse)
k = Reduced frequency ($\omega c/2U$)	α_0 = Zero lift angle
k_1 = Reduced pitch rate ($\alpha \pi c/360U$)	ω = Angular frequency (rad/s)
U = Free stream velocity (m/s)	

1. INTRODUCTION

In 1929, the National Advisory Committee for Aeronautics (NACA) began studying the aerodynamic characteristics of a systematic series of aerofoils in an effort to find the shapes that were best suited for specific purposes. Since then, much data has been collected and a fundamental understanding of the dependence of static stall on aerofoil geometry has been obtained [1]. However, since the advent of the helicopter, a new type of stall became apparent. This characteristic became known as dynamic stall and was a direct result of the highly unsteady conditions found within the rotor flow field. As with the static stall characteristics, a knowledge of the dependence of dynamic stall on aerofoil geometry would be extremely useful.

In recent years there has been significant progress in both theoretical and semi-empirical prediction codes used to model the unsteady effects associated with dynamic stall (a selection of these methods are reviewed in Ref. [2]). Clearly, semi-empirical modelling relies heavily on unsteady wind tunnel test data and a knowledge of the factors which effect dynamic stall [3]. One such factor is the influence of trailing edge separation on the sequential timing of the dynamic stall process.

From the analysis of integrated pressure data, Beddoes [3] concluded that, to a first order, there was a common time scale associated with dynamic stall events. The present paper considers the effect of trailing-edge separation on these events by comparing the unsteady performance of two aerofoils which differ only in trailing edge geometry.

2. TEST CONDITIONS

All tests described in this paper were carried out at Glasgow University using an existing rig [4] designed to assess the unsteady airloads over an aerofoil undergoing a significant time dependent variance in incidence. Aerofoil performance under static, oscillatory pitch and steady

*Presented at the 12th European Rotocraft Forum, Garmisch-Partenkirchen, F.R.G., 22-25 September 1986.

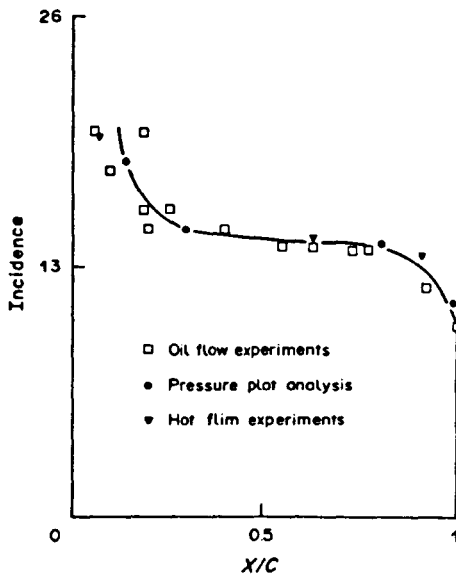


Fig. 1. Separation characteristics for the NACA 23012 aerofoil.

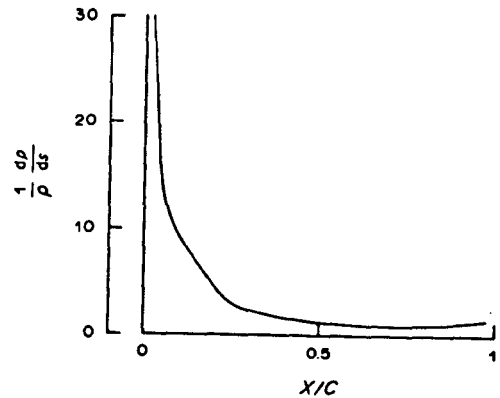


Fig. 2. Inviscid pressure gradient (NACA 23012).

pitch rate (or ramp) conditions can be studied. Chordwise pressure distributions were measured at the mid-span position by 30 transducers mounted within the model. Data acquisition and reduction was carried out by a DEC MINC (PDP 11/23) minicomputer [5] and during the data processing no account was taken of tunnel blockage or interference effects; these were treated as being unknown.

All the tests were carried out at a Reynolds number of 1.5×10^6 which corresponded to a tunnel Mach number of 0.11.

3. TEST AEROFOIL—A MODIFIED NACA 23012 AEROFOIL

Choice of basic aerofoil

The NACA 23012 represents a typical helicopter rotor profile which utilises the effects of camber to increase its overall aerodynamic performance. For many years this aerofoil has been the subject of intensive testing and the subsequent accumulation of data well documented within the literature. One dominating feature of this profile is its unusual stalling characteristics. On the basis of its abrupt lift collapse one might have expected a leading-edge type stall. However, as predicted by Gault [1] this aerofoil should exhibit a trailing-edge stall. This apparent contradiction is due to a rapid growth of trailing-edge separation at a critical angle of incidence.

Using standard experimental techniques [6, 7], the trailing-edge separation front can be monitored and recorded. As expected, Fig. 1 shows the NACA 23012 aerofoil to have a rapid forward movement of separation at a critical angle of approx. 14° . For the past few years the NACA 23012 aerofoil has been the subject of exhaustive testing at Glasgow University. This has allowed a reasonable picture of its unsteady stalling characteristics to be obtained and, for this reason, it became the prime candidate for modification.

Type of modification

A useful modification to the NACA 23012 aerofoil is one which retains the leading edge conditions whilst forcing an earlier and more gradual trailing-edge separation growth.

It is well known [7] that a region of adverse pressure gradient will, if persistent enough, cause a boundary layer to separate. It follows from this that in order to increase the probability of boundary layer separation, within a given region, one should increase the applied adverse pressure gradient. Therefore, in order to change the separation characteristics of the NACA 23012, a change in adverse pressure gradient over the rear portion should suffice.

A standard vortex panel program [8] was used to calculate the inviscid pressure gradient over the NACA 23012 aerofoil (see Fig. 2). The upper surface pressure gradient between the 25 and

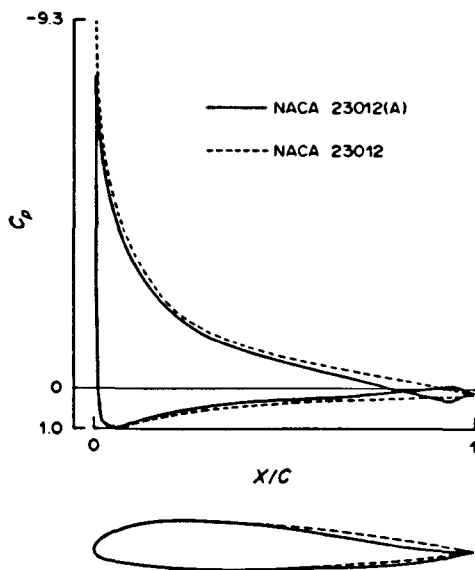


Fig. 3. Results from aerofoil design procedure.

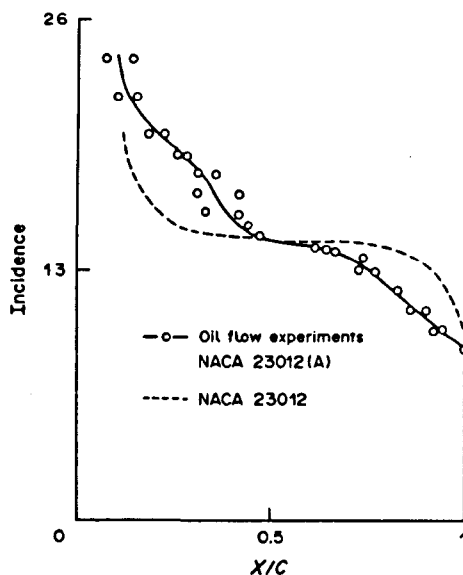


Fig. 4. Separation characteristics for the NACA 23012(A) aerofoil

100% chord position was then increased in severity [9] and a new distribution of velocity calculated. An inverse vortex panel program [10] was then used to generate an aerofoil possessing this new velocity distribution. This inverse program simply took the "basic" NACA 23012 aerofoil and modified the influence coefficients of the panel matrix to satisfy the new velocity distribution; it was an iterative procedure and, for small modifications in pressure gradient, converged well. The new aerofoil was designated the NACA 23012 (A) and is compared to the NACA 23012 aerofoil in Fig. 3.

Verification of modification

To verify that the NACA 23012 (A) aerofoil had the desired trailing-edge separation characteristics, a surface oil-film flow visualisation technique [6] was used. The static results obtained by this method are shown in Fig. 4 where a more persistent and gradual trailing-edge separation may clearly be seen.

4. STATIC PERFORMANCE

Static data was obtained at a Reynolds number of 1.5×10^6 and is presented in Fig. 5. The main feature displayed by the NACA 23012(A) aerofoil was the rounding-off in lift-curve slope at a stall angle of 13.6 (0.8° less than the NACA 23012 aerofoil), indicating a trailing-edge type stall. Also observed was a positive pre-stall pitching moment of 0.05 and a positive zero-lift angle of 1.5° ; these both being consequences of the reflex trailing-edge.

A further, and interesting, observation that may be made is the obvious nonlinearity in pre-stall lift-curve slope. Initial considerations suggested this was a flow phenomenon associated with the reflex trailing-edge; a similar nonlinearity is displayed by the GO 738 aerofoil [12], at a Reynolds number of 0.5×10^6 , which also has a reflex trailing-edge.

5. OSCILLATORY CHARACTERISTICS

Overall performance

The variation of C_n and C_m with α is shown in Fig. 6 for the two aerofoils during oscillatory pitch cycles of $10 \pm 8^\circ$ at various reduced frequencies. As expected, both aerofoils displayed the distinctive aerodynamic loadings generally associated with dynamic stall [13].

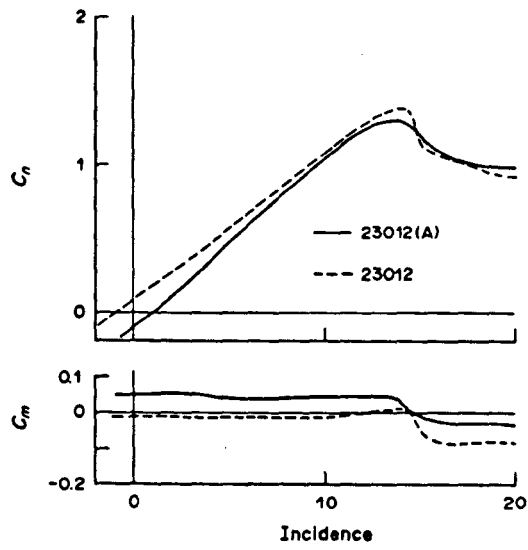


Fig. 5. Wind tunnel characteristics (Static data)

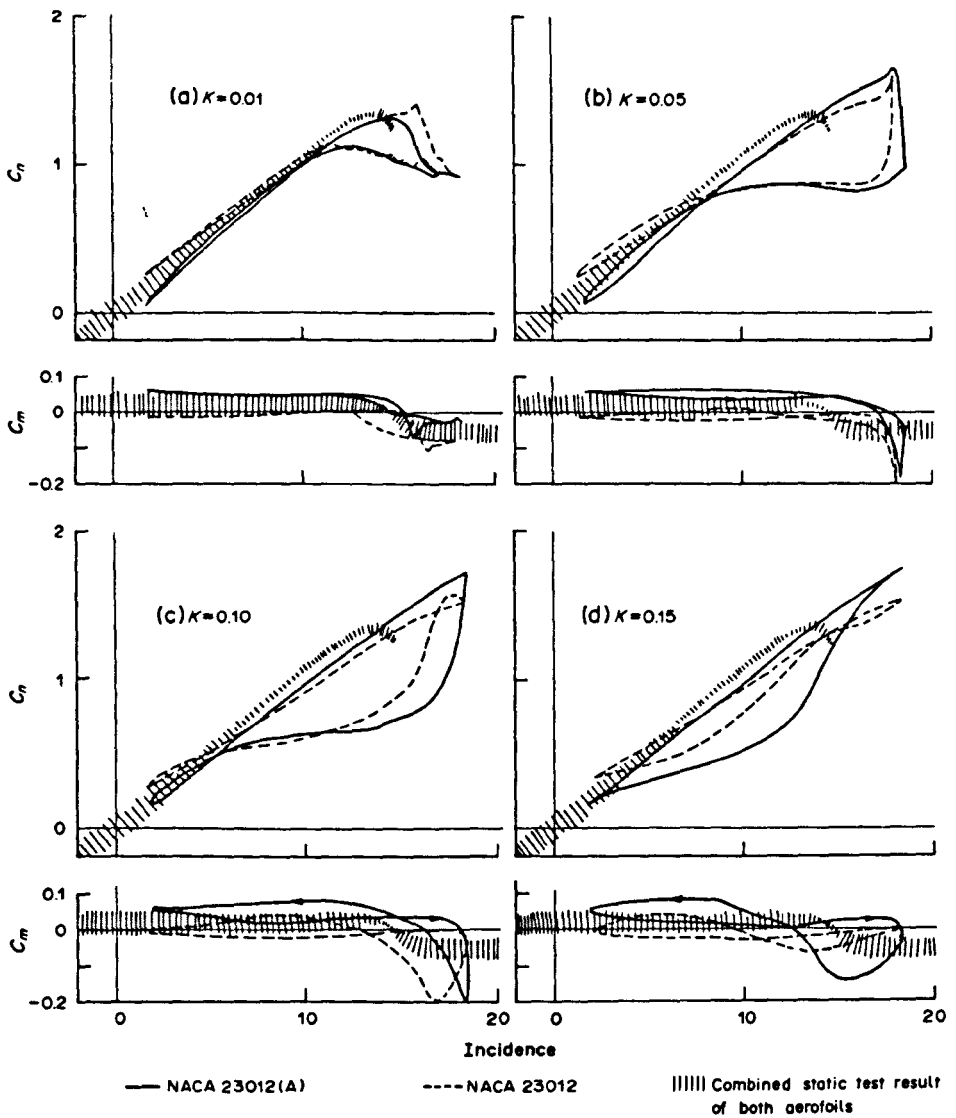


Fig. 6. Performance during oscillatory tests. Unbroken line: NACA 23012(A); broken line: NACA 23012; the hatched area represents combined static test results of both aerofoils.

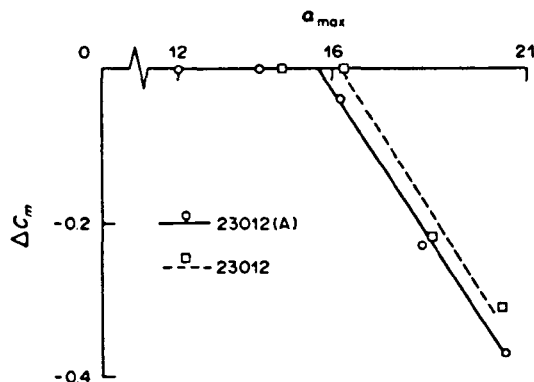


Fig. 7. Critical angle calculation.

At low reduced frequency (Fig. 7a) both aerofoils exhibited similar characteristics, although the NACA 23012(A) displayed a more gradual stall at maximum lift. As the reduced frequency was increased distinct differences between the two aerofoil's characteristics became apparent. Since the two aerofoils had identical nose profiles, it is suggested that these observed differences were due to the influence of trailing-edge separation on the dynamic stall process. These differences, for the 23012(A), may be described as follows:

- Increased size in C_n and C_m hysteresis (Fig. 6c); this is due to the different timing of flow re-attachment during the downstroke.
- Earlier and more gentle C_{ma} break (Fig. 6b); this is due to the earlier and more gradual forward movement of the trailing-edge separation front.
- Non-suppression of trailing-edge separation (Fig. 6d); the more persistent separation had a slower suppression response to increased reduced frequency. At a reduced frequency of 0.15 the NACA 23012(A) aerofoil clearly exhibited a drop in C_m , at the beginning of the downstroke, which suggested a local increase in rear loading that would accompany a rear separation with re-attachment.

Critical angle calculation

Following the argument presented by Wilby [14, 15] a series of oscillatory tests, that took each aerofoil from unstalled to highly stalled conditions, was carried out. This was achieved by keeping both amplitude, $\pm 8^\circ$, and reduced frequency, 0.1, constant whilst varying the mean angle. From the results of these tests, the maximum deviation in C_m , from its pre-stall single loop, was calculated and plotted against the maximum angle of incidence attained in the cycle (see Fig. 7). The intercept with the $C_m = 0$ line gives the maximum value of incidence that a given aerofoil can reach before there will be a break in the pitching moment. This angle is known as the critical angle, α_c . For aerofoils intended for use on helicopter rotor blades, it is the difference between the critical angle and the zero-lift incidence, α_0 , that is important. The following data were obtained from static and oscillatory tests:

$$\begin{array}{l} \text{NACA 23012(A)} \\ \text{NACA 23012} \end{array} \left\{ \begin{array}{l} \alpha_0 = 1.5^\circ \\ \alpha_{ss} = 13.6 \text{ giving } \alpha_c - \alpha_0 = 14.1^\circ \\ \alpha_c = 15.6^\circ \\ \alpha_0 = -1.0^\circ \\ \alpha_{ss} = 14.2^\circ \text{ giving } \alpha_c - \alpha_0 = 17.2^\circ \\ \alpha_c = 16.2^\circ \end{array} \right.$$

Since the leading-edge pressure distributions of both aerofoils are similar, the lower value of α_c exhibited by the NACA 23012(A) aerofoil must be caused by trailing-edge separation aggravated by the more severe rear pressure gradient. The lower value of α_c , coupled with a higher value of α_0 , gives the NACA 23012(A) aerofoil a greatly reduced value of $\alpha_c - \alpha_0$ indicating a poorer performance in the unsteady regime.

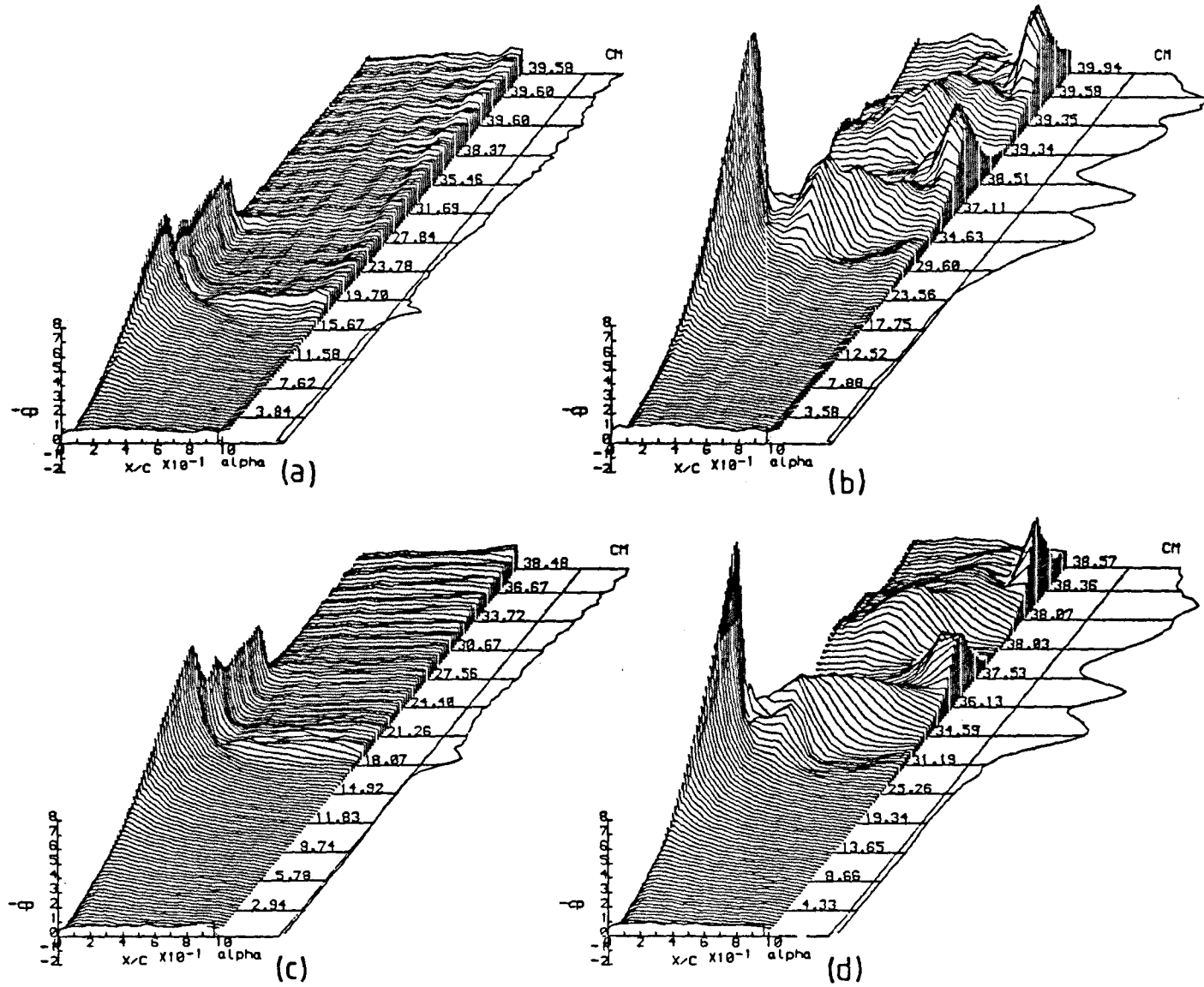


Fig. 8. Upper surface pressure/time history—ramp tests. NACA 23012(A): (a) $k_1 = 0.004$; (b) $k_1 = 0.04$.
NACA 23012: (c) $k_1 = 0.004$; (d) $k_1 = 0.04$.

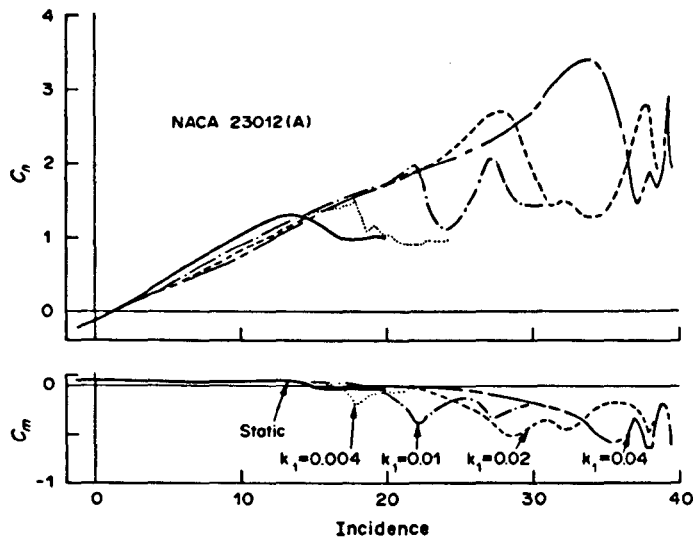


Fig. 9. Performance during ramp tests, NACA 23012(A).

6. RAMP CHARACTERISTICS

Overall performance

The dynamic stall rig at Glasgow University provides a useful facility to obtain the aerodynamic characteristics of an aerofoil undergoing a ramp like variation in incidence. These ramp motions are of great value in studying the effects of pitch rate on the sequential timing [16] and manner of dynamic stall.

At significant values of pitch rate (i.e. $k_1 > 0.004$) Seto and Galbraith [17] observed the stall to acquire certain typical characteristics. These were: (a) large dynamic overshoot of C_n and C_m ; (b) vortex shedding (see Fig. 8) and subsequent increase in C_n ; and (c) collapse of C_n and associated development of a large negative pitching moment.

The effect of pitch rate on the upper surface pressure distribution, during the stall process, is illustrated in Fig. 8. Figures 9 and 10 show the unsteady lift and pitching moments for the NACA 23012 and 23012(A) aerofoils respectively. Although the overall characteristics are very similar, the NACA 23012(A) exhibits, generally, more gradual variations in lift and pitching moment, especially at the higher pitch rates. It also displays a larger reduction in the unstalled static lift-curve slope and an earlier development of the maximum negative pitching moment.

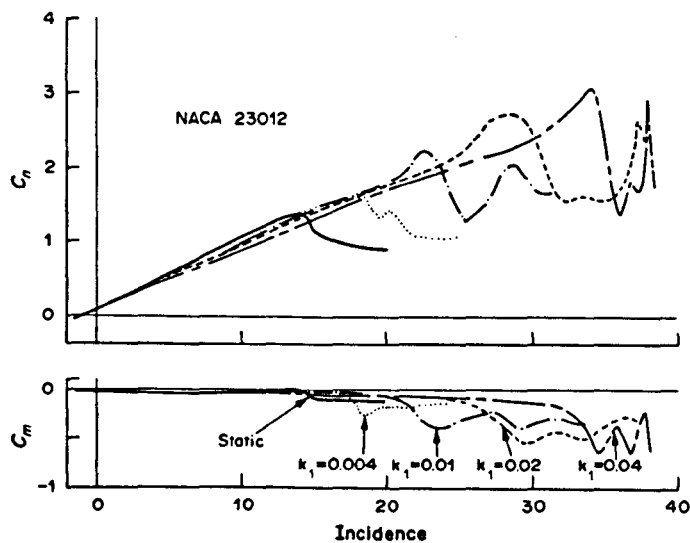


Fig. 10. Performance during ramp tests (NACA 23012).

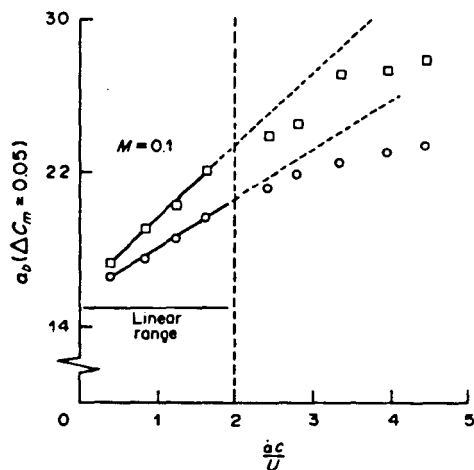


Fig. 11. Time delay calculation—ramp tests.

Pitching-moment break

In Beddoes' analysis [3] he concluded that, during a dynamic increase in incidence, an aerofoil will incur a break in pitching-moment, a period of time, Δt , after passing, and remaining above, its static pitching-moment break incidence. Beddoes gave the value of this time delay as

$$\Delta t = \frac{nc}{U}$$

where $n = 2.44$.

From the ramp data, collected at Glasgow University, the variation of pitching-moment break with pitch rate was obtained for each aerofoil. Subsequent analysis followed that given by Wilby [14], in which a definition of pitching-moment break is taken as the angle of incidence, α_b , for which the value of C_m had fallen by 0.05 below its maximum value. Plotting these values against $\dot{\alpha}c/U$ and calculating the resultant slope gives a value for n in the above equation.

It is apparent, from Fig. 11, that the variation of α_b , does not possess a unique linear dependence on $\dot{\alpha}c/U$ throughout the full range of pitch rates. However, in conformation with those data obtained by Wilby [14], it was inferred that a linear relationship existed for values of $\dot{\alpha}c/U$ less than 2.0. The results from these analyses and their implications are discussed below.

Sequential timing of dynamic stall

For the NACA 23012(A) aerofoil, a value of 2.5 was obtained for n which was consistent with that given by Beddoes. However, a high value of 3.8 was measured for the NACA 23012. Although the extent to which these time delays are effected by local tunnel conditions is arguable, the important feature of Fig. 11 is the different slopes obtained for each aerofoil. The implication then is that, since both aerofoils were tested under similar conditions, the variation in time delay was mainly due to the influence of trailing-edge separation on the onset of dynamic stall.

Figures 12a and 12b present, in the manner of Ref. [18], chordal C_p values for both aerofoils undergoing a ramp variation of incidence at a reduced pitch rate of 0.01. These data contained evidence that the two aerofoils exhibited subtle differences in their unsteady stalling characteristics; comparing any two C_p traces clearly demonstrates this. This can cause difficulties when attempting to quantify the sequential timing of events incurred during dynamic stall [16].

7. CONCLUSIONS

On the basis of the data and discussions presented, the following conclusions have been drawn.

- (a) Aerofoils displaying a prominent trailing-edge stall under static conditions are likely to exhibit dynamic stall triggered by a rear separation. However, this separation can be suppressed by increasing the pitch rate.

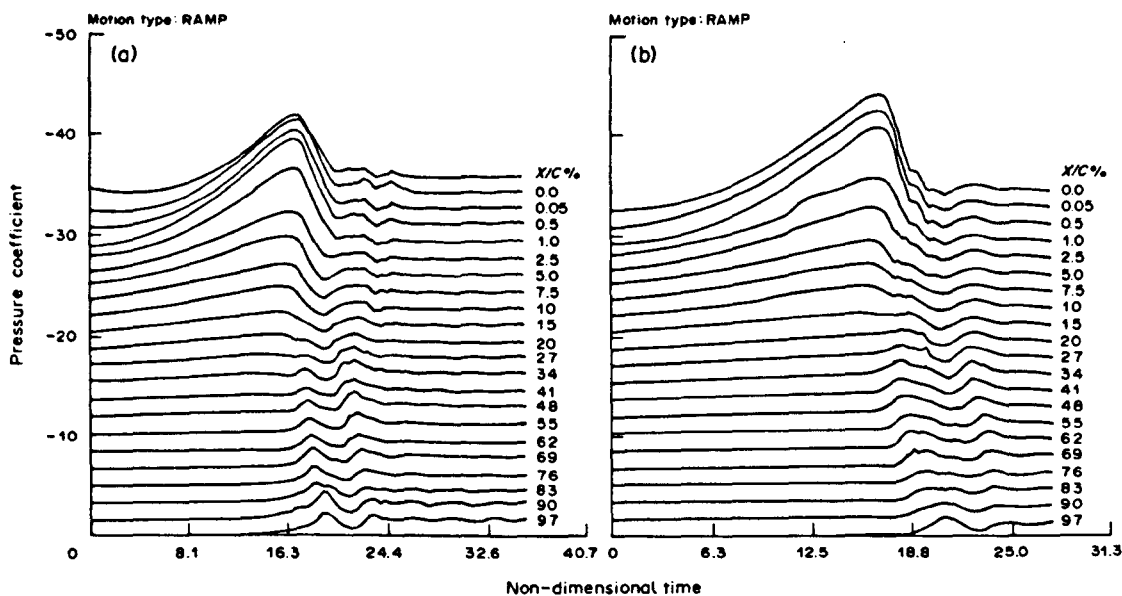


Fig. 12. Pseudo 3-D pressure history—upper surface.

(b) The exact mechanism by which rear separation effects dynamic stall is, at present, unclear although it does tend to give an aerofoil a poorer unsteady performance.

Acknowledgements—The authors wish to express their thanks to Professor Richards for his support and encouragement. Also to P. Wilby (RAE, Farnborough) and T. Beddoes (Westland Helicopters), for their continued help and discussions. The work was carried out in collaboration with Westland Helicopters via an SERC CASE award No. 8051/3408 and MOD Agreement No. 2048/026 XR/STR.

REFERENCES

1. D. E. Gault, A correlation of low-speed airfoil-section stalling characteristics with Reynolds number and airfoil geometry. NACA TN 3963 (1937).
2. T. S. Beddoes, Prediction methods for unsteady separated flows. AGARD Lecture Series on Unsteady Aerodynamics, VKI (1980).
3. T. S. Beddoes, A synthesis of unsteady aerodynamic effects including stall hysteresis. *Proc. 1st European Rotorcraft Forum*, Southampton (1975).
4. G. J. Leishman, Contributions to the experimental investigation and analysis of aerofoil dynamic stall. Ph.D. dissertation, University of Glasgow, Scotland.
5. R. A. McD. Galbraith and J. G. Leishman, A microcomputer based test facility for the investigation of dynamic stall. *Int. Conf. Use of the Micro in Fluid Engineering* (1983).
6. L. Y. Seto, Leishman and R. A. McD. Galbraith, An investigation of three-dimensional stall J.G. developments on NACA 23012 and NACA 0012 aerofoils. Glasgow University Aero Report No. 8300, October (1984).
7. P. K. Chang, *Control of Flow Separation*. Hemisphere, Washington (1976).
8. J. G. Leishman and R. A. McD. Galbraith, An algorithm for the calculation of the potential flow about an arbitrary two-dimensional aerofoil. Glasgow University Aero Report No. 8092, May (1981).
9. A. J. Niven and R. A. McD. Galbraith, A design procedure to modify the trailing edge upper surface pressure gradient of a given aerofoil. Glasgow University Aero Report No. 8408, July (1984).
10. M. Vezza and R. A. McD. Galbraith, A comparison of two methods for the design of aerofoils with specific pressure distributions. Glasgow University Aero Report No. 8303, June (1983).
11. B. Thwaites, *Incompressible Aerodynamics*. Cambridge University Press (1961).
12. S. J. Miley, A catalog of low-Reynolds-number aerofoil data for wind-turbine applications. Dept. of Aerospace Engineering, Texas A&M University, February (1982).
13. T. Beddoes, A qualitative discussion of dynamic stall. AGARD Lecture Series on Unsteady Aerodynamics, VKI (1980).
14. P. G. Wilby, The aerodynamic characteristics of some new RAE blade sections and their potential influence on rotor performance. *Vertica* 4, 121-133 (1980).
15. P. G. Wilby, An experimental investigation of the influence of a range of aerofoil design features on dynamic stall onset. *10th European Rotorcraft Forum*, August (1984).
16. R. A. McD. Galbraith, A. J. Niven and L. Y. Seto, On the duration of low speed dynamic stall. *1986 ICAS Conf.*, London, England, September (1986).
17. L. Y. Seto and R. A. McD. Galbraith, The effect of pitch rate on the dynamic stall of a NACA 23012 aerofoil. *11th European Rotorcraft Forum*, London, England, September (1985).
18. W. J. McCroskey, K. W. McAlister, L. W. Carr and S. L. Pucci, Dynamic stall on advanced airfoil sections. *J. Am. Helicopter Soc.* 26, 80-1-1-80-1-25 (1981).

REFERENCES

- Abbott, I.H., v Doenhoff, A.E. (1959) *Theory of Wing Sections*. Dover Publications, New York, ISBN 486-60586-8.
- Beddoes, T.S. (1975) *A Synthesis of Unsteady Aerodynamic Effects including Stall Hysteresis*. Proceedings: 1st European Rotorcraft and Powered Lift Forum. September.
- Beddoes, T.S. (1978) *Onset of Leading Edge Separation Effects under Dynamic Conditions and Low Mach Number*. 34th Annual National Forum of the American Helicopter Society. Preprint No. 78-63, May.
- Beddoes, T.S. (1980) *Prediction Methods for Unsteady Separated Flows*. AGARD Report 679, Paper 15.
- Beddoes, T.S. (1983) *Representation of Airfoil Behaviour*. *Vertica*, Vol. 7, No. 2, pp 183-197.
- Bippes, H., Turk, M. (1981) *Half Model Testing Applied to Wings above and below Stall*. In: *Unsteady Turbulent Shear Flows* (Ed. R. Michel, J. Cousteix, R. Houdeville). Springer-Verlag, New York.
- Carr, L.W., McAlister, K.W., McCroskey, W.J. (1977) *Analysis of the Development of Dynamic Stall based on Oscillating Airfoil Experiments*. NASA TN D-8382, January.

- Carr, L.W. (1981) *A Review of Unsteady Turbulent Boundary-Layer Experiments*. In: *Unsteady Turbulent Shear Flows* (Ed. R. Michel, J. Cousteix, R. Houdeville). Springer-Verlag, New York.
- Carta, F.O. (1967) *An Analysis of the Stall Flutter Instability of Helicopter Rotor Blades*. J. American Helicopter Soc., Vol. 12, No. 4, pp 1-18.
- Carta, F.O. (1971) *A Theoretical Study of the Effect of Unsteady Pressure Gradient on Dynamic Stall Delay*. J. Aircraft, No. 10, pp 839-841.
- Carta, F.O. (1974) *Analysis of Oscillatory Pressure Data including Dynamic Stall Effects*. NASA CR-2394.
- Cebeci, T., Carr, L.W. (1981) *Computation of Unsteady Turbulent Boundary Layers with Flow Reversal and Evaluation of Two Separate Turbulence Models*. NASA TM-81259.
- Chang, P.K. (1976) *Control of Flow Separation*. Hemisphere Publishing Corp., Washington, ISBN 0-07-010513-8
- Covert, E.E., Lorber, P.F. (1984) *Unsteady Turbulent Boundary Layers in Adverse Pressure Gradients*. AIAA Journal, Vol. 22, No. 1, pp 22-28, January.

- Dadone, L. (1978) *Rotor Airfoil Optimization: An Understanding of the Physical Limits*. 34th Annual National Forum of the American Helicopter Society, May.
- Davenport, F.J., Front, J.V. (1966) *Airfoil Sections for Rotor Blades - a Reconsideration*. 22nd Annual National Forum of the American Helicopter Society, May.
- Dutt, H.N.V., Sreekanth, A.K. (1980) *Design of Aerofoils for Prescribed Pressure Distribution in Viscous Incompressible Flows*. *Aeronautical Quarterly*, pp 42-55, February.
- Ericsson, L.E., Reding, J.P. (1988) *Fluid Mechanics of Dynamic Stall Part 1: Unsteady Flow Concepts*. *J. Fluids and Structures*, Vol. 2, pp 1-33.
- Galbraith, R.A.McD., Niven, A.J., Seto, L.Y. (1986) *On the Duration of Low Speed Dynamic Stall*. *Proceedings of ICAS Conference*, pp 522-531, London.
- Gault, D.E. (1957) *A Correlation of Low-Speed Airfoil-Section Stalling Characteristics with Reynolds Number and Airfoil Geometry*. NACA TN 3963, March.
- Greagory, N., Quincey, V.G., O'Reilly, C.L., Hall, P.J. (1970) *Progress Report on Observations of Three-Dimensional Flow Patterns obtained during Stall Development on Aerofoils, and on the Problem of Measuring Two-Dimensional Characteristics*. A.R.C. CP 1146.

- Harris, F.D., Pruyn, R.R. (1968) *Blade Stall - Half Fact, Half Fiction*. 23rd Annual National Forum of the American Helicopter Society, No. 101, May.
- Johnson, W., Ham, N.D. (1972) *On the Mechanism of Dynamic Stall*. J. American Helicopter Society, Vol. 17, No. 4, pp 36-45.
- Johnson, W. (1986) *Recent Developments in Rotary-Wing Aerodynamic Theory*. AIAA Journal, Vol. 24, No. 8, August.
- Kline, S.J., Bardina, J., Strawn, R. (1981) *Correlation and Computation of Detachment and Reattachment of Turbulent Boundary Layers on Two-Dimensional Faired Surfaces*. AIAA Paper 81-1220, AIAA 14th Fluid and Plasma Dynamics Conference, Palo Alto, California, June.
- Lang, J.D., Francis, M.S. (1985) *Unsteady Aerodynamics and Dynamic Aircraft Maneuverability*. In: AGARD CP-386, Paper No. 29, November.
- Leishman, J.G., Galbraith, R.A.McD. (1981) *An Algorithm for the Calculation of the Potential Flow about an Arbitrary Two-Dimensional Aerofoil*. G.U. Aero Report 8102, University of Glasgow, Scotland.
- Leishman, J.G. (1984) *Contributions to the Experimental Investigation and Analysis of Aerofoil Dynamic Stall*. Ph.D Dissertation, University of Glasgow, Scotland.
- Leitch, E., Galbraith, R.A.McD. (1987) *Guide to Glasgow University's Aerofoil Database - Version 1*. G.U. Aero Report 8700, University of Glasgow, Scotland.

- Liiva, J., Davenport, F.J., Gray, L., Walton, I.C. (1969) *Two-Dimensional Tests of Airfoils Oscillating near Stall, Vol. 1: Summary and Evaluation of Results*. U.S. Army Aviation Material Lab., Tech. Report 68-13A, April.
- Meier, M.U., Kreplin, H.P., Fang, L.W. (1981) *Experimental Study of Two and Three Dimensional Boundary Layer Separation*. In: *Unsteady Turbulent Shear Flows* (Ed. R. Michel, J. Cousteix, R. Houdeville). Springer-Verlag, New York.
- Miley, S.J. (1982) *A Catalog of Low-Reynolds-number Aerofoil Data for Wind-Turbine Applications*. Dept. of Aerospace Engineering, RFP-3387, Texas A&M University, February.
- Moran, J. (1984) *An Introduction to Theoretical and Computational Aerodynamics*. John Wiley & Sons, ISBN 0-471-87491-4.
- McAlister, K.W., Carr, L.W. (1978) *Water Tunnel Experiments on an Oscillating Airfoil at $Re = 21,000$* . NASA TM-78446, March.
- McCroskey, W.J., Fisher, R.K. (1972) *Detailed Aerodynamic Measurements on a Model Rotor in the Blade Stall Regime*. J. American Helicopter Society, Vol. 17, No. 1, pp 20-30.
- McCroskey, W.J. (1973) *Inviscid Flowfield of an Unsteady Airfoil*. AIAA Journal, Vol. 11, No. 8, pp 1130-1137.

McCroskey, W.J., Philippe, J.J. (1975) *Unsteady Viscous Flow on Oscillating Airfoils*. AIAA Journal, Vol. 13, No. 1, pp 71-79, January.

McCroskey, W.J. (1975) *Recent Developments in Dynamic stall*. Proceedings of Symposium on unsteady Aerodynamics (Ed. R. B. Kinney), Vol. 1, pp 1-33, University of Arizona, Tucson, Arizona.

McCroskey, W.J., Carr, L.W., McAlister, K.W. (1976) *Dynamic Stall Experiments on Oscillating Airfoils*. AIAA Journal, Vol. 14, No. 1, pp 57-63, January.

McCroskey, W.J., McAlister, K.W., Carr, L.W., Pucci, S.L., Lambert, O., Indergand, R.F. (1980) *Dynamic Stall on Advanced Airfoil Sections*. American Helicopter Society Preprint 80-01.

McCroskey, W.J. (1981) *The Phenomenon of Dynamic Stall*. NASA TM-81264, March.

McCroskey, W.J., McAlister, K.W., Carr, L.W., Pucci, S.L. (1982) *An Experimental Study of Dynamic Stall on Advanced Airfoil Sections, Vol. 3: Hot-Wire and Hot-Film Measurements*. NASA TM-84245, July.

Parikh, P.G., Reynolds, W.C., Jayaraman, R., Carr, L.W. (1981) *Dynamic Behaviour of an Unsteady Turbulent Boundary Layer*. NASA TM-81304.

Pope, A. (1954) *Wind-Tunnel Testing*. John Wiley & Sons.

Prouty, R.W. (1975) *A State-of-the-Art Survey of Two-Dimensional Airfoil Data*. J. American Helicopter Society, Vol. 20, No. 10, pp 14-24.

Robinson, M.C., Luttgies, M.W. (1983) *Unsteady Flow Separation and Attachment Induced by Pitching Airfoils*. AIAA Paper 83-0131, AIAA 21st Aerospace Sciences Meeting, Reno, Nevada, January.

Rogers, E.W.E. (1959) *A Background to the Problems of Wind-Tunnel Interference*. AGARD Report No. 292, March.

Schlichting, H. (1979) *Boundary-Layer Theory*. McGraw-Hill, ISBN 0-07-055334-3.

Scruggs, R.M., Nash, J.F., Singleton, R.E. (1974) *Analysis of Dynamic Stall using Unsteady Boundary-Layer Theory*. NASA CR-2462, October.

Seto, L.Y., Leishman, J.G., Galbraith, R.A.McD. (1983) *An Investigation of Three-Dimensional Stall Developments on NACA 23012 and NACA 0012 Aerofoils*. G.U. Aero Report No. 8300, University of Glasgow, January.

- Seto, L.Y., Galbraith, R.A.McD. (1985) *The Effect of Pitch rate on the Dynamic Stall of a NACA 23012 Aerofoil*. 11th European Rotorcraft Forum, Paper No. 34, London, September 10-13.
- Simpson, R.L., Shivaprasad, B.G., Chew, Y.T. (1981) *Some Features of Unsteady Separating Turbulent Boundary Layers*. In: *Unsteady Turbulent Shear Flows* (Ed. R. Michel, J. Cousteix, R. Houdeville). Springer-Verlag, New York.
- Tarzanin, F.J. Jr. (1972) *Prediction of Control Loads due to Blade Stall*. J. American Helicopter Society, Vol. 17, No. 2, pp 33-46.
- Veza, M. (1986) *Numerical Methods for the Design and Unsteady Analysis of Airfoils*. Ph.D Dissertation, University of Glasgow.
- Ward, J.F., Young, W.H. Jr. (1972) *A Summary of Current Research in Rotor Unsteady Aerodynamics with Emphasis on Work at the Langley Research Center*. AGARD CP-111, Paper 10.
- Wilby, P.G. (1980) *The Aerodynamic Characteristics of some New RAE Blade sections, and their Potential Influence on Rotor Performance*. Vertica, Vol. 4, pp 121-133.

Wilby, P.G. (1984) *An Experimental Investigation of the Influence of a Range of Aerofoil Design Features on Dynamic Stall Onset*. 10th European Rotorcraft Forum, Paper No. 2, August 28-31.

Young, W.H. Jr. (1981) *Fluid Mechanics Mechanisms in the Stall Process for Helicopters*. NASA TM-81956, March.

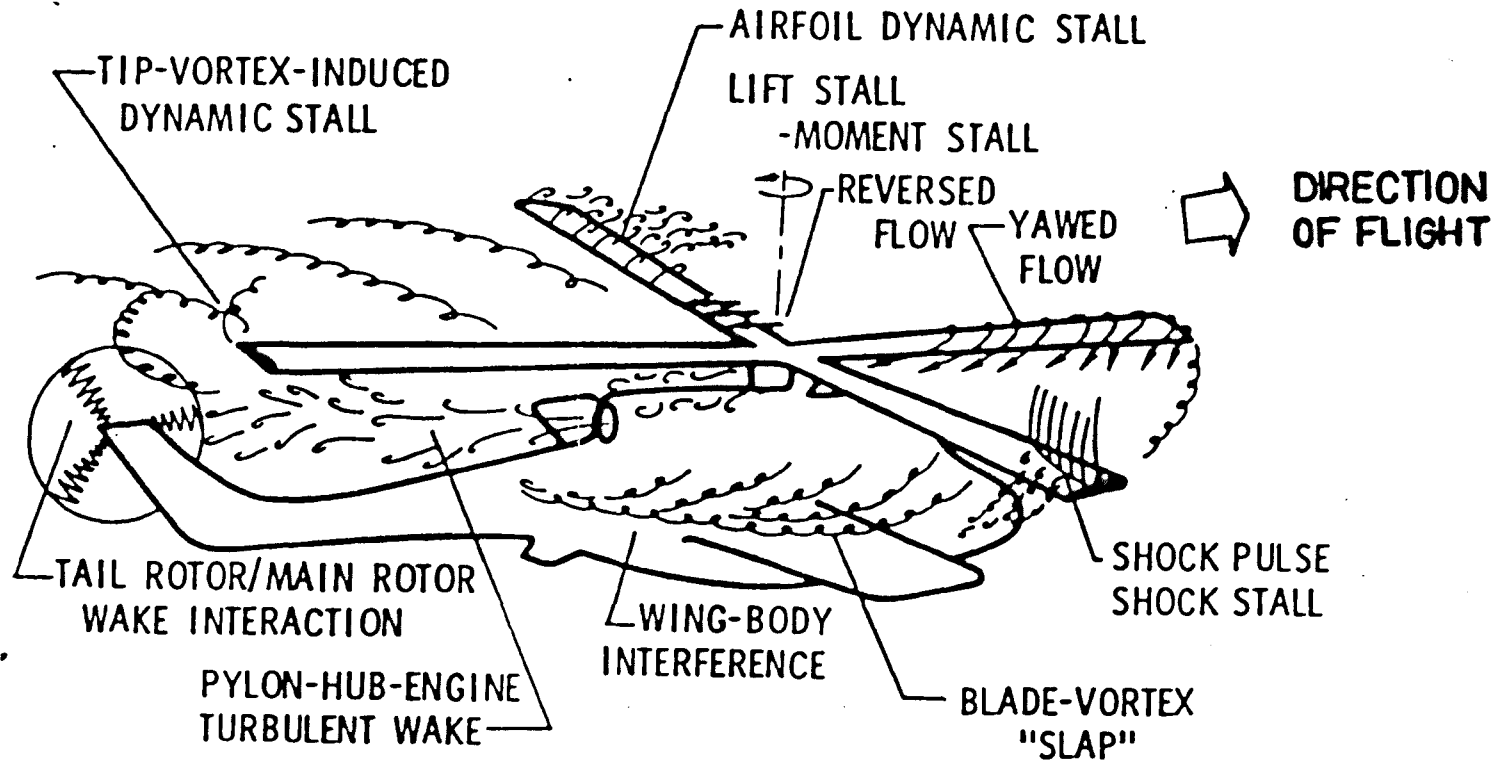


FIGURE 1.1 Helicopter Flowfield Phenomena
 (from Vard and Young, 1972).

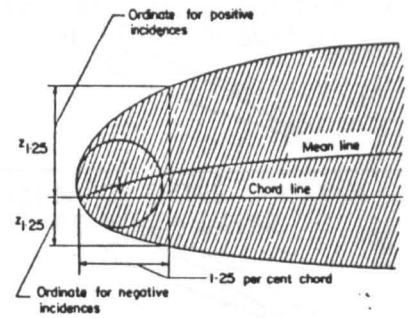
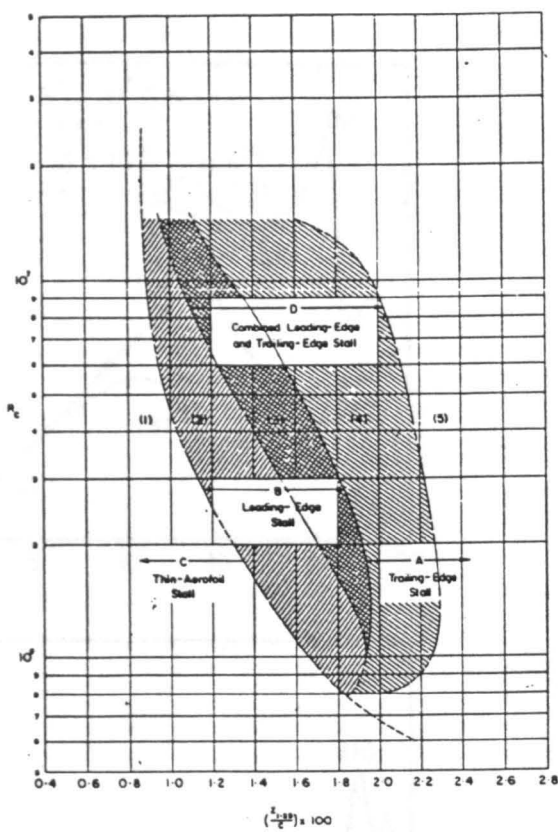


FIGURE 1.2 The Low-Speed Stalling Characteristics of Aerofoil Sections Correlated with Reynolds number and Upper-Surface Ordinate (see insert) (from Gault, 1957).

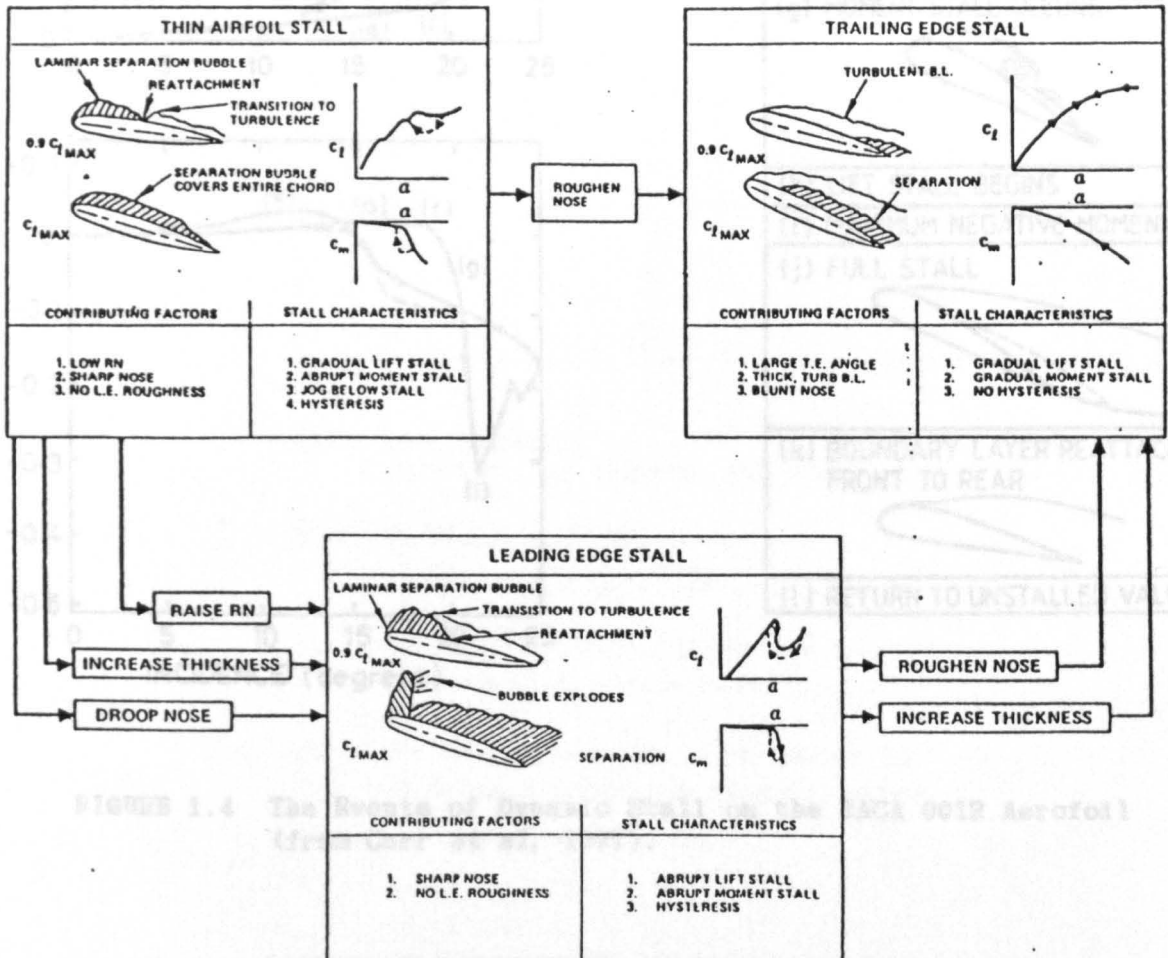


FIGURE 1.3 Steady-State Aerofoil Stalling Characteristics (from Prouty, 1975)

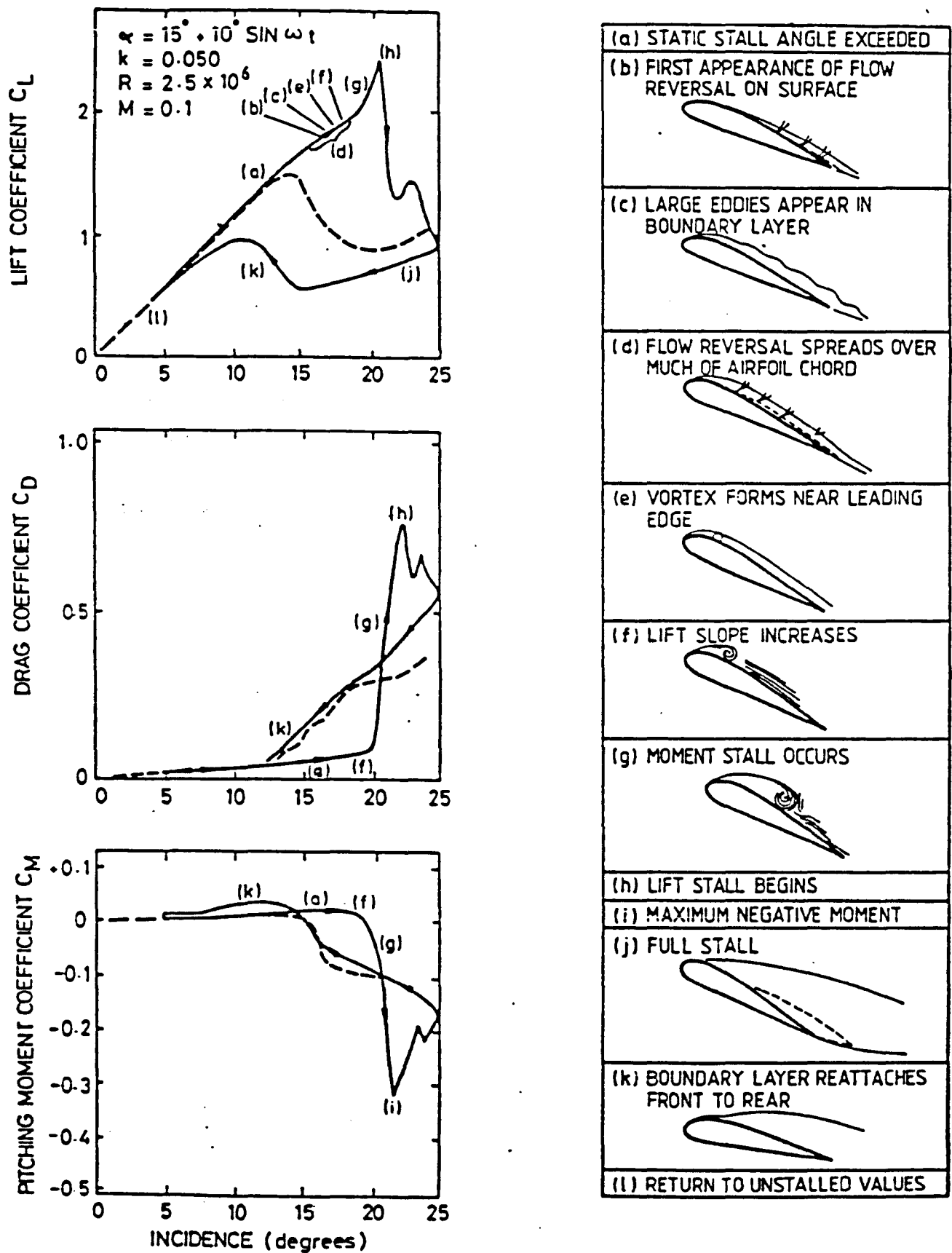


FIGURE 1.4 The Events of Dynamic Stall on the NACA 0012 Aerofoil (from Carr et al, 1977).

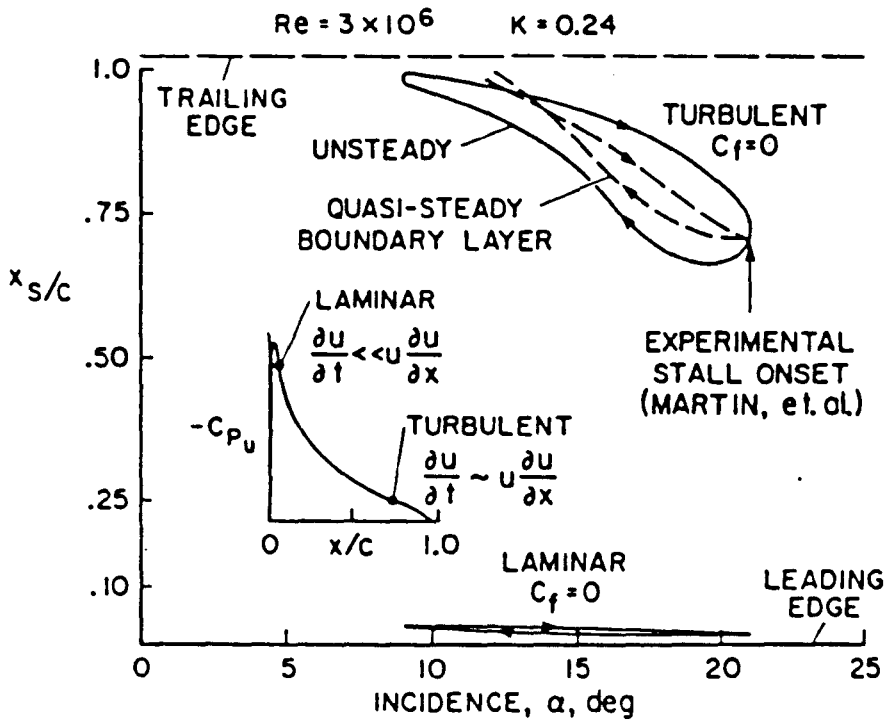
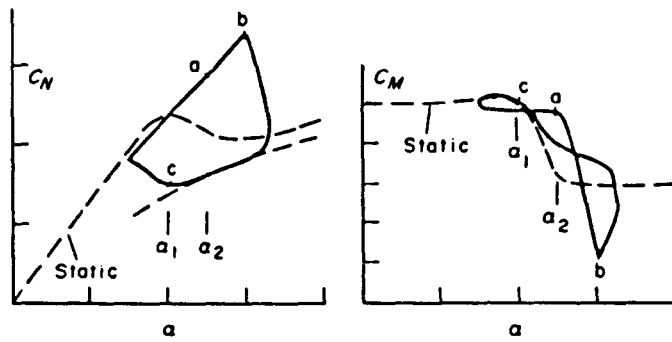


FIGURE 1.5 Calculations of the Loci of Laminar and Turbulent Flow Reversal on an Oscillating NACA 0012 Aerofoil (from McCroskey, 1975).



Static data idealised:

C_M break at a_1 , separation stabilised at a_2

Dynamic stall progression:

Exceed a_1 without separation, start time delay.

- (a) Time delay (τ_1) exceeded. Vortex shed from L.E. lift maintained, moment diverges $\sim C.P.$
 $= f(a, t)$
- (b) Time delay (τ_2) exceeded. Vortex passes T.E. lift decays \sim reflected in moment variation.
- (c) Flow reattaches for $a < a_1$.

FIGURE 1.6 Dynamic Stall Time Delay Model (from Beddoes, 1983).

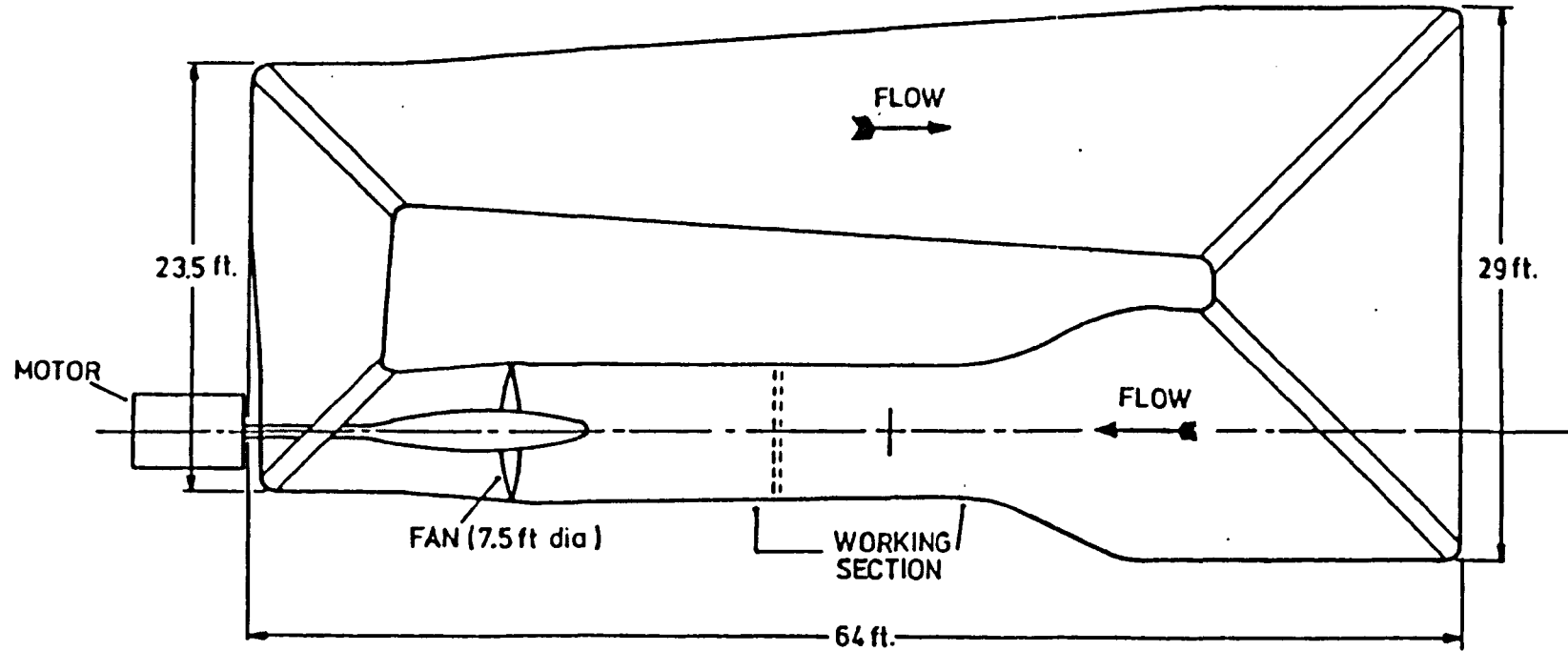


FIGURE 2.1 Plan View of the Glasgow University 'Handley Page' Wind Tunnel.

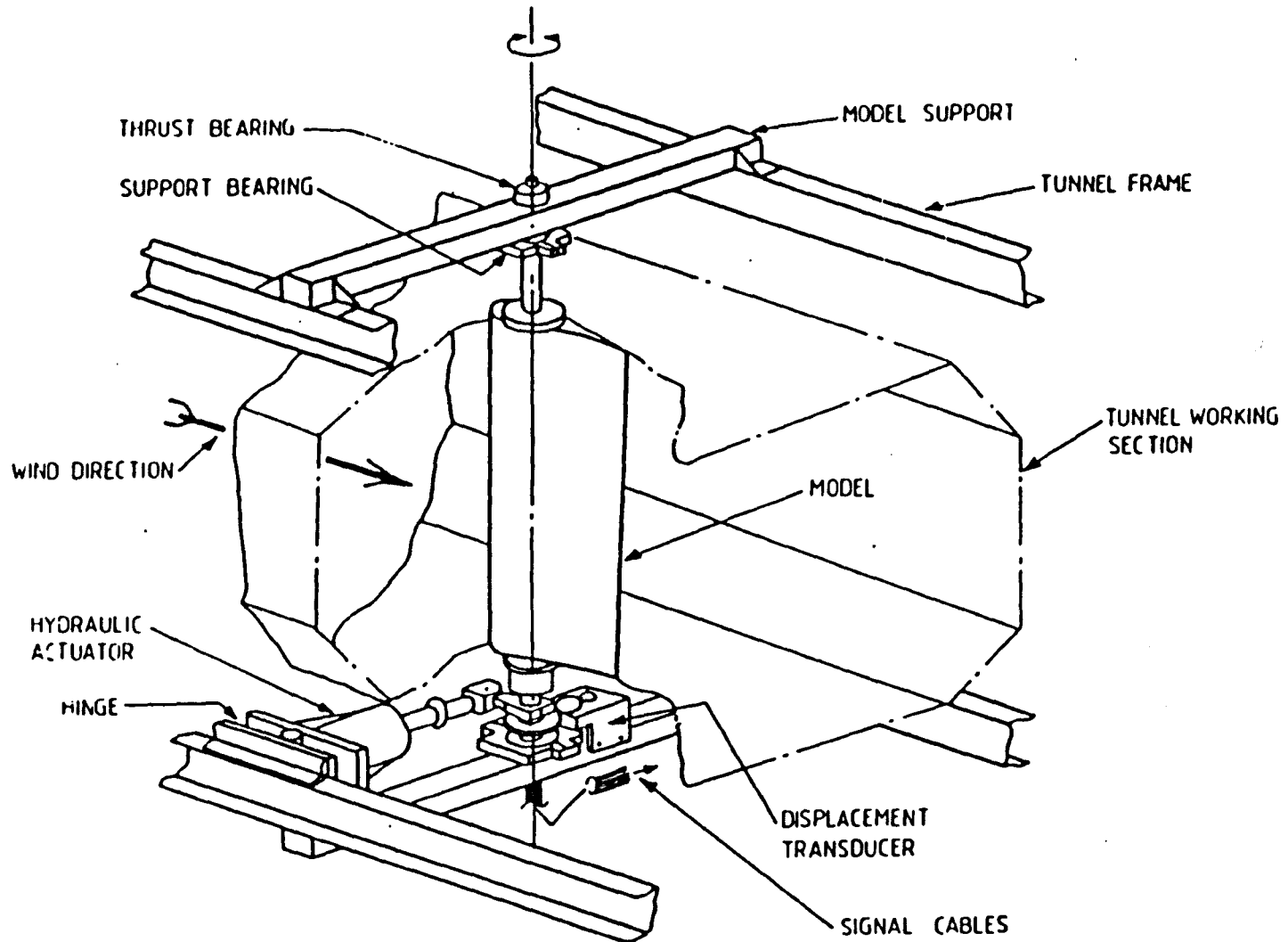


FIGURE 2.2 The Glasgow University Unsteady Aerofoil Test Facility.

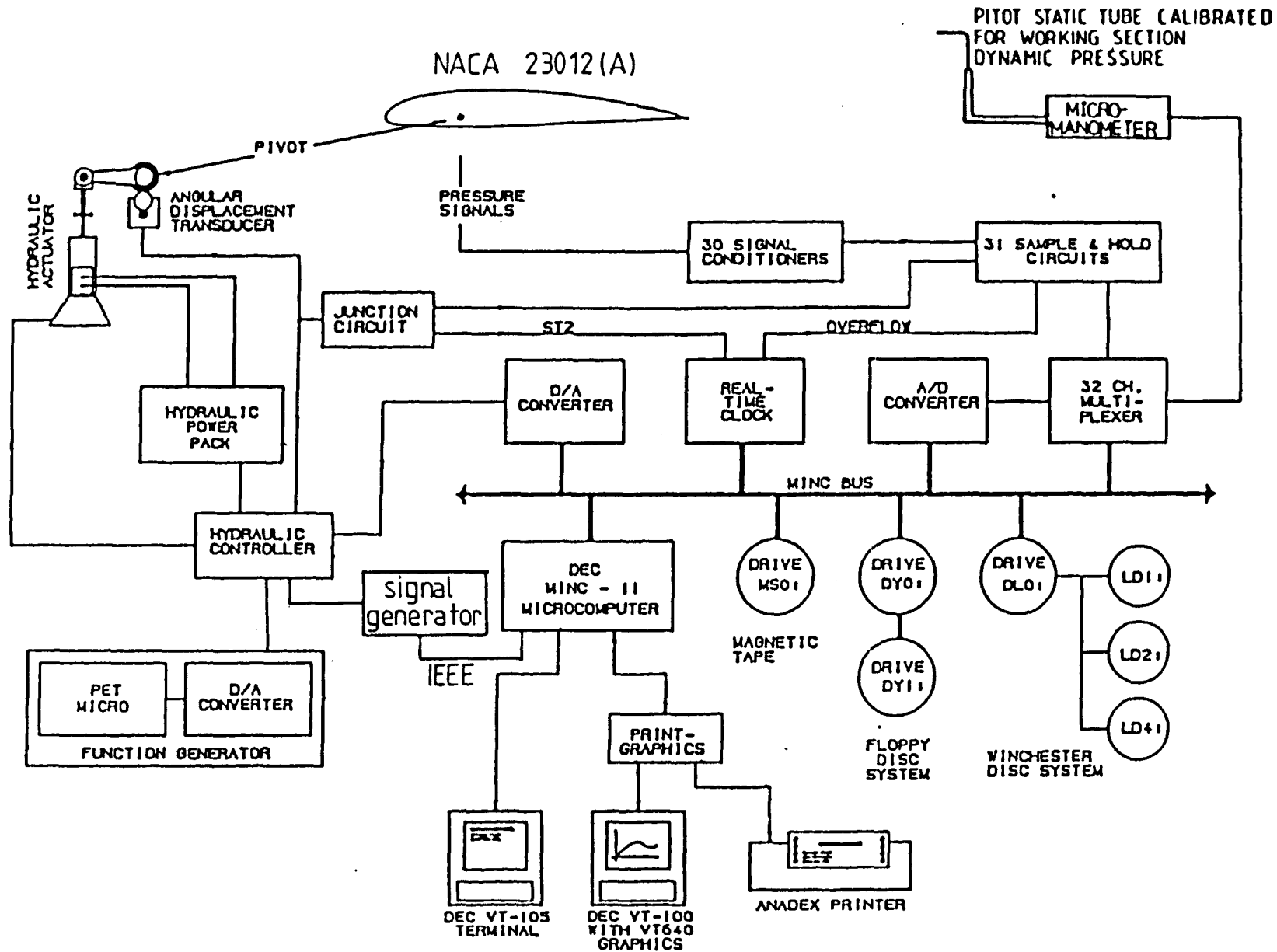
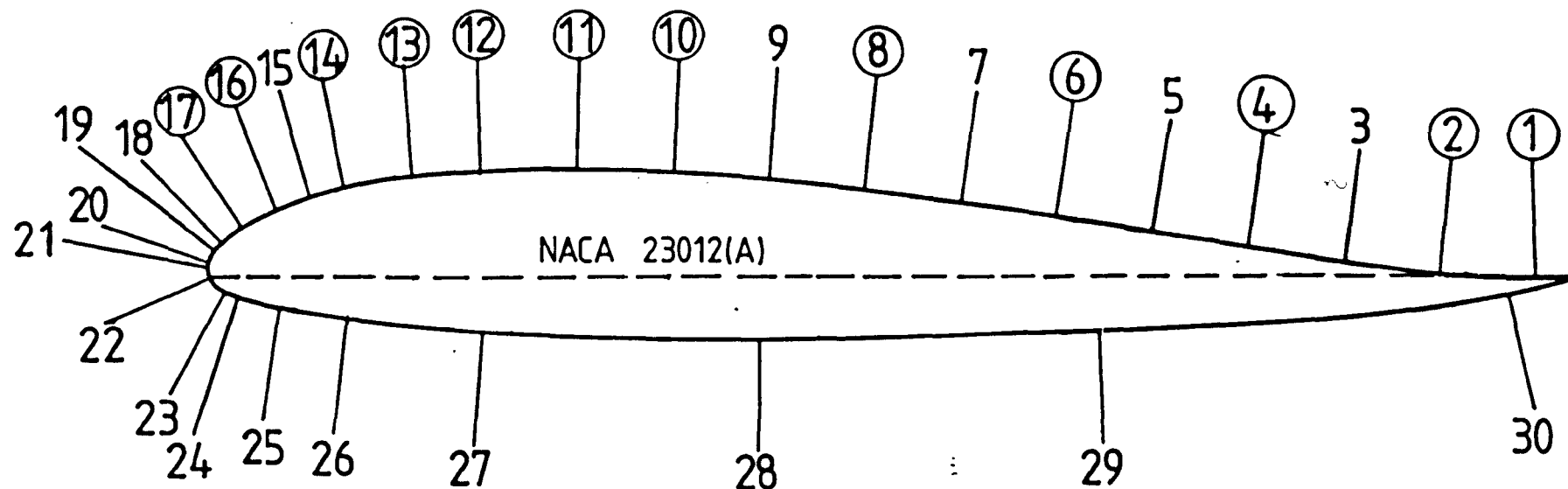


FIGURE 2.3 Schematic Arrangement of Data Acquisition and Control System.



TRANSDUCER LOCATIONS NACA 23012(A)					
No.	x/c	No.	x/c	No.	x/c
1	0.97	11	0.27	21	0.00
2	0.90	12	0.20	22	0.00
3	0.83	13	0.15	23	0.01
4	0.76	14	0.10	24	0.02
5	0.69	15	0.075	25	0.05
6	0.62	16	0.05	26	0.10
7	0.55	17	0.025	27	0.20
8	0.48	18	0.01	28	0.40
9	0.41	19	0.005	29	0.65
10	0.34	20	0.0005	30	0.95

○ Hot-Film Location

FIGURE 2.4 Location of Pressure Transducers and Hot-Film Gauges for the NACA 23012(A) Aerofoil.

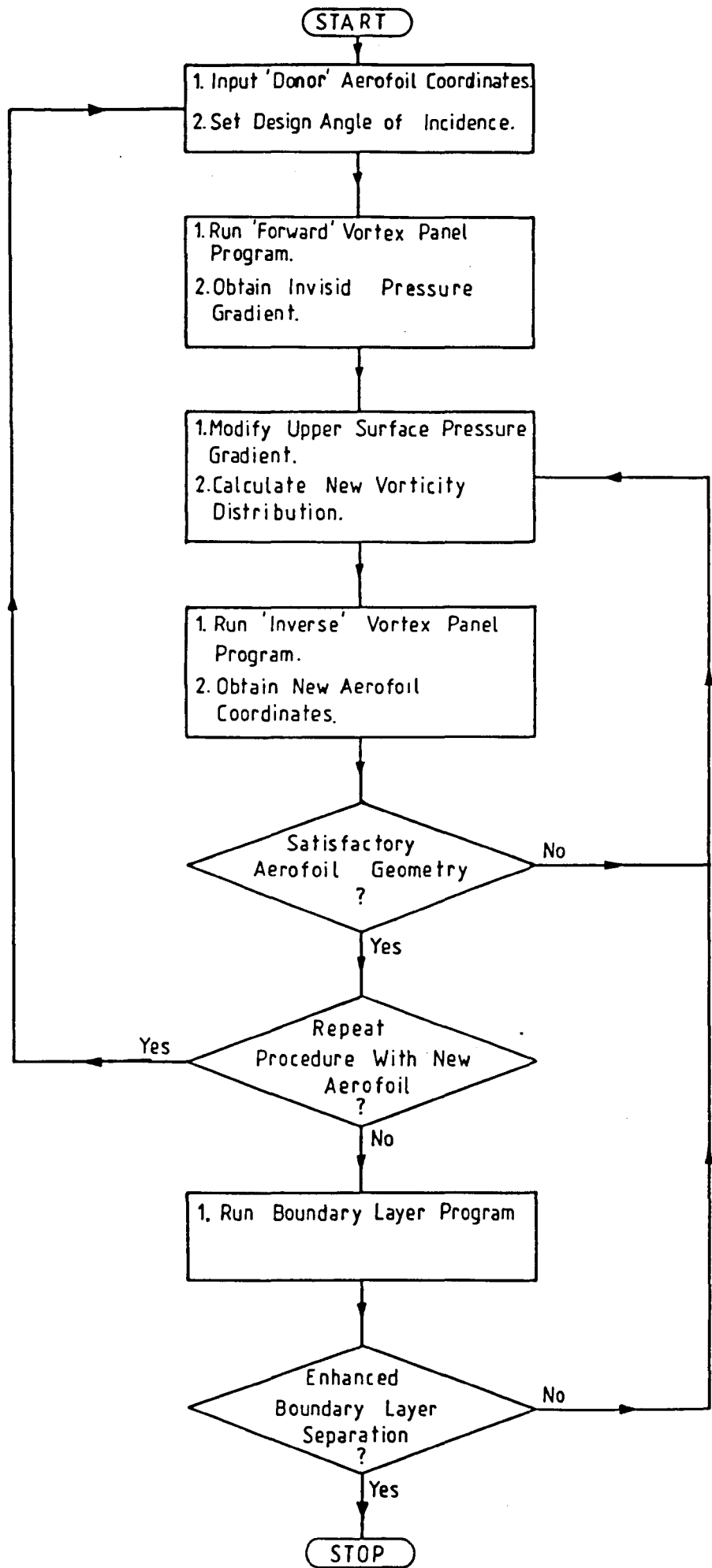


FIGURE 3.1 Inverse Aerofoil Design Technique.

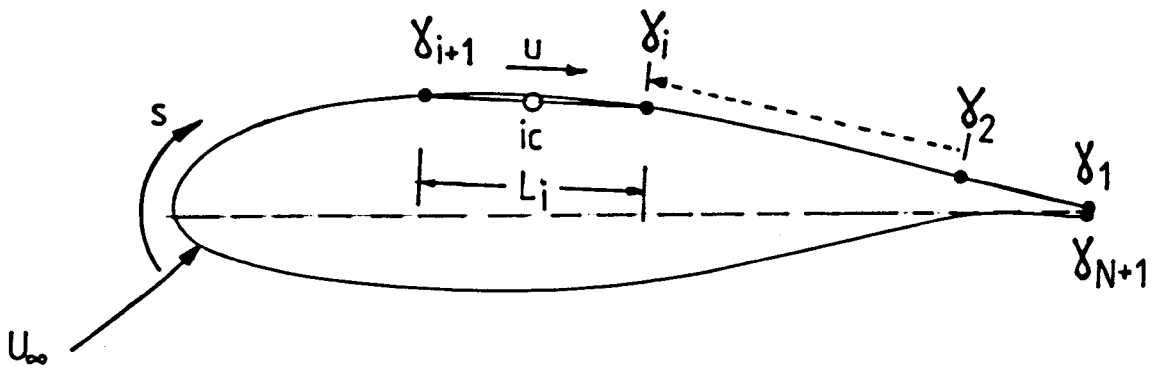


FIGURE 3.2 Panel Method Notation.

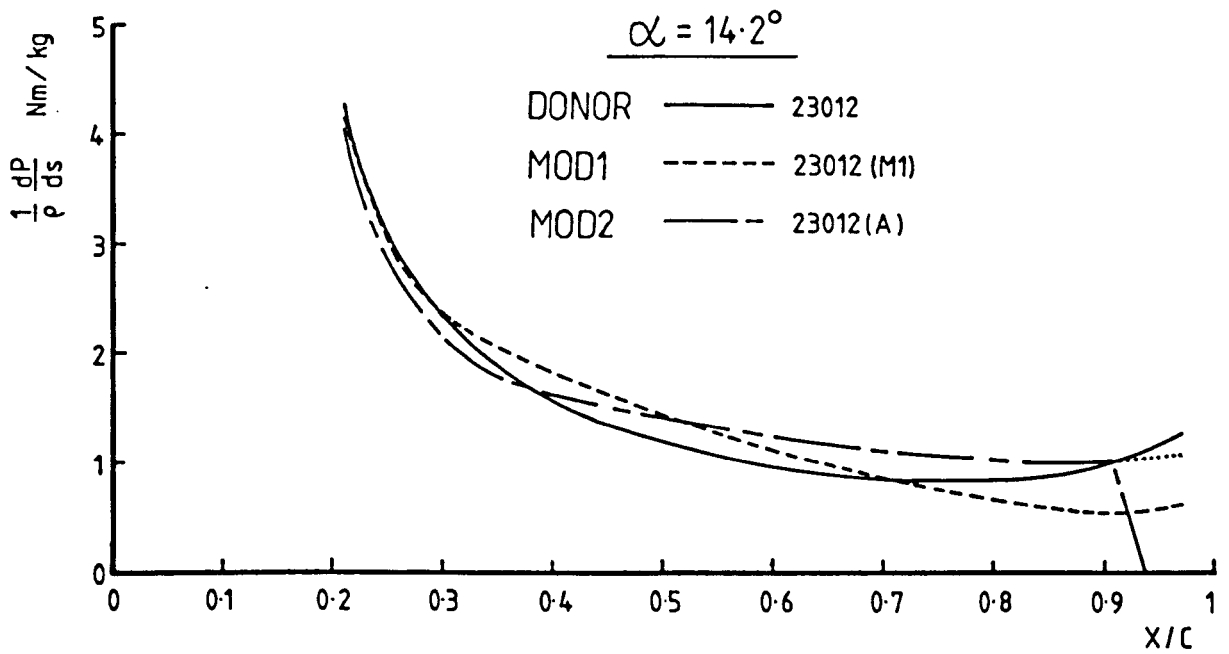


FIGURE 3.3 Theoretical Pressure Gradient Comparison.

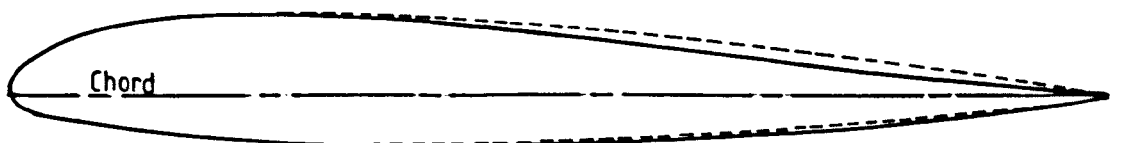


FIGURE 3.4 The NACA 23012(M1) Aerofoil.

----- 23012
 ————— 23012(M1)

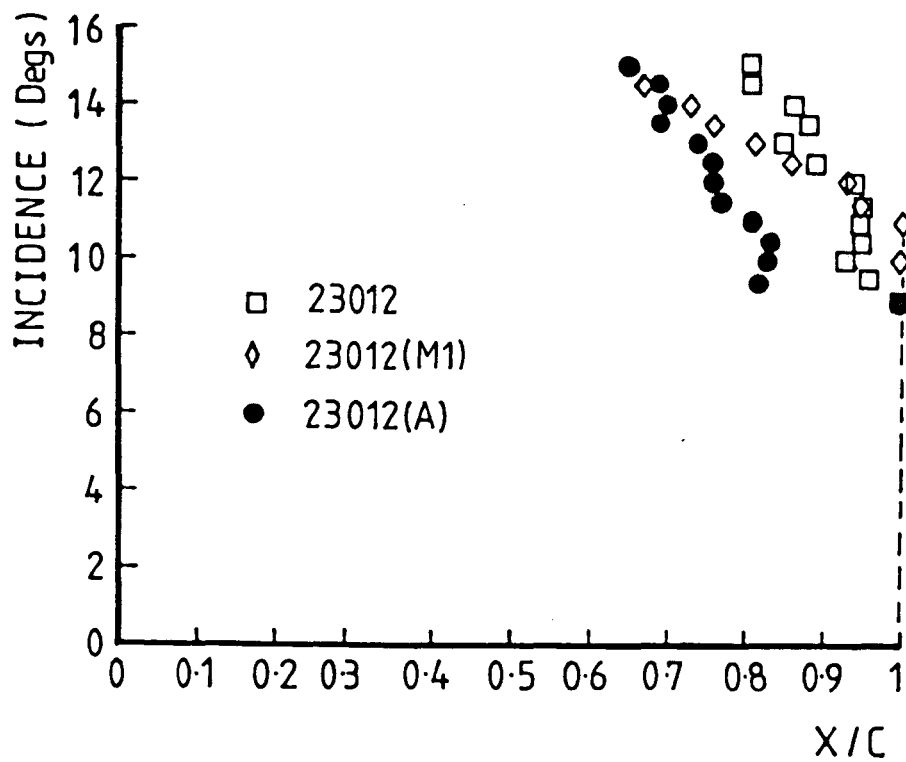


FIGURE 3.5 Theoretical Variation of Aerofoil Upper Surface Turbulent Boundary-Layer Separation with Incidence.

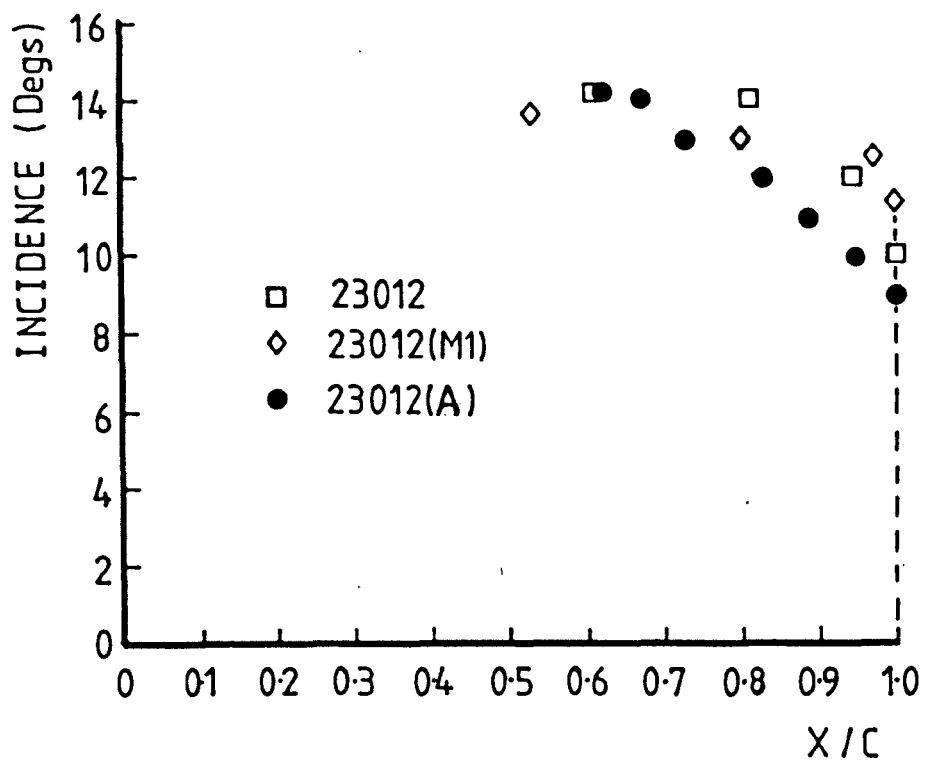


FIGURE 3.6 Experimental Variation of Aerofoil Upper Surface Turbulent Boundary-Layer Separation with Incidence (estimated from Oil-Flow Tests).

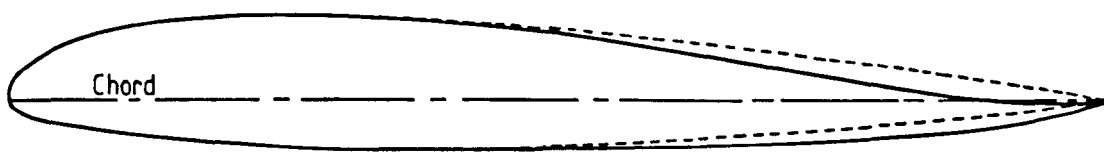


FIGURE 3.7 The NACA 23012(A) Aerofoil.

----- 23012
 ———— 23012(A)

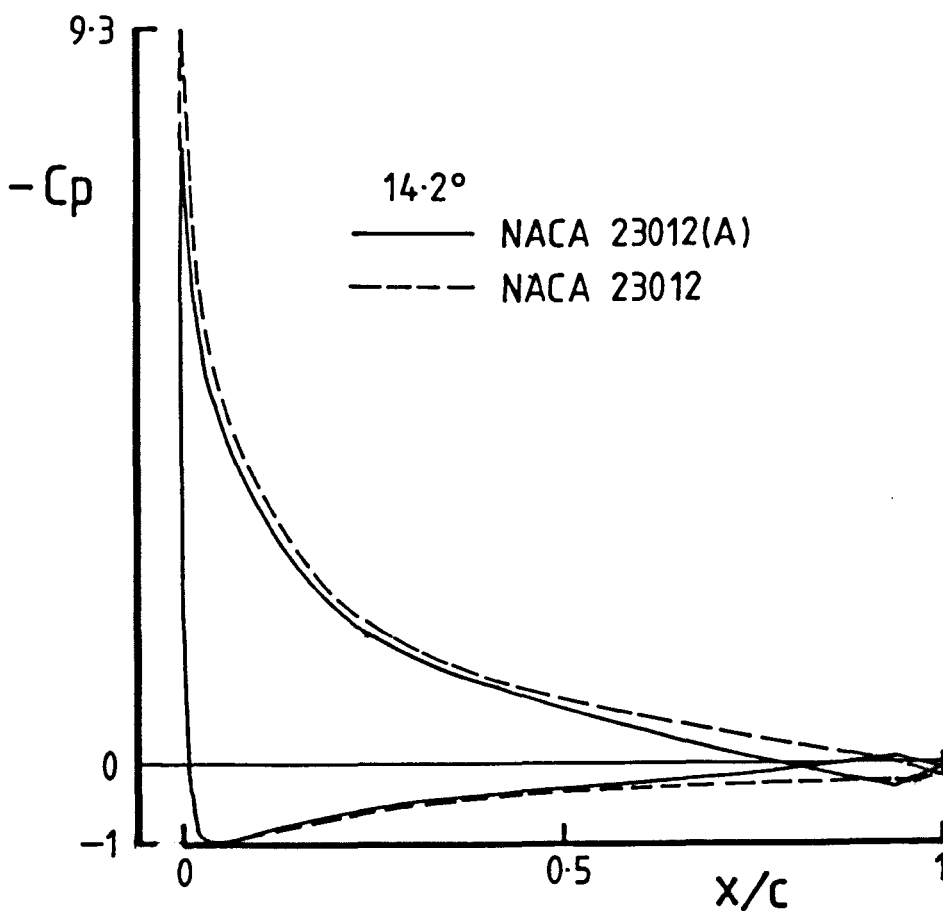
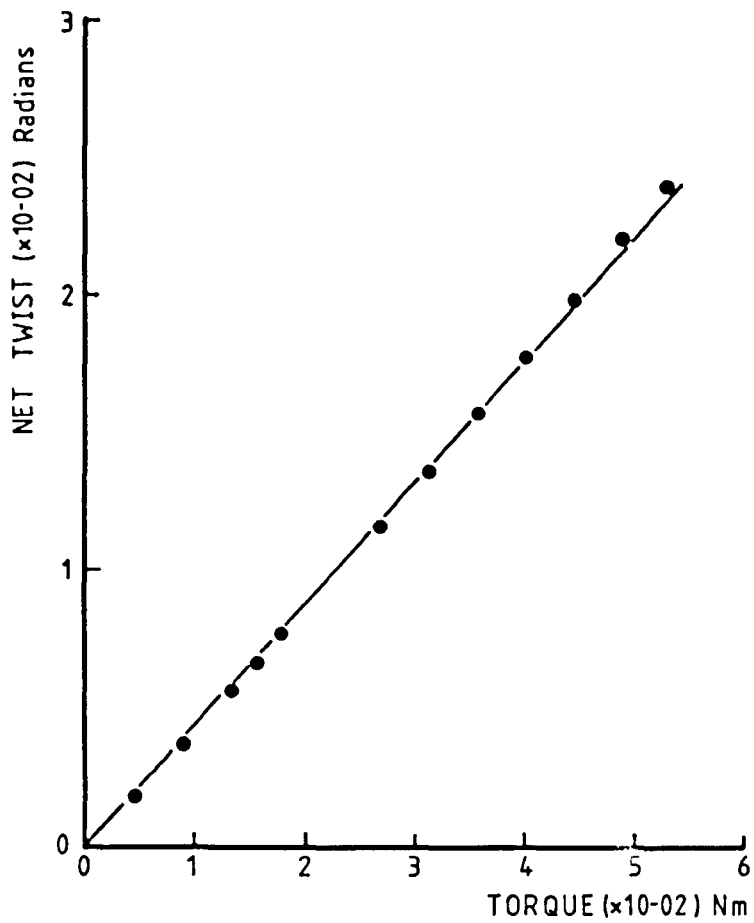
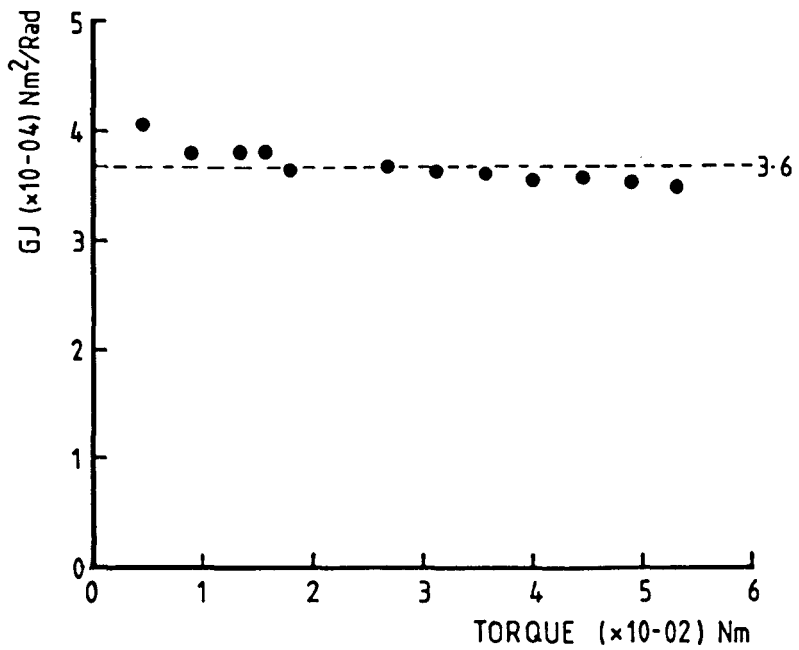


FIGURE 3.8 Theoretical Chordwise Pressure Distribution Comparison.



(a) Torsional Stiffness.



(b) Torsional Rigidity.

FIGURE 3.9 Structural Properties of Wind Tunnel Model (without Internal Spar).

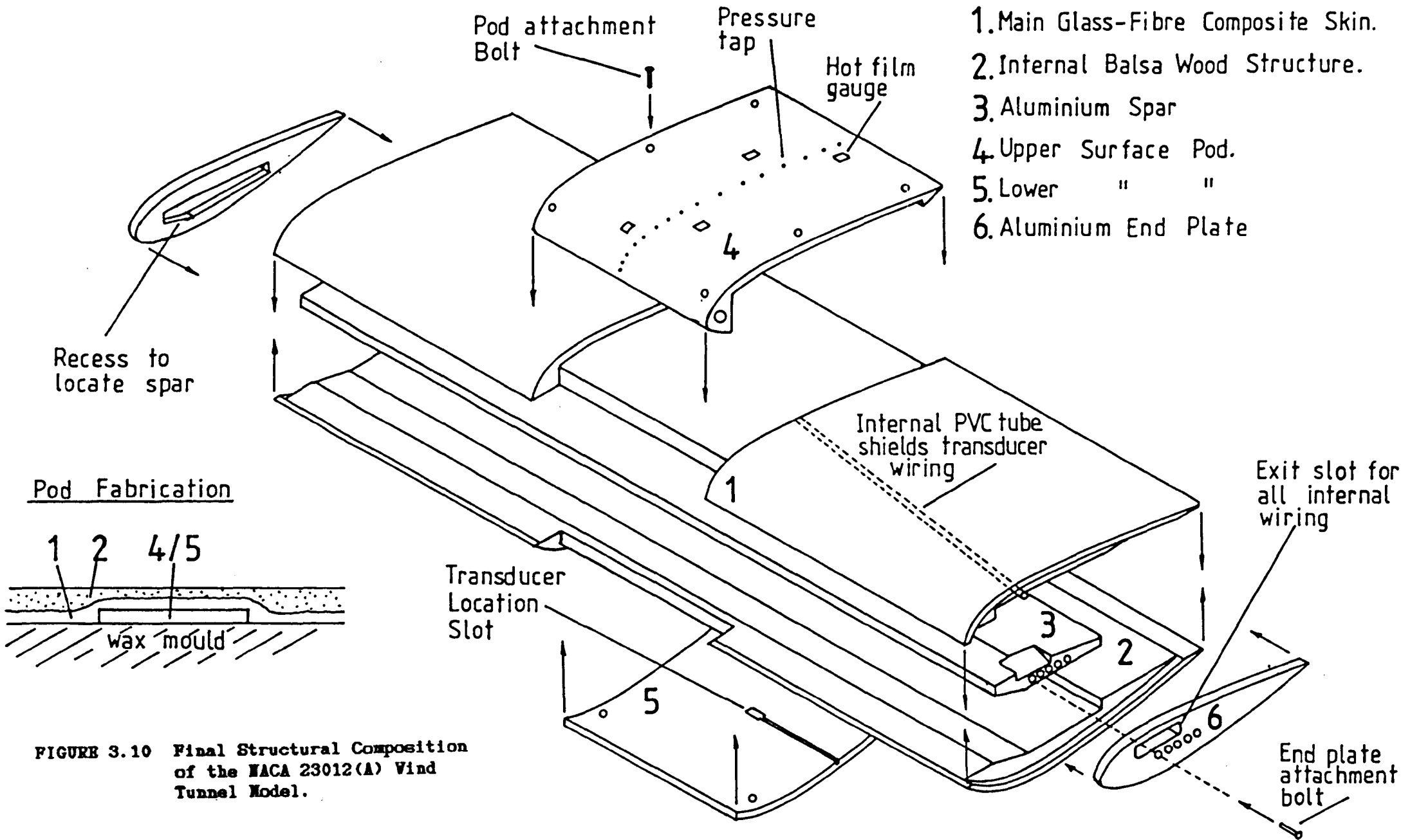


FIGURE 3.10 Final Structural Composition of the NACA 23012(A) Wind Tunnel Model.

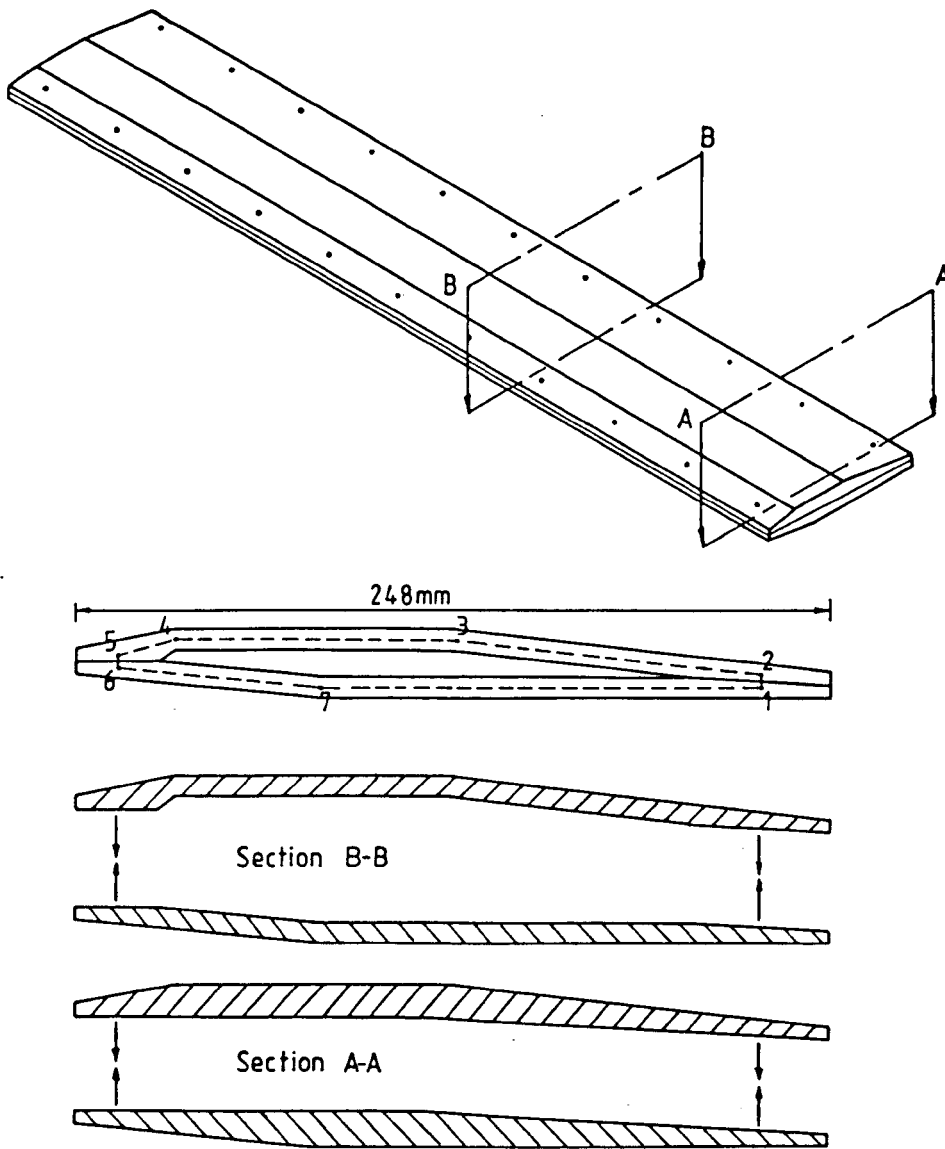


FIGURE 3.11 Internal Spar of NACA 23012(A) Wind Tunnel Model.

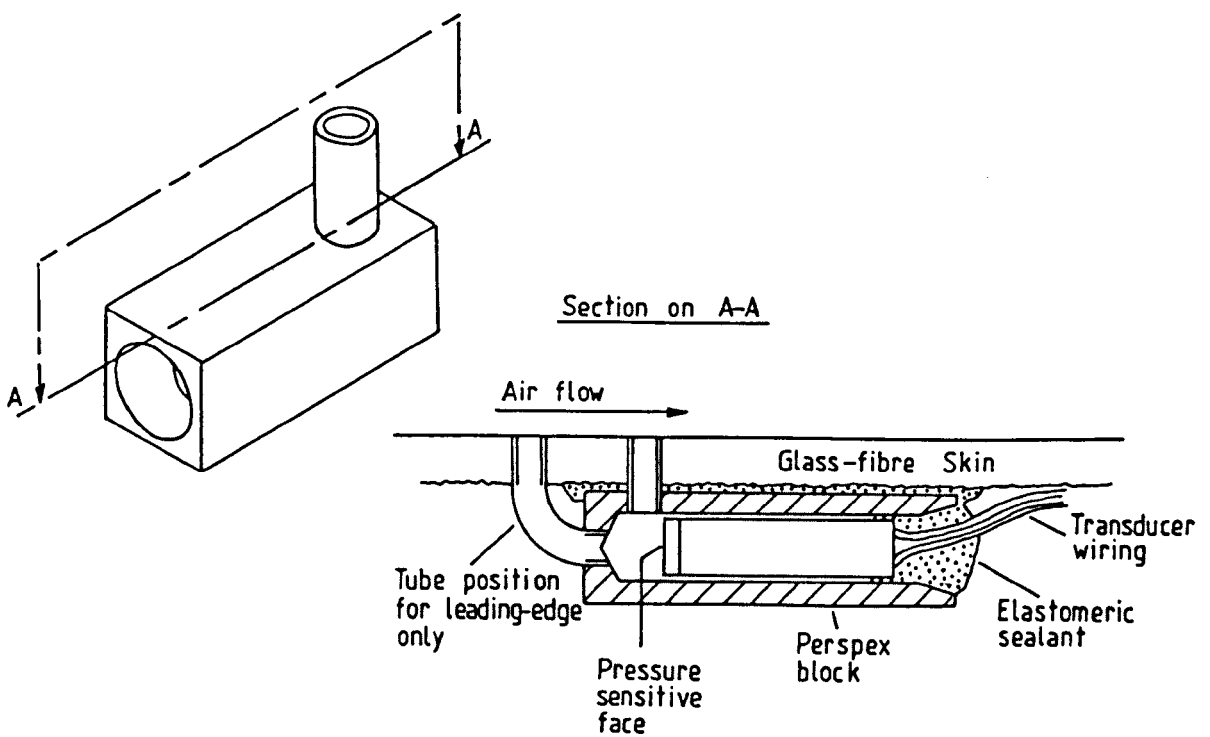
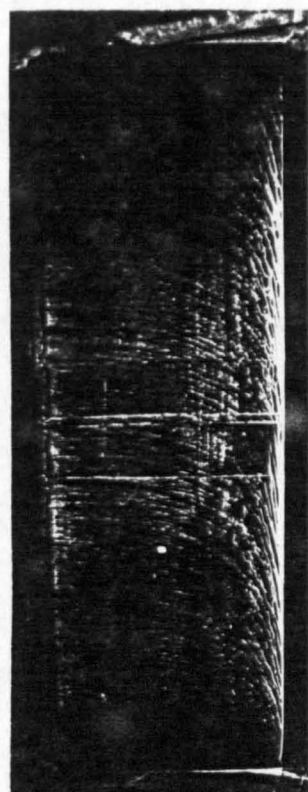
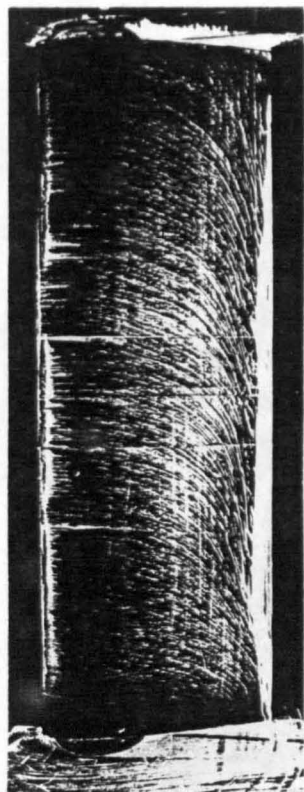


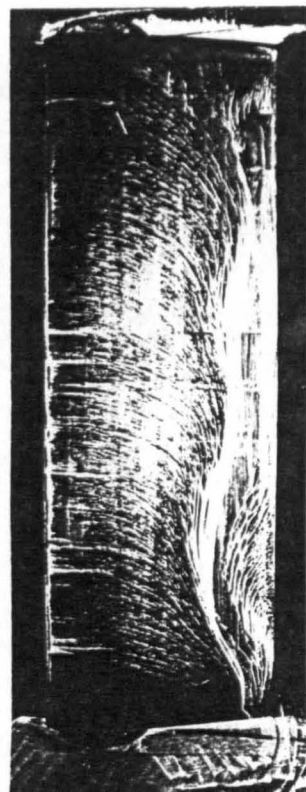
FIGURE 3.12 Pressure Transducer Housing.



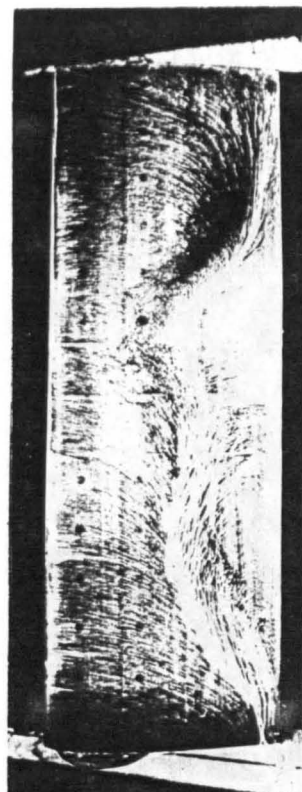
(a) $\alpha = 10.0^\circ$



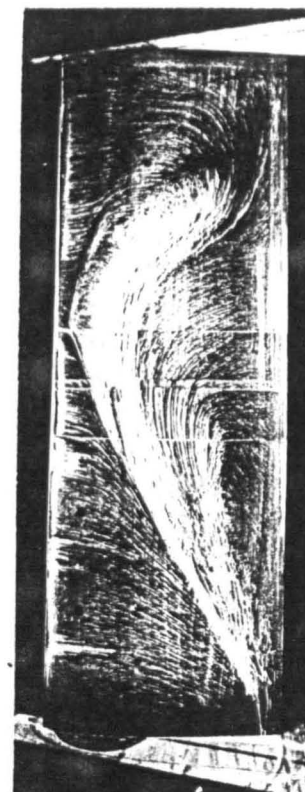
(b) $\alpha = 12.0^\circ$



(c) $\alpha = 14.0^\circ$



(d) $\alpha = 14.2^\circ$



(e) $\alpha = 15.0^\circ$

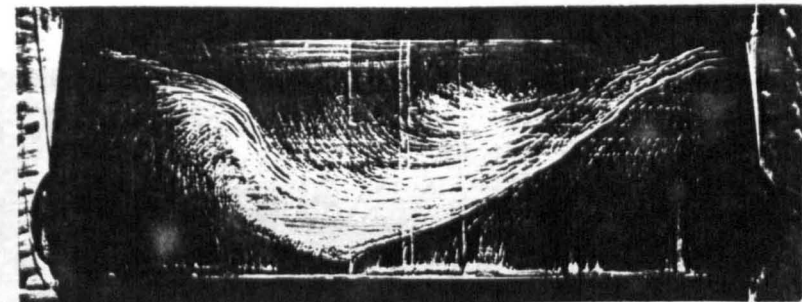
FIGURE 4.1 Results from Oil-Flow Experiments carried out on the NACA 23012 Aerofoil at 1.5×10^6 Reynolds number (from Seto et al, 1984).



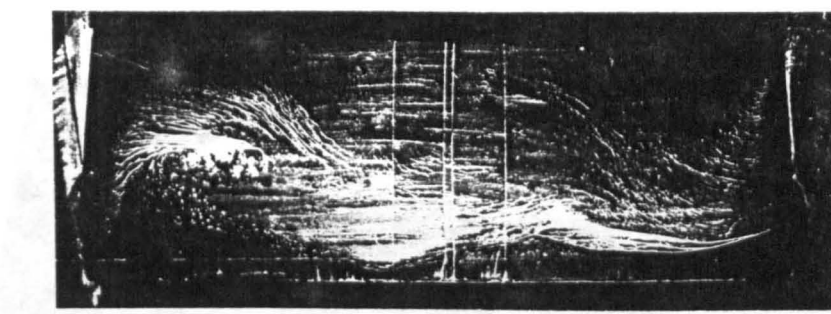
(a) $\alpha = 16.4^\circ$



(b) $\alpha = 16.0^\circ$



(f) $\alpha = 16.0^\circ$



(g) $\alpha = 20.0^\circ$

FIGURE 4.2. Scattering of light from a surface of a polymer film. (a) $\alpha = 16.4^\circ$, (b) $\alpha = 16.0^\circ$, (f) $\alpha = 16.0^\circ$, (g) $\alpha = 20.0^\circ$.

FIGURE 4.1. Completed.

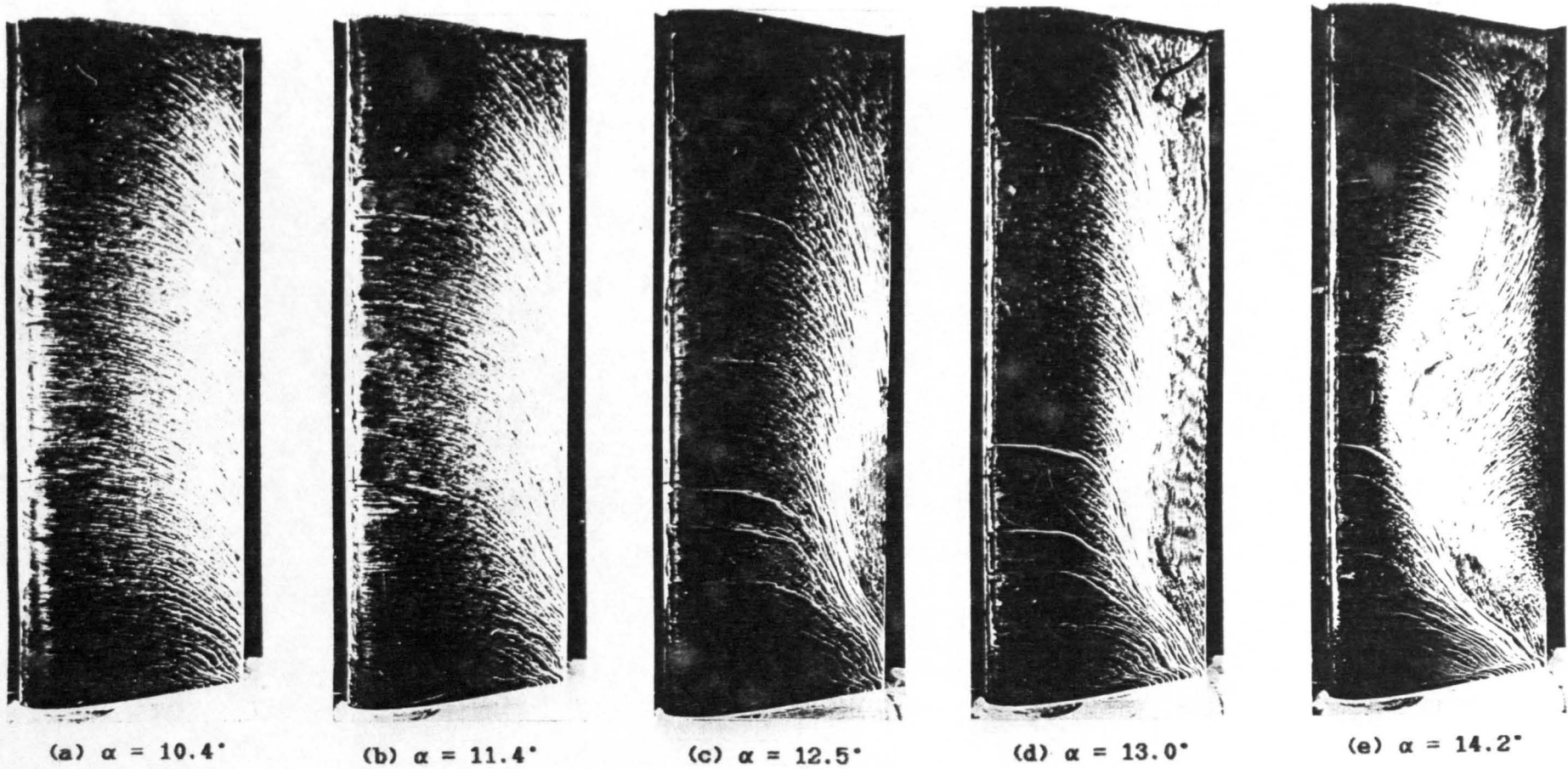
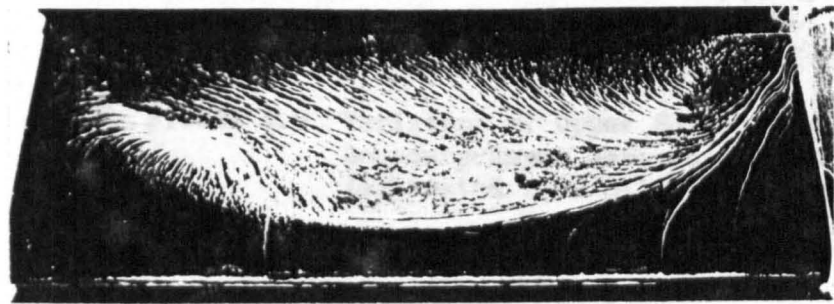
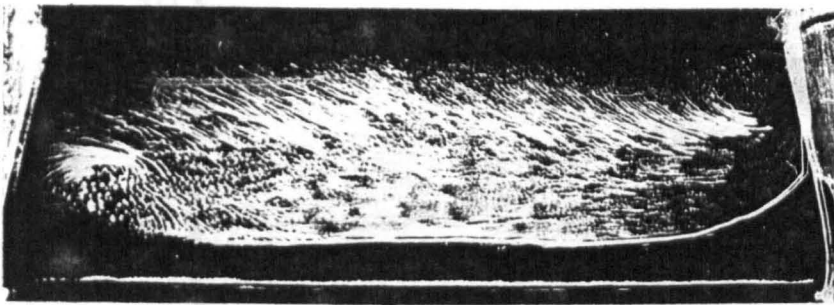


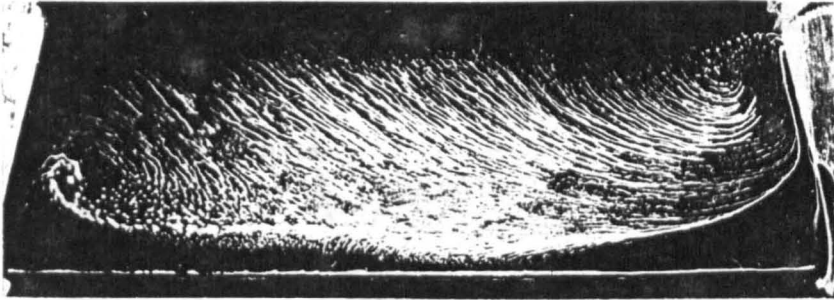
FIGURE 4.2 Results from Oil-Flow Experiments carried out on the NACA 23012(N1) Aerofoil at 1.5×10^6 Reynolds number.



(f) $\alpha = 15.7^\circ$



(g) $\alpha = 18.7^\circ$



(h) $\alpha = 20.4^\circ$

FIGURE 4.2 Completed

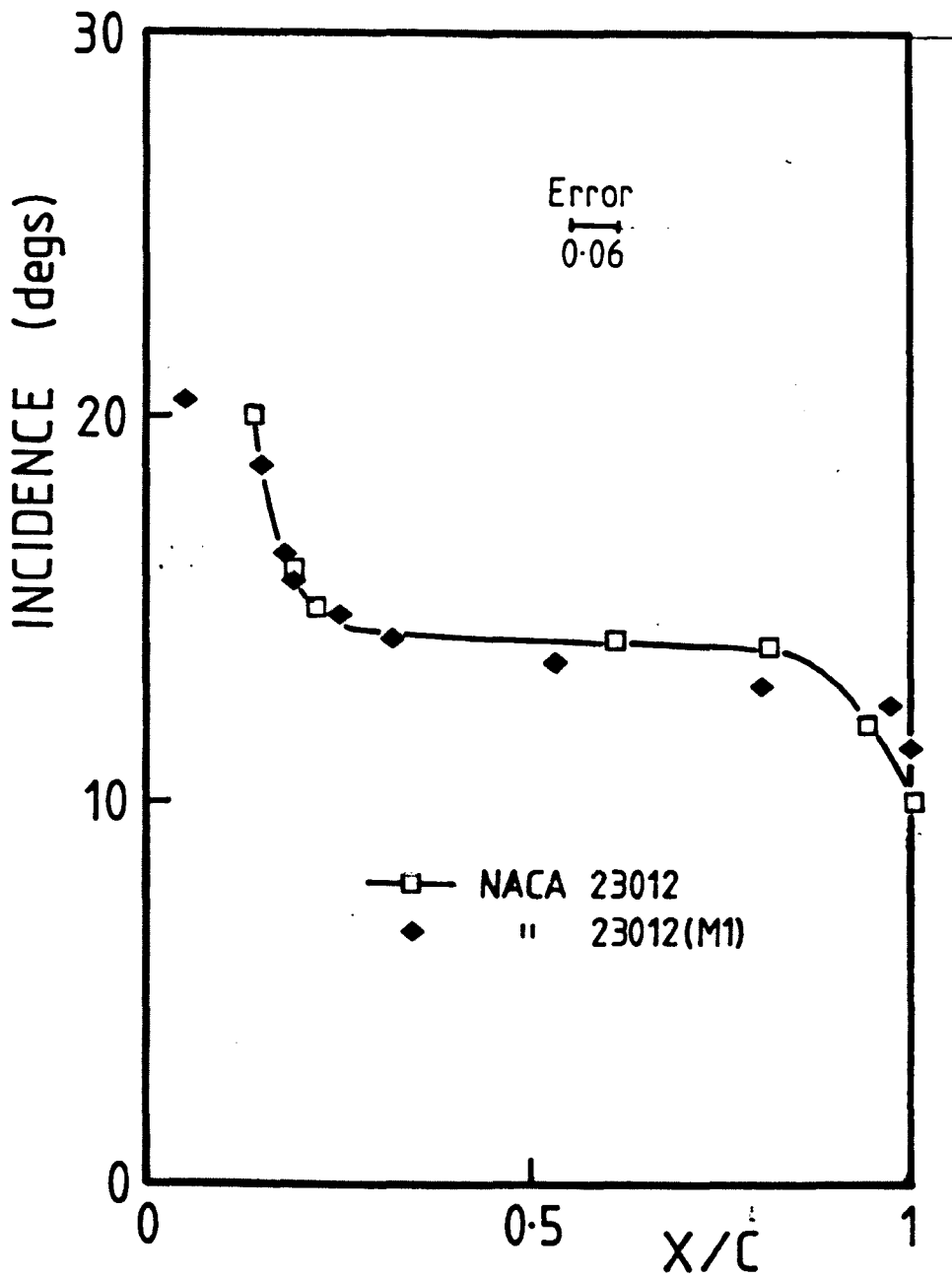


FIGURE 4.3 Variation of Upper Surface Turbulent Boundary-Layer Separation with Incidence (estimated from Oil-Flow Tests).

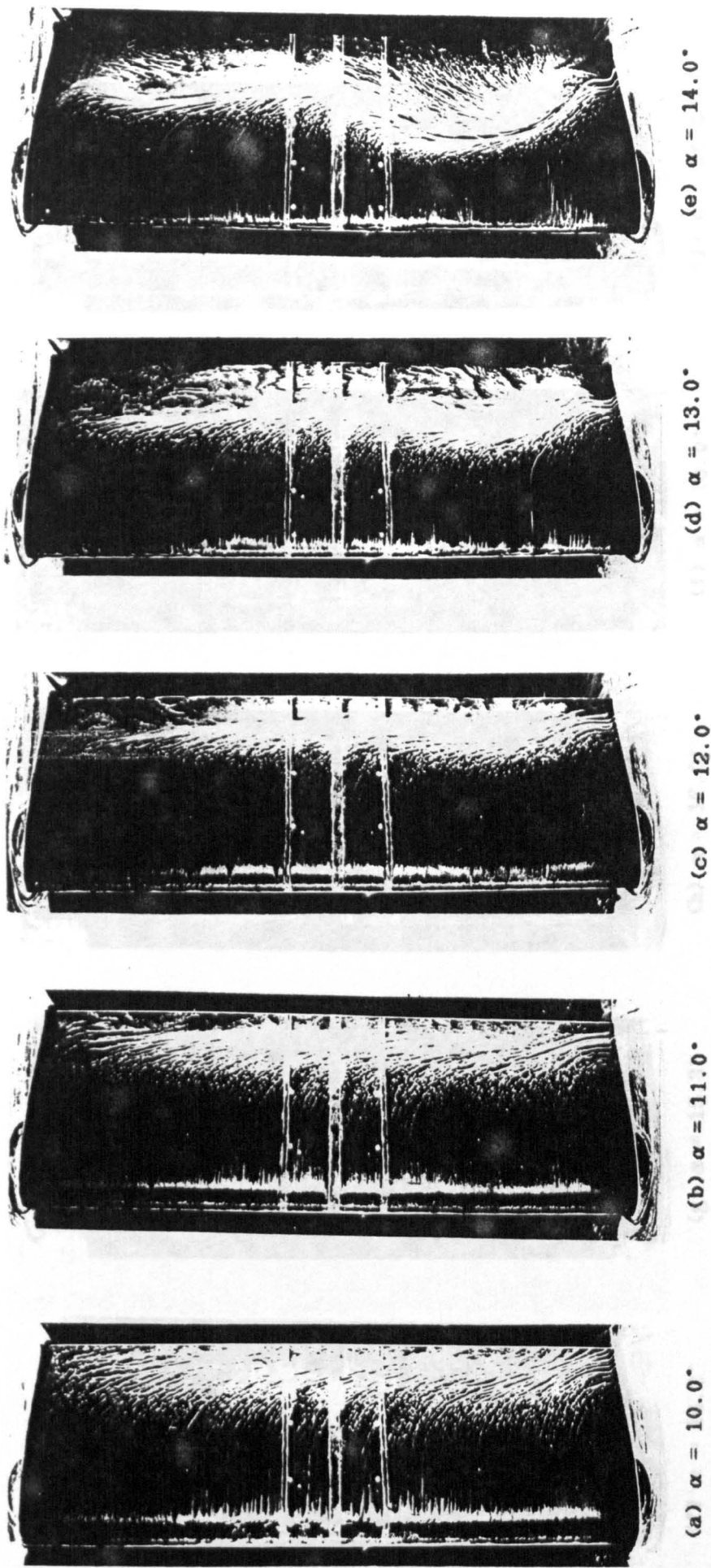
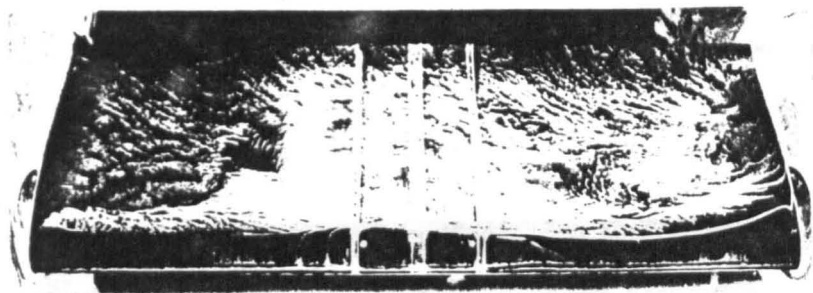
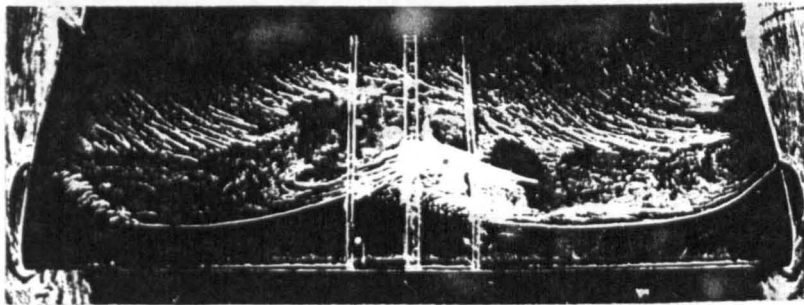


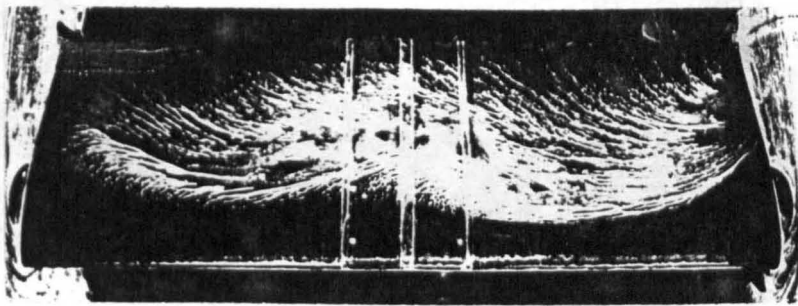
FIGURE 4.4 Results from Oil-Flow Experiments carried out on the IACA 23012(A) Aerofoil at 1.5×10^6 Reynolds number.



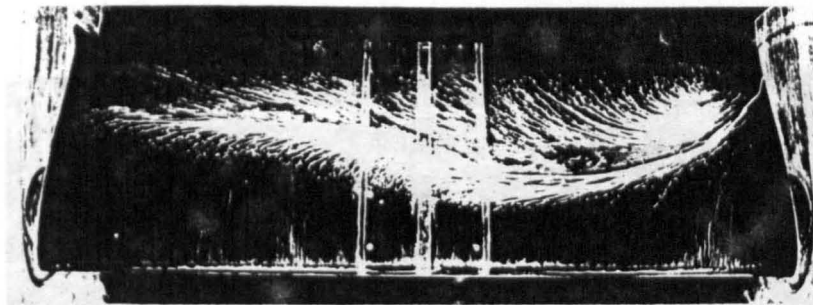
(j) $\alpha = 20.0^\circ$



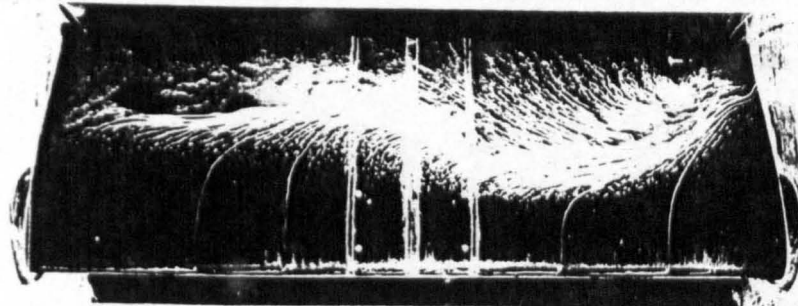
(i) $\alpha = 18.0^\circ$



(h) $\alpha = 17.0^\circ$



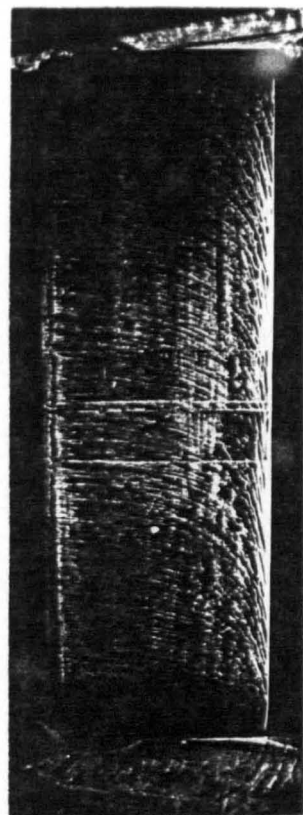
(g) $\alpha = 15.3^\circ$



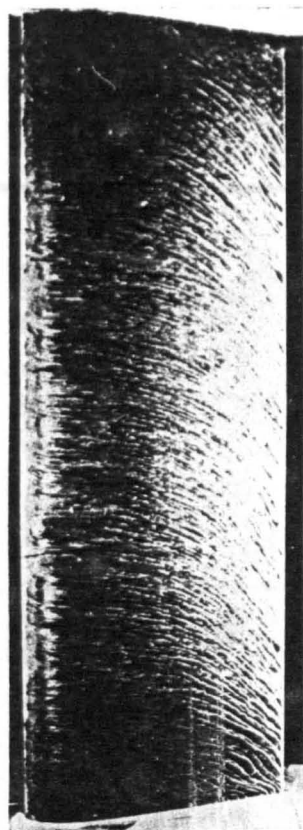
(f) $\alpha = 14.2^\circ$

FIGURE 4.3. Illustration of the progressive increase in curvature of the three tubes, measured at one-tenth degree intervals of α .

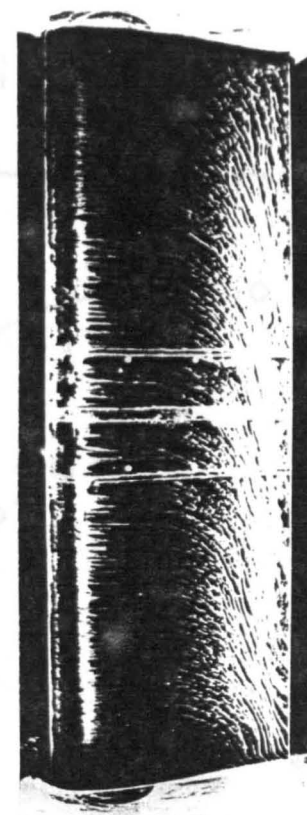
FIGURE 4.4. Completed.



(a) NACA 23012



(b) NACA 23012(M1)



(c) NACA 23012(A)

FIGURE 4.5 Visualisation of the Progressive Increase in Trailing-Edge Adverse Pressure Gradient between the Three Test Aerofoils (as implied from the Downward Flow of Oil). $\alpha = 10^\circ$.

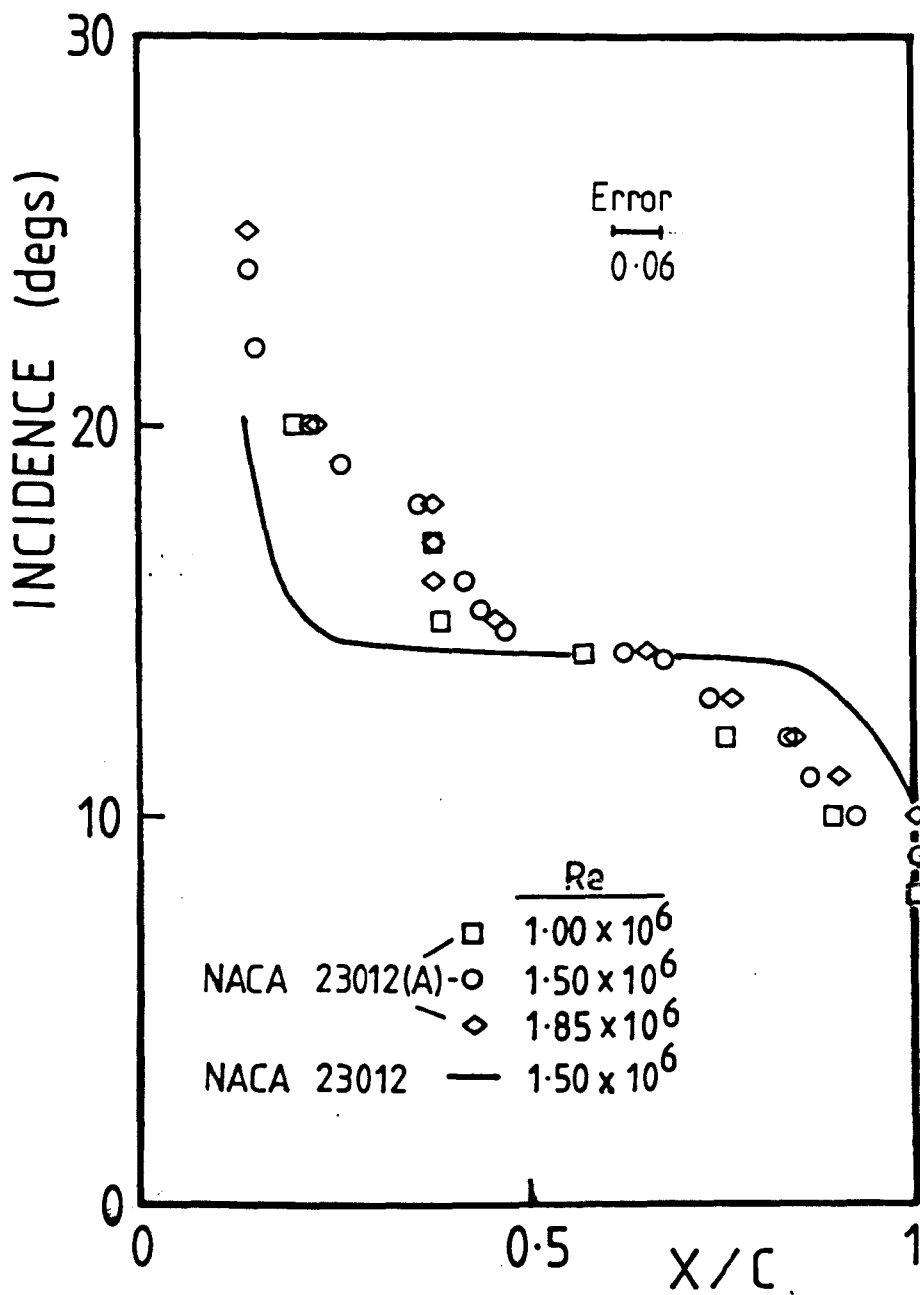


FIGURE 4.6 Variation of Upper Surface Turbulent Boundary-Layer Separation with Incidence (estimated from Oil-Flow Tests).

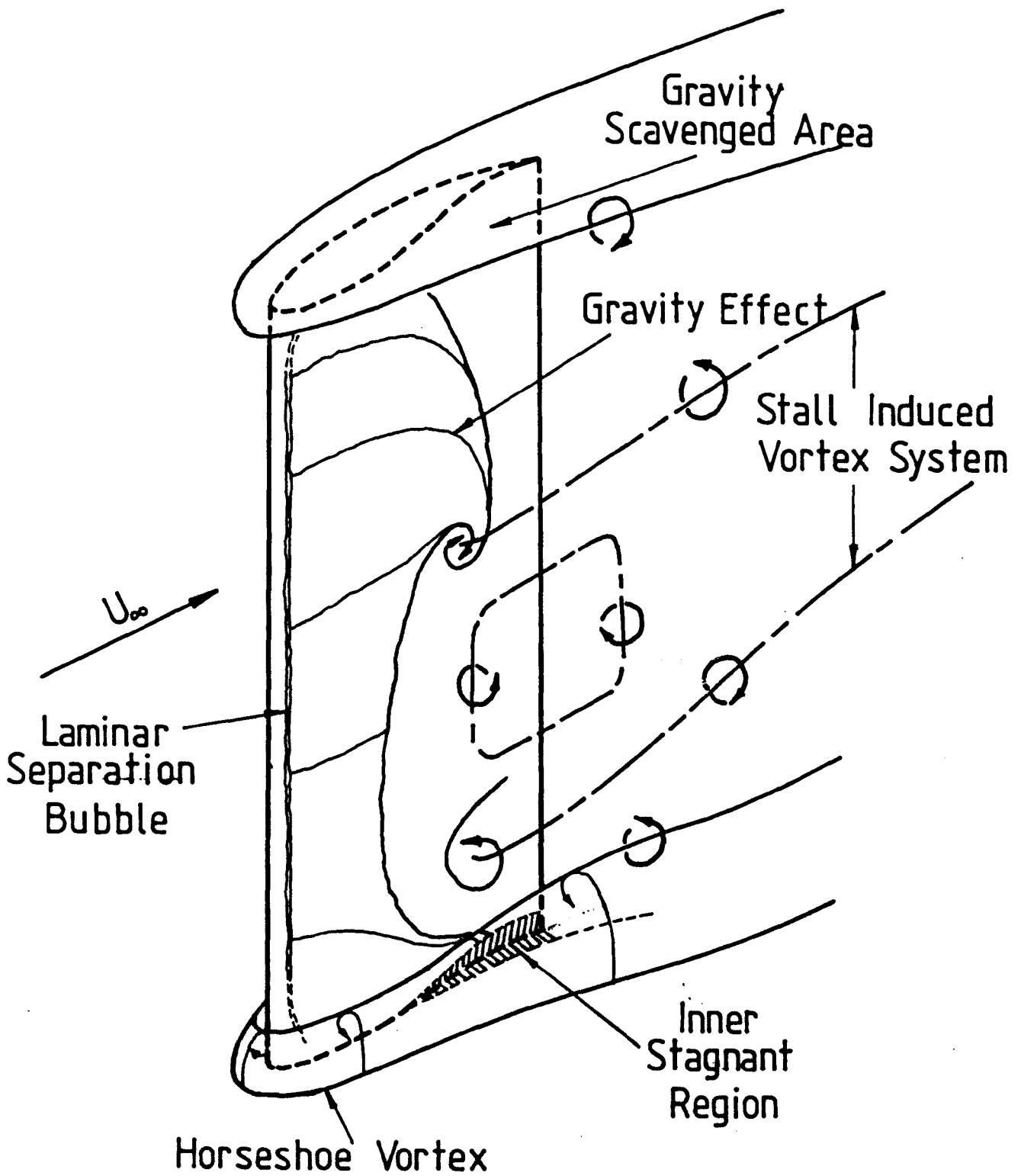
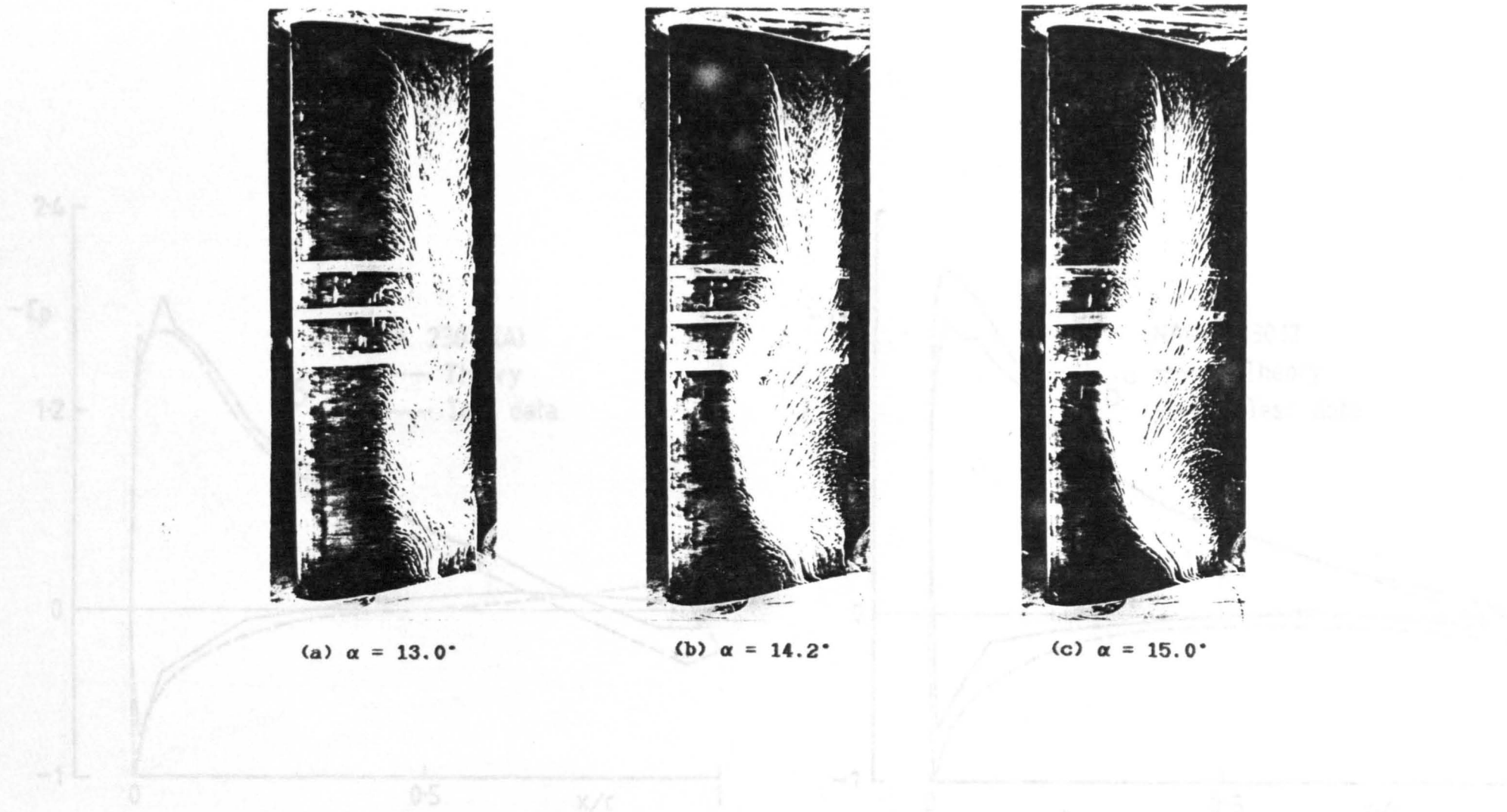


FIGURE 4.7 Typical Phenomena Associated with Oil-Flow Experiments.



(a) $\alpha = 13.0^\circ$

(b) $\alpha = 14.2^\circ$

(c) $\alpha = 15.0^\circ$

FIGURE 4.8 Results from Slow Ramp Tests on the WACA 23012(A).

FIGURE 5.1 Comparison between Theoretical Predictions and Wind Tunnel Results at 6° Incidence.

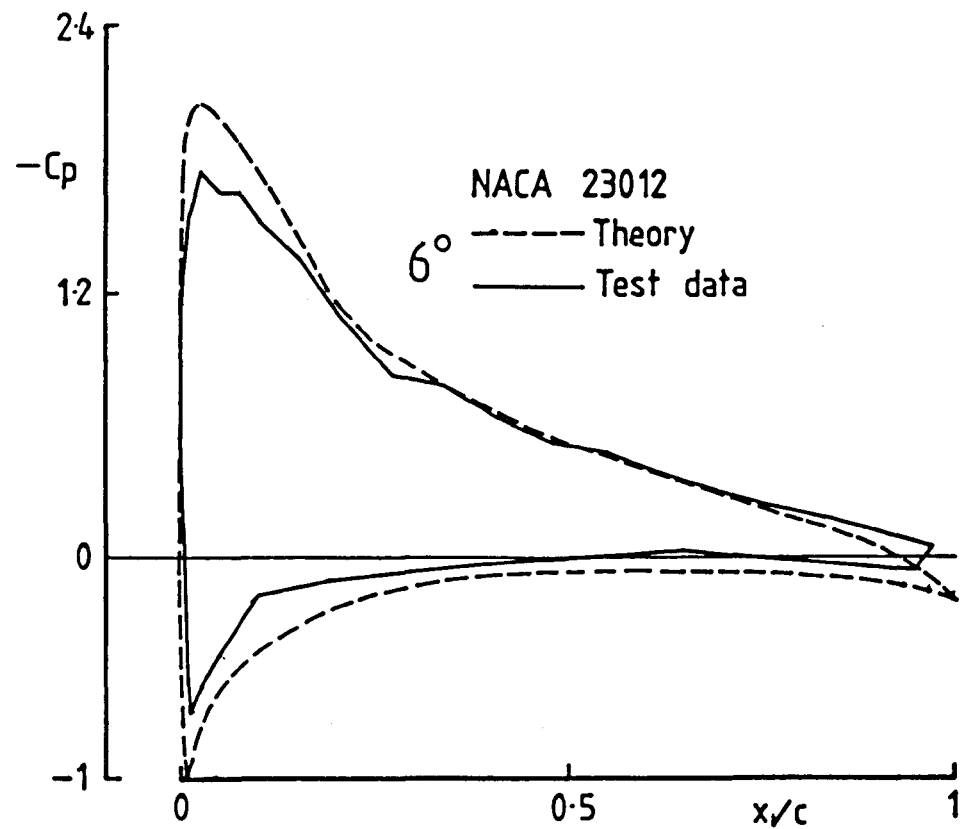
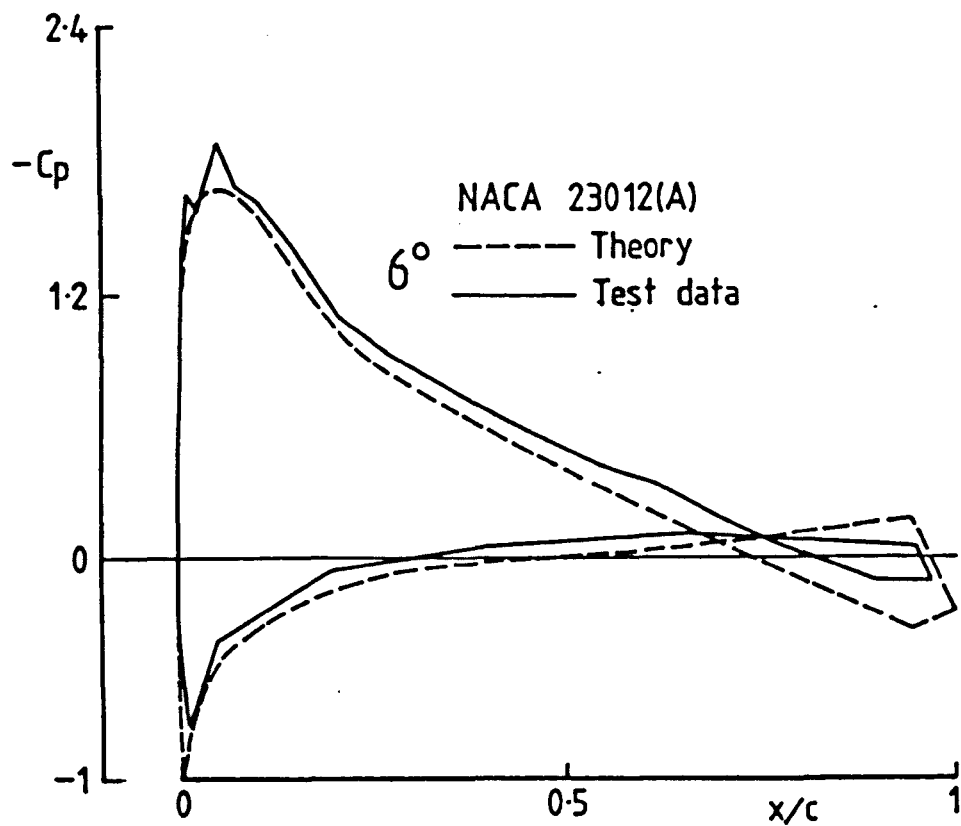


FIGURE 5.1 Comparisons between Theoretical Predictions and Wind Tunnel Results at 6° Incidence.

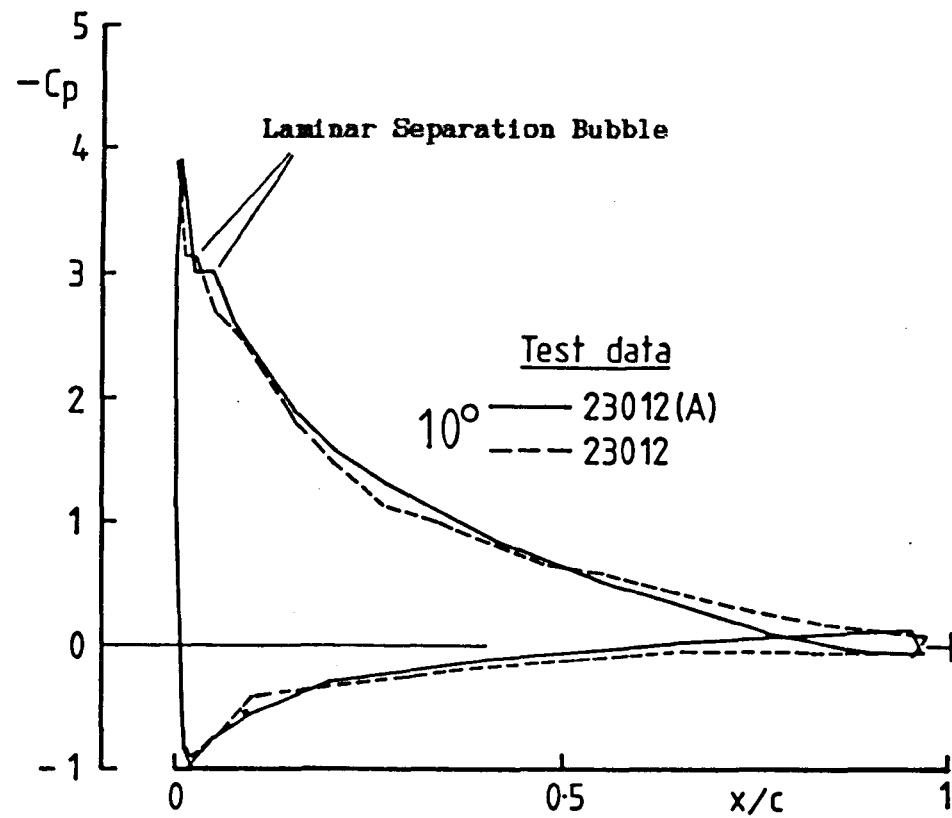
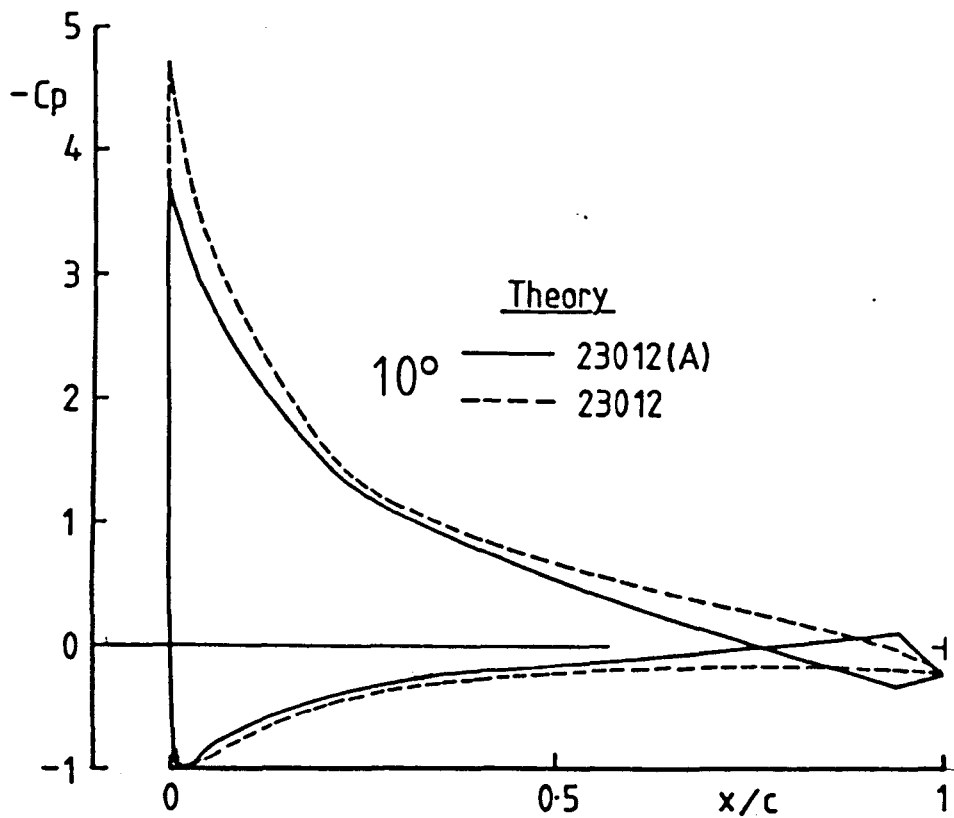


FIGURE 5.2 Comparison of Relative Differences in Pressure Distribution between the NACA 23012 and 23012(A) Aerofoils.

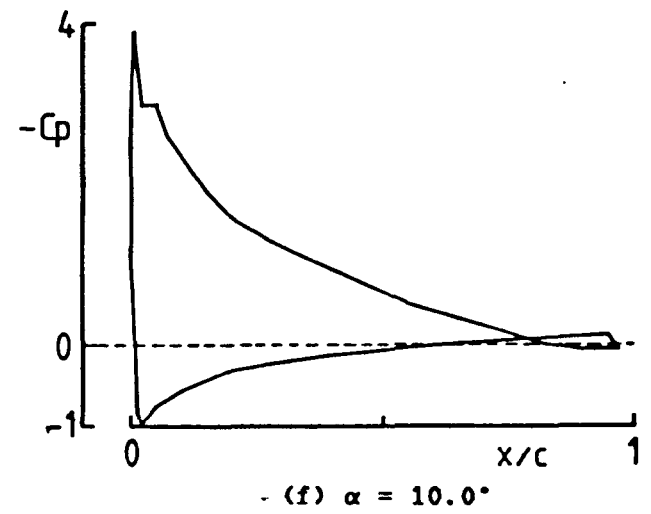
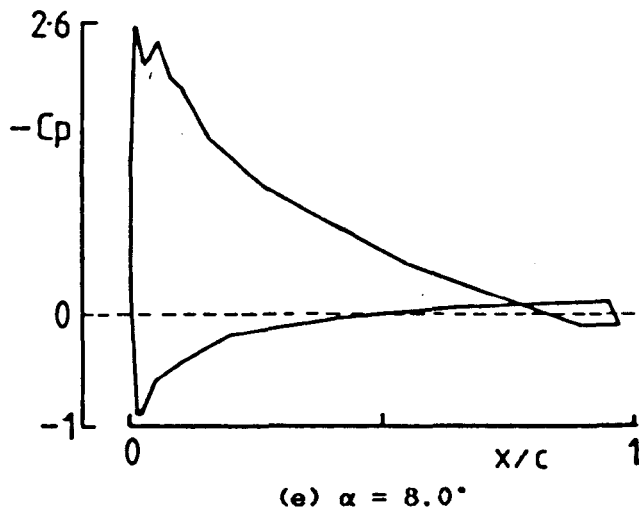
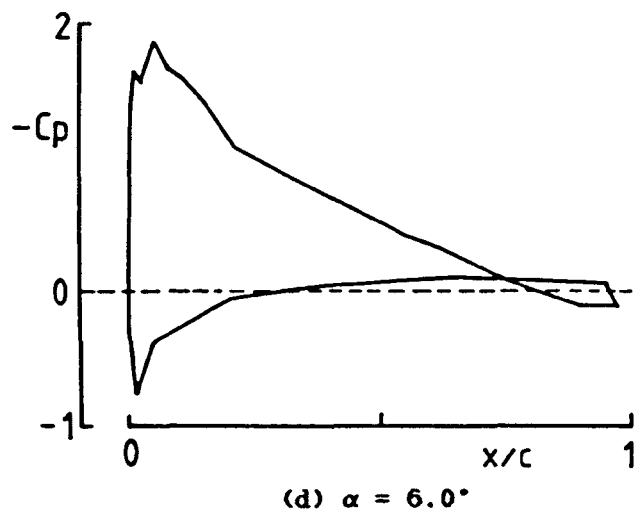
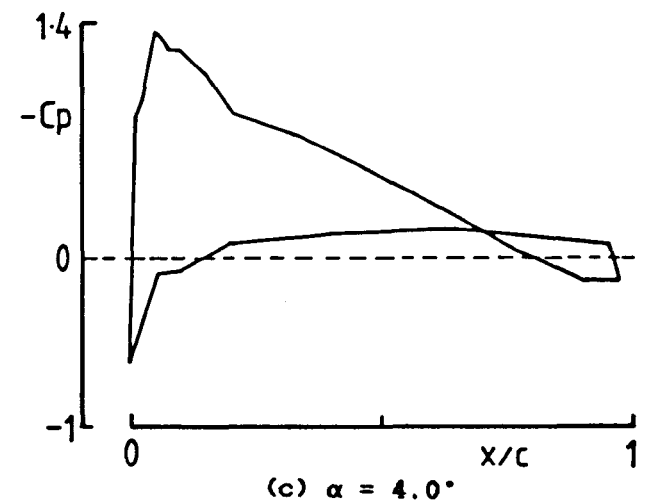
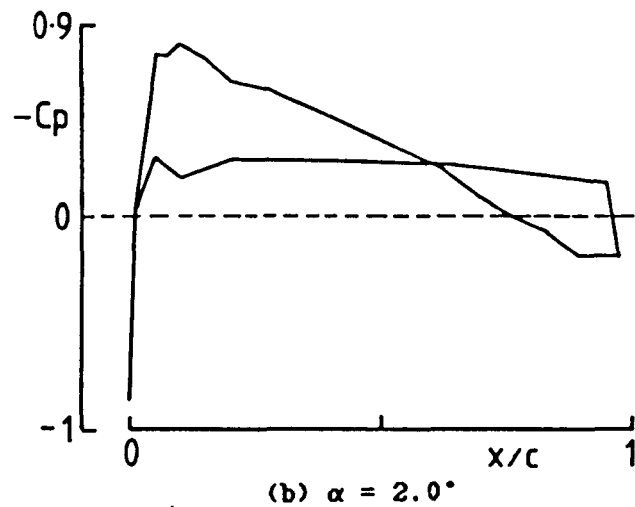
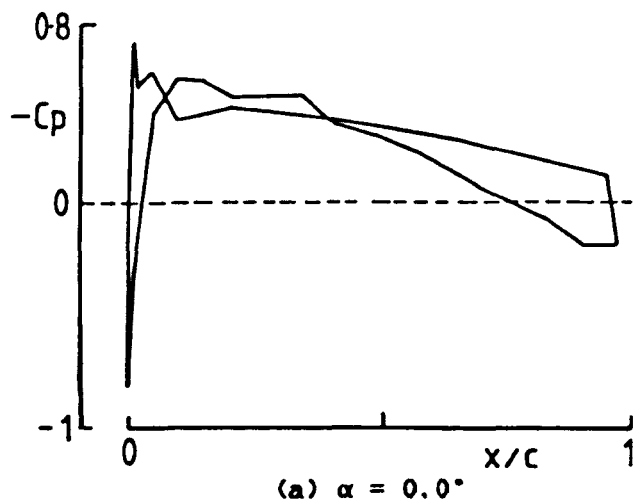
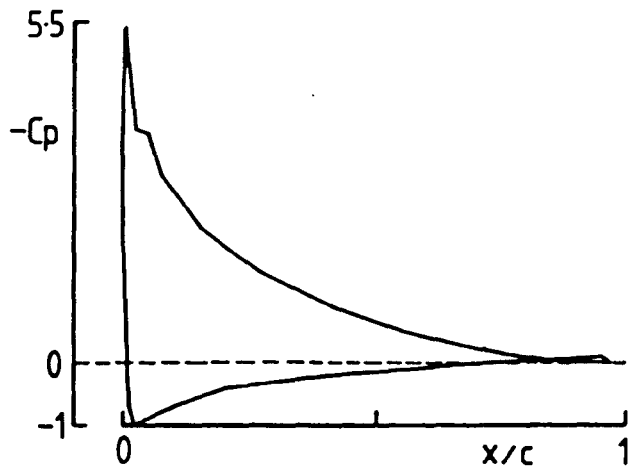
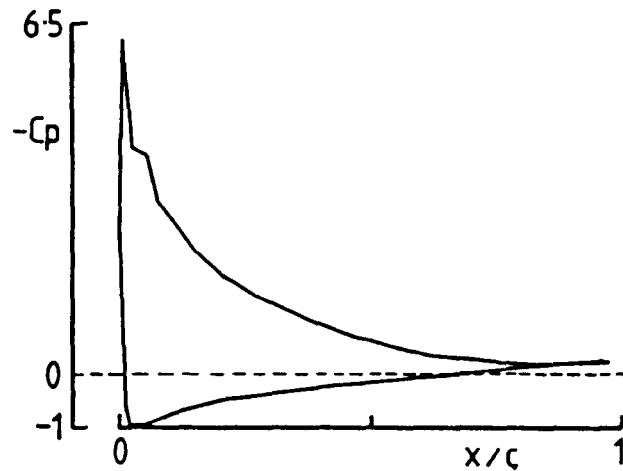


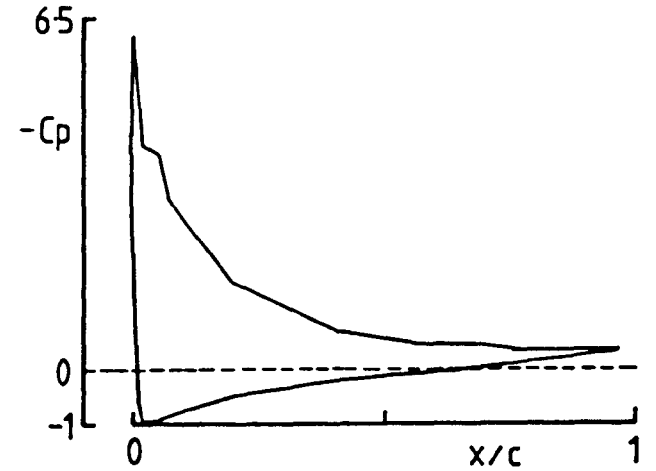
FIGURE 5.3 Discrete Chordwise Pressure Distributions obtained during a Typical Static Test on the WACA 23012(A) at a Reynolds number of 1.5×10^6 .



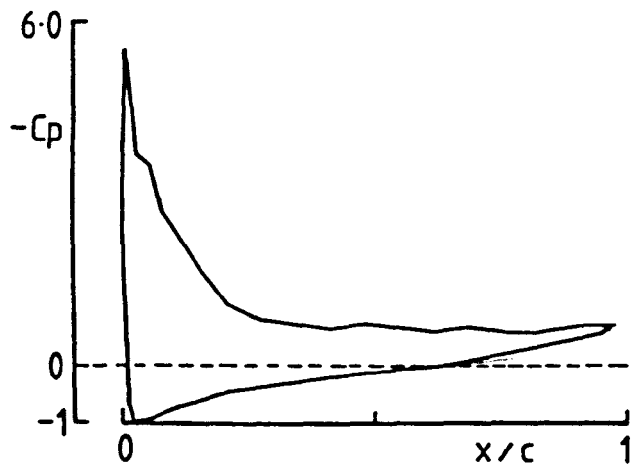
(g) $\alpha = 12.0^\circ$



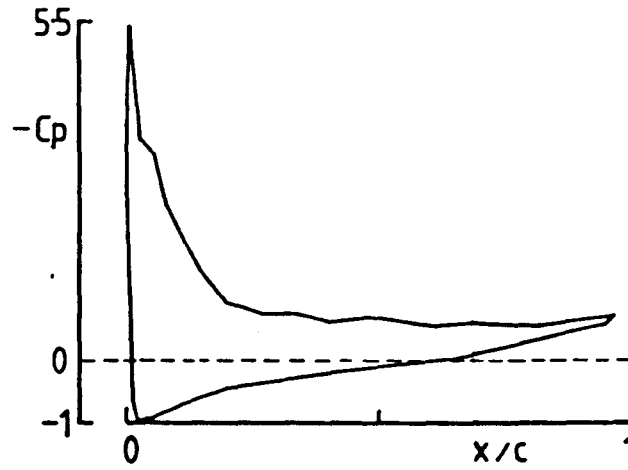
(h) $\alpha = 13.6^\circ$



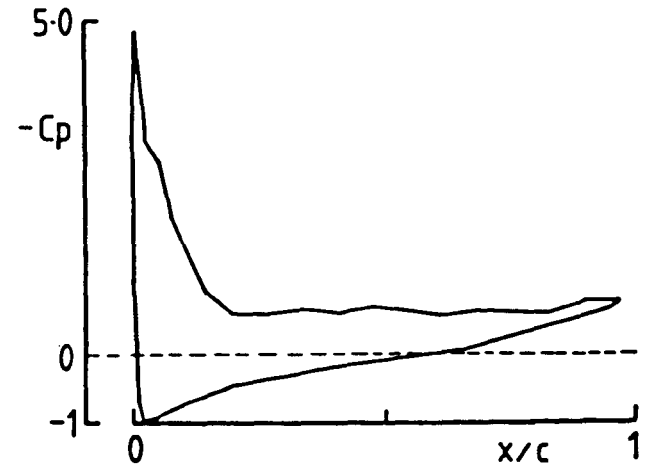
(i) $\alpha = 14.1^\circ$



(j) $\alpha = 14.6^\circ$



(k) $\alpha = 15.1^\circ$



(l) $\alpha = 16.2^\circ$

FIGURE 5.3 Continued.

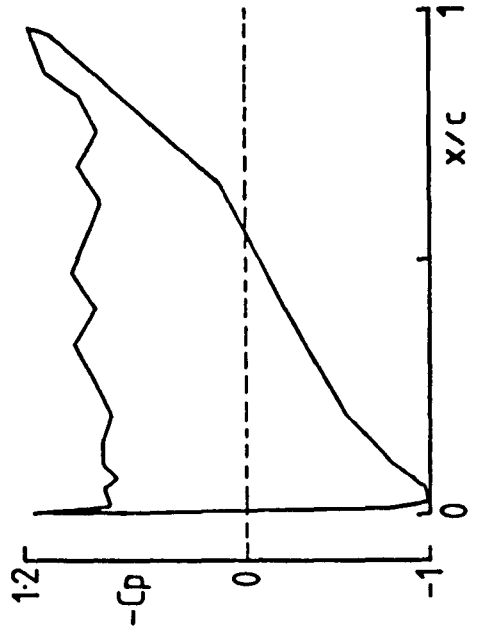
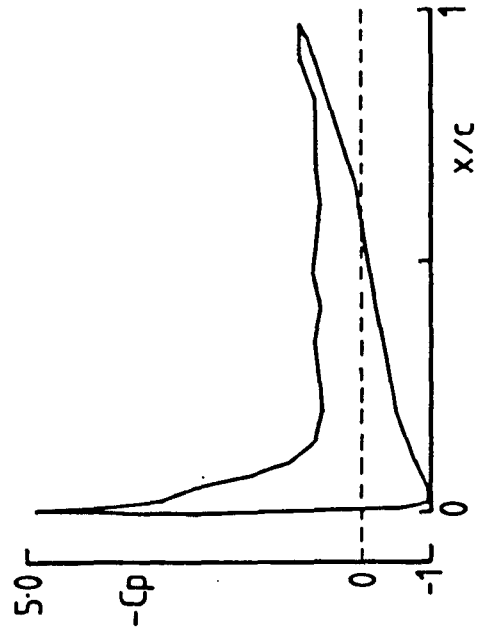
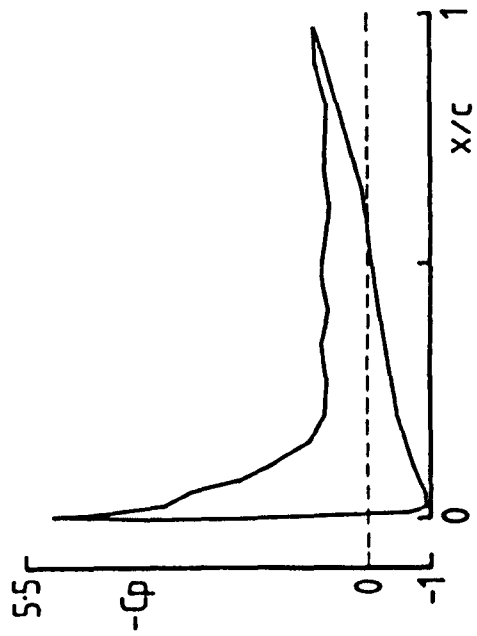


FIGURE 5.3 Completed.

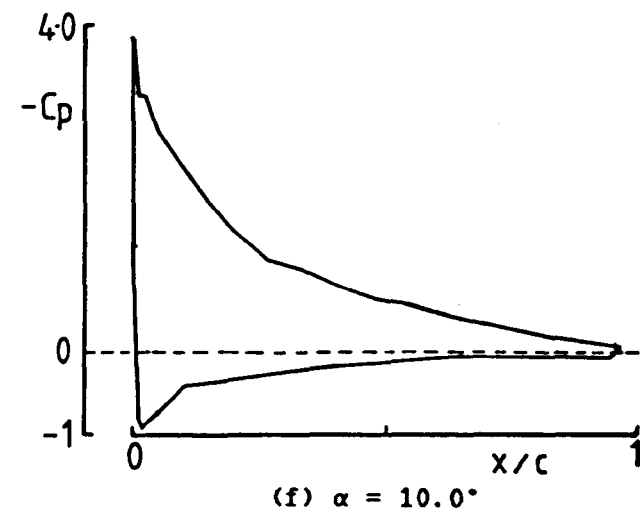
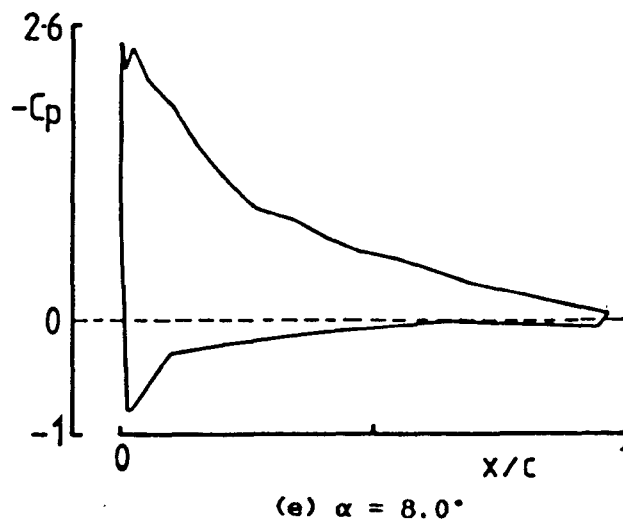
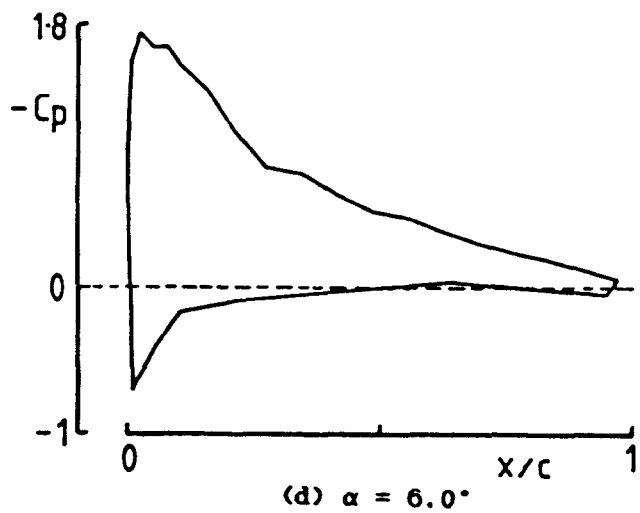
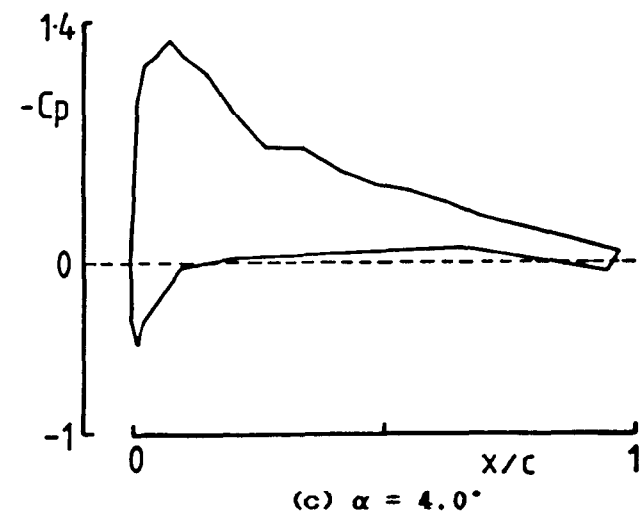
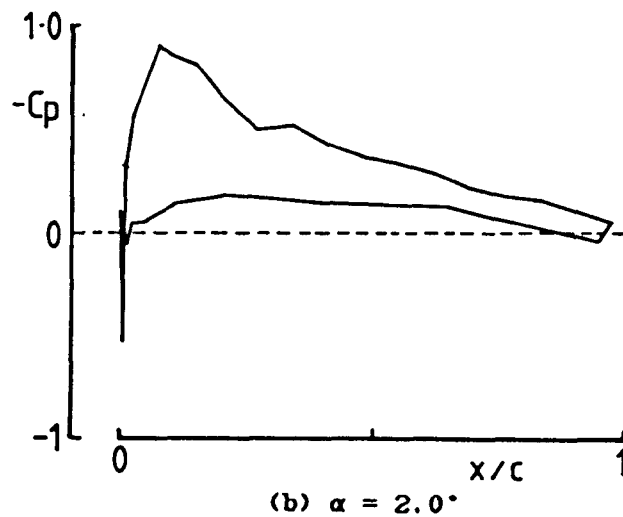
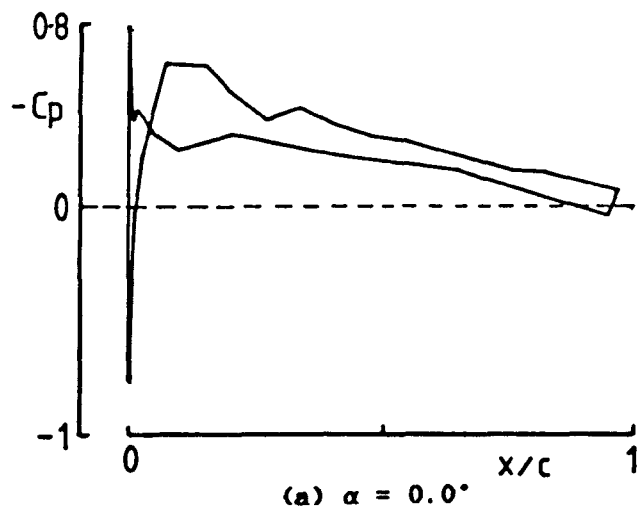


FIGURE 5.4 Discrete Chordwise Pressure Distributions obtained during a Typical Static Test on the NACA 23012 at a Reynolds number of 1.5×10^6 .

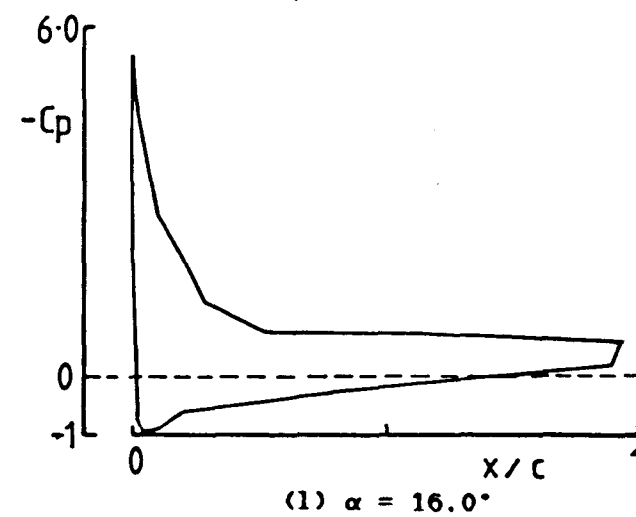
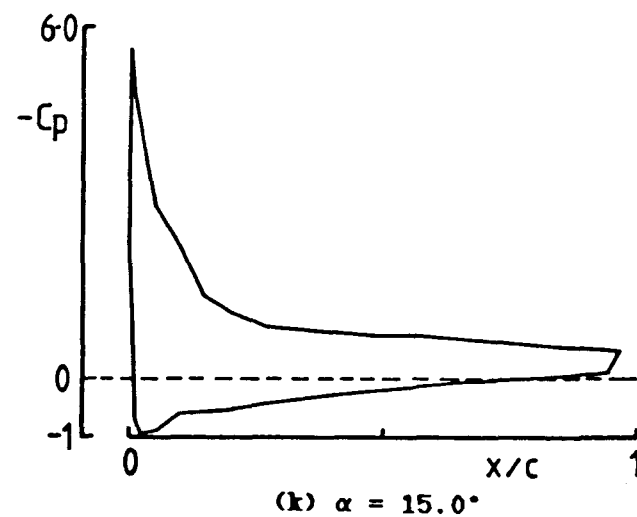
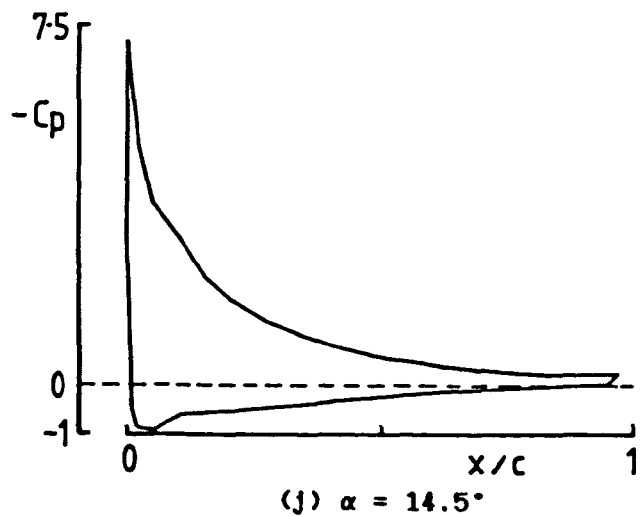
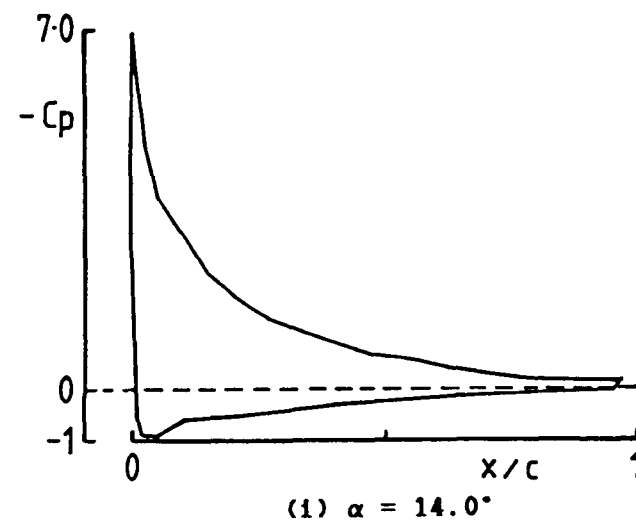
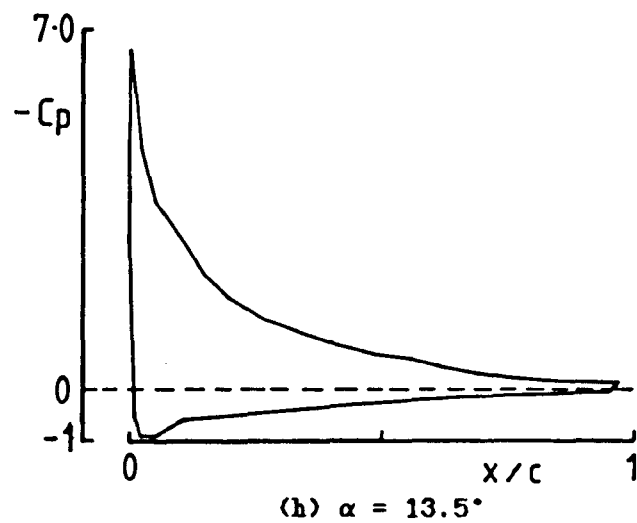
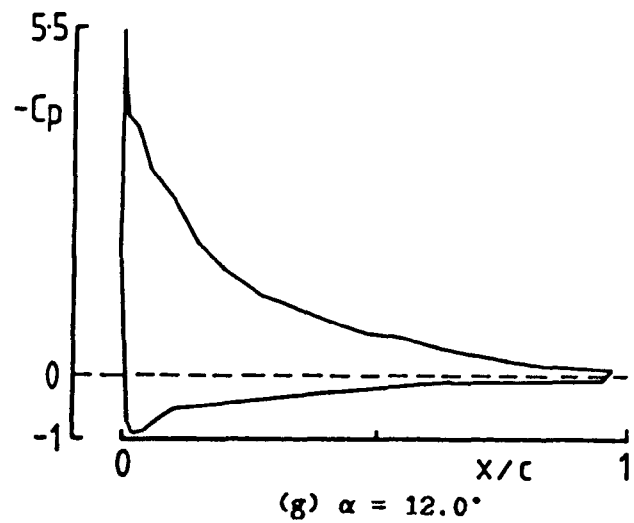


FIGURE 5.4 Continued.

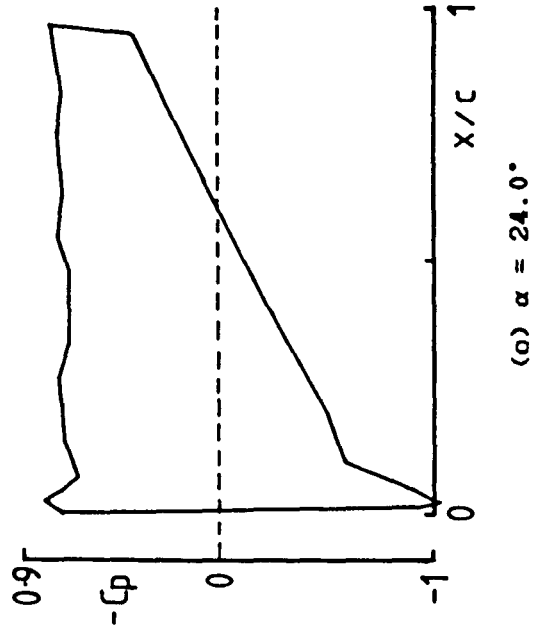
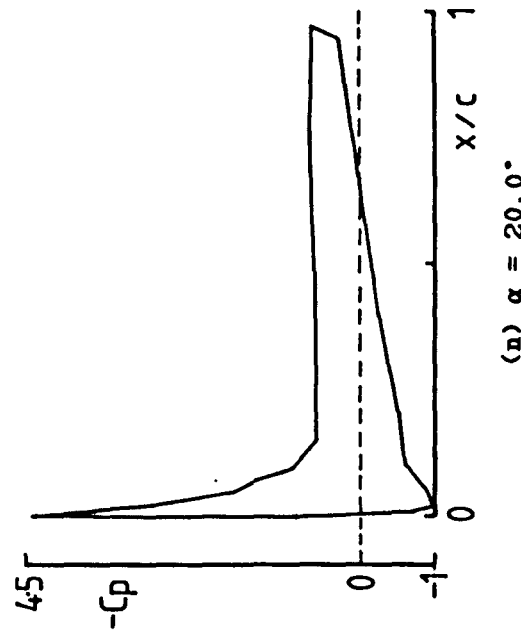
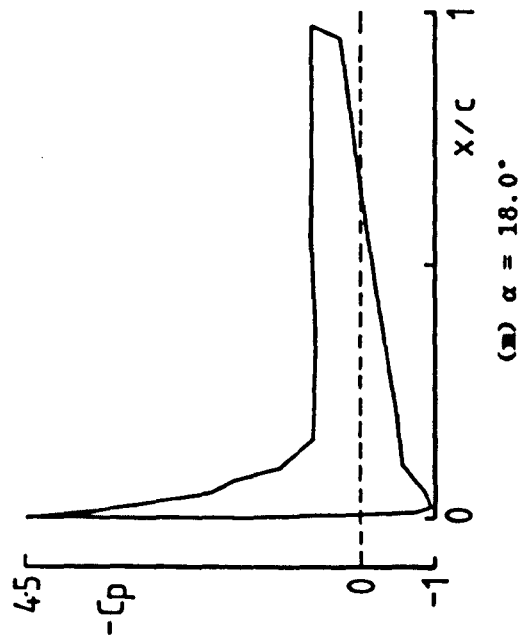


FIGURE 5.4 Completed.

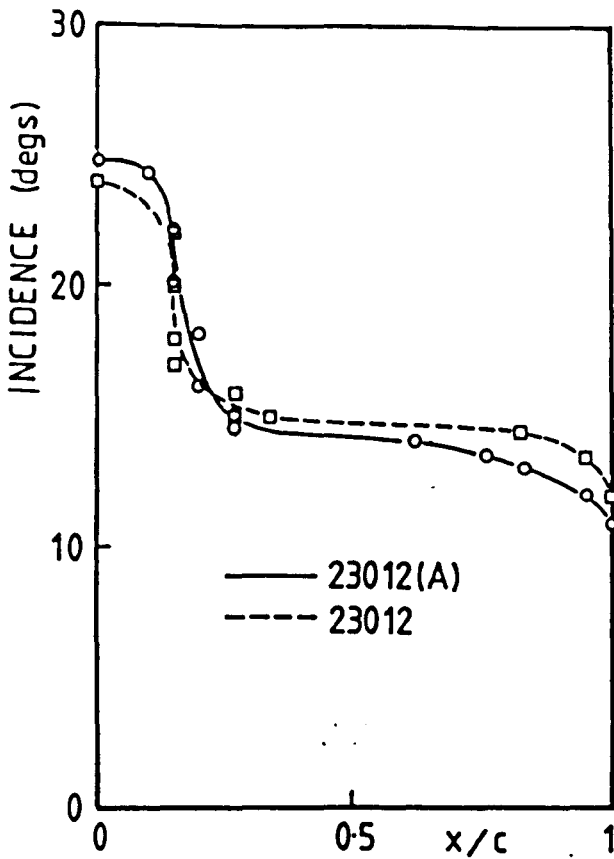


FIGURE 5.5 Estimated Steady-State Separation Loci from Pressure Distributions (1.5×10^6 Reynolds number).

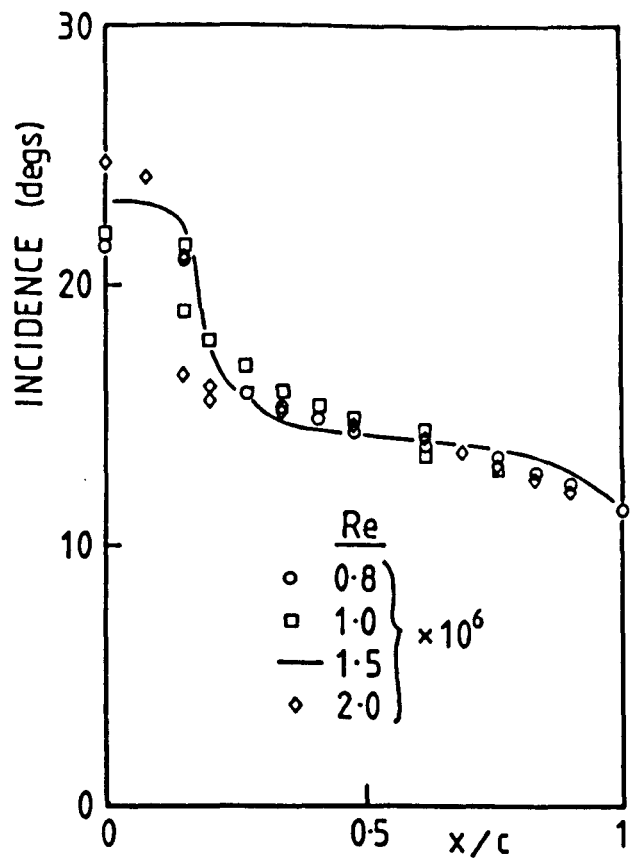


FIGURE 5.6 Estimated Variation in Steady-State Separation Loci with Reynolds number from Pressure Distributions for the NACA 23012(A).

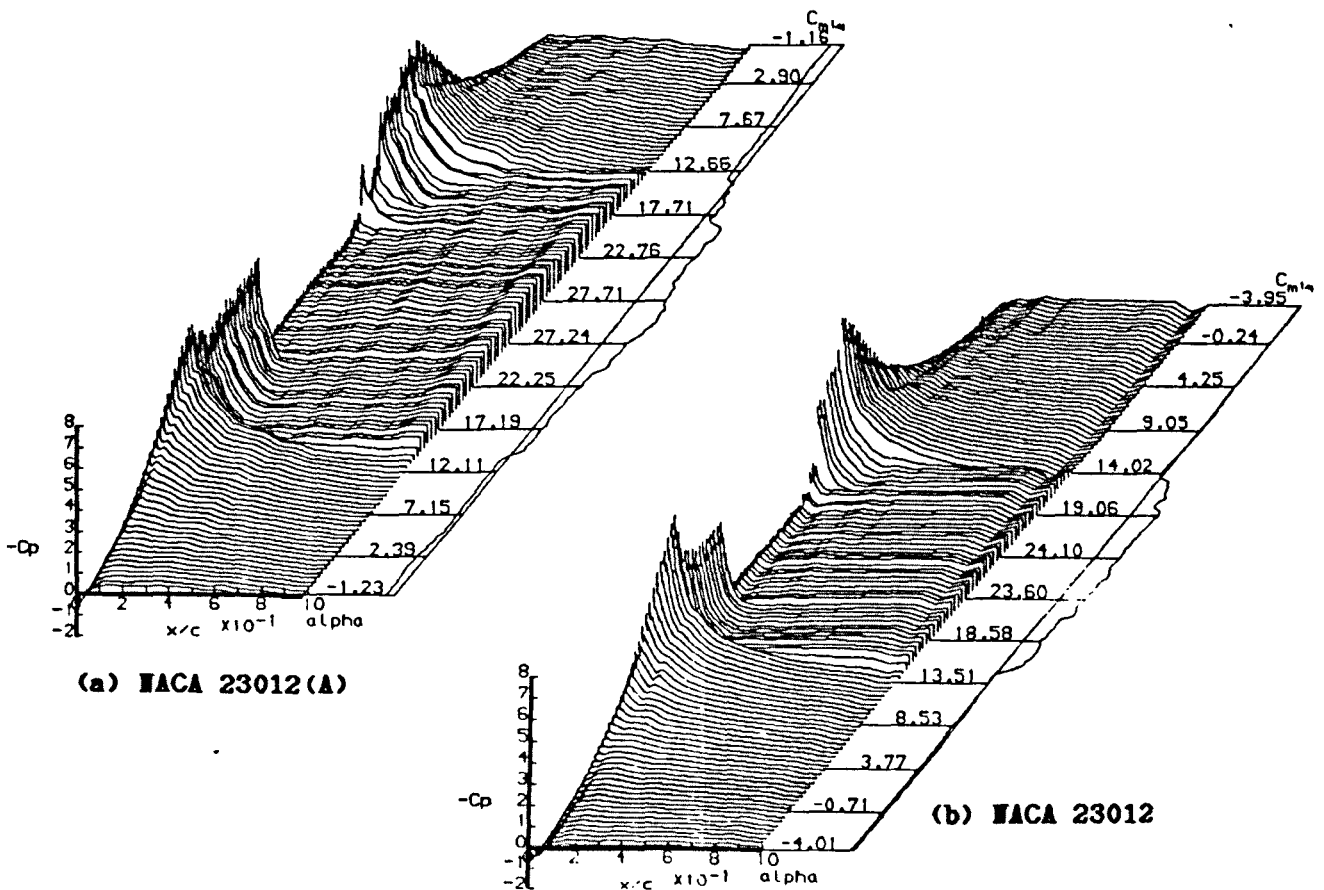


FIGURE 5.7 Steady-State Three-Dimensional representations of the Chordwise Pressure Distributions obtained at 1.5×10^6 Reynolds number.

DYNAMIC CHARACTERISTICS FOR THE NACA23012A MODEL02

RUN REFERENCE NUMBER: 101

DATE OF TEST: 4-3-86

REYNOLDS NUMBER = 1511935.

MACH NUMBER = 0.114

DYNAMIC PRESSURE = 996.12 Nm⁻²

AIR TEMPERATURE = 29.0°C

NUMBER OF CYCLES = 1

SAMPLING FREQUENCY = 100.00 Hz.

MOTION TYPE: STATIC

AVERAGED DATA OF 1 CYCLES

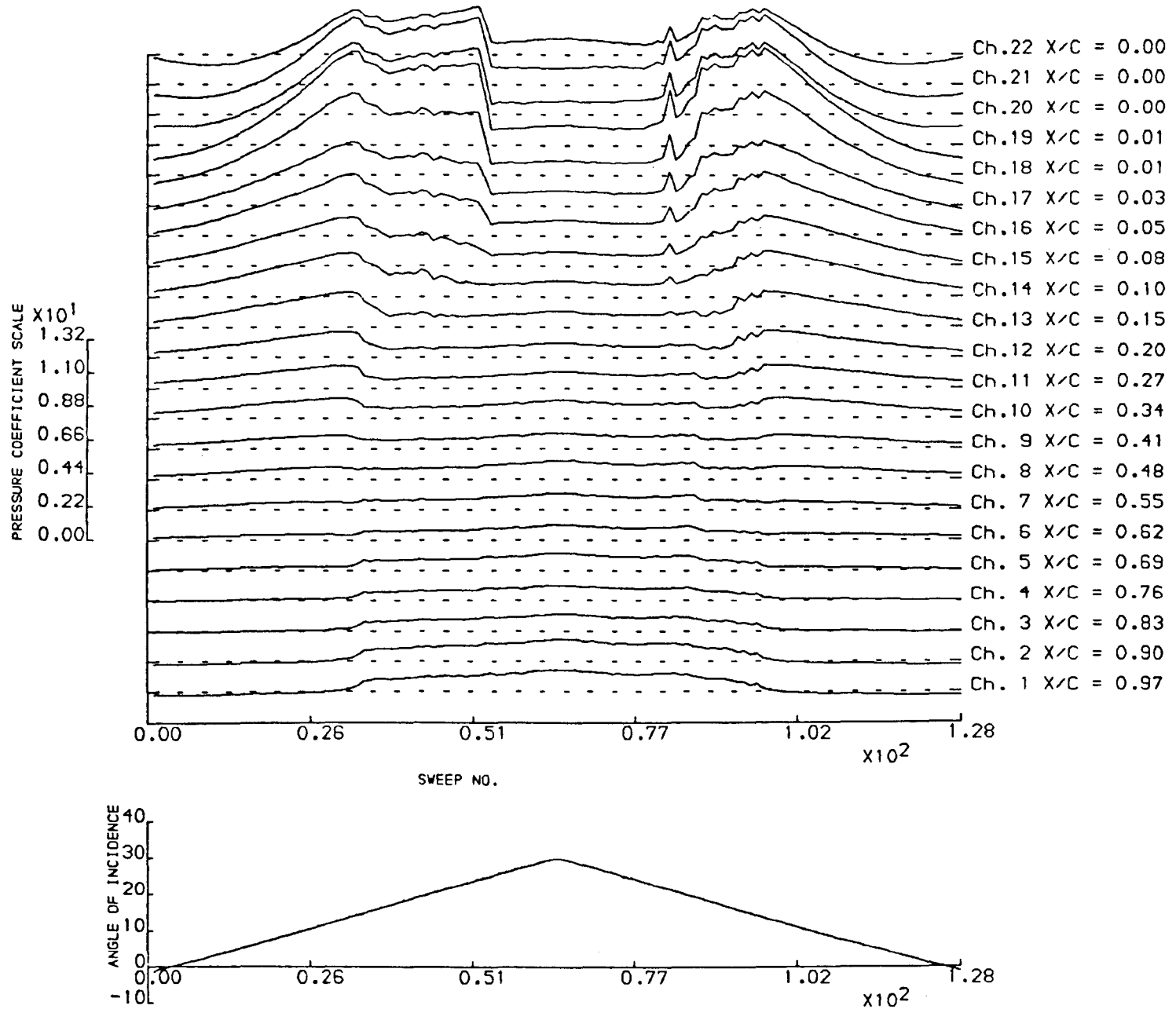


FIGURE 5.8 Pressure Coefficient versus Sweep Number obtained for the NACA 23012(A) at 1.5×10^6 Reynolds number.

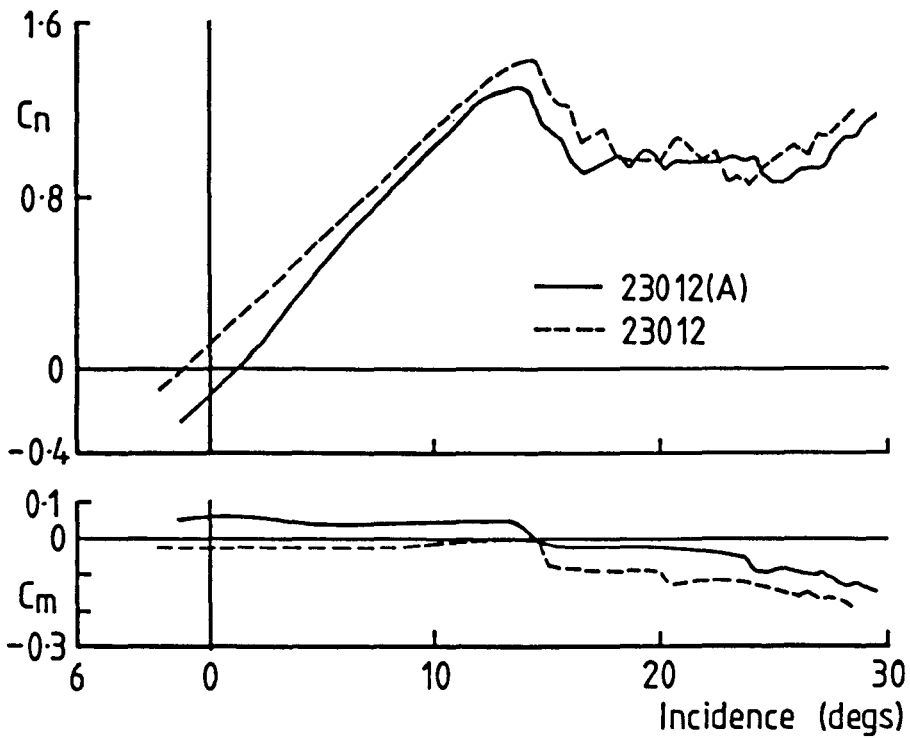


FIGURE 5.9 Variations in Normal Force and Pitching-Moment Coefficient with Incidence for the NACA 23012 and 23012(A) Aerofoils at 1.5×10^6 Reynolds number.

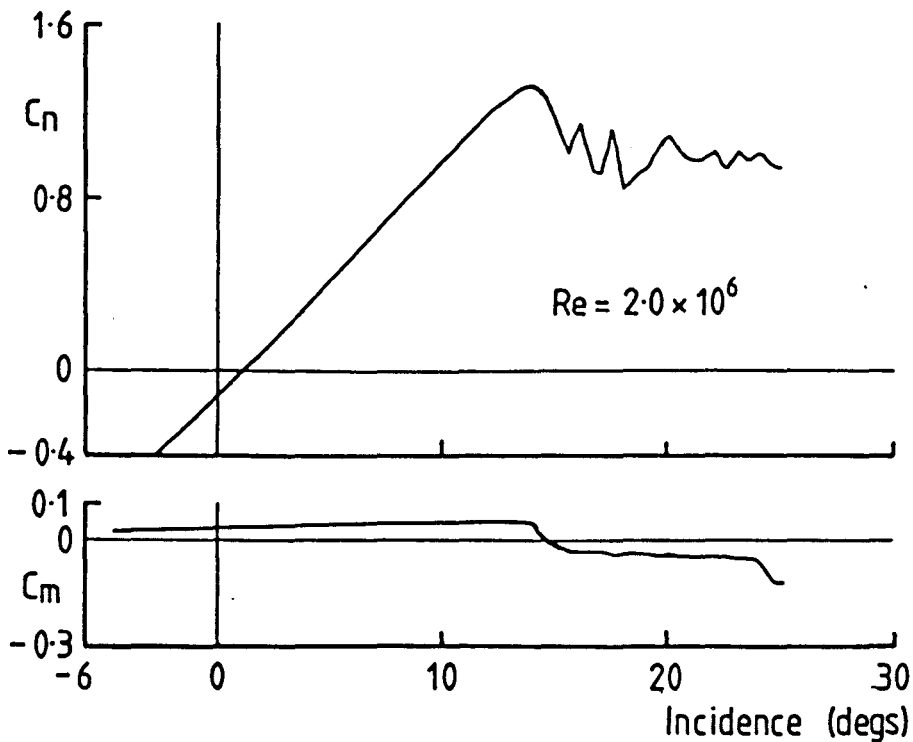


FIGURE 5.10 Variation in Normal Force and Pitching-Moment Coefficient with Incidence for the NACA 23012(A) at 2.0×10^6 Reynolds number.

DYNAMIC CHARACTERISTICS FOR THE NACA23012A MODEL02

RUN REFERENCE NUMBER: 10401

DATE OF TEST: 7/ 3/86

REYNOLDS NUMBER = 1488829.

MACH NUMBER = 0.111

DYNAMIC PRESSURE = 964.82 N/sq. m

AIR TEMPERATURE = 30.0

NUMBER OF CYCLES = 10

SAMPLING FREQUENCY = 298.24 Hz.

MOTION TYPE: SINUSOIDAL

REDUCED FREQUENCY = 0.103

MEAN ANGLE = 1.00

AMPLITUDE = 10.00

OSCILLATION FREQUENCY = 2.330Hz.

AVERAGED DATA OF 10 CYCLES

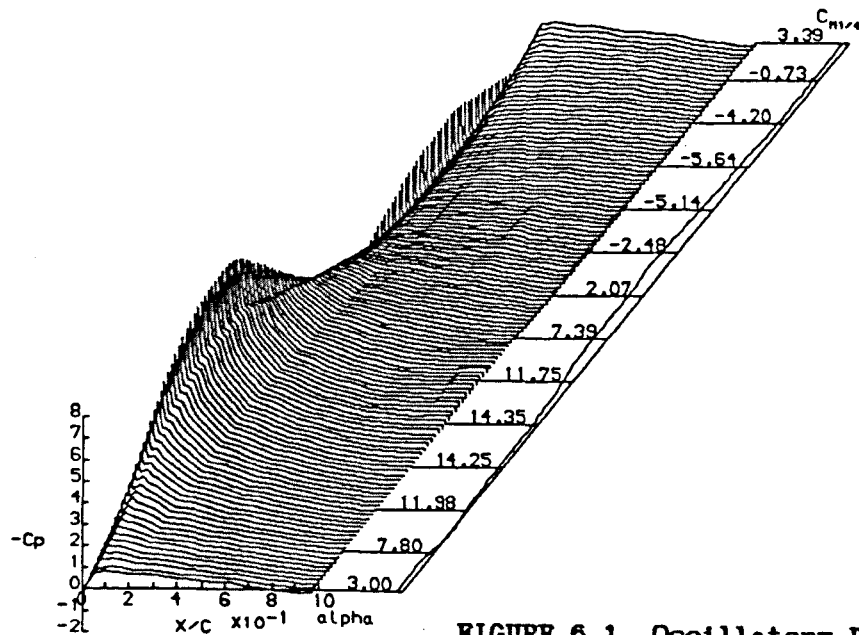
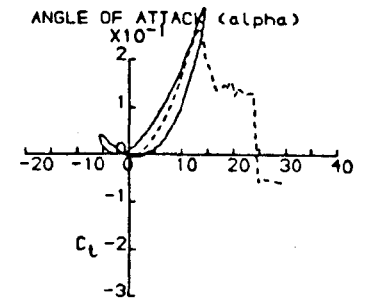
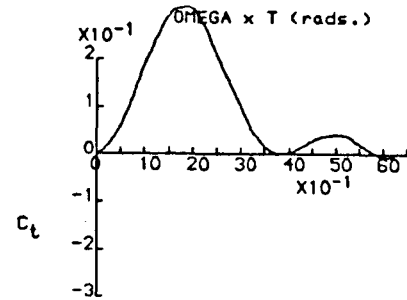
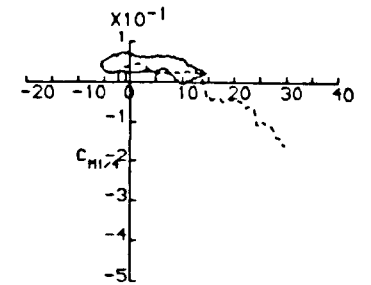
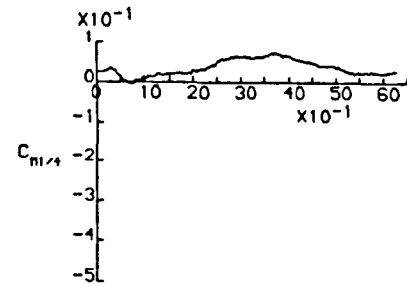
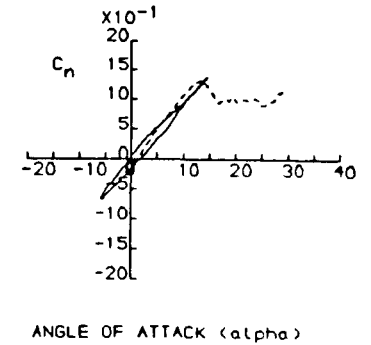
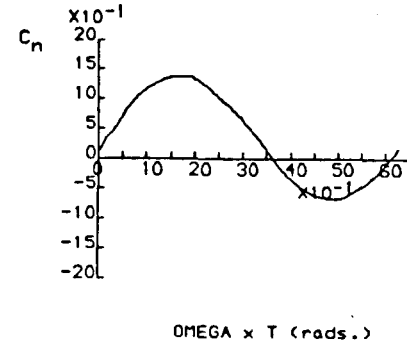
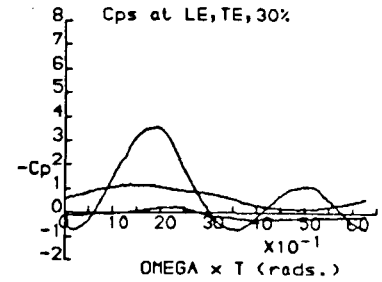
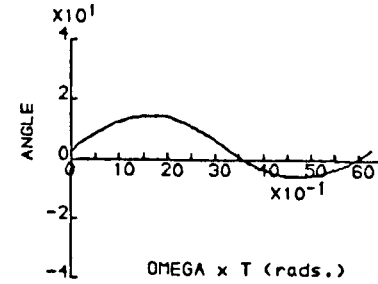


FIGURE 6.1 Oscillatory Data obtained for the NACA 23012(A).



DYNAMIC CHARACTERISTICS FOR THE NACA 23012 MODEL 2

RUN REFERENCE NUMBER: 10481

DATE OF TEST: 12/ 3/86

REYNOLDS NUMBER = 1481786.

MACH NUMBER = 0.112

DYNAMIC PRESSURE = 962.08 N/sq. m

AIR TEMPERATURE = 30.0

NUMBER OF CYCLES = 10

SAMPLING FREQUENCY = 298.24 Hz.

MOTION TYPE: SINUSOIDAL

REDUCED FREQUENCY = 0.103

MEAN ANGLE = 6.00

AMPLITUDE = 10.00

OSCILLATION FREQUENCY = 2.330Hz.

AVERAGED DATA OF 10 CYCLES

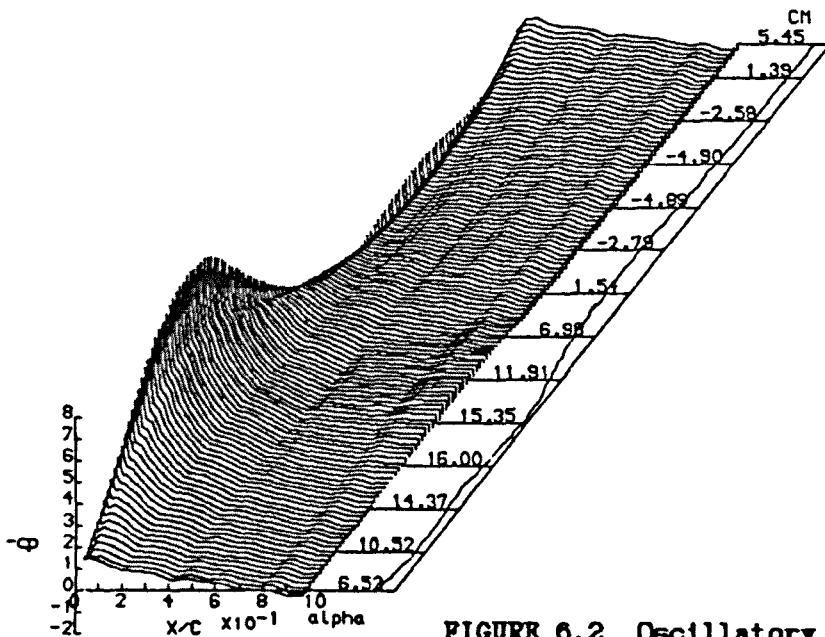
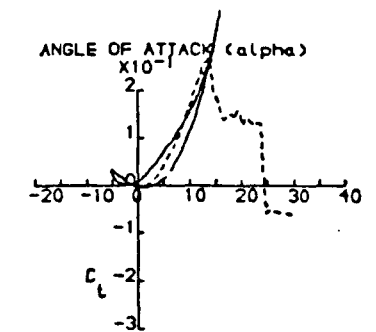
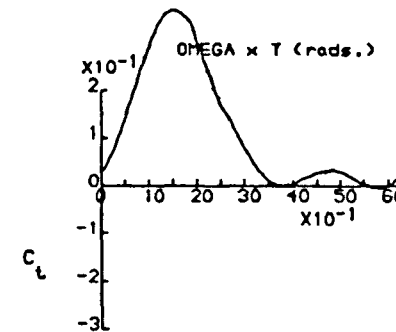
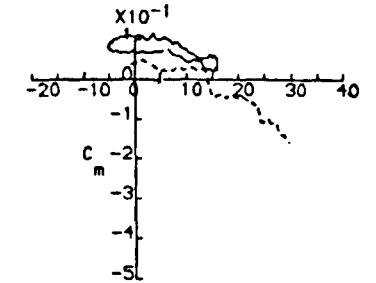
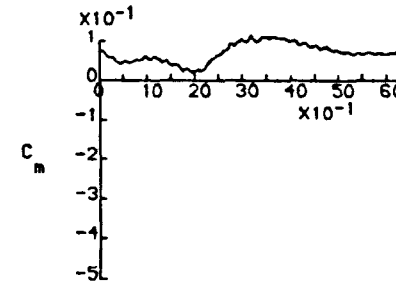
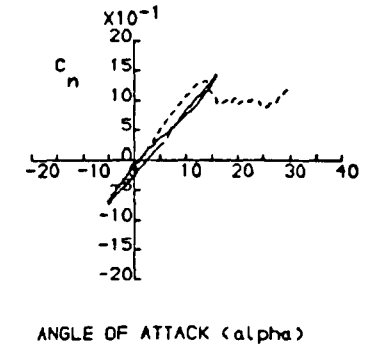
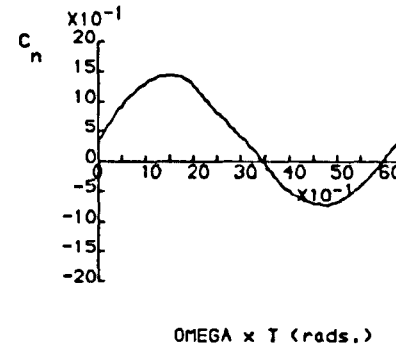
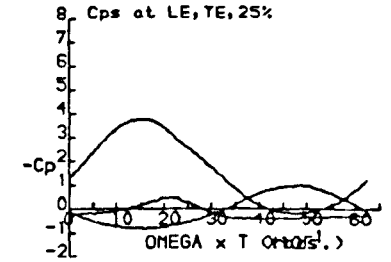
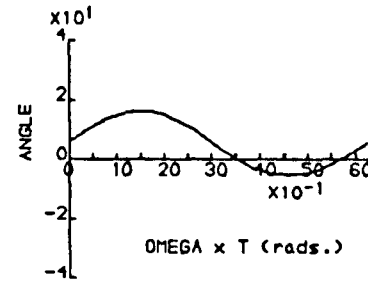


FIGURE 6.2 Oscillatory Data obtained for the NACA 23012(A).



DYNAMIC CHARACTERISTICS FOR THE NACA 23012 MODEL01

RUN REFERENCE NUMBER: 13551	DATE OF TEST: 16/ 6/83
REYNOLDS NUMBER = 1522811.	MACH NUMBER = 0.112
DYNAMIC PRESSURE = 1004.80 N/sq. M	AIR TEMPERATURE = 33.0
NUMBER OF CYCLES = 10	SAMPLING FREQUENCY = 298.24 Hz.
MOTION TYPE: SINUSOIDAL	REDUCED FREQUENCY = 0.102
MEAN ANGLE = 6.00	AMPLITUDE = 10.00
OSCILLATION FREQUENCY = 2.330Hz.	
AVERAGED DATA OF 10 CYCLES	

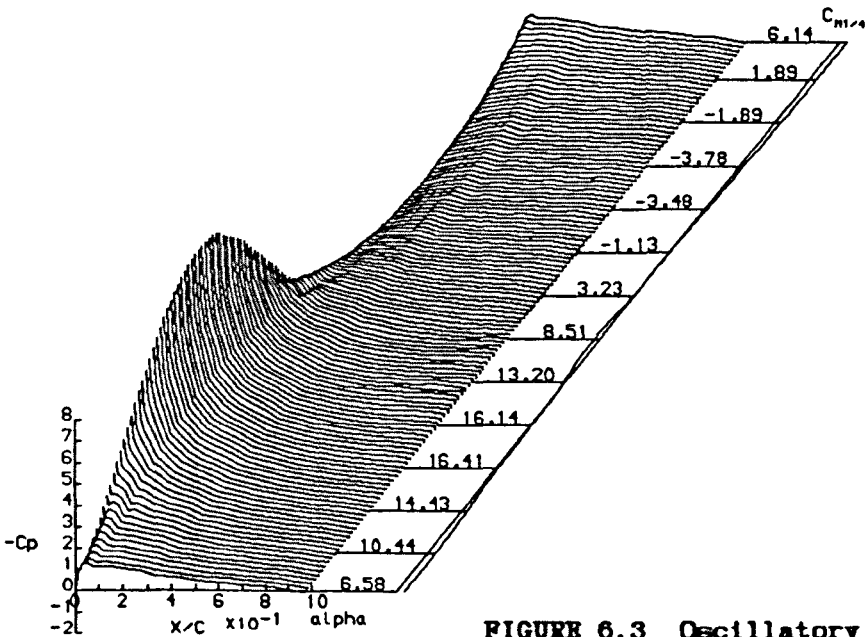
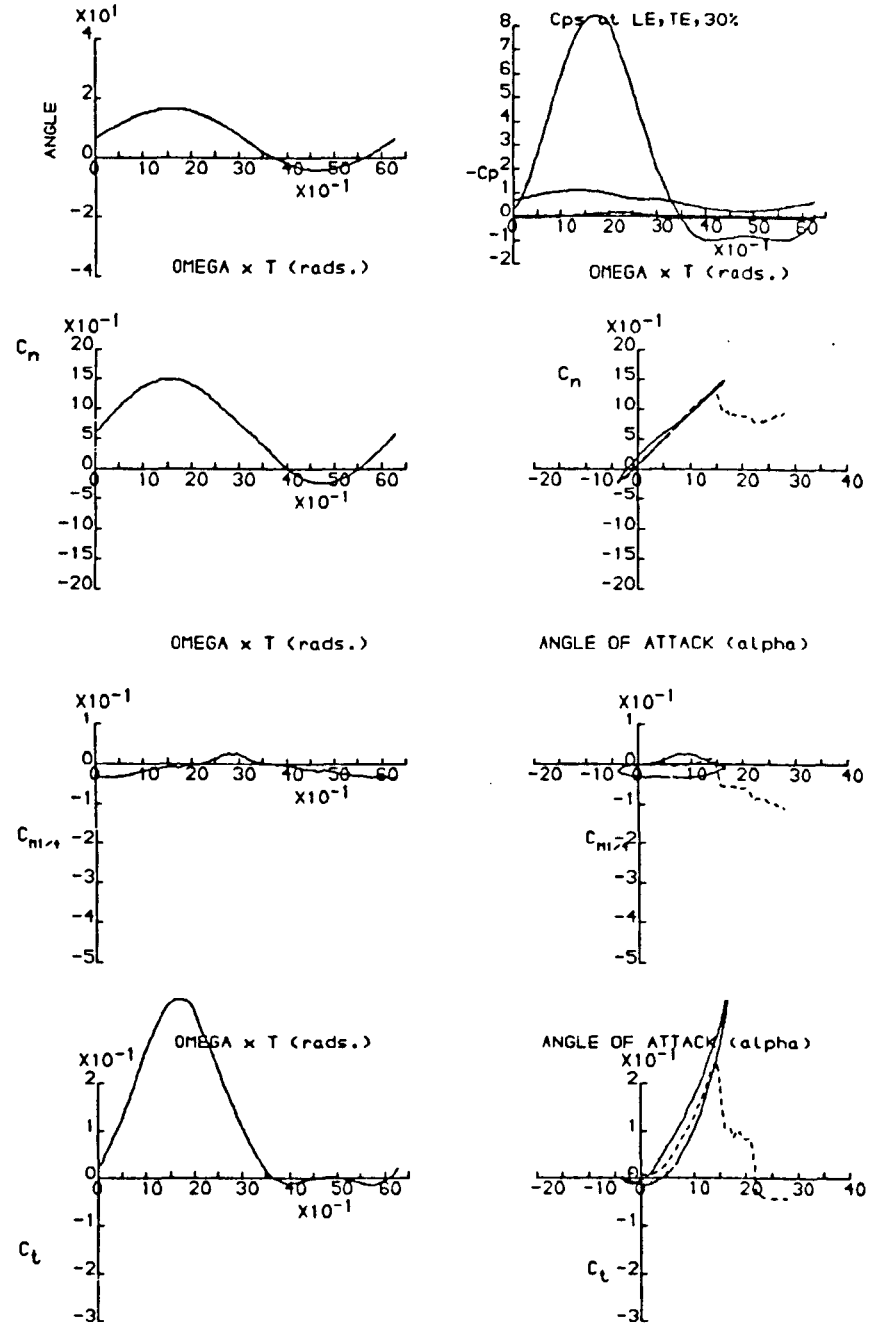


FIGURE 6.3 Oscillatory Data obtained for the NACA 23012.



DYNAMIC CHARACTERISTICS FOR THE NACA23012A MODEL02

RUN REFERENCE NUMBER: 10561
 REYNOLDS NUMBER = 1466227.
 DYNAMIC PRESSURE = 941.98 N/sq. m
 NUMBER OF CYCLES = 10
 MOTION TYPE: SINUSOIDAL
 MEAN ANGLE = 8.00
 OSCILLATION FREQUENCY = 2.330Hz.
 AVERAGED DATA OF 10 CYCLES

DATE OF TEST: 12/ 3/86
 MACH NUMBER = 0.110
 AIR TEMPERATURE = 30.0
 SAMPLING FREQUENCY = 298.24 Hz.
 REDUCED FREQUENCY = 0.104
 AMPLITUDE = 10.00

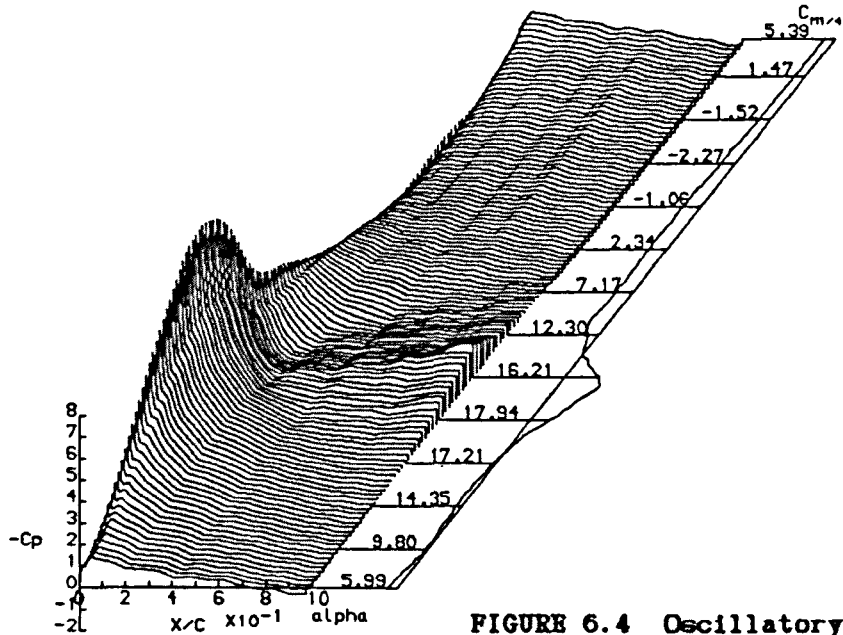
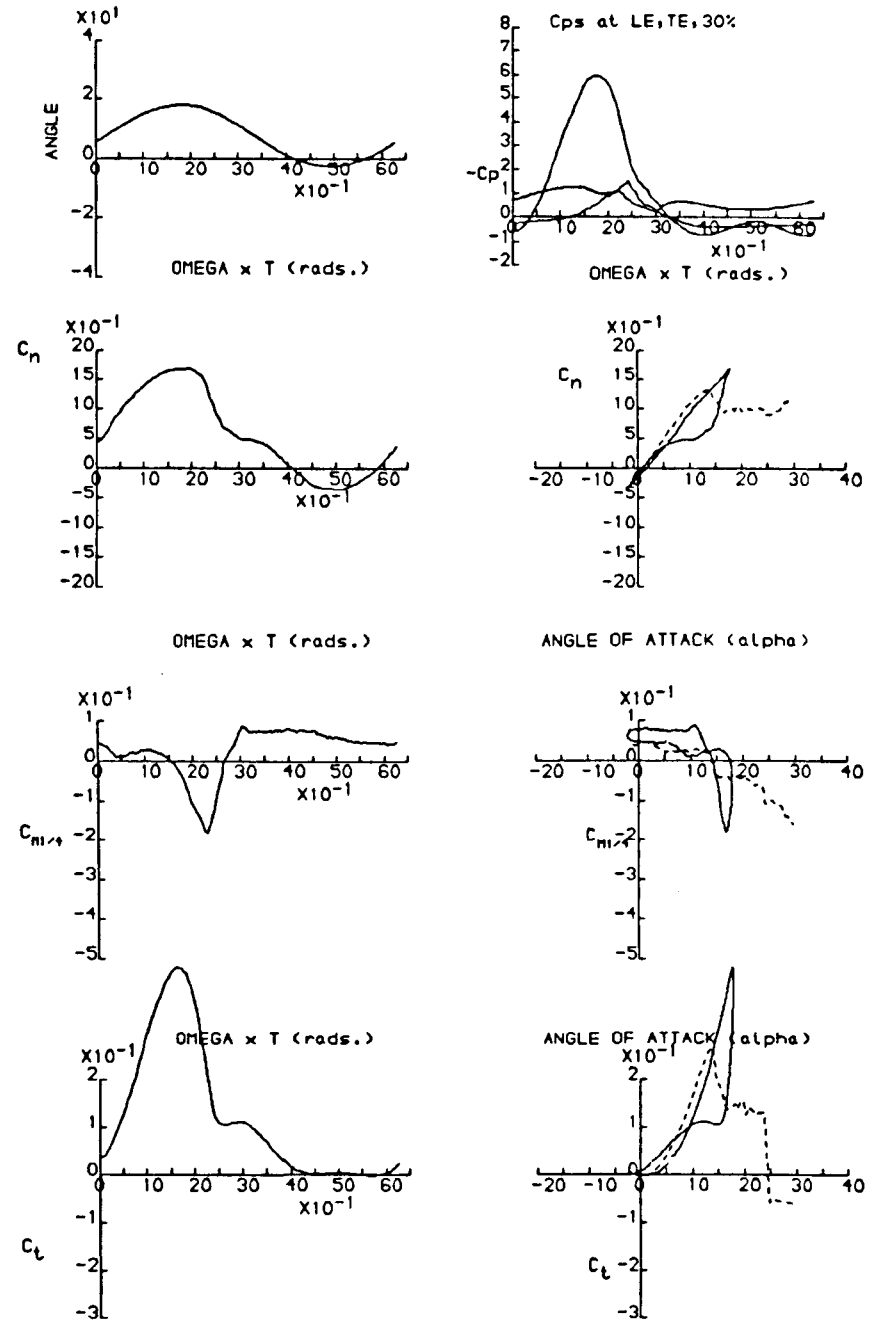


FIGURE 6.4 Oscillatory Data obtained for the NACA 23012(A).



DYNAMIC CHARACTERISTICS FOR THE NACA 23012 MODEL01

RUN REFERENCE NUMBER: 13601
 REYNOLDS NUMBER = 1523400.
 DYNAMIC PRESSURE = 1005.54 N/sq. M
 NUMBER OF CYCLES = 10
 MOTION TYPE: SINUSOIDAL
 MEAN ANGLE = 8.00
 OSCILLATION FREQUENCY = 2.330Hz.
 AVERAGED DATA OF 10 CYCLES

DATE OF TEST: 16/ 6/83
 MACH NUMBER = 0.112
 AIR TEMPERATURE = 33.0
 SAMPLING FREQUENCY = 298.24 Hz.
 REDUCED FREQUENCY = 0.102
 AMPLITUDE = 10.00

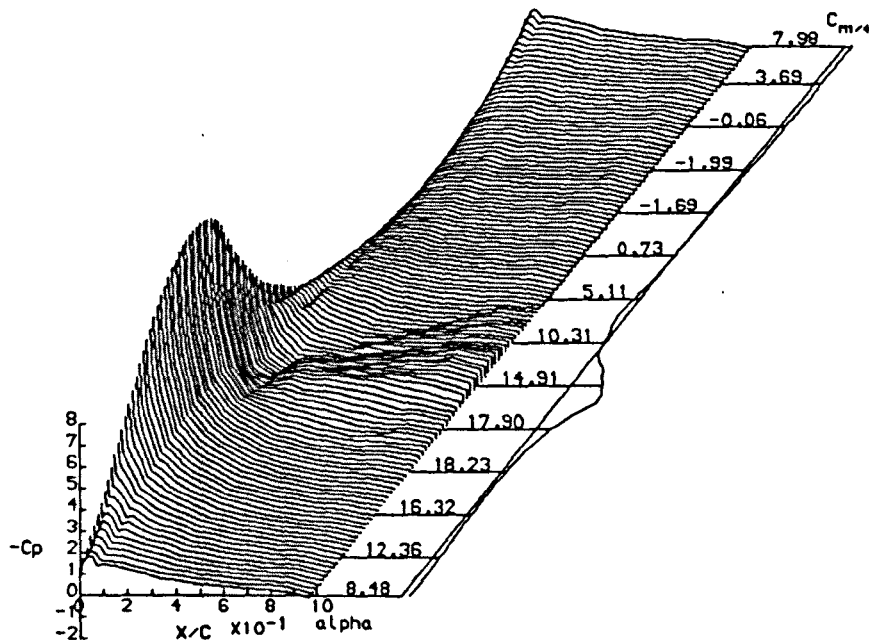
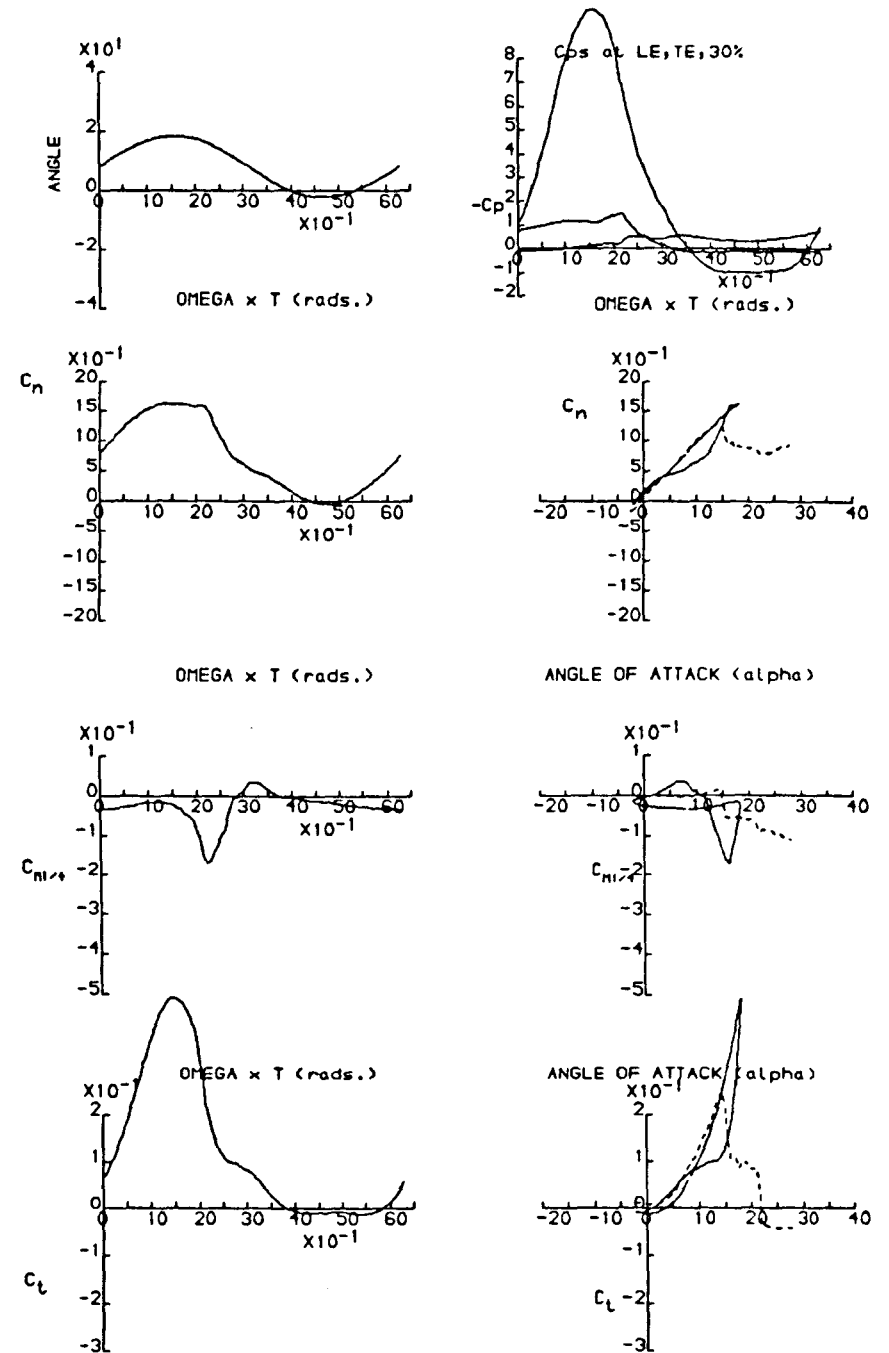


FIGURE 6.5 Oscillatory Data obtained for the NACA 23012.



DYNAMIC CHARACTERISTICS FOR THE NACA 23012 MODEL 2

RUN REFERENCE NUMBER: 10801

DATE OF TEST: 17/ 3/86

REYNOLDS NUMBER = 1486036.

MACH NUMBER = 0.111

DYNAMIC PRESSURE = 954.88 N/sq. M

AIR TEMPERATURE = 30.0

NUMBER OF CYCLES = 10

SAMPLING FREQUENCY = 298.24 Hz.

MOTION TYPE: SINUSOIDAL

REDUCED FREQUENCY = 0.104

MEAN ANGLE = 10.00

AMPLITUDE = 10.00

OSCILLATION FREQUENCY = 2.330Hz.

AVERAGED DATA OF 10 CYCLES

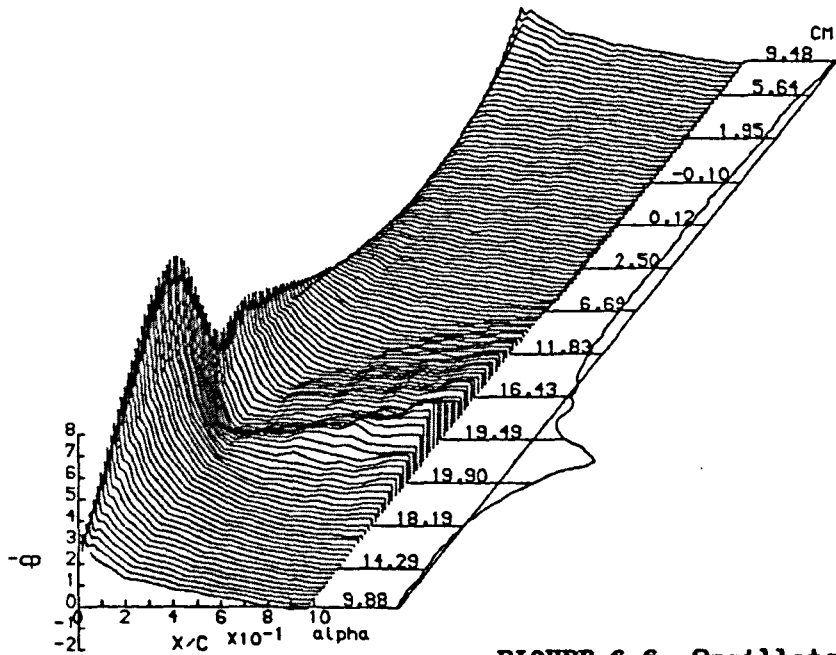
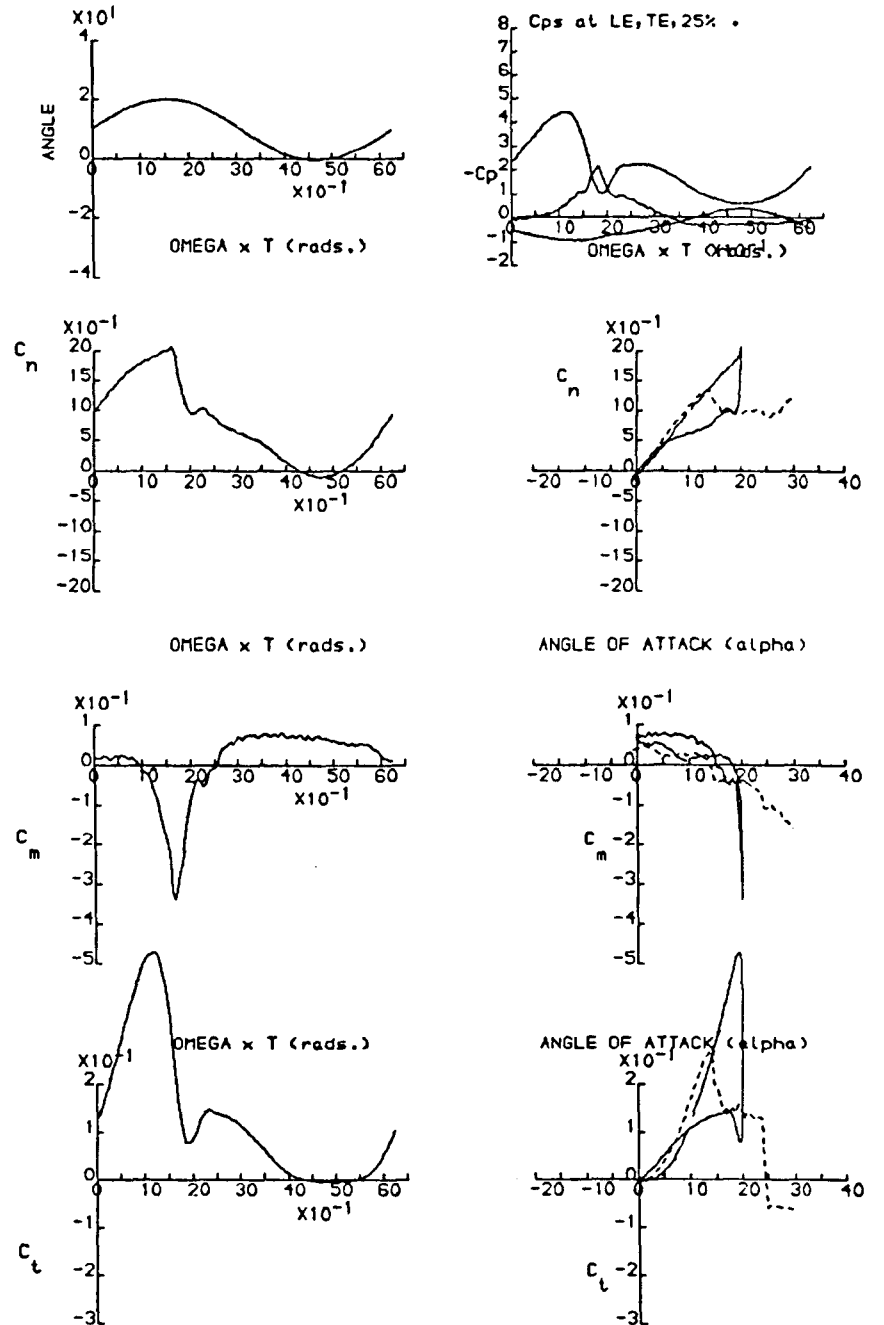


FIGURE 6.6 Oscillatory Data obtained for the NACA 23012(A).



DYNAMIC CHARACTERISTICS FOR THE NACA 23012 MODEL01

RUN REFERENCE NUMBER: 13651

DATE OF TEST: 16/ 6/83

REYNOLDS NUMBER = 1514791.

MACH NUMBER = 0.112

DYNAMIC PRESSURE = 999.61 N/sq. m

AIR TEMPERATURE = 34.0

NUMBER OF CYCLES = 10

SAMPLING FREQUENCY = 298.24 Hz.

MOTION TYPE: SINUSOIDAL

REDUCED FREQUENCY = 0.102

MEAN ANGLE = 10.00

AMPLITUDE = 10.00

OSCILLATION FREQUENCY = 2.330Hz.

AVERAGED DATA OF 10 CYCLES

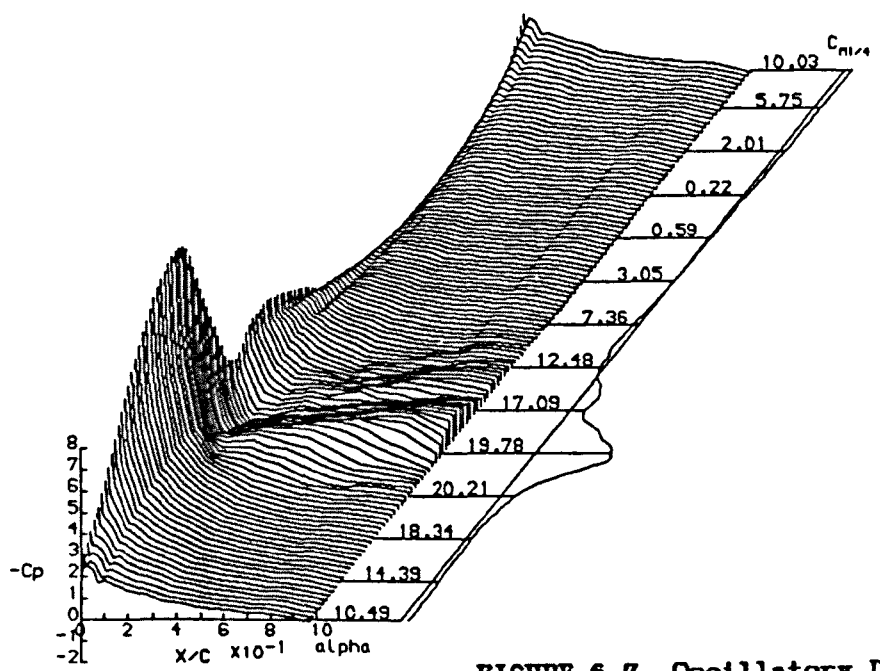
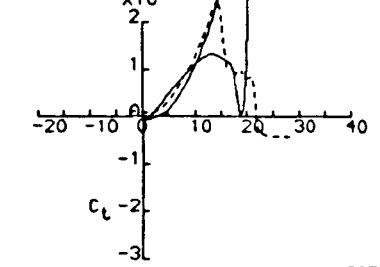
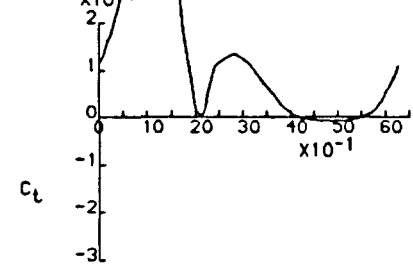
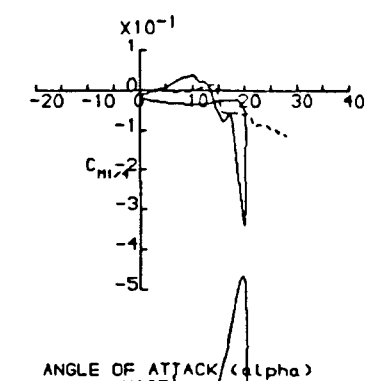
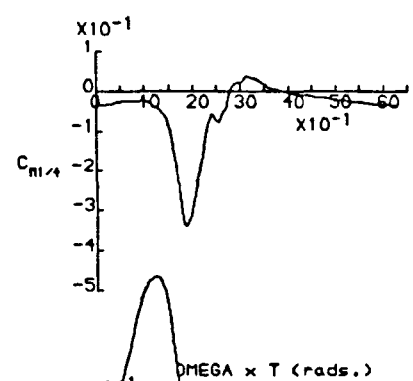
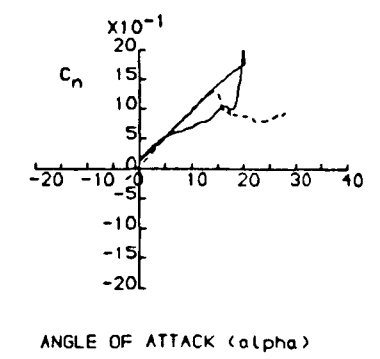
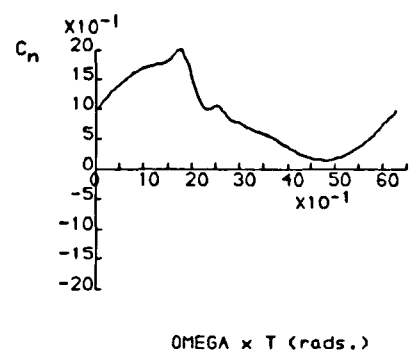
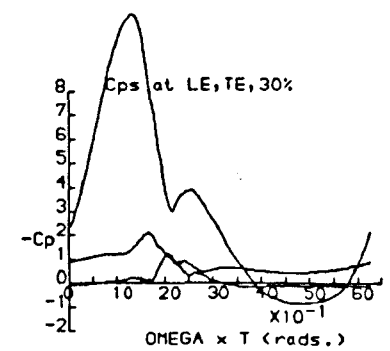
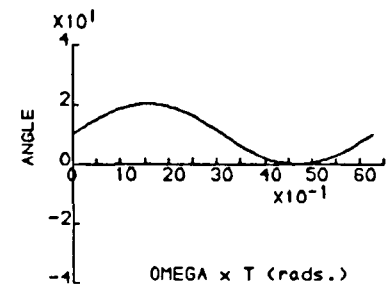


FIGURE 6.7 Oscillatory Data obtained for the NACA 23012.



DYNAMIC CHARACTERISTICS FOR THE NACA23012A MODEL02

RUN REFERENCE NUMBER: 10641	DATE OF TEST: 14/ 3/86
REYNOLDS NUMBER = 1461159.	MACH NUMBER = 0.110
DYNAMIC PRESSURE = 939.33 N/sq. M	AIR TEMPERATURE = 30.0
NUMBER OF CYCLES = 10	SAMPLING FREQUENCY = 298.24 Hz.
MOTION TYPE: SINUSOIDAL	REDUCED FREQUENCY = 0.104
MEAN ANGLE = 15.00	AMPLITUDE = 10.00
OSCILLATION FREQUENCY = 2.330Hz.	
AVERAGED DATA OF 10 CYCLES	

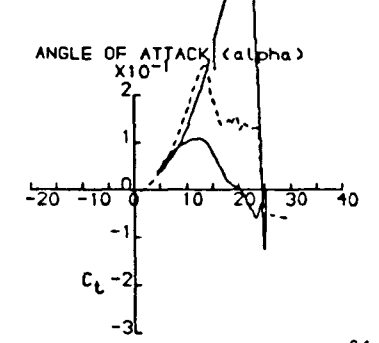
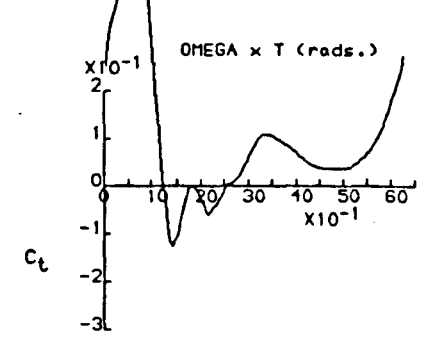
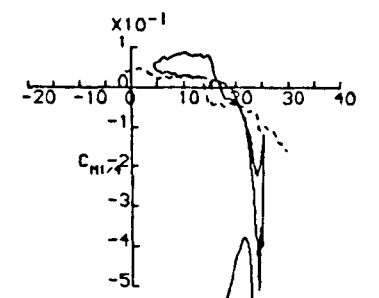
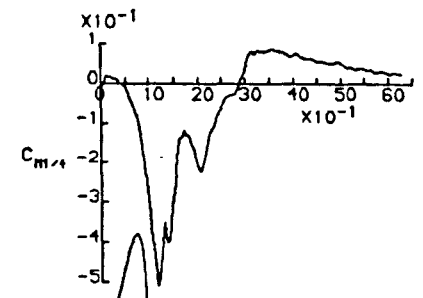
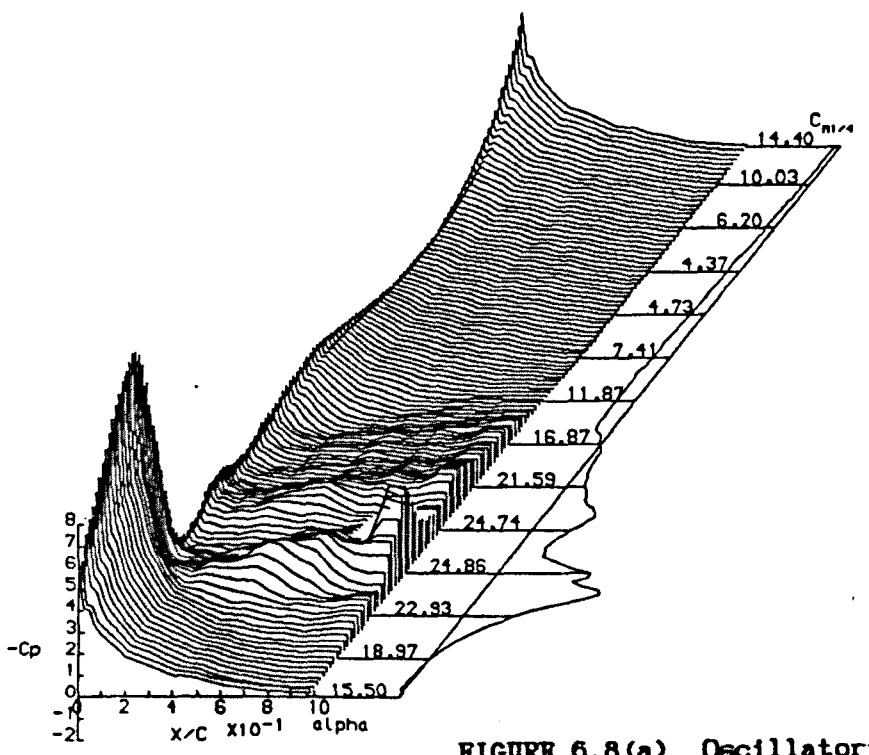
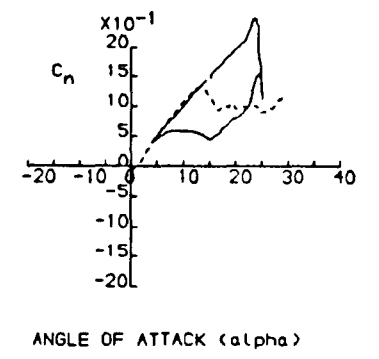
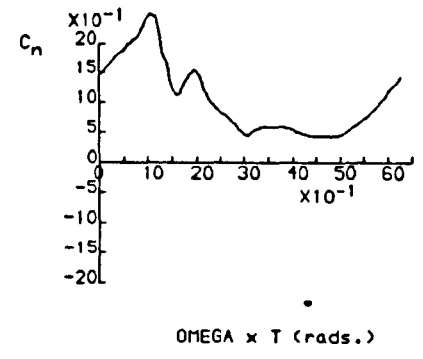
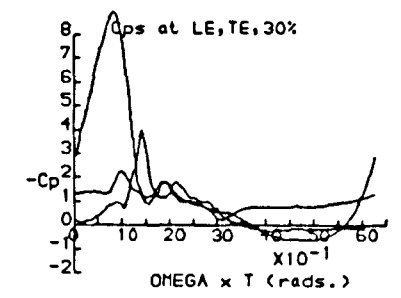
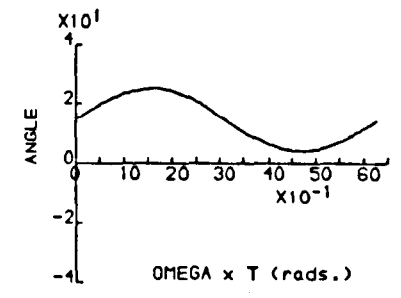


FIGURE 6.8(a) Oscillatory Data obtained for the NACA 23012(A).

DYNAMIC CHARACTERISTICS FOR THE NACA 23012 MODEL01

RUN REFERENCE NUMBER: 13851
 REYNOLDS NUMBER = 1528216.
 DYNAMIC PRESSURE = 1005.15 N/sq. M
 NUMBER OF CYCLES = 10
 MOTION TYPE: SINUSOIDAL
 MEAN ANGLE = 15.00
 OSCILLATION FREQUENCY = 2.330Hz.
 AVERAGED DATA OF 10 CYCLES

DATE OF TEST: 17/ 6/83
 MACH NUMBER = 0.112
 AIR TEMPERATURE = 32.0
 SAMPLING FREQUENCY = 298.24 Hz.
 REDUCED FREQUENCY = 0.102
 AMPLITUDE = 10.00

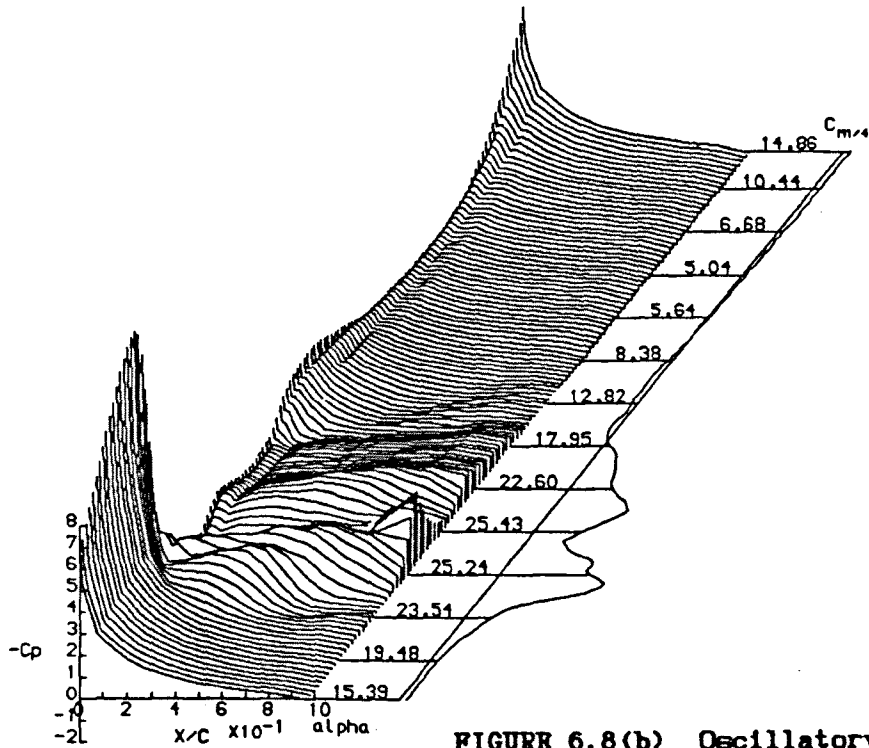
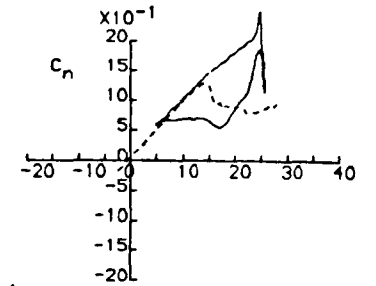
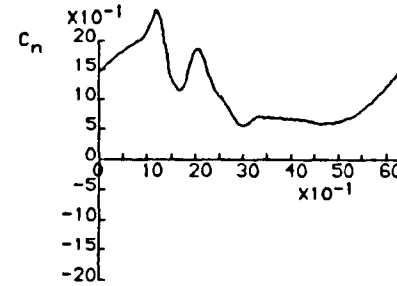
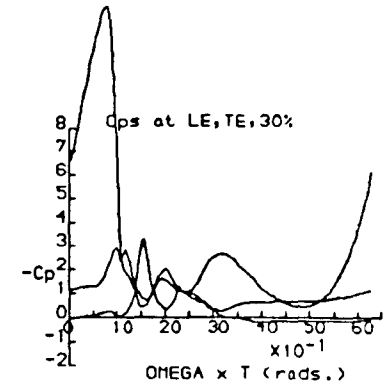
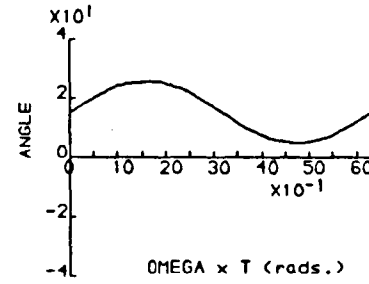
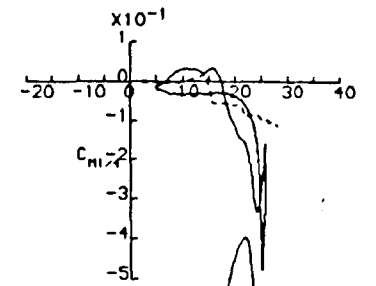
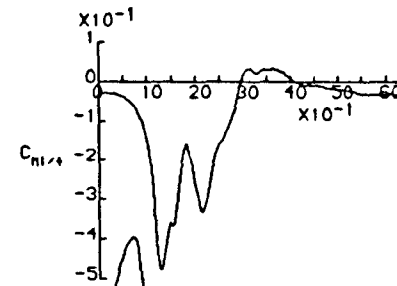


FIGURE 6.8(b) Oscillatory Data obtained for the NACA 23012.



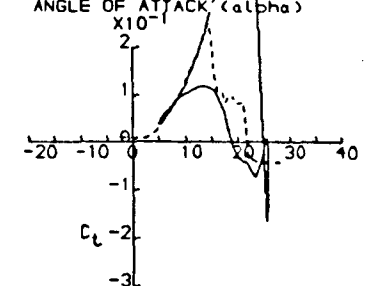
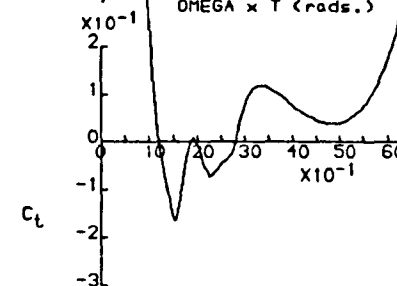
OMEGA x T (rads.)

ANGLE OF ATTACK (alpha)



OMEGA x T (rads.)

ANGLE OF ATTACK (alpha)



DYNAMIC CHARACTERISTICS FOR THE NACA23012A MODEL02

RUN REFERENCE NUMBER: 10721

DATE OF TEST: 14/ 3/86

REYNOLDS NUMBER = 1461955.

MACH NUMBER = 0.110

DYNAMIC PRESSURE = 936.50 N/sq. M

AIR TEMPERATURE = 30.0

NUMBER OF CYCLES = 10

SAMPLING FREQUENCY = 298.24 Hz.

MOTION TYPE: SINUSOIDAL

REDUCED FREQUENCY = 0.105

MEAN ANGLE = 20.00

AMPLITUDE = 10.00

OSCILLATION FREQUENCY = 2.330Hz.

AVERAGED DATA OF 10 CYCLES

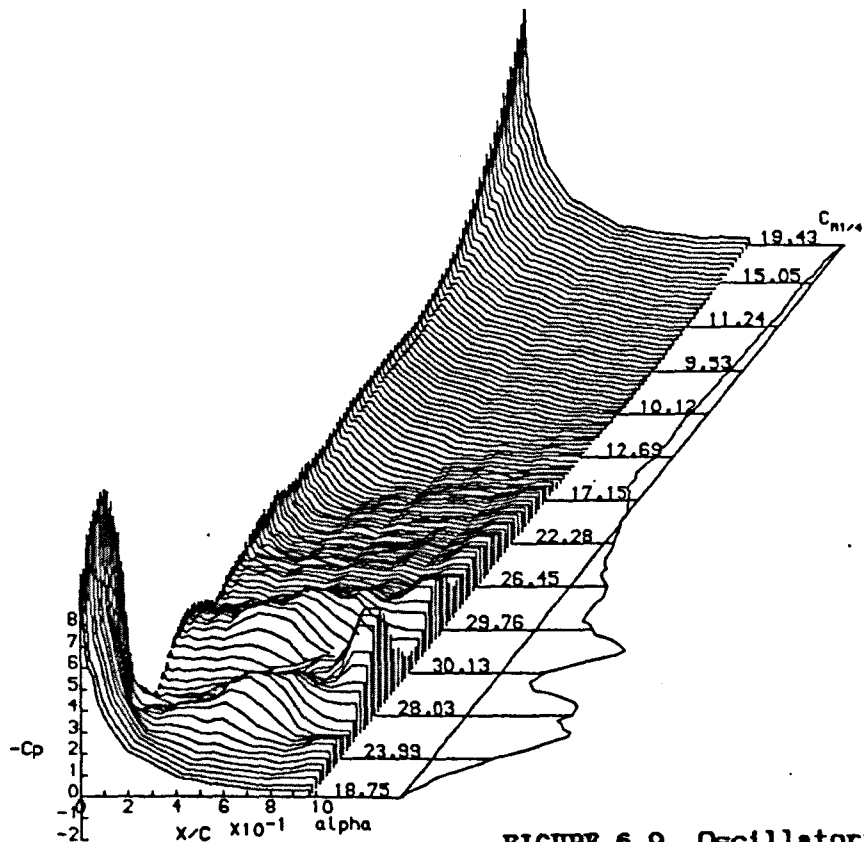
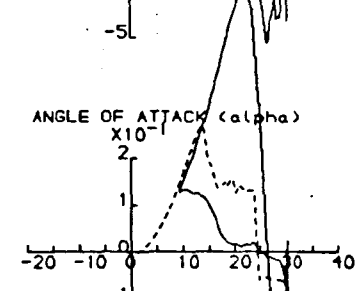
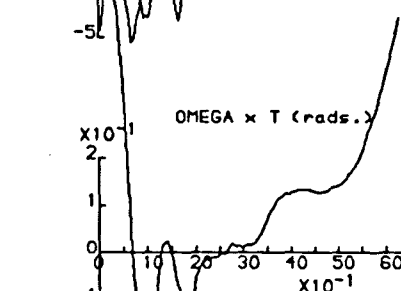
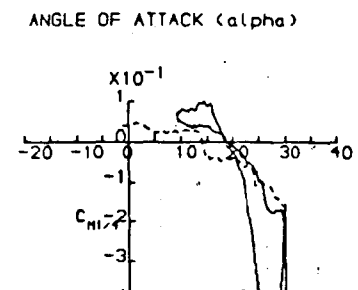
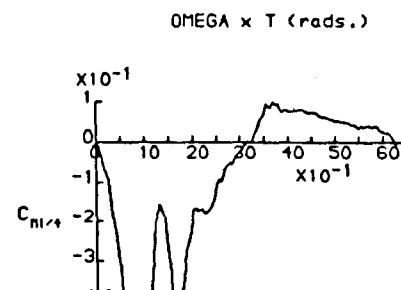
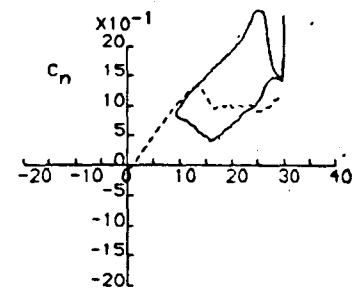
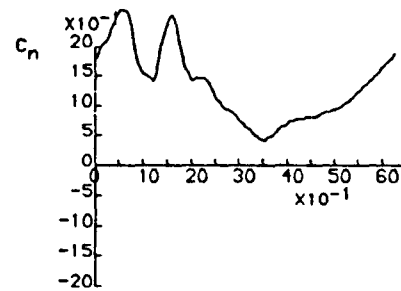
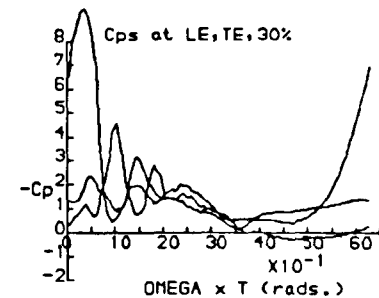
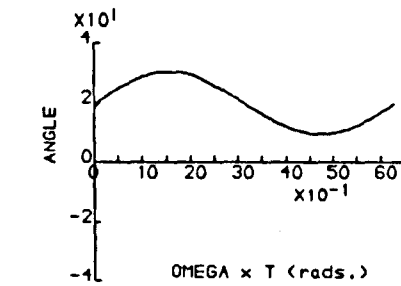


FIGURE 6.9 Oscillatory Data obtained for the NACA 23012(A).



DYNAMIC CHARACTERISTICS FOR THE NACA23012A MODEL02

RUN REFERENCE NUMBER: 10461

DATE OF TEST: 12/3/86

REYNOLDS NUMBER = 1469549.

MACH NUMBER = 0.111

DYNAMIC PRESSURE = 946.26 Nm⁻²

AIR TEMPERATURE = 30.0°C

NUMBER OF CYCLES = 10

SAMPLING FREQUENCY = 149.12 Hz.

MOTION TYPE: SINUSOIDAL

REDUCED FREQUENCY = 0.052

MEAN ANGLE = 6.00°

AMPLITUDE = 10.00°

OSCILLATION FREQUENCY = 1.165 Hz.

AVERAGED DATA OF 10 CYCLES

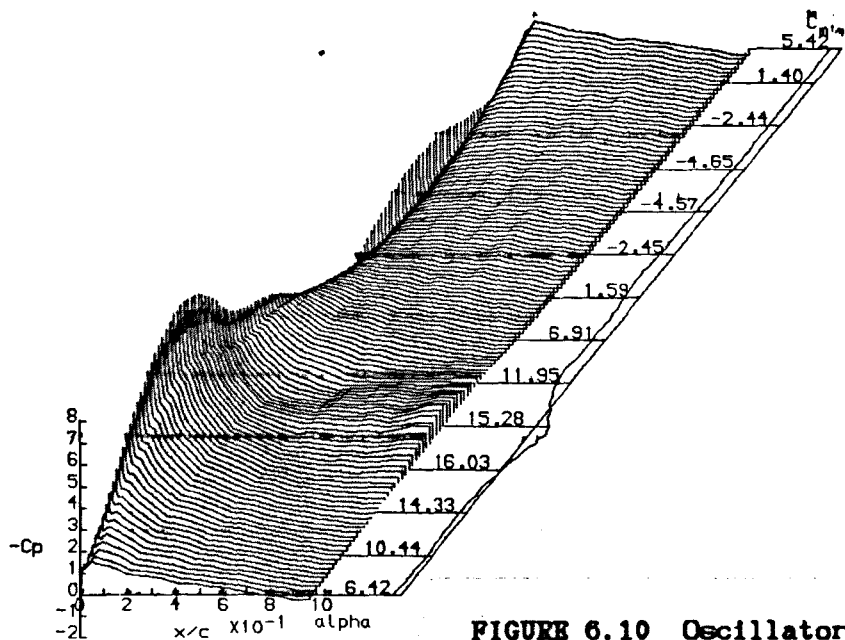
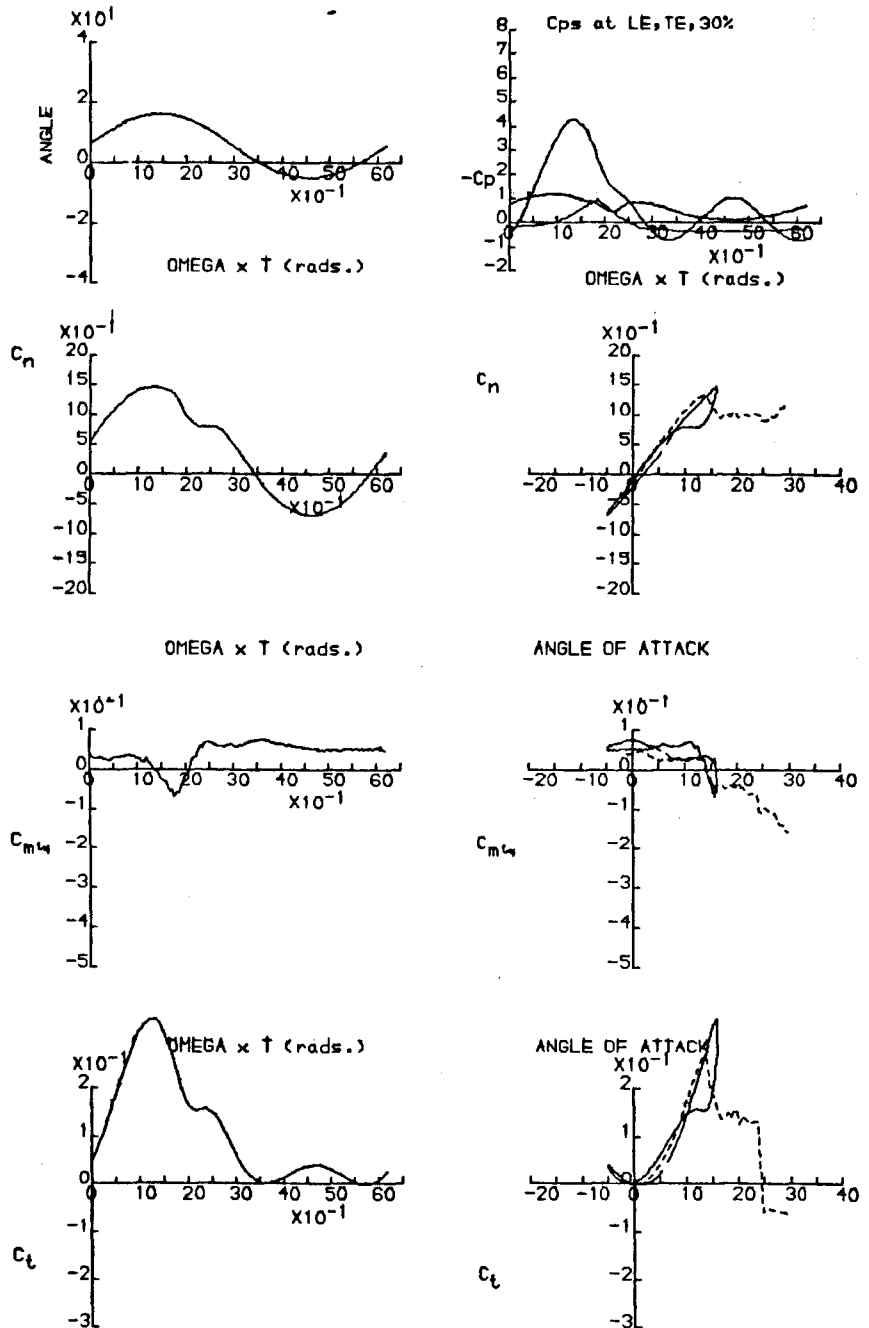


FIGURE 6.10 Oscillatory Data obtained for the NACA 23012(A).



DYNAMIC CHARACTERISTICS FOR THE NACA23012A MODEL02

RUN REFERENCE NUMBER: 10511 DATE OF TEST: 12/3/86
 REYNOLDS NUMBER = 1485515. MACH NUMBER = 0.112
 DYNAMIC PRESSURE = 966.93 Nm⁻² AIR TEMPERATURE = 30.0°C
 NUMBER OF CYCLES = 10 SAMPLING FREQUENCY = 521.92 Hz.
 MOTION TYPE: SINUSOIDAL REDUCED FREQUENCY = 0.180
 MEAN ANGLE = 6.00° AMPLITUDE = 10.00°
 OSCILLATION FREQUENCY = 4.078 Hz.
 AVERAGED DATA OF 10 CYCLES

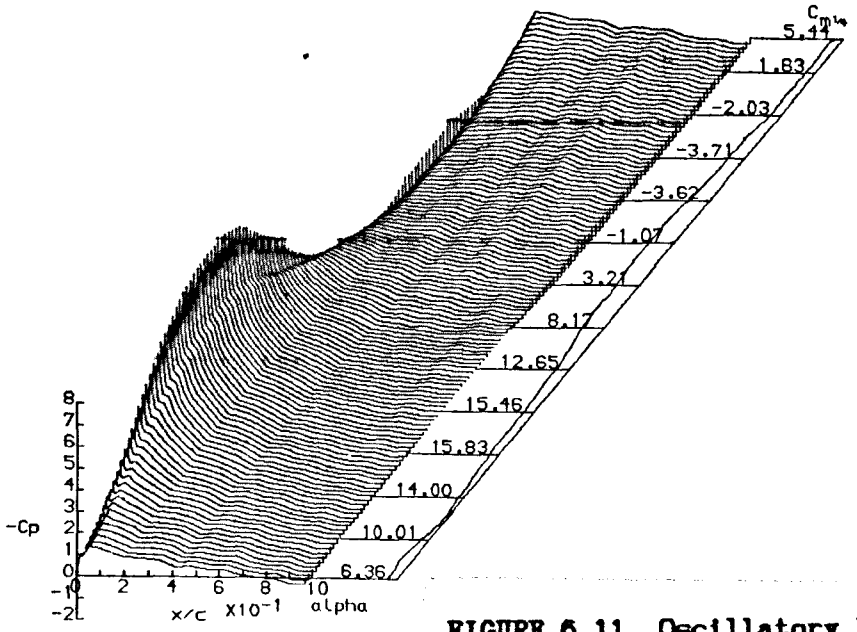
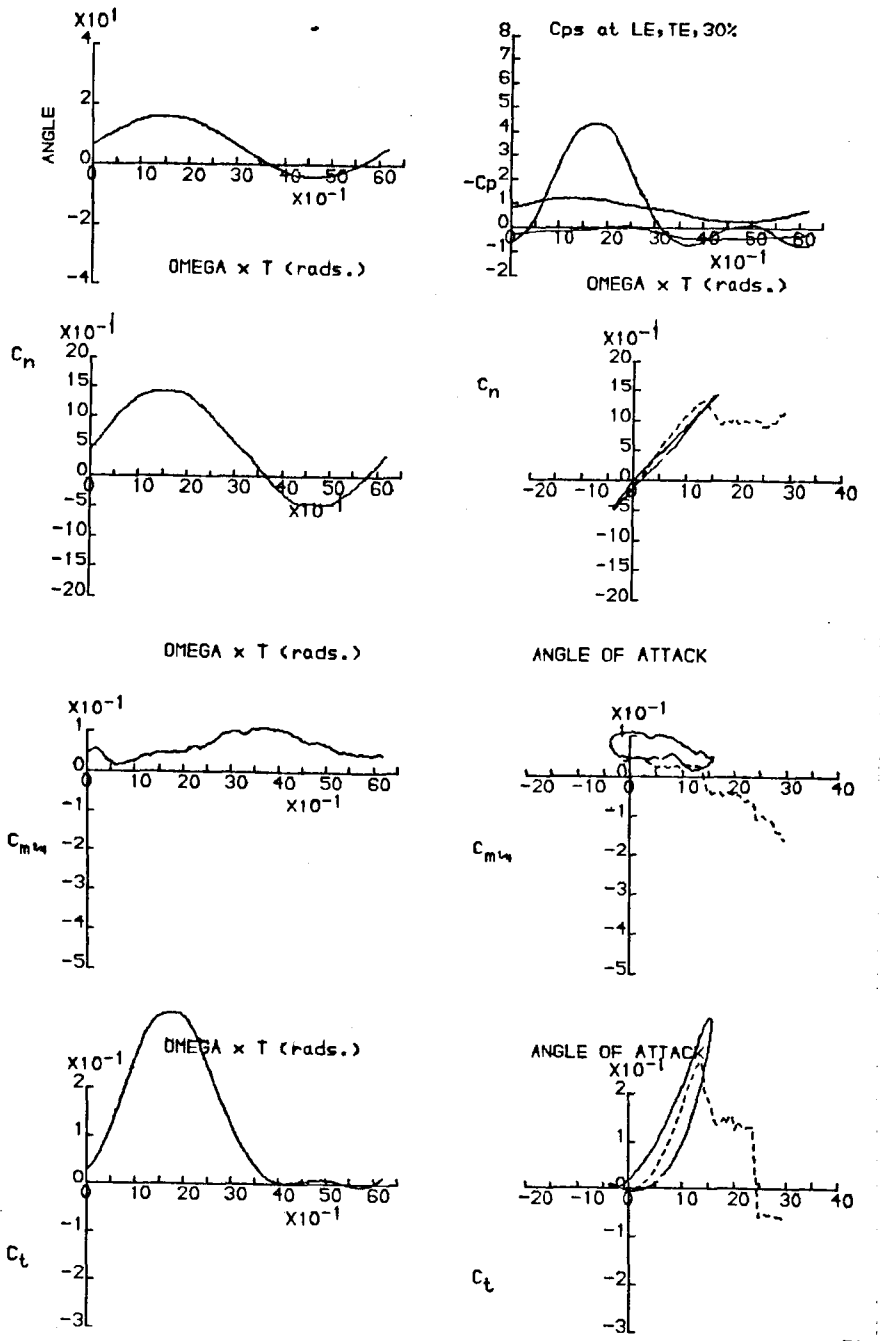
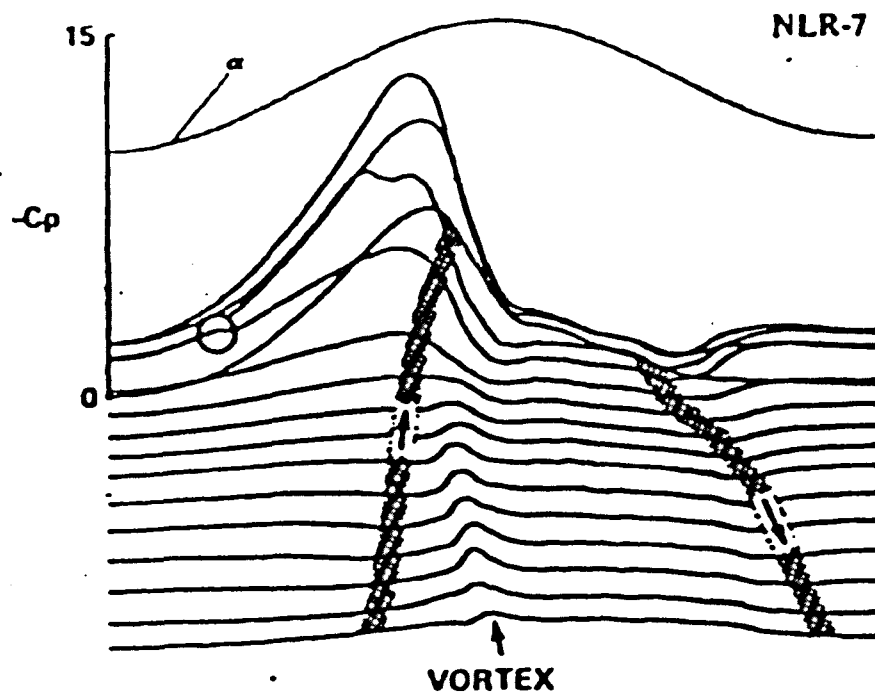
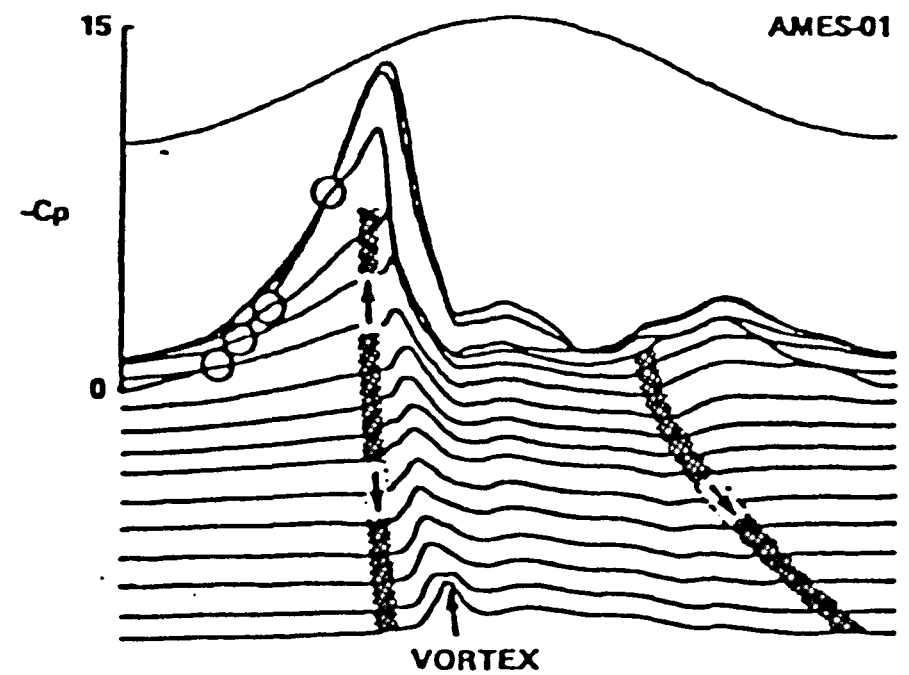


FIGURE 6.11 Oscillatory Data obtained for the NACA 23012(A).





(a) Trailing-Edge Stall



(b) Mixed Stall

FIGURE 6.12 Unsteady Stall Categorisation via Pressure Time Histories obtained at $M_\infty = 0.25$, $\alpha = 15 + 10 \sin \omega t$ @ $k = 0.10$ (from McCroskey *et al*, 1980).

UNSTEADY PRESSURE/TIME DISTRIBUTION - UPPER SURFACE

RUN REFERENCE NUMBER: 10641

DATE OF TEST: 14/ 3/86

REYNOLDS NUMBER = 1464159.

MACH NUMBER = 0.110

DYNAMIC PRESSURE = 939.33 N/sq. m

AIR TEMPERATURE = 30.0

NUMBER OF CYCLES = 10

SAMPLING FREQUENCY = 298.24 Hz.

MOTION TYPE: SINUSOIDAL

REDUCED FREQUENCY = 0.104

MEAN ANGLE = 15.00

AMPLITUDE = 10.00

OSCILLATION FREQUENCY = 2.330Hz.

AVERAGED DATA OF 10 CYCLES

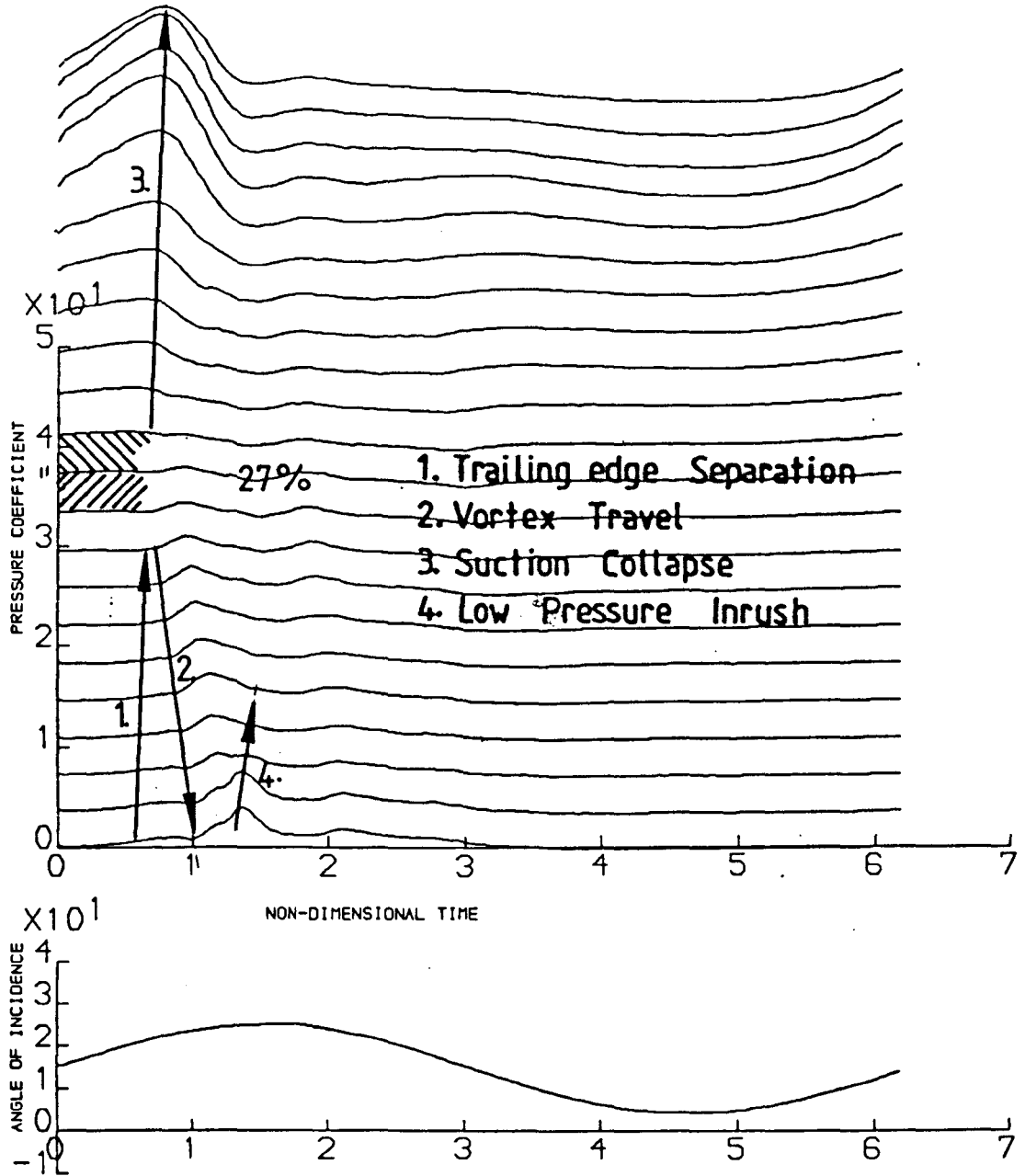


FIGURE 6.13 Unsteady Stall Categorisation of the NACA 23012(A) via Pressure Time Histories.

UNSTEADY PRESSURE/TIME DISTRIBUTION - UPPER SURFACE

RUN REFERENCE NUMBER: 13851

DATE OF TEST: 17/ 6/83

REYNOLDS NUMBER = 1528246.

MACH NUMBER = 0.112

DYNAMIC PRESSURE = 1005.15 N/sq. M

AIR TEMPERATURE = 32.0

NUMBER OF CYCLES = 10

SAMPLING FREQUENCY = 298.24 Hz.

MOTION TYPE: SINUSOIDAL

REDUCED FREQUENCY = 0.102

MEAN ANGLE = 15.00

AMPLITUDE = 10.00

OSCILLATION FREQUENCY = 2.330Hz.

AVERAGED DATA OF 10 CYCLES

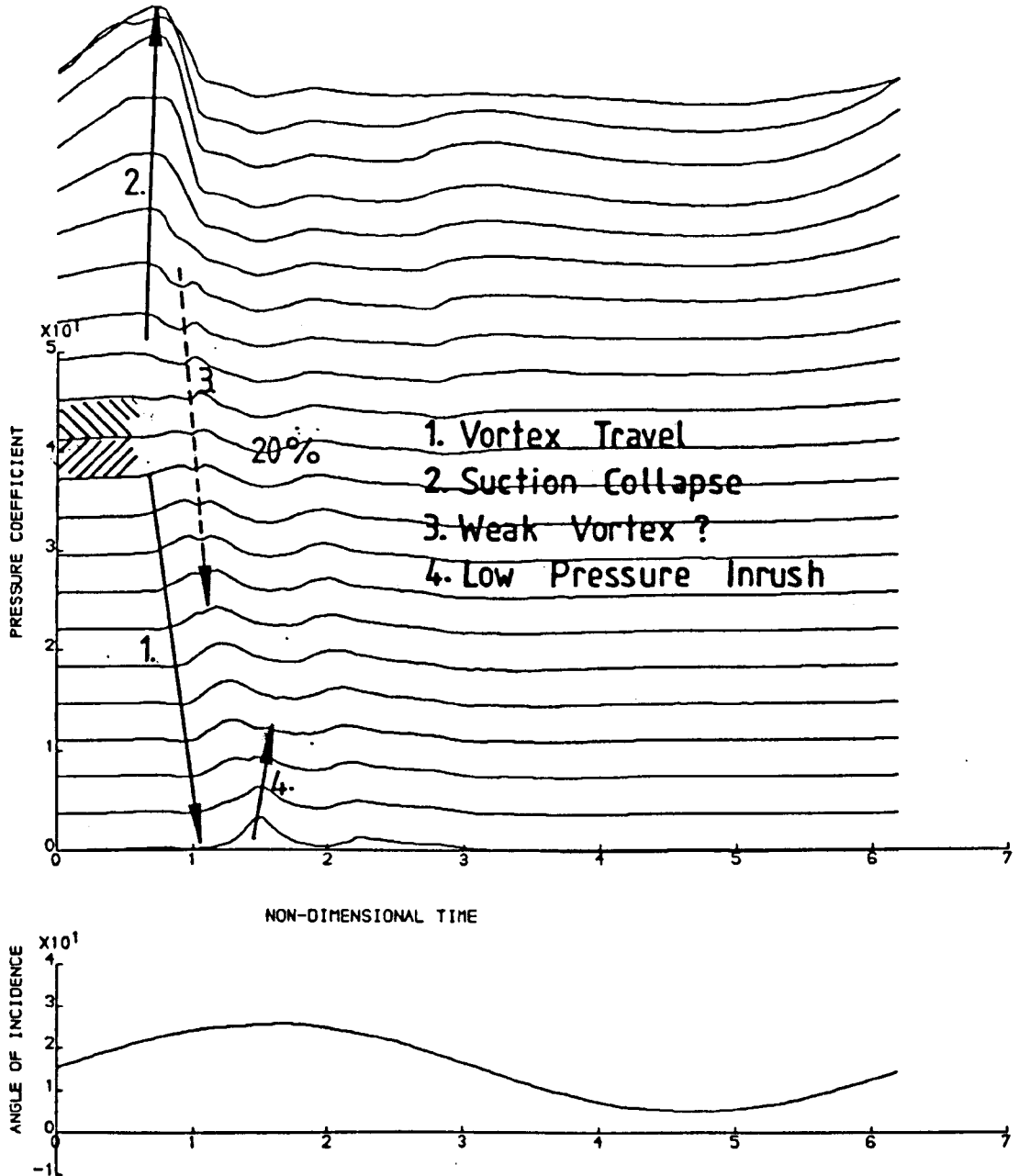


FIGURE 6.14 Unsteady Stall Categorisation of the NACA 23012 via Pressure Time Histories.

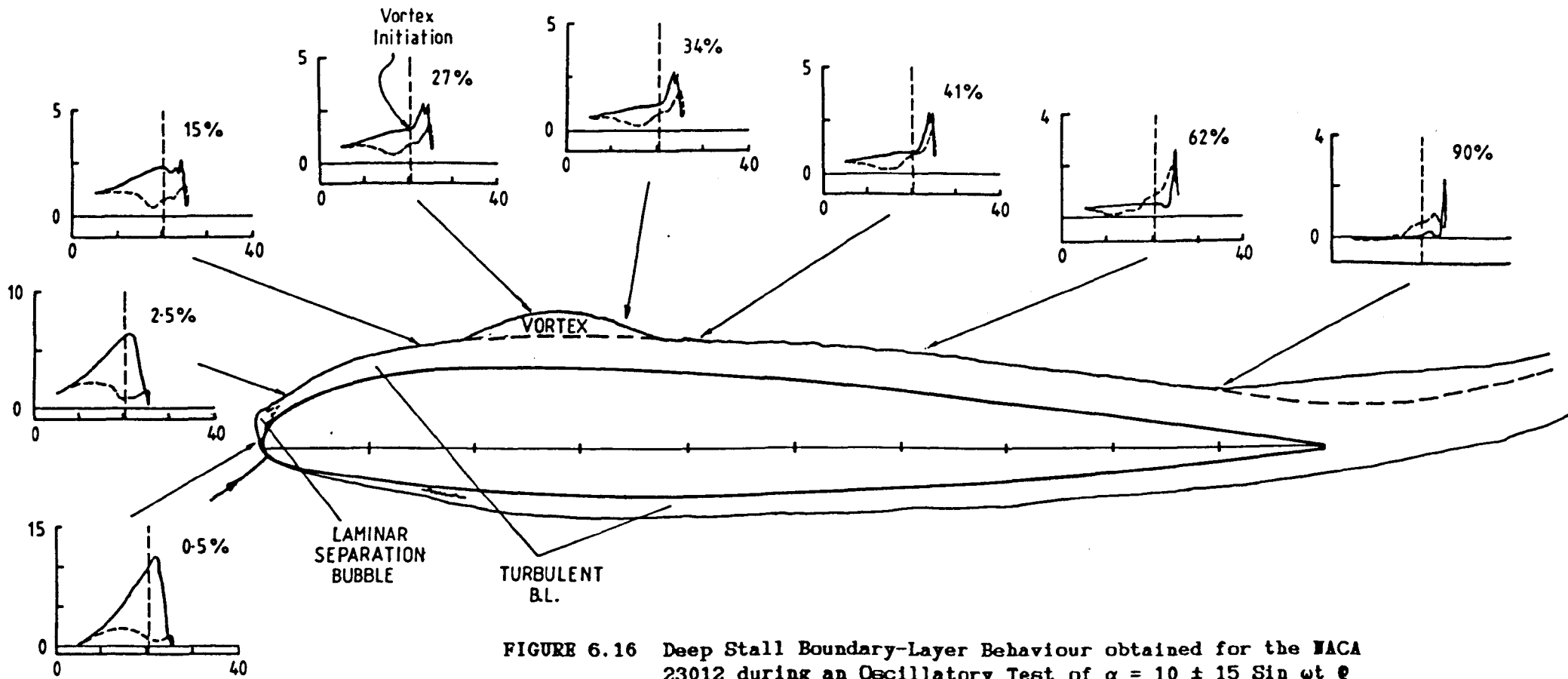


FIGURE 6.16 Deep Stall Boundary-Layer Behaviour obtained for the NACA 23012 during an Oscillatory Test of $\alpha = 10 \pm 15 \sin \omega t$ @ $k = 0.15$.

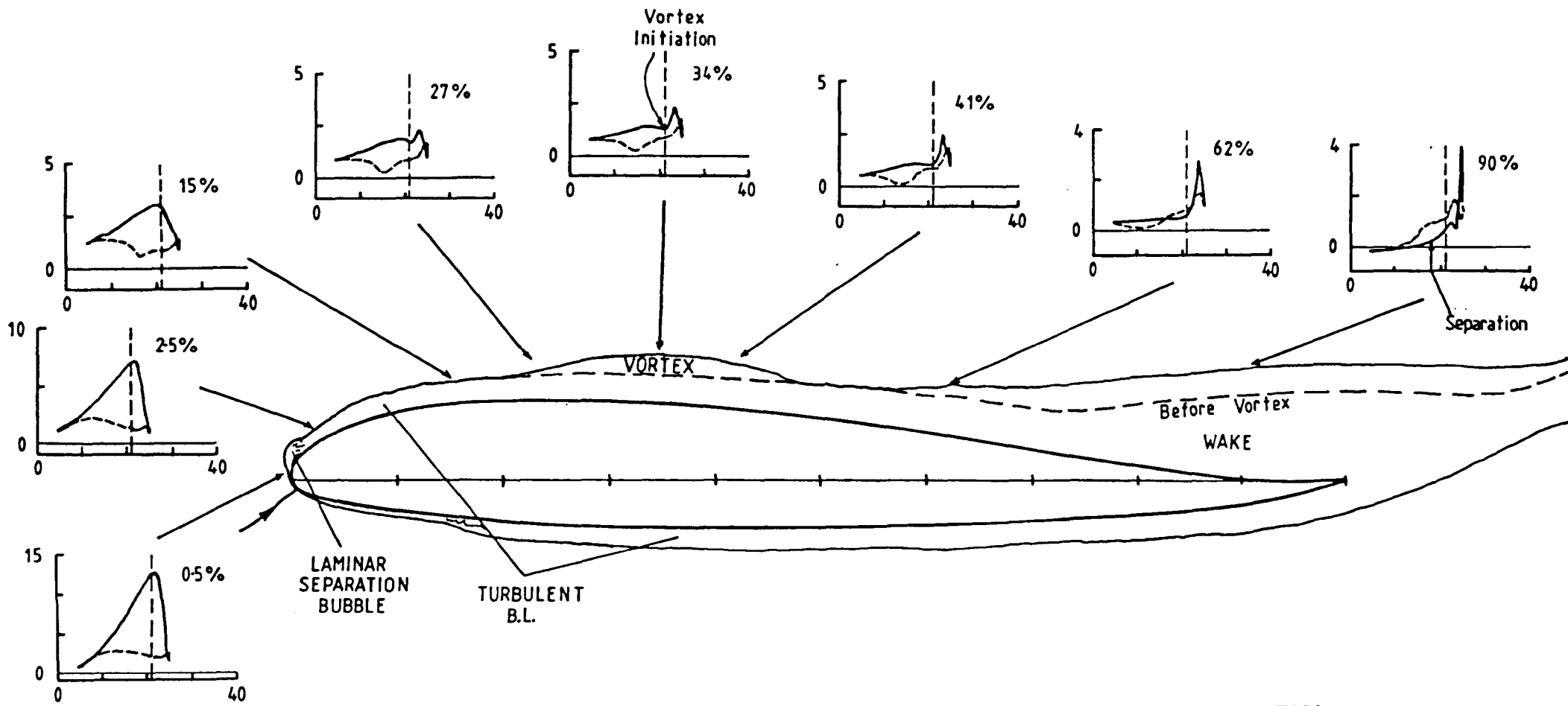


FIGURE 6.15 Deep Stall Boundary-Layer Behaviour obtained for the NACA 23012(A) during an Oscillatory Test of $\alpha = 10 \pm 15 \sin \omega t$ @ $k = 0.15$.

DYNAMIC CHARACTERISTICS FOR THE NACA 23012 MODEL 2

RUN REFERENCE NUMBER: 10881

DATE OF TEST: 24/ 7/85

REYNOLDS NUMBER = 1507681.

MACH NUMBER = 0.112

DYNAMIC PRESSURE = 961.35 N/sq. m

AIR TEMPERATURE = 26.0

NUMBER OF CYCLES = 10

SAMPLING FREQUENCY = 298.24 Hz.

MOTION TYPE: SINUSOIDAL

REDUCED FREQUENCY = 0.104

MEAN ANGLE = 4.00

AMPLITUDE = 8.00

OSCILLATION FREQUENCY = 2.330Hz.

AVERAGED DATA OF 10 CYCLES

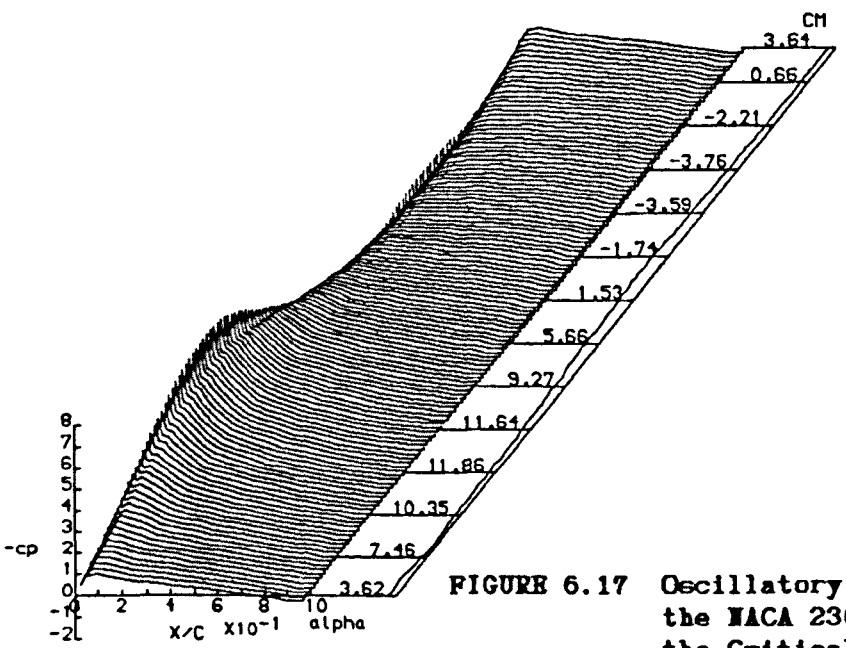
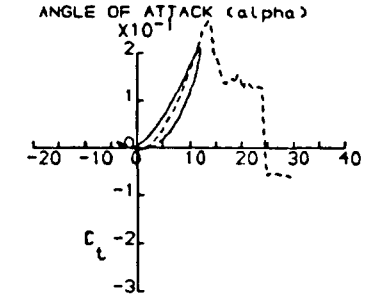
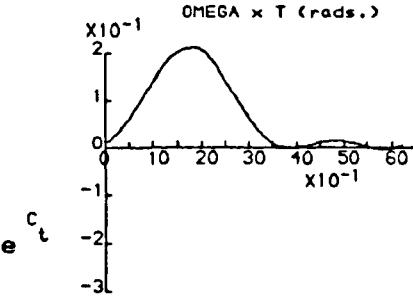
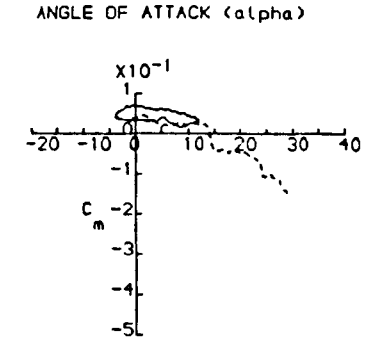
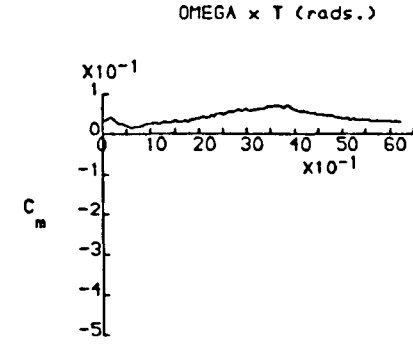
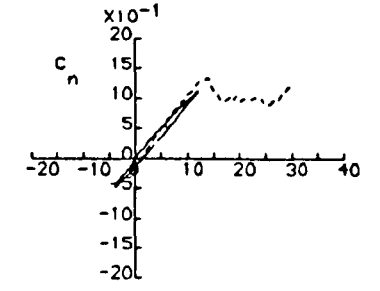
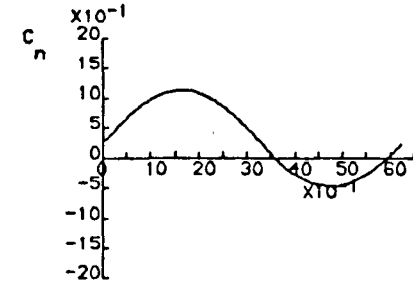
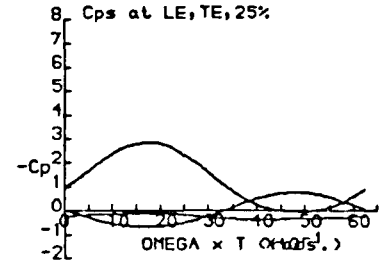
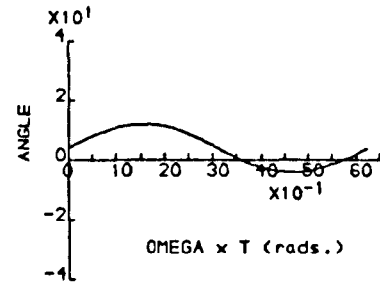


FIGURE 6.17 Oscillatory Data obtained for the NACA 23012(A) to Calculate the Critical Angle.

DYNAMIC CHARACTERISTICS FOR THE NACA 23012 MODEL 2

RUN REFERENCE NUMBER: 10891
 REYNOLDS NUMBER = 1499009.
 DYNAMIC PRESSURE = 950.32 N/sq. m
 NUMBER OF CYCLES = 10
 MOTION TYPE: SINUSOIDAL
 MEAN ANGLE = 6.00
 OSCILLATION FREQUENCY = 2.330Hz.
 AVERAGED DATA OF 10 CYCLES

DATE OF TEST: 24/ 7/85
 MACH NUMBER = 0.111
 AIR TEMPERATURE = 26.0
 SAMPLING FREQUENCY = 298.24 Hz.
 REDUCED FREQUENCY = 0.105
 AMPLITUDE = 8.00

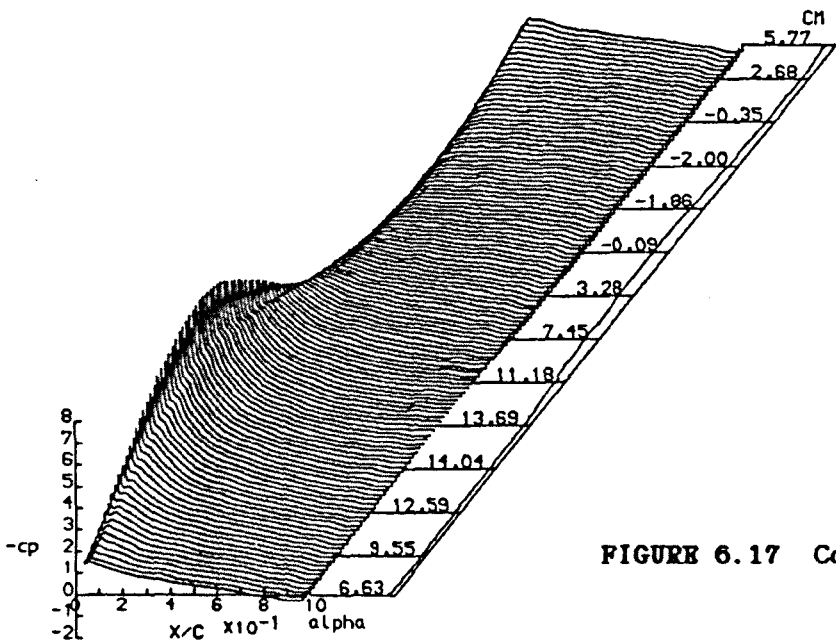
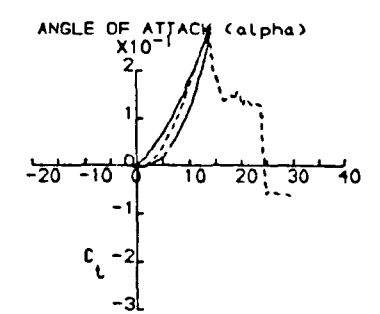
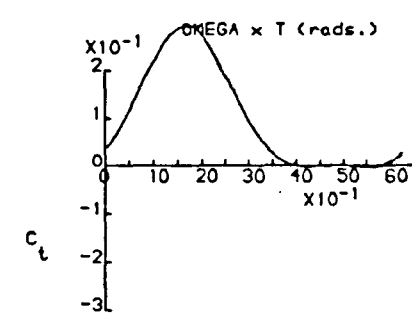
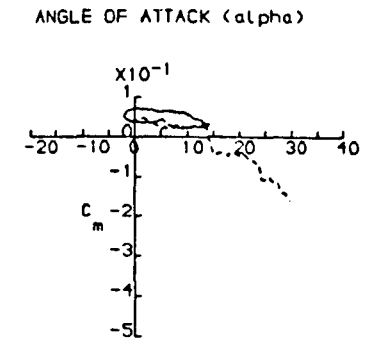
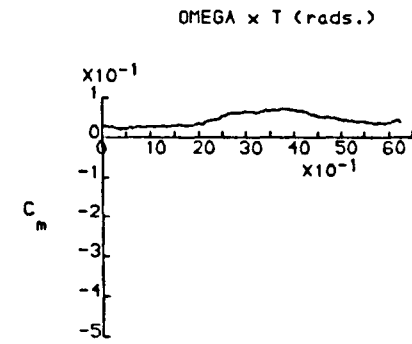
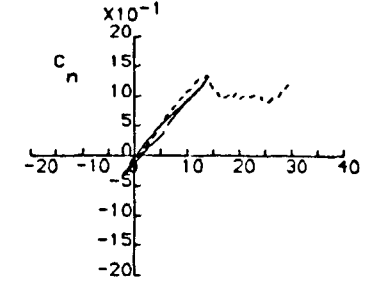
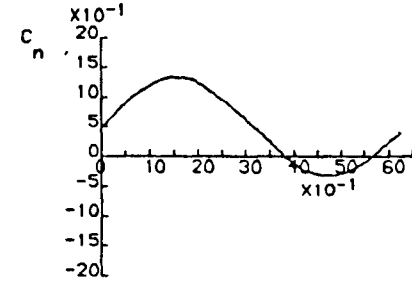
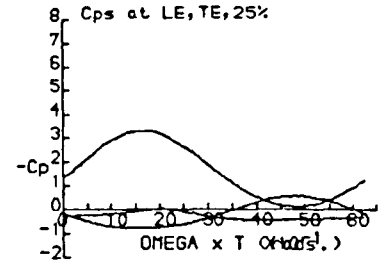
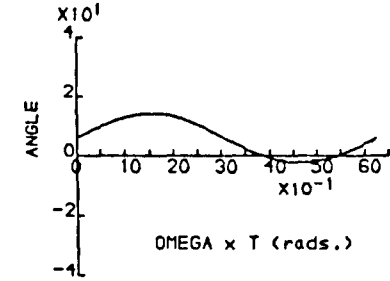


FIGURE 6.17 Continued.

DYNAMIC CHARACTERISTICS FOR THE NACA 23012 MODEL 2

RUN REFERENCE NUMBER: 10901

DATE OF TEST: 24/ 7/85

REYNOLDS NUMBER = 1495997.

MACH NUMBER = 0.111

DYNAMIC PRESSURE = 946.50 N/sq. M

AIR TEMPERATURE = 26.0

NUMBER OF CYCLES = 10

SAMPLING FREQUENCY = 298.24 Hz.

MOTION TYPE: SINUSOIDAL

REDUCED FREQUENCY = 0.105

MEAN ANGLE = 8.00

AMPLITUDE = 8.00

OSCILLATION FREQUENCY = 2.330Hz.

AVERAGED DATA OF 10 CYCLES

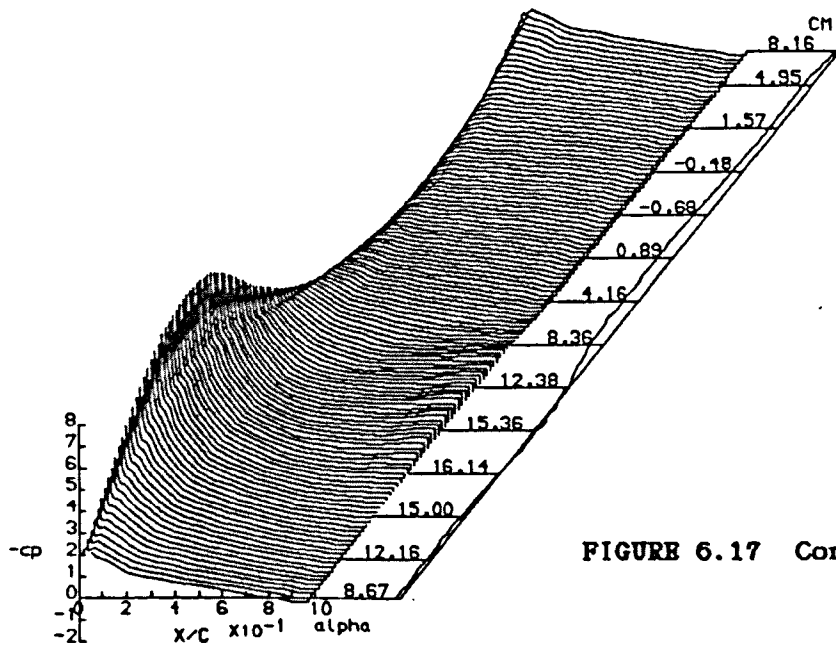
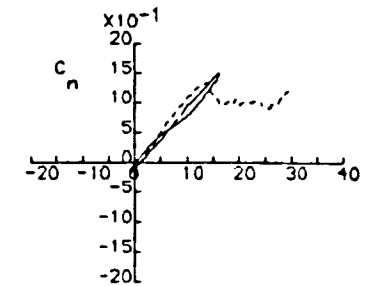
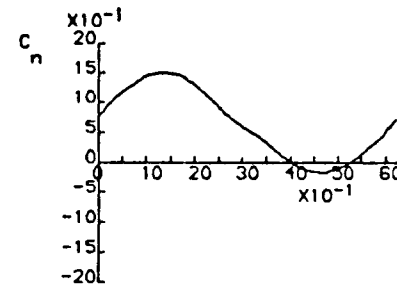
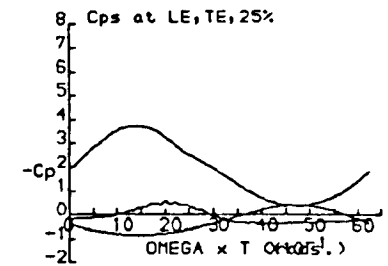
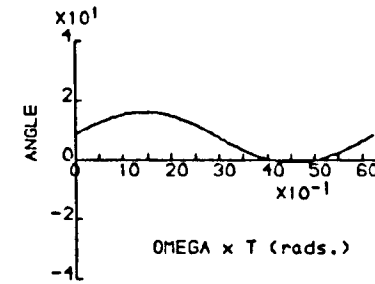
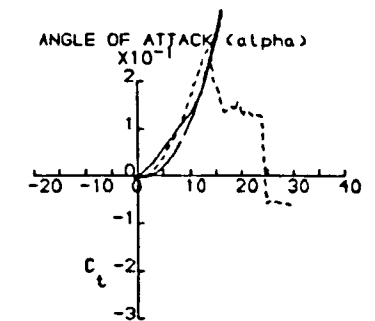
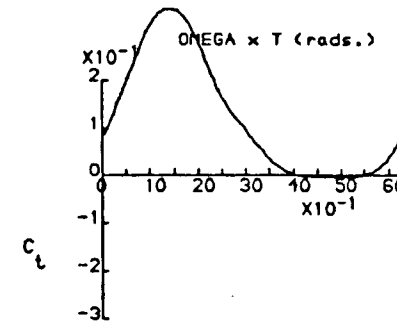
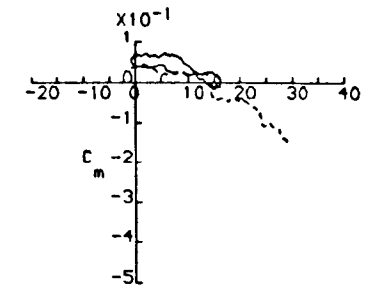
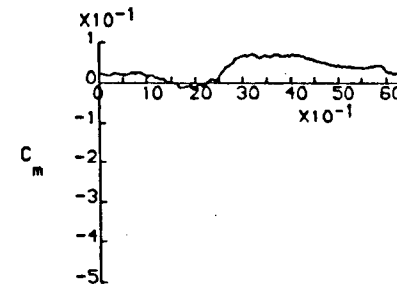


FIGURE 6.17 Continued.



$\Omega \times T$ (rads.)

ANGLE OF ATTACK (α)



DYNAMIC CHARACTERISTICS FOR THE NACA 23012 MODEL 2

RUN REFERENCE NUMBER: 10911

DATE OF TEST: 24/ 7/85

REYNOLDS NUMBER = 1312815.

MACH NUMBER = 0.114

DYNAMIC PRESSURE = 1006.67 N/sq. m

AIR TEMPERATURE = 26.0

NUMBER OF CYCLES = 10

SAMPLING FREQUENCY = 298.24 Hz.

MOTION TYPE: SINUSOIDAL

REDUCED FREQUENCY = 0.102

MEAN ANGLE = 10.00

AMPLITUDE = 8.00

OSCILLATION FREQUENCY = 2.330Hz.

AVERAGED DATA OF 10 CYCLES

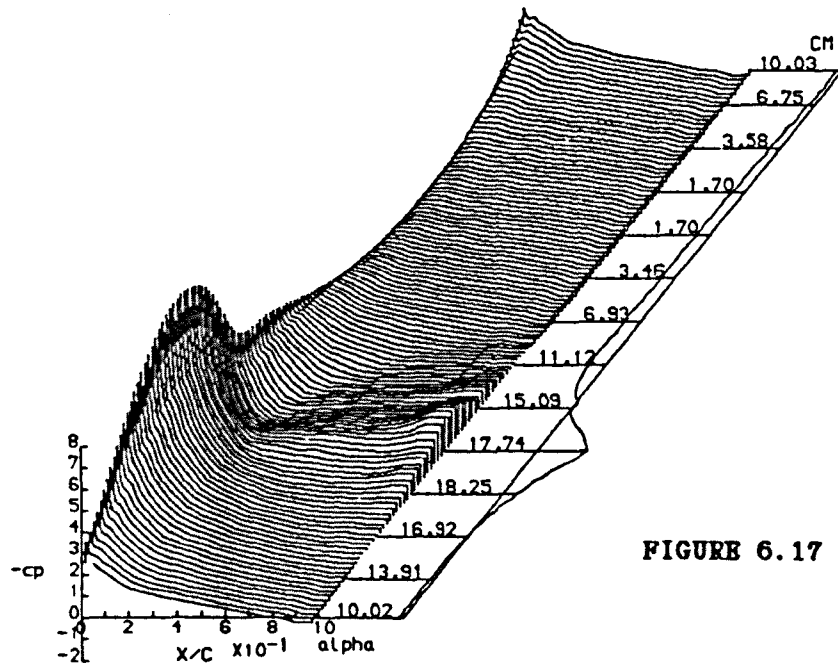
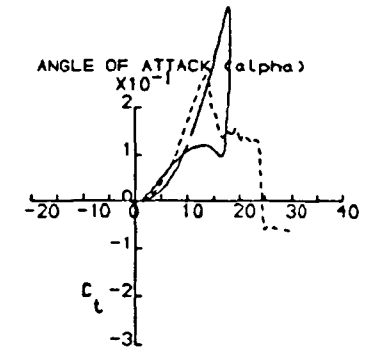
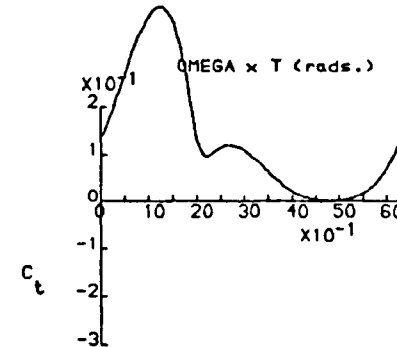
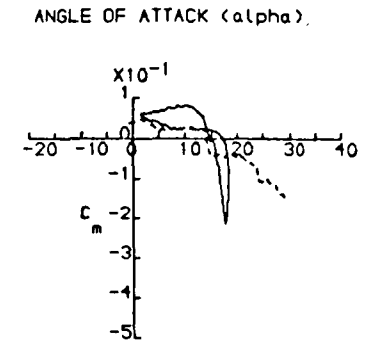
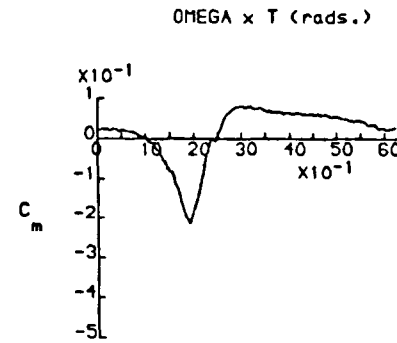
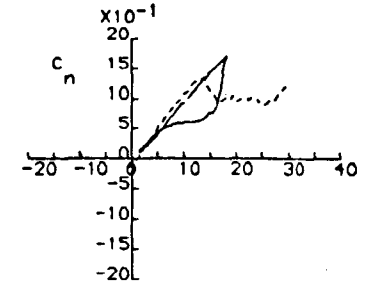
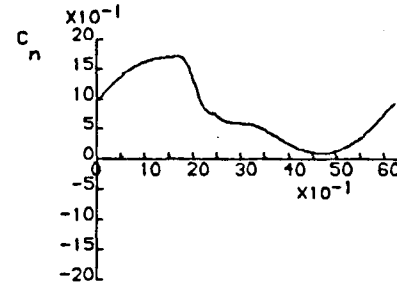
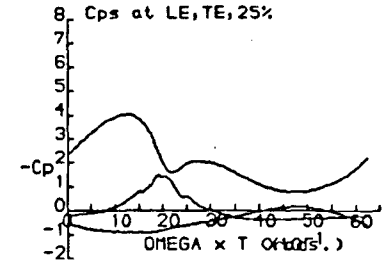
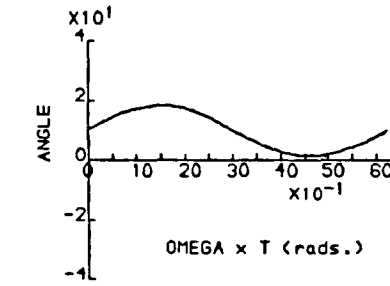


FIGURE 6.17 Continued.



DYNAMIC CHARACTERISTICS FOR THE NACA 23012 MODEL 2

RUN REFERENCE NUMBER: 10921
 REYNOLDS NUMBER = 1327392.
 DYNAMIC PRESSURE = 986.65 N/sq. m
 NUMBER OF CYCLES = 10
 MOTION TYPE: SINUSOIDAL
 MEAN ANGLE = 12.00
 OSCILLATION FREQUENCY = 2.330Hz.
 AVERAGED DATA OF 10 CYCLES

DATE OF TEST: 24/ 7/85
 MACH NUMBER = 0.113
 AIR TEMPERATURE = 26.0
 SAMPLING FREQUENCY = 298.24 Hz.
 REDUCED FREQUENCY = 0.103
 AMPLITUDE = 8.00

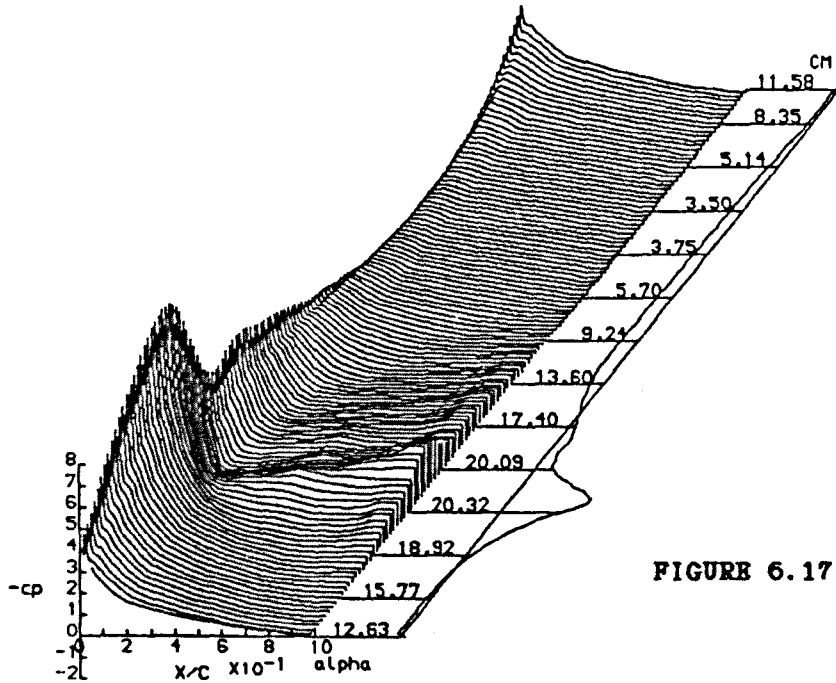
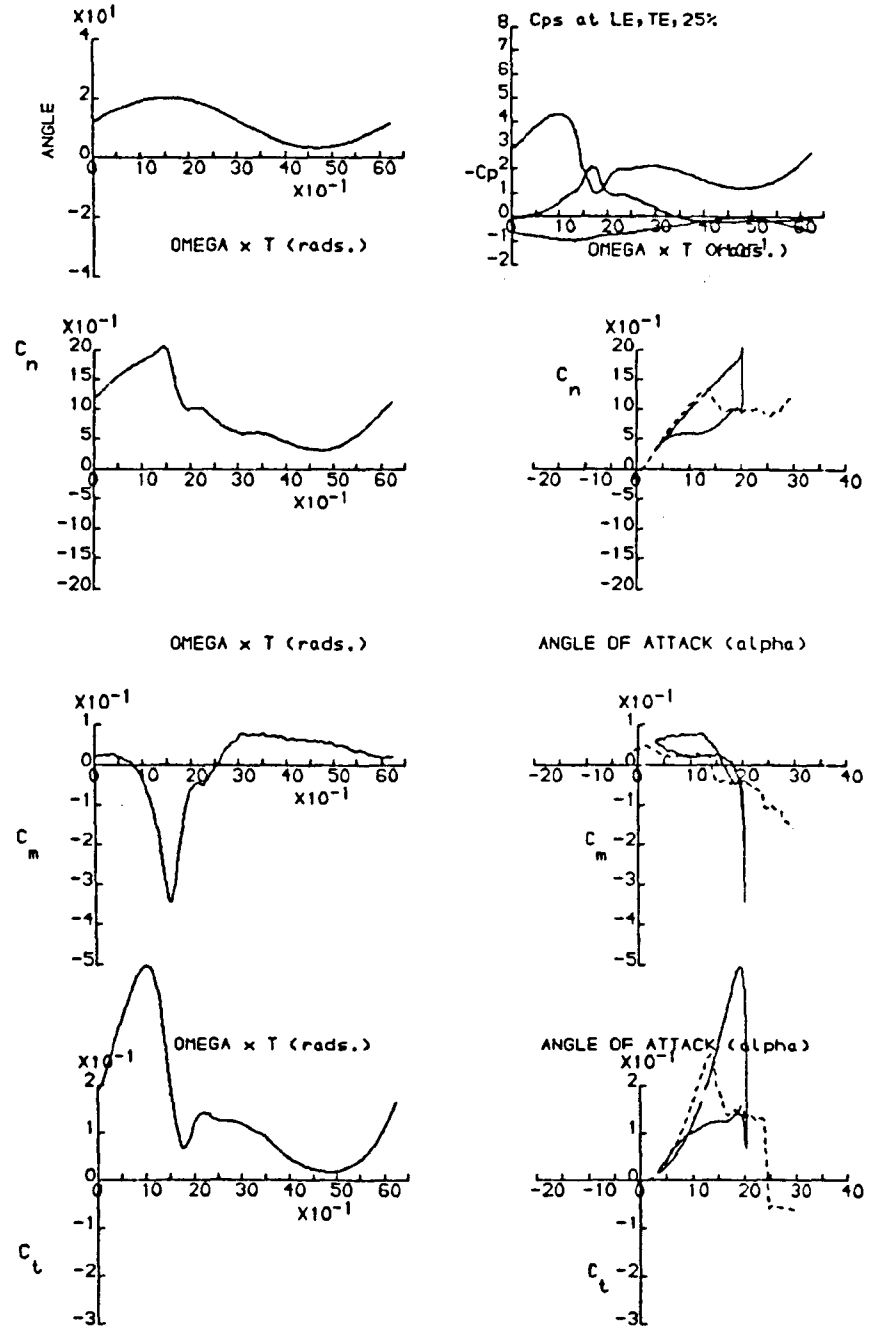


FIGURE 6.17 Continued.



DYNAMIC CHARACTERISTICS FOR THE NACA 23012 MODEL 2

RUN REFERENCE NUMBER: 10931

DATE OF TEST: 24/ 7/85

REYNOLDS NUMBER = 1526854.

MACH NUMBER = 0.113

DYNAMIC PRESSURE = 985.95 N/sq. m

AIR TEMPERATURE = 26.0

NUMBER OF CYCLES = 10

SAMPLING FREQUENCY = 298.24 Hz.

MOTION TYPE: SINUSOIDAL

REDUCED FREQUENCY = 0.103

MEAN ANGLE = 17.00

AMPLITUDE = 8.00

OSCILLATION FREQUENCY = 2.330Hz.

AVERAGED DATA OF 10 CYCLES

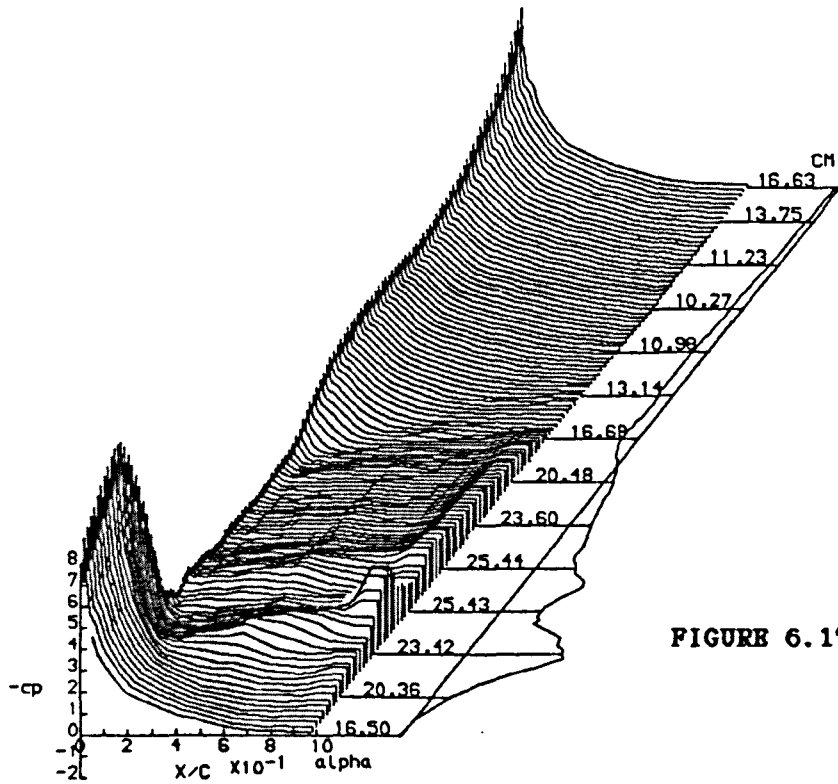
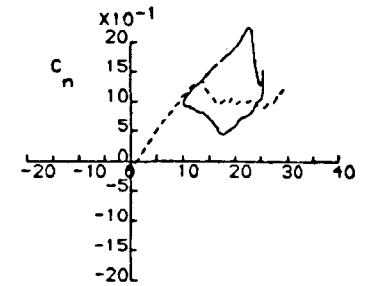
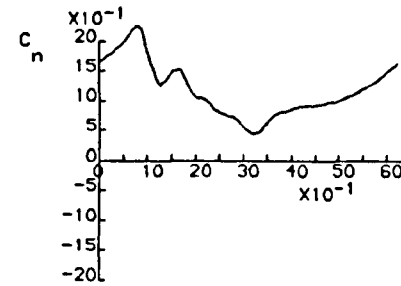
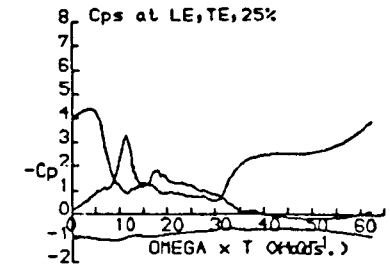
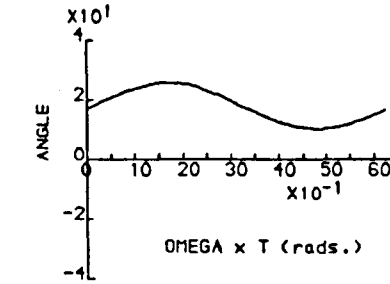
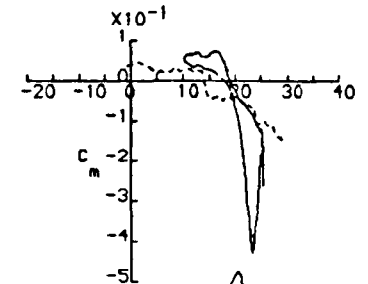
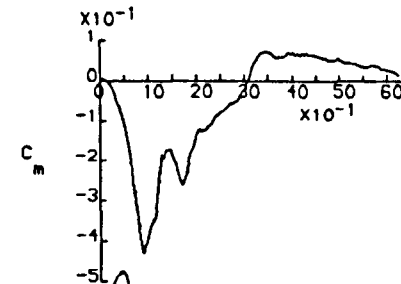


FIGURE 6.17 Completed.



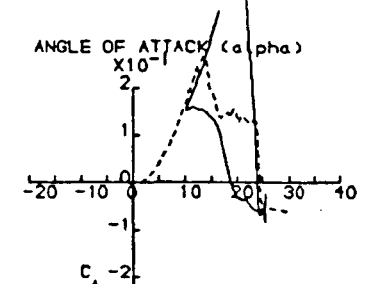
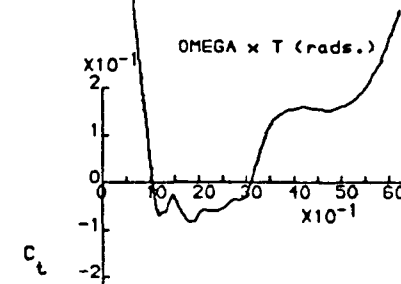
OMEGA x T (rads.)

ANGLE OF ATTACK (α)



OMEGA x T (rads.)

ANGLE OF ATTACK (α)



C_t

C_t

DYNAMIC CHARACTERISTICS FOR THE NACA 23012 MODEL01

RUN REFERENCE NUMBER: 13511

DATE OF TEST: 16/ 6/83

REYNOLDS NUMBER = 1524106.

MACH NUMBER = 0.112

DYNAMIC PRESSURE = 998.27 N/sq. m

AIR TEMPERATURE = 31.5

NUMBER OF CYCLES = 10

SAMPLING FREQUENCY = 298.24 Hz.

MOTION TYPE: SINUSOIDAL

REDUCED FREQUENCY = 0.103

MEAN ANGLE = 6.00

AMPLITUDE = 8.00

OSCILLATION FREQUENCY = 2.330Hz.

AVERAGED DATA OF 10 CYCLES

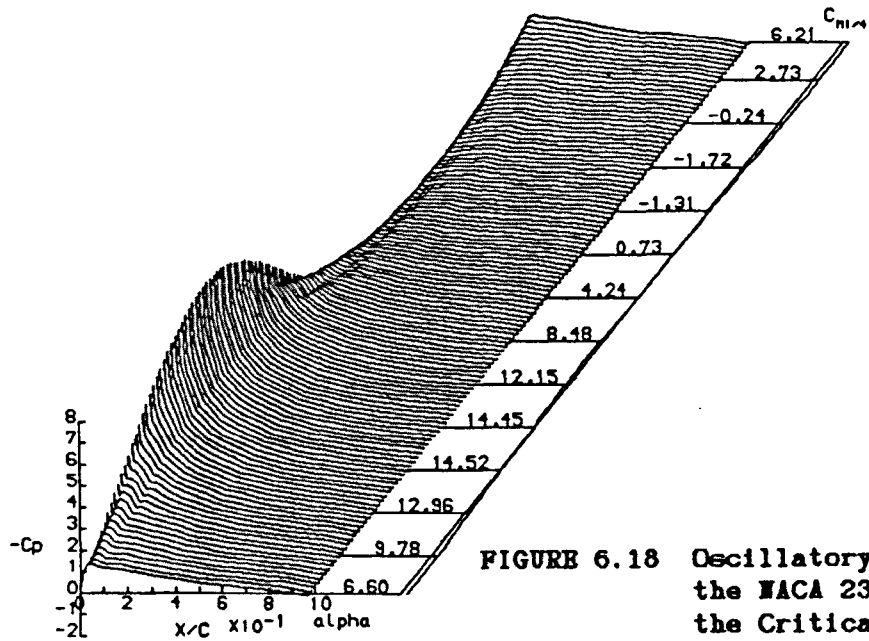
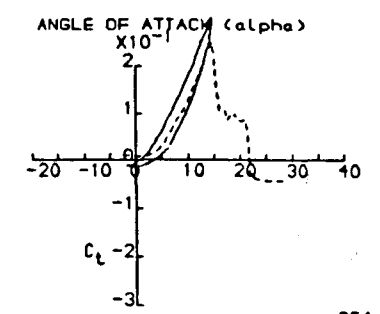
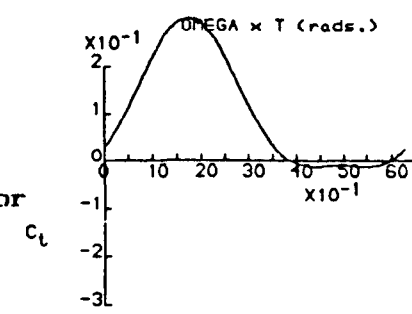
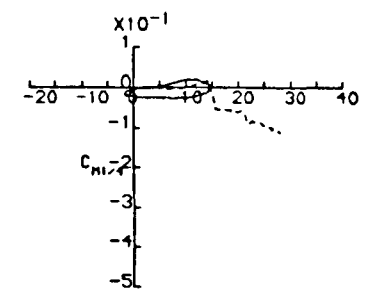
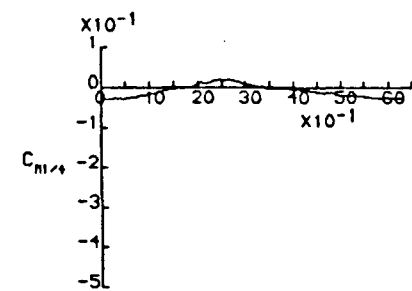
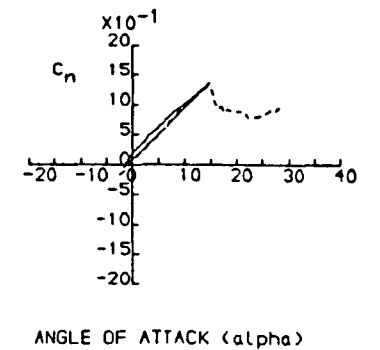
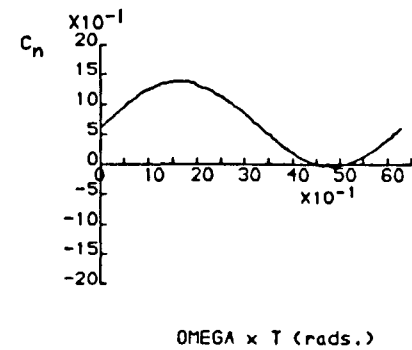
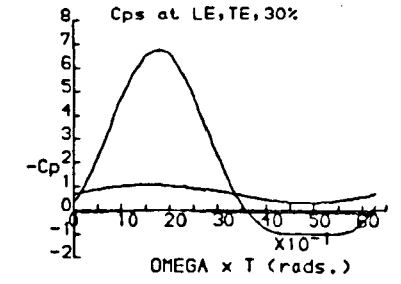
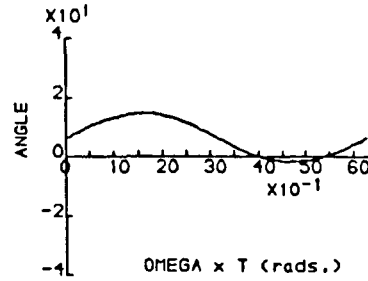


FIGURE 6.18 Oscillatory Data obtained for the NACA 23012 to Calculate C_t the Critical Angle.

DYNAMIC CHARACTERISTICS FOR THE NACA 23012 MODEL 01

RUN REFERENCE NUMBER: 13591 DATE OF TEST: 16/ 6/83
 REYNOLDS NUMBER = 1529997. MACH NUMBER = 0.113
 DYNAMIC PRESSURE = 1014.27 N/sq. M AIR TEMPERATURE = 33.0
 NUMBER OF CYCLES = 10 SAMPLING FREQUENCY = 298.24 Hz.
 MOTION TYPE: SINUSOIDAL REDUCED FREQUENCY = 0.102
 MEAN ANGLE = 8.00 AMPLITUDE = 8.00
 OSCILLATION FREQUENCY = 2.330Hz.
 AVERAGED DATA OF 10 CYCLES

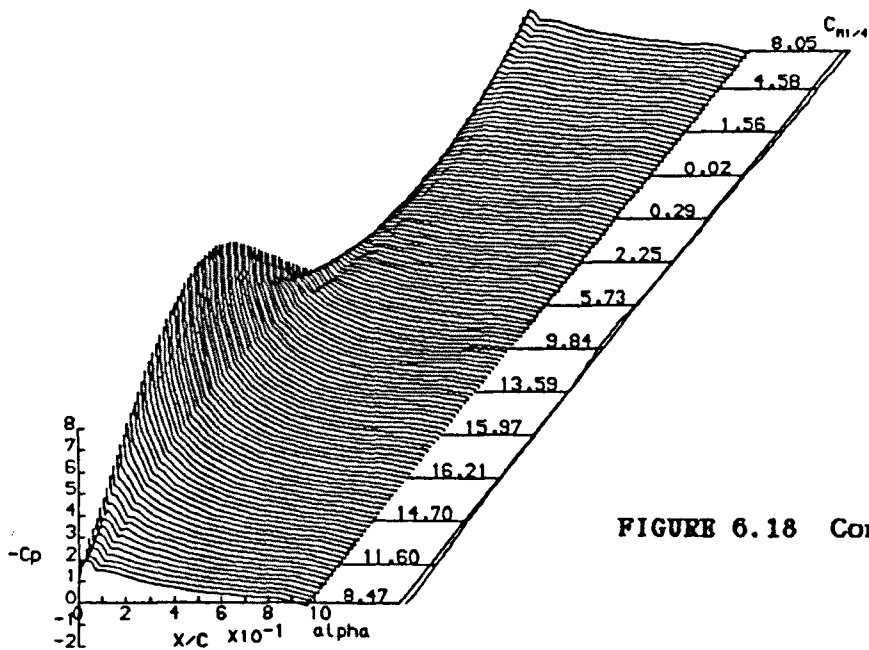
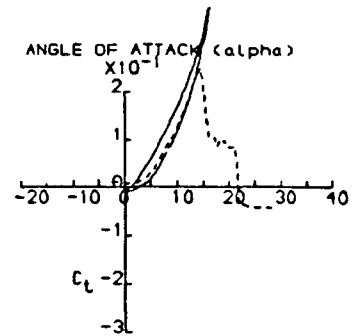
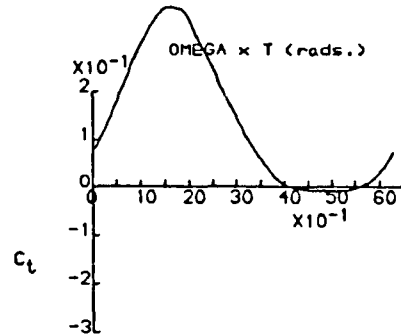
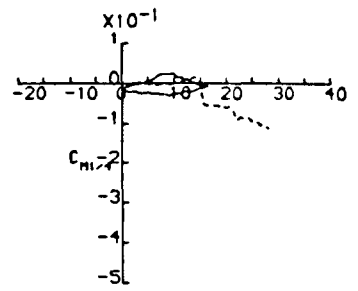
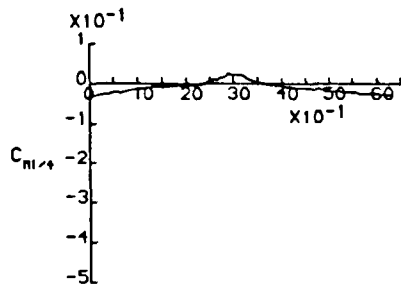
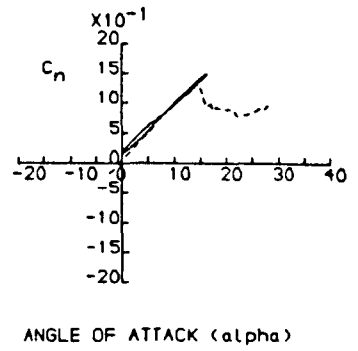
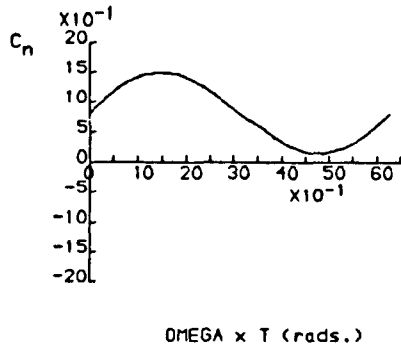
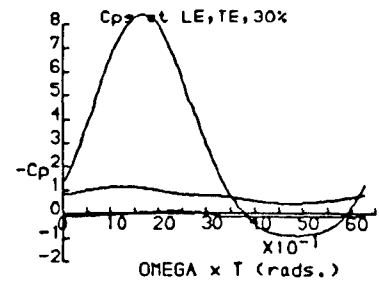
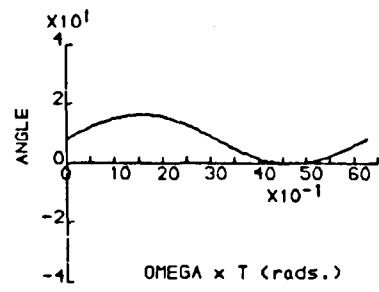


FIGURE 6.18 Continued.

DYNAMIC CHARACTERISTICS FOR THE NACA 23012 MODEL 01

RUN REFERENCE NUMBER: 13641
 REYNOLDS NUMBER = 1530193.
 DYNAMIC PRESSURE = 1020.04 N/sq. M
 NUMBER OF CYCLES = 10
 MOTION TYPE: SINUSOIDAL
 MEAN ANGLE = 10.00
 OSCILLATION FREQUENCY = 2.330Hz.
 AVERAGED DATA OF 10 CYCLES

DATE OF TEST: 16/ 6/83
 MACH NUMBER = 0.113
 AIR TEMPERATURE = 34.0
 SAMPLING FREQUENCY = 298.24 Hz.
 REDUCED FREQUENCY = 0.101
 AMPLITUDE = 8.00

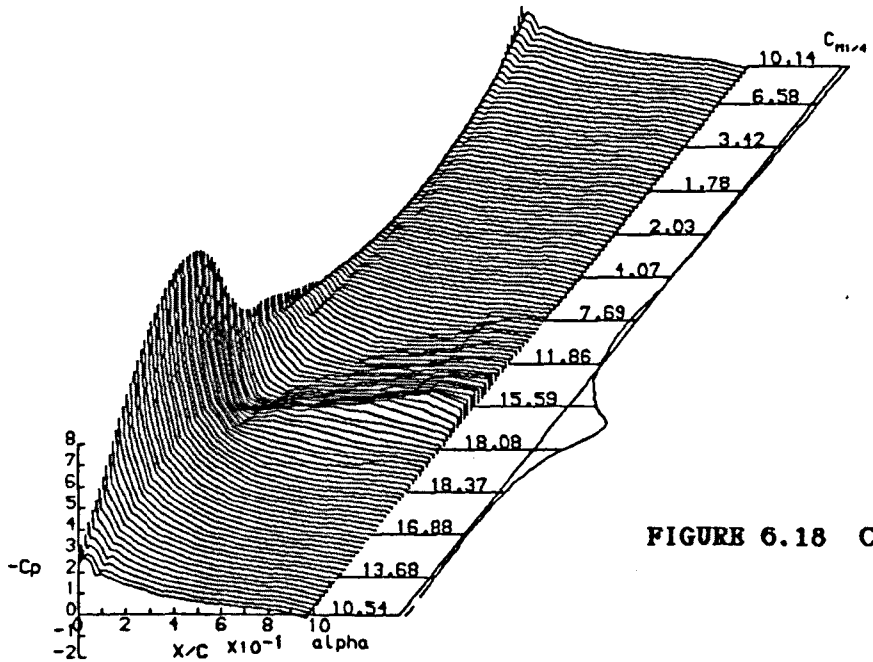
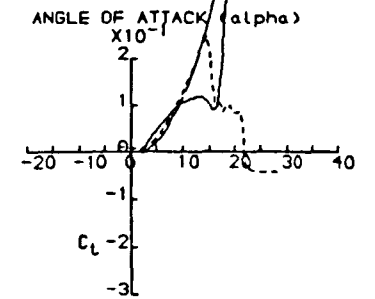
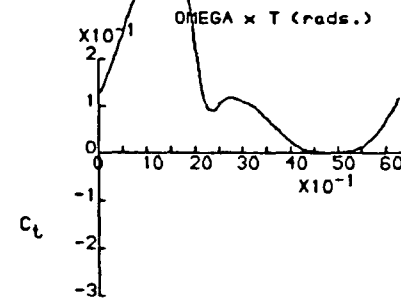
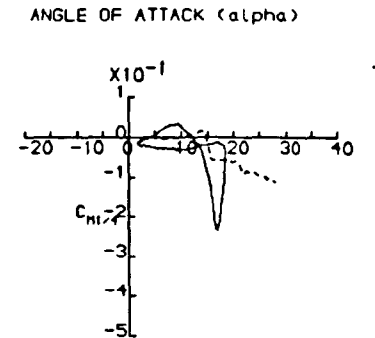
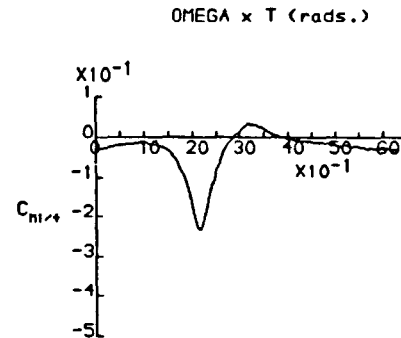
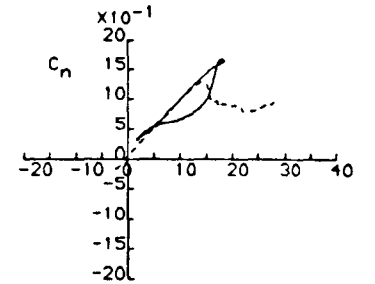
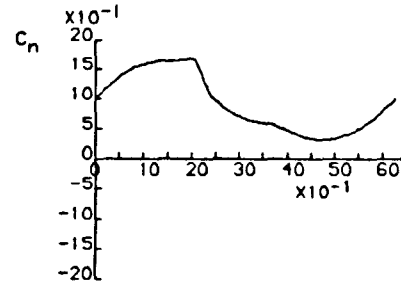
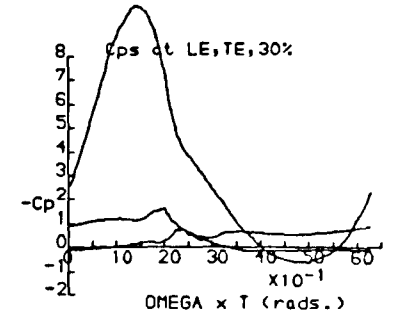
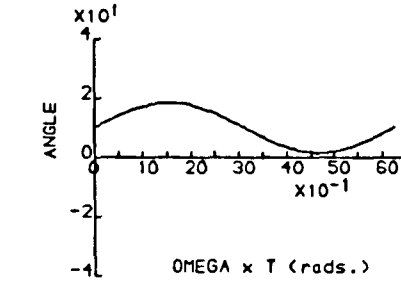


FIGURE 6.18 Continued.



DYNAMIC CHARACTERISTICS FOR THE NACA 23012 MODEL01

RUN REFERENCE NUMBER: 13691

DATE OF TEST: 16/ 6/83

REYNOLDS NUMBER = 1491800.

MACH NUMBER = 0.110

DYNAMIC PRESSURE = 978.68 N/sq. M

AIR TEMPERATURE = 35.0

NUMBER OF CYCLES = 10

SAMPLING FREQUENCY = 298.24 Hz.

MOTION TYPE: SINUSOIDAL

REDUCED FREQUENCY = 0.104

MEAN ANGLE = 12.00

AMPLITUDE = 8.00

OSCILLATION FREQUENCY = 2.330Hz.

AVERAGED DATA OF 10 CYCLES

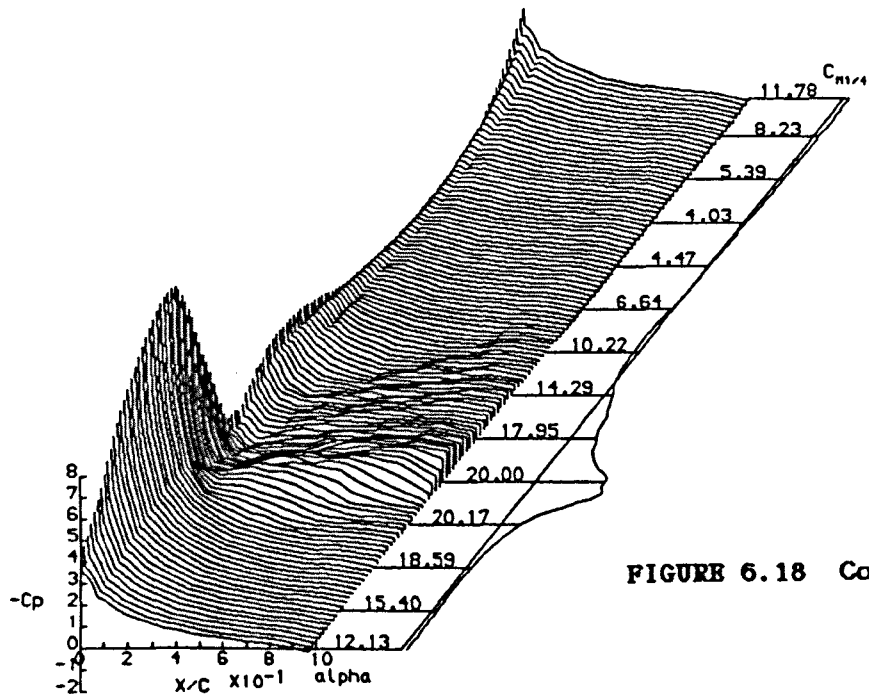
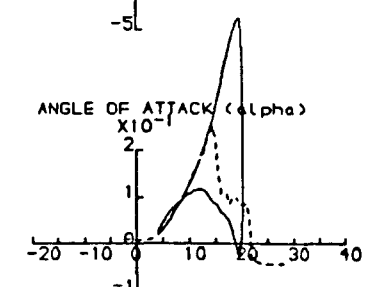
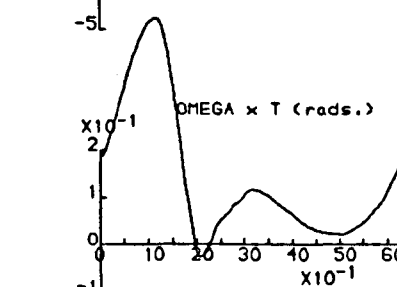
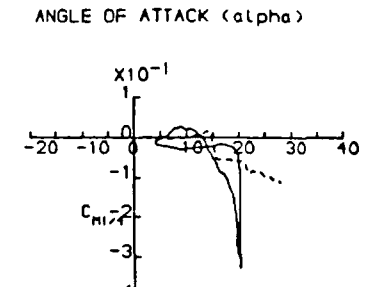
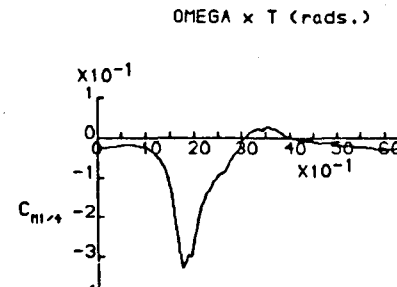
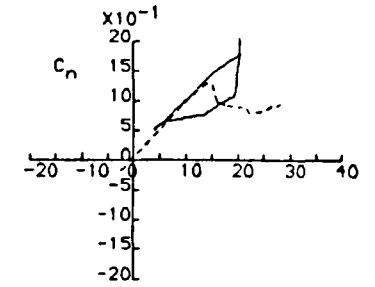
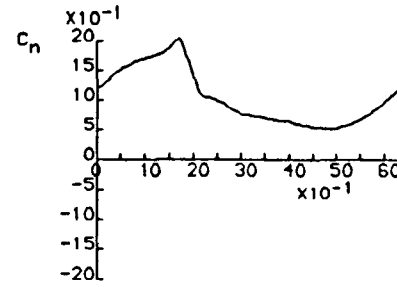
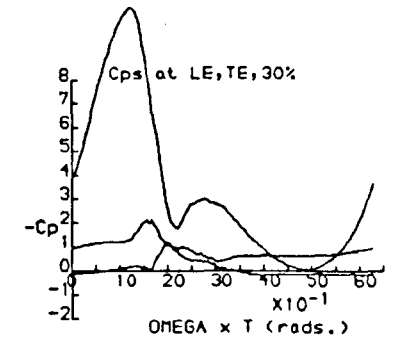
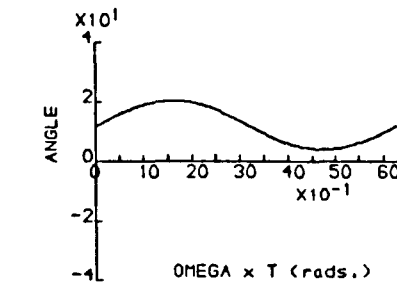


FIGURE 6.18 Continued.



DYNAMIC CHARACTERISTICS FOR THE NACA 23012 MODEL01

RUN REFERENCE NUMBER: 13791

DATE OF TEST: 17/ 6/83

REYNOLDS NUMBER = 1509850.

MACH NUMBER = 0.111

DYNAMIC PRESSURE = 973.07 N/sq. M

AIR TEMPERATURE = 30.5

NUMBER OF CYCLES = 10

SAMPLING FREQUENCY = 298.24 Hz.

MOTION TYPE: SINUSOIDAL

REDUCED FREQUENCY = 0.104

MEAN ANGLE = 14.00

AMPLITUDE = 8.00

OSCILLATION FREQUENCY = 2.330Hz.

AVERAGED DATA OF 10 CYCLES

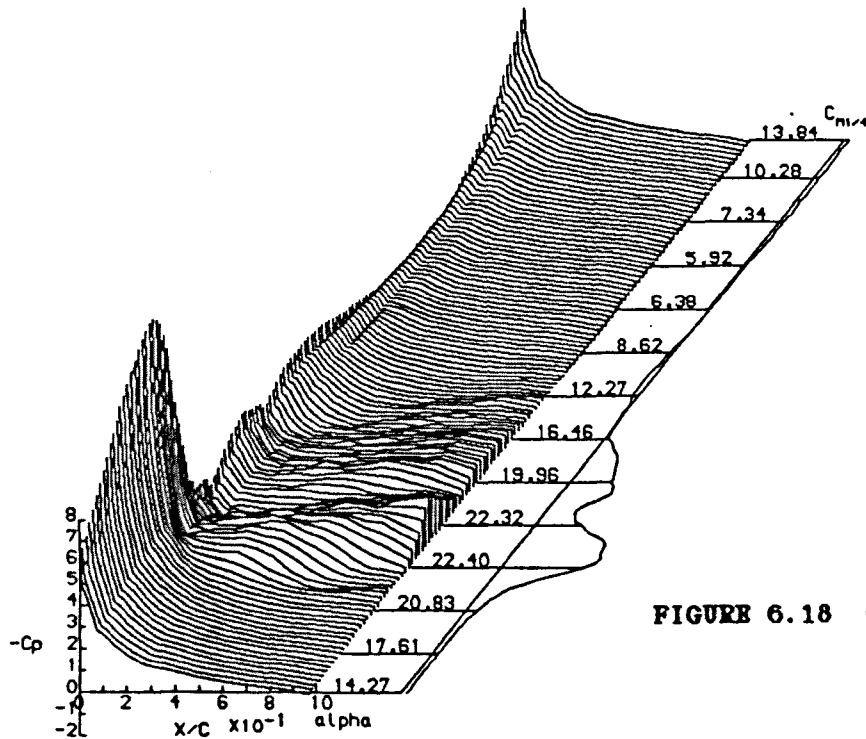
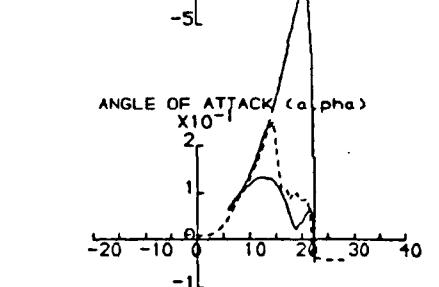
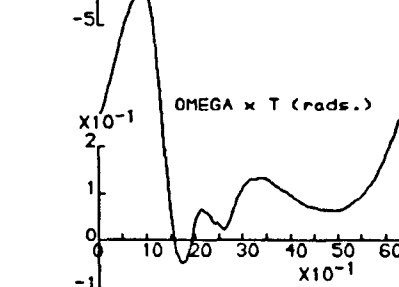
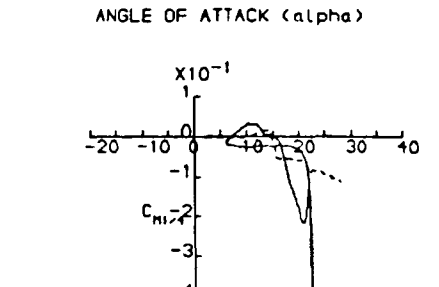
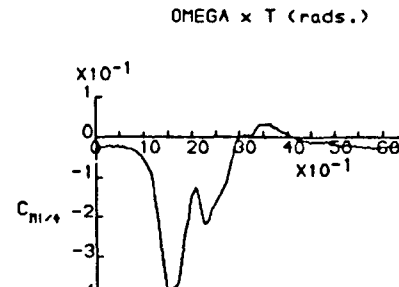
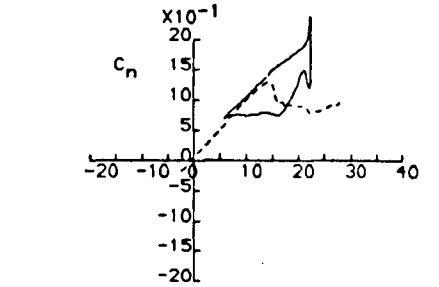
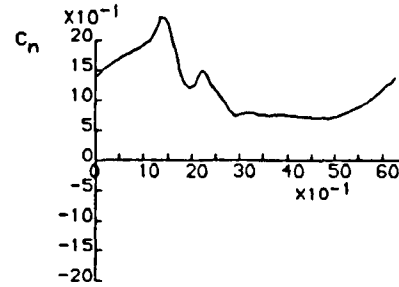
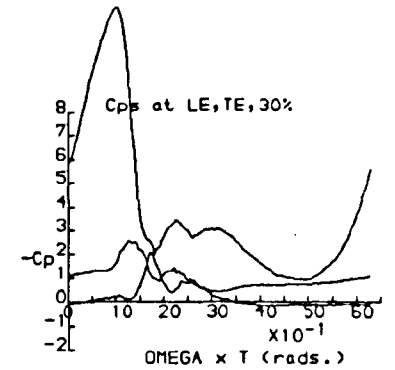
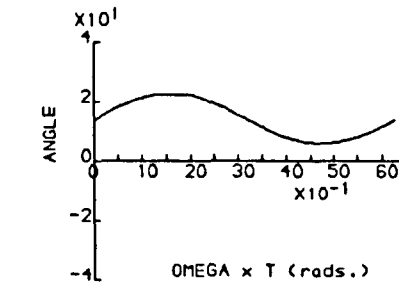


FIGURE 6.18 Continued.



DYNAMIC CHARACTERISTICS FOR THE NACA 23012 MODEL 01

RUN REFERENCE NUMBER: 13891
 REYNOLDS NUMBER = 1520761.
 DYNAMIC PRESSURE = 1000.76 N/sq. M
 NUMBER OF CYCLES = 10
 MOTION TYPE: SINUSOIDAL
 MEAN ANGLE = 16.00
 OSCILLATION FREQUENCY = 2.330Hz.
 AVERAGED DATA OF 10 CYCLES

DATE OF TEST: 17/ 6/83
 MACH NUMBER = 0.112
 AIR TEMPERATURE = 33.0
 SAMPLING FREQUENCY = 298.24 Hz.
 REDUCED FREQUENCY = 0.103
 AMPLITUDE = 8.00

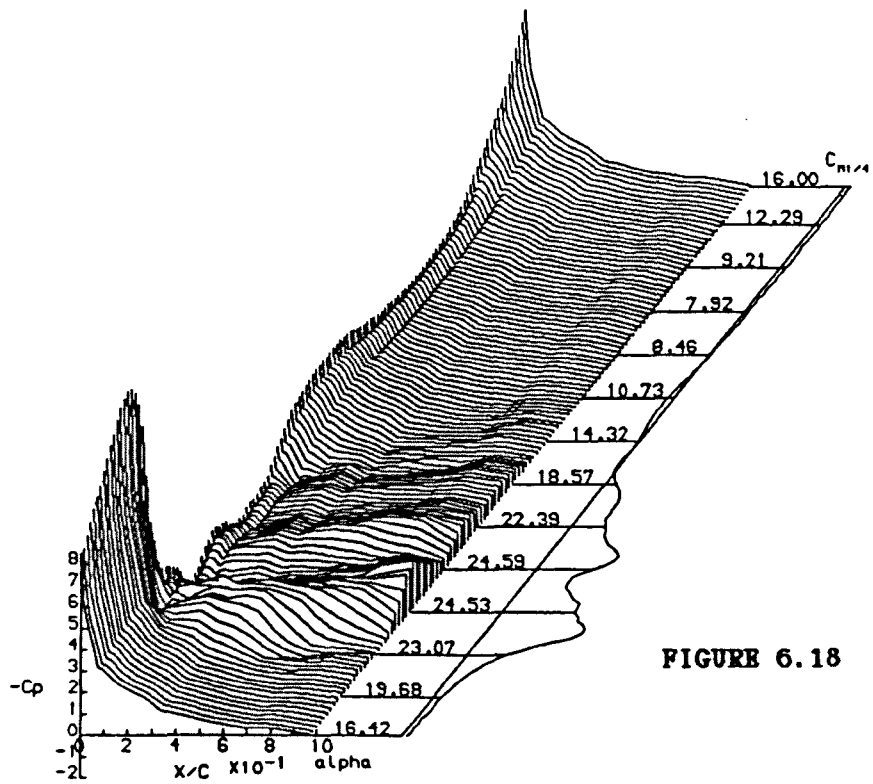
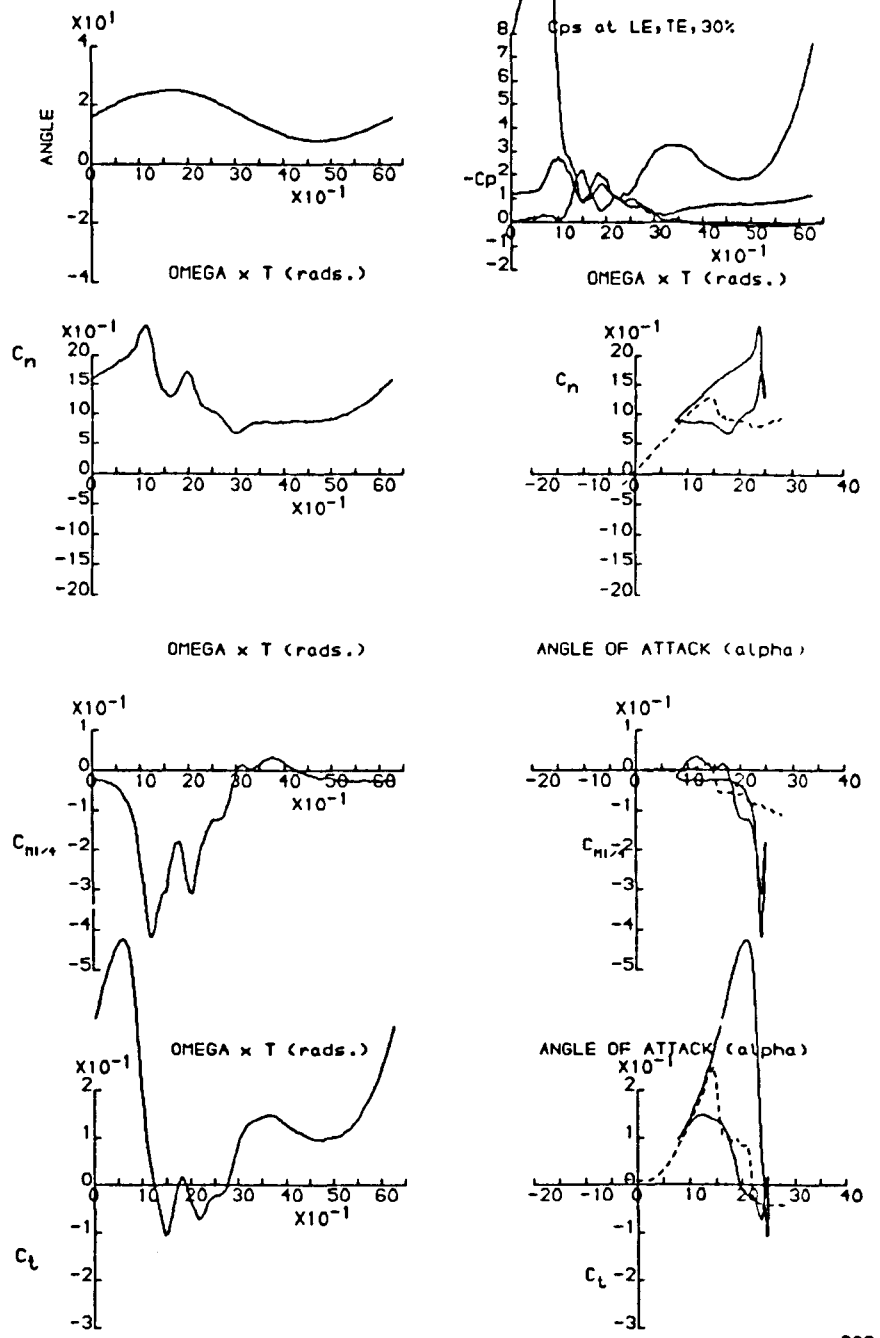


FIGURE 6.18 Completed.



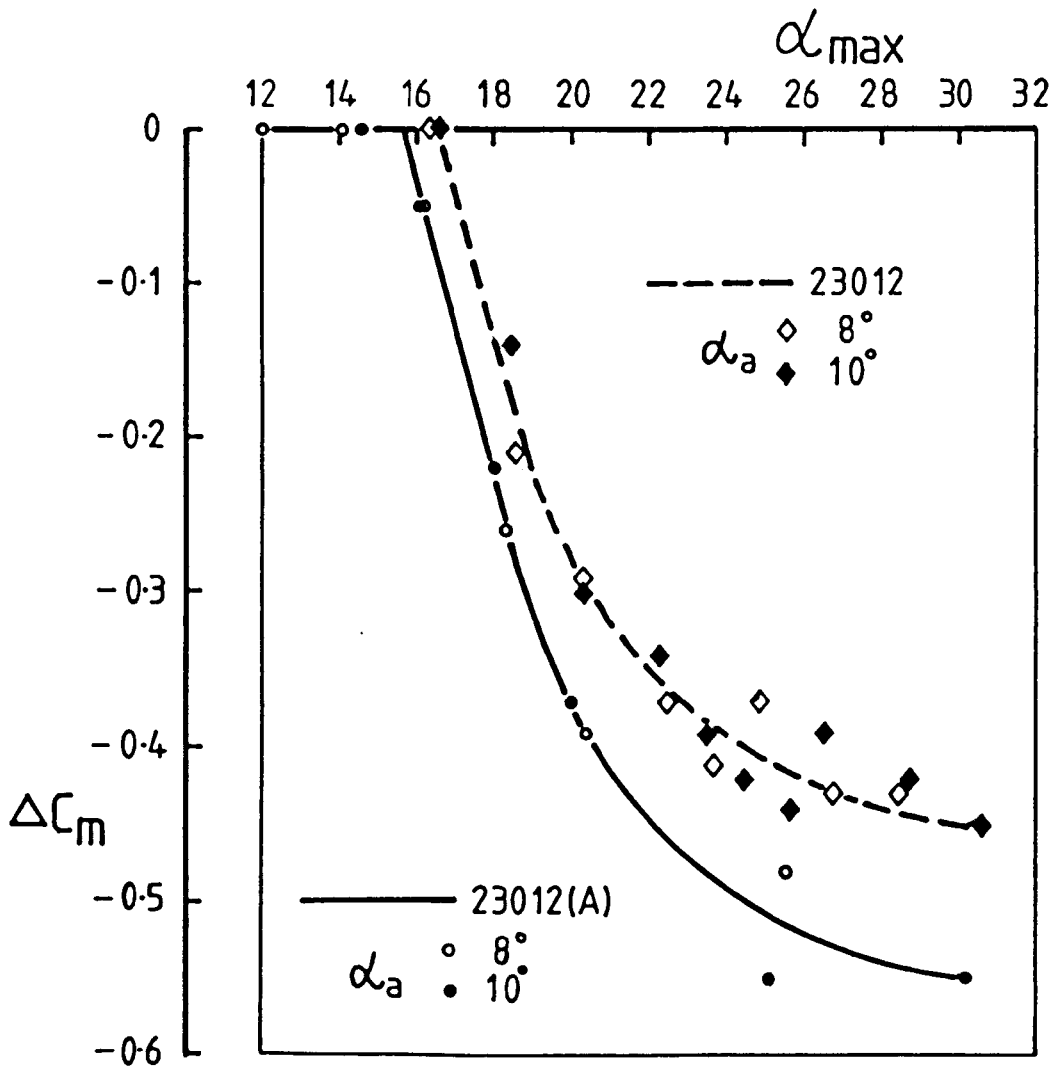
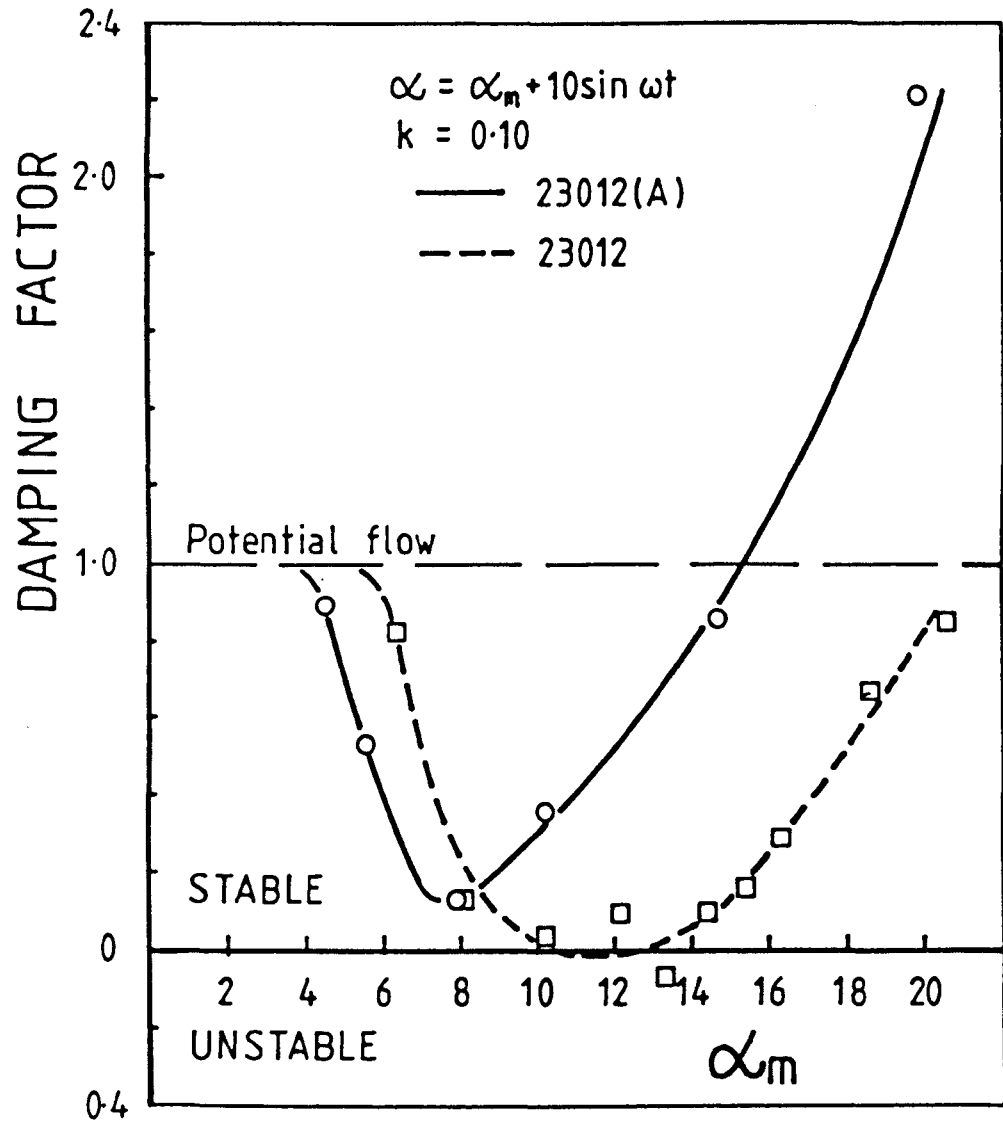
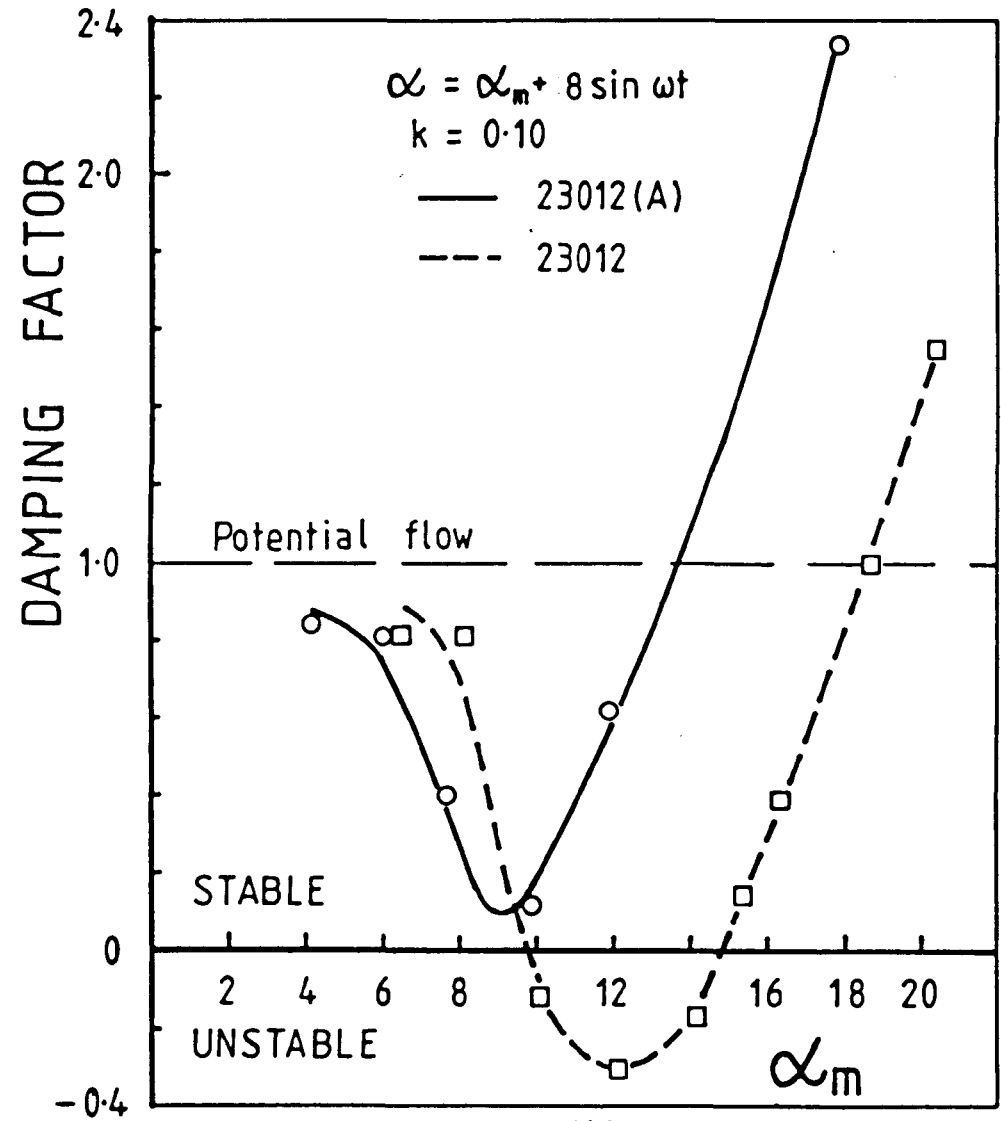


FIGURE 6.19 Critical Angle Calculation obtained for the WACA 23012 and 23012(A) Aerofoils at $\alpha = \alpha_m \pm 8 \sin \omega t$ and $\alpha = \alpha_m \pm 10 \sin \omega t$ at $k = 0.10$ (see Figures 6.17 and 6.18).



(a)



(b)

FIGURE 6.20 Variation of Damping Factor with Amplitude at 1.5×10^6 Reynolds number.

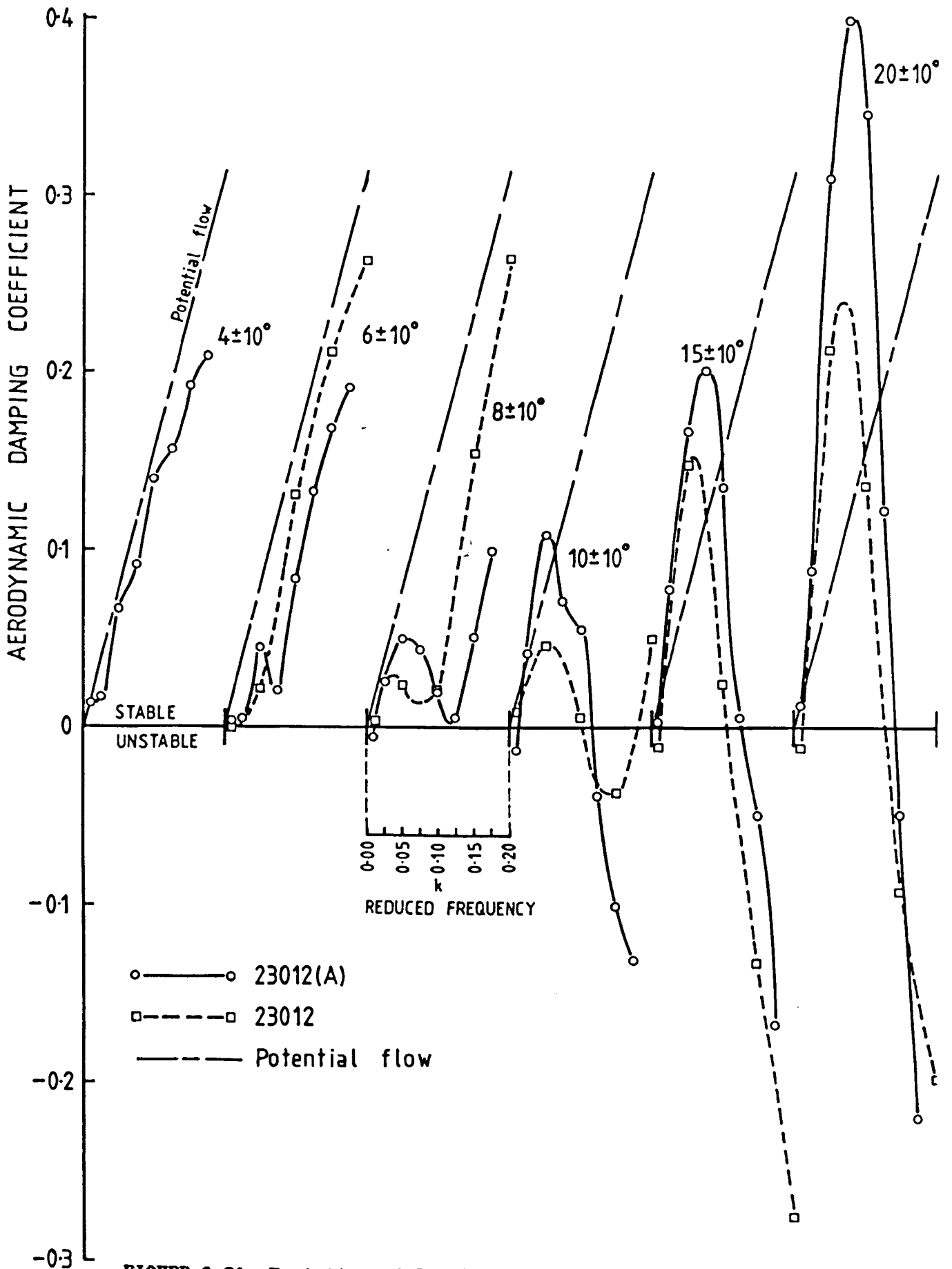


FIGURE 6.21 Variation of Damping Coefficient with Reduced Frequency at 1.5×10^6 Reynolds number.

DYNAMIC CHARACTERISTICS FOR THE NACA23012A MODEL02

RUN REFERENCE NUMBER: 20031 DATE OF TEST: 25/2/86
 REYNOLDS NUMBER = 1503912. MACH NUMBER = 0.110
 DYNAMIC PRESSURE = 965.29 Nm⁻² AIR TEMPERATURE = 30.0°C
 NUMBER OF CYCLES = 5 SAMPLING FREQUENCY = 7.33 Hz.
 MOTION TYPE: RAMP UP REDUCED PITCH RATE = 0.00040
 START ANGLE = -1.00° LINEAR PITCH RATE = 2.91°S⁻¹
 RAMP ARC = 41.000°
 AVERAGED DATA OF 5 CYCLES

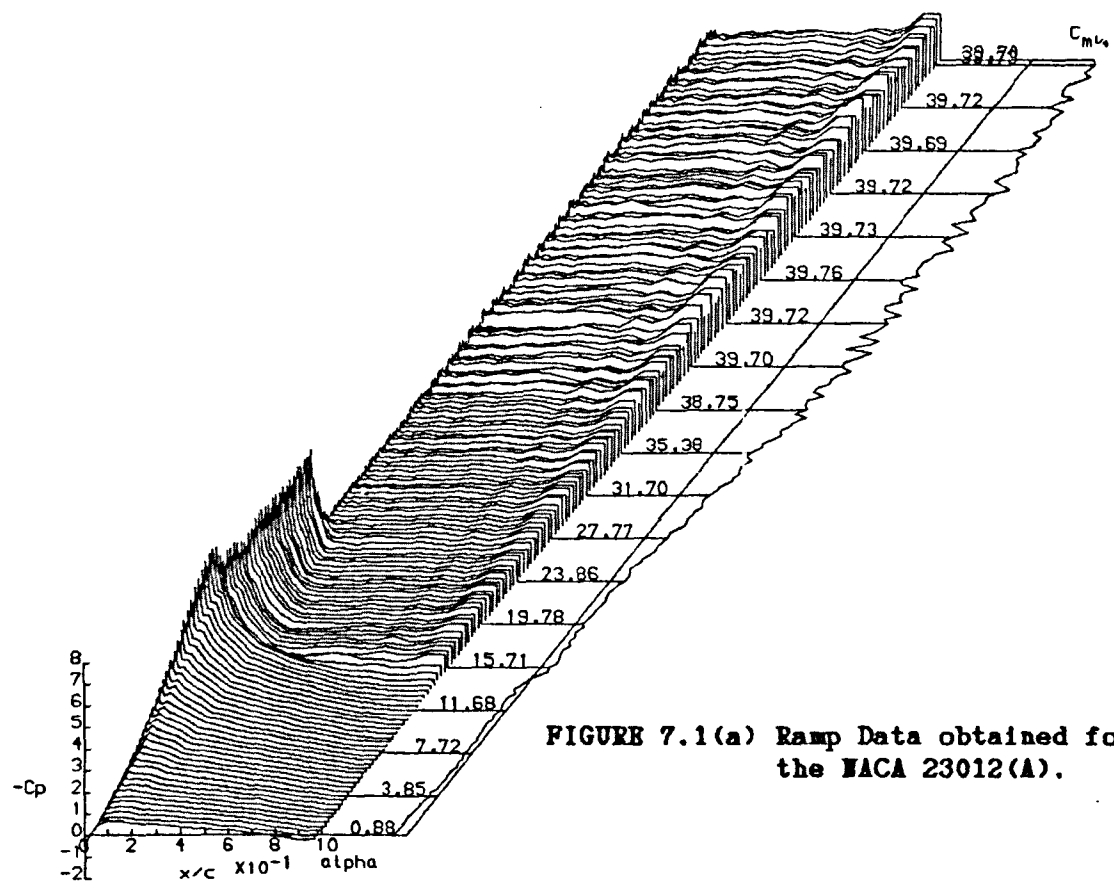
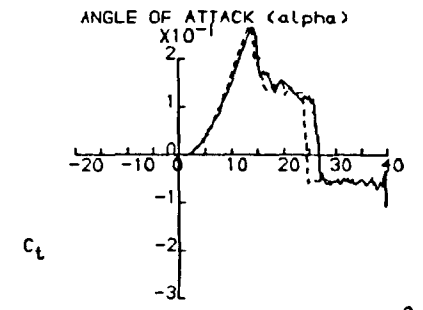
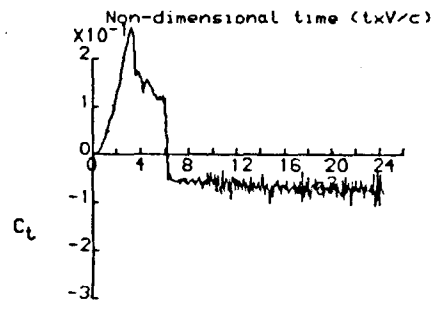
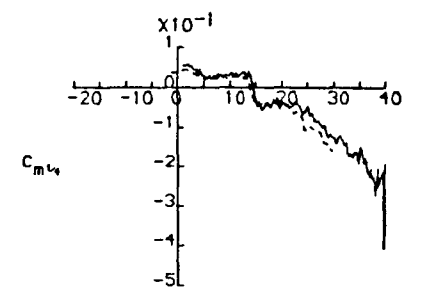
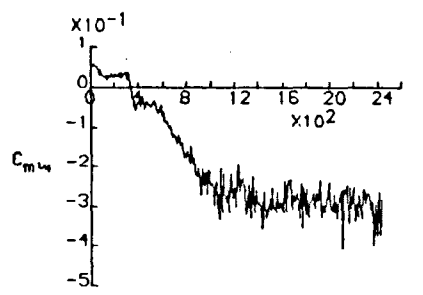
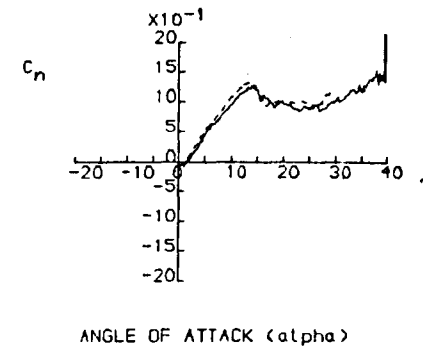
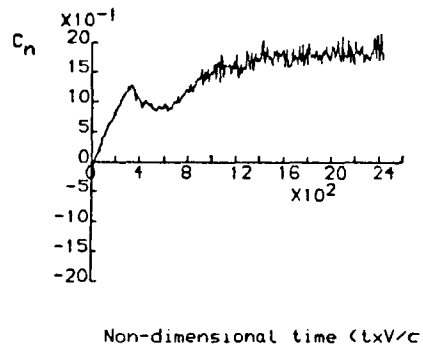
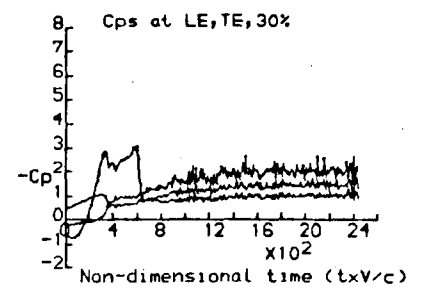
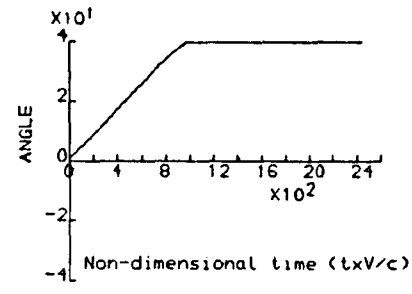


FIGURE 7.1(a) Ramp Data obtained for the NACA 23012(A).



DYNAMIC CHARACTERISTICS FOR THE NACA23012A MODEL02

RUN REFERENCE NUMBER: 20081
 REYNOLDS NUMBER = 1509525.
 DYNAMIC PRESSURE = 972.50 Nm⁻²
 NUMBER OF CYCLES = 5
 MOTION TYPE: RAMP UP
 START ANGLE = -1.00°
 RAMP ARC = 41.000°
 AVERAGED DATA OF 5 CYCLES

DATE OF TEST: 28/2/86
 MACH NUMBER = 0.111
 AIR TEMPERATURE = 30.0°C
 SAMPLING FREQUENCY = 73.38 Hz.
 REDUCED PITCH RATE = 0.00370
 LINEAR PITCH RATE = 30.01°S⁻¹

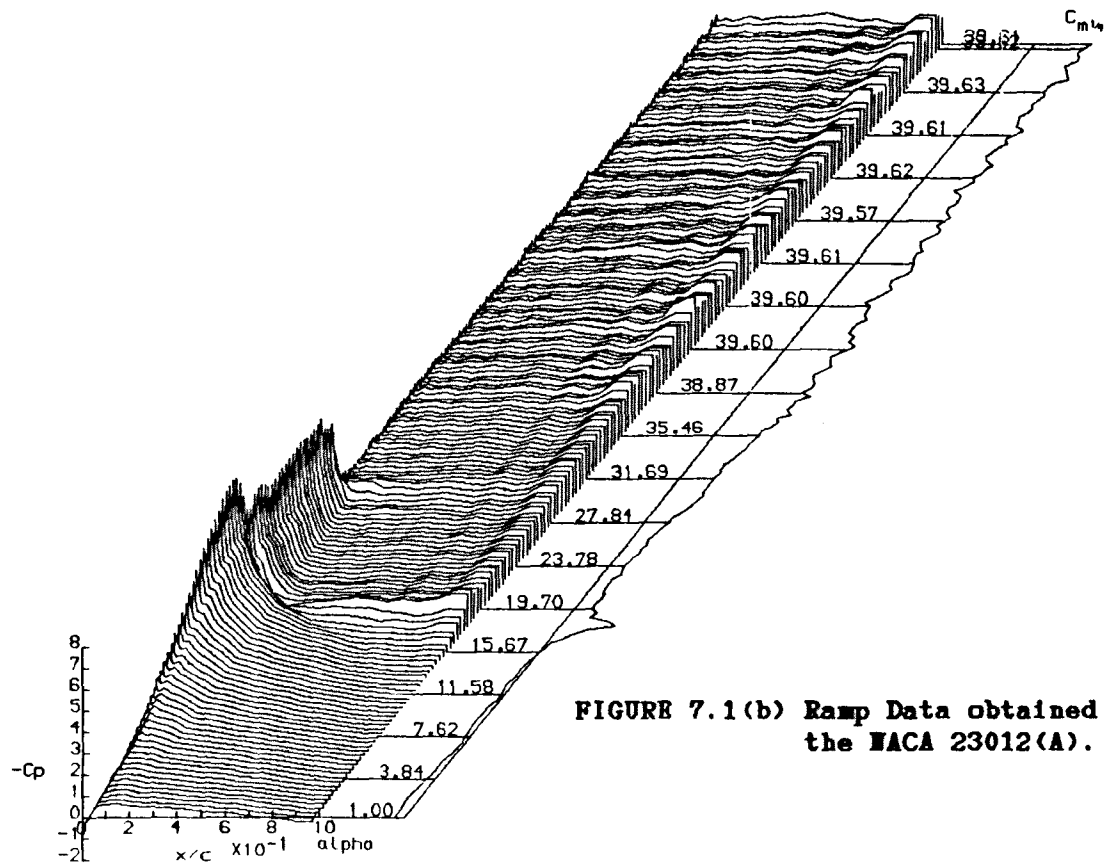
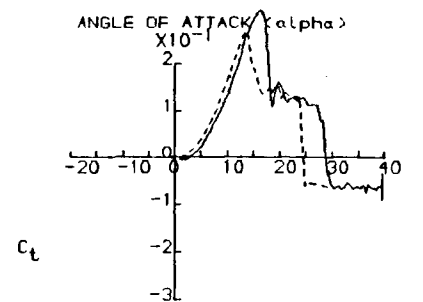
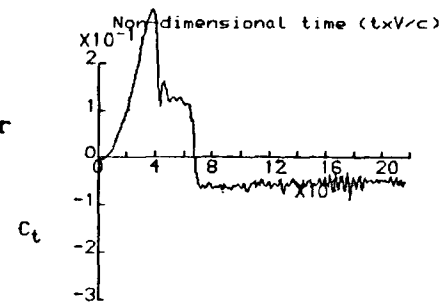
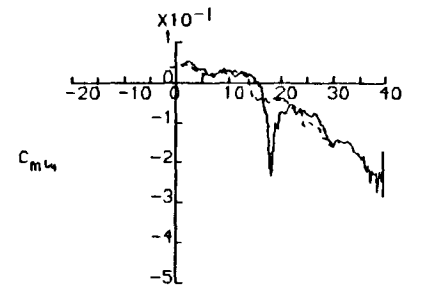
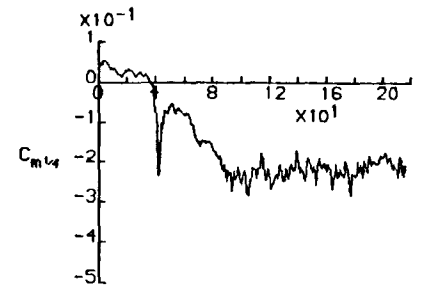
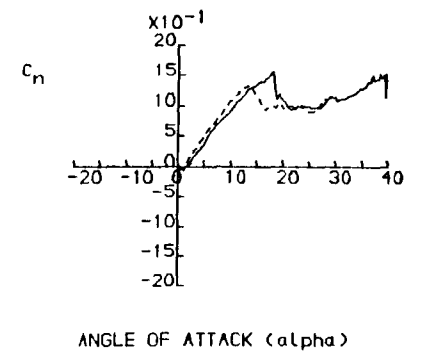
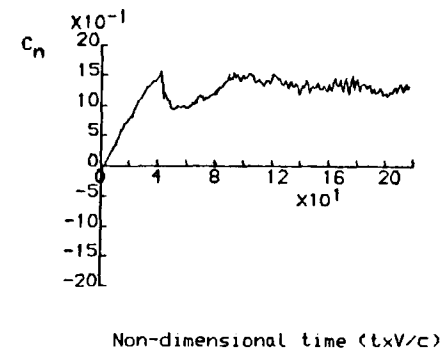
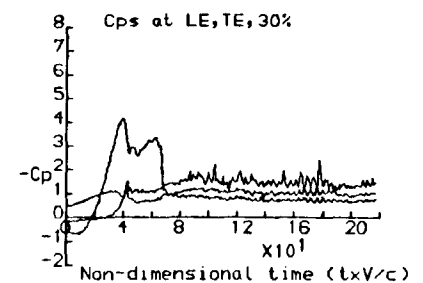
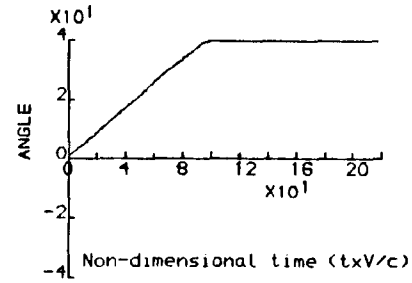


FIGURE 7.1(b) Ramp Data obtained for the NACA 23012(A).



DYNAMIC CHARACTERISTICS FOR THE NACA23012A MODEL02

RUN REFERENCE NUMBER: 20171

DATE OF TEST: 28/2/86

REYNOLDS NUMBER = 1531268.

MACH NUMBER = 0.112

DYNAMIC PRESSURE = 1000.72 Nm⁻²

AIR TEMPERATURE = 30.0°C

NUMBER OF CYCLES = 5

SAMPLING FREQUENCY = 403.55 Hz.

MOTION TYPE: RAMP UP

REDUCED PITCH RATE = 0.01950

START ANGLE = -1.00°

LINEAR PITCH RATE = 159.64°S⁻¹

RAMP ARC = 41.000°

AVERAGED DATA OF 5 CYCLES

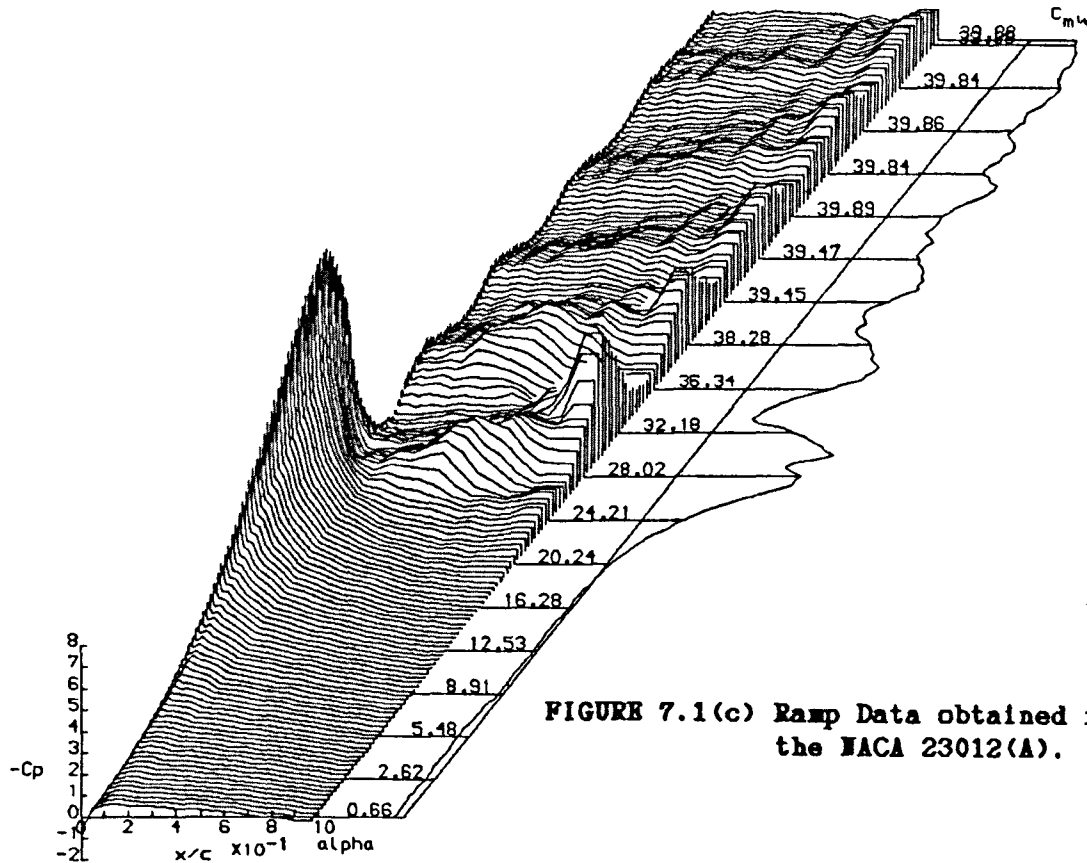
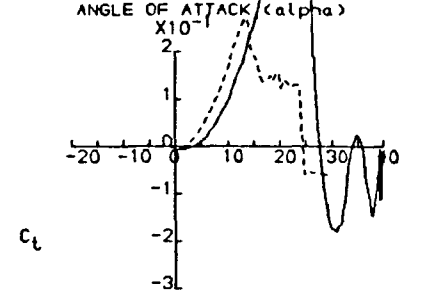
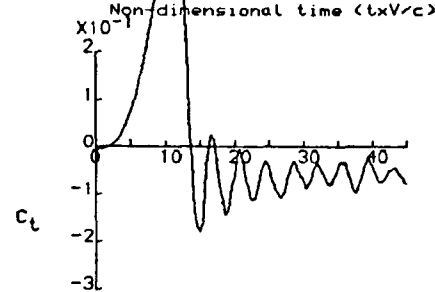
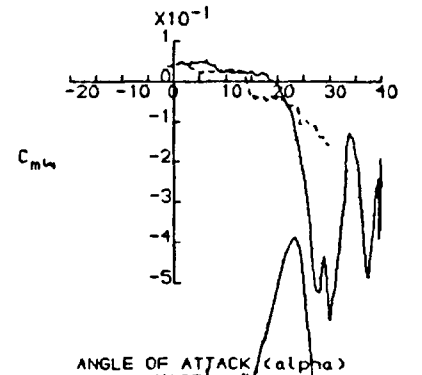
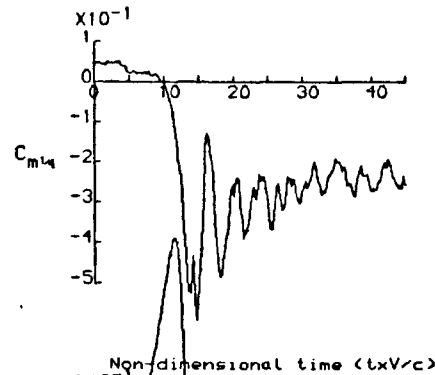
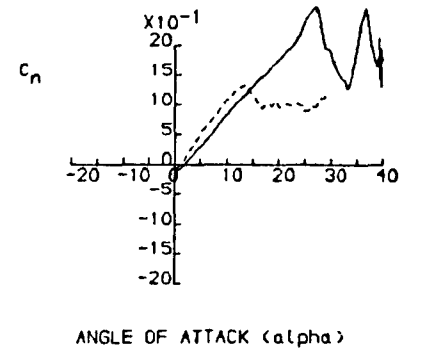
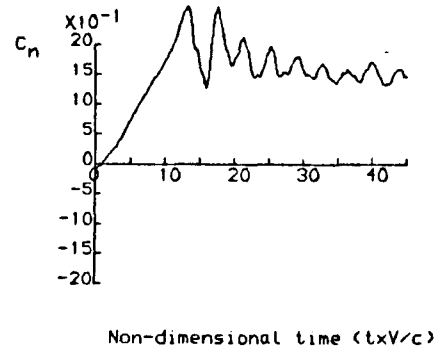
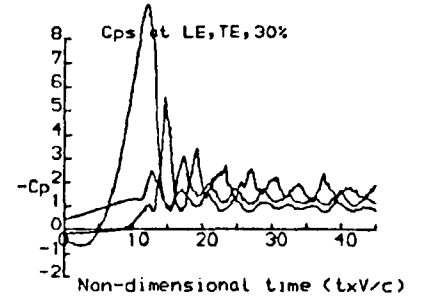
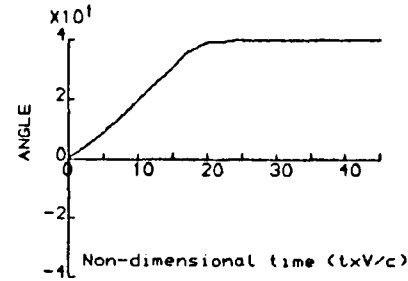


FIGURE 7.1(c) Ramp Data obtained for the NACA 23012(A).



DYNAMIC CHARACTERISTICS FOR THE NACA 23012 MODEL01

RUN REFERENCE NUMBER: 20321

DATE OF TEST: 23/5/84

REYNOLDS NUMBER = 1508968.

MACH NUMBER = 0.112

DYNAMIC PRESSURE = 977.49 Nm⁻²

AIR TEMPERATURE = 28.0°C

NUMBER OF CYCLES = 5

SAMPLING FREQUENCY = 9.78 Hz.

MOTION TYPE: RAMP UP

REDUCED PITCH RATE = 0.00029

START ANGLE = -1.00°

LINEAR PITCH RATE = 2.39°s⁻¹

RAMP ARC = 31.000°

AVERAGED DATA OF 5 CYCLES

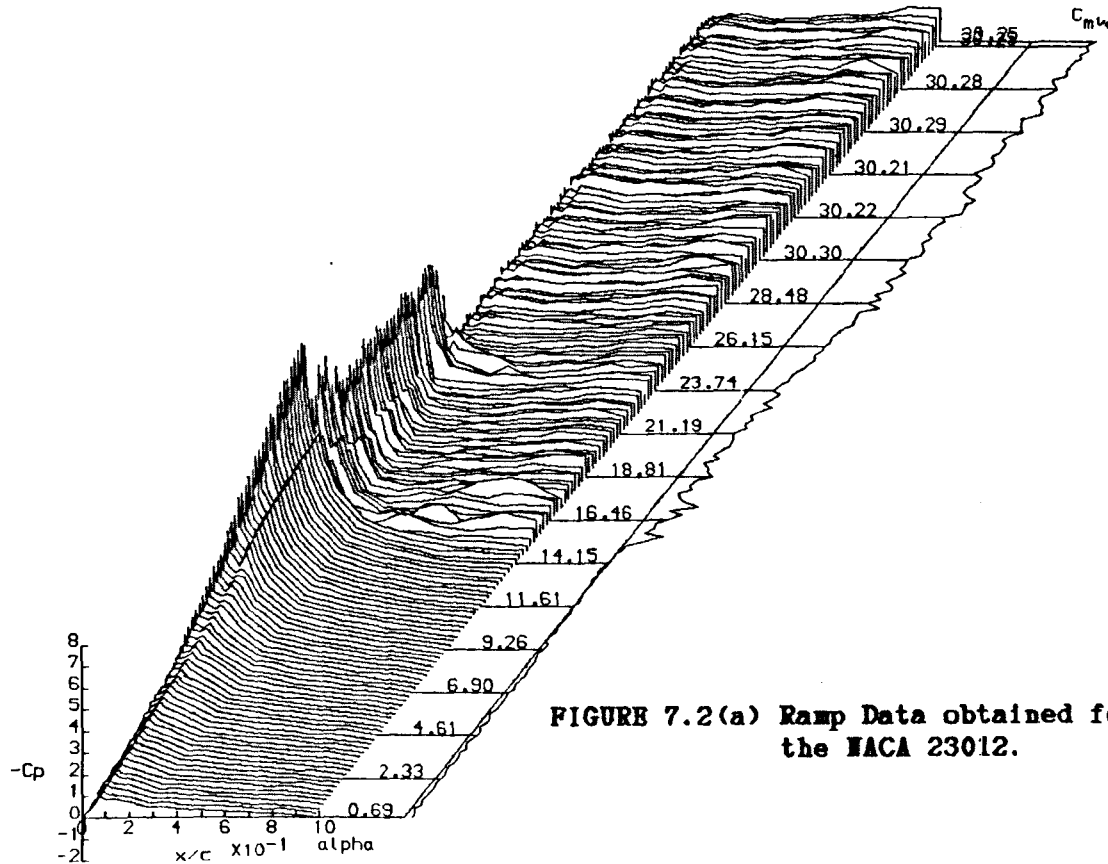
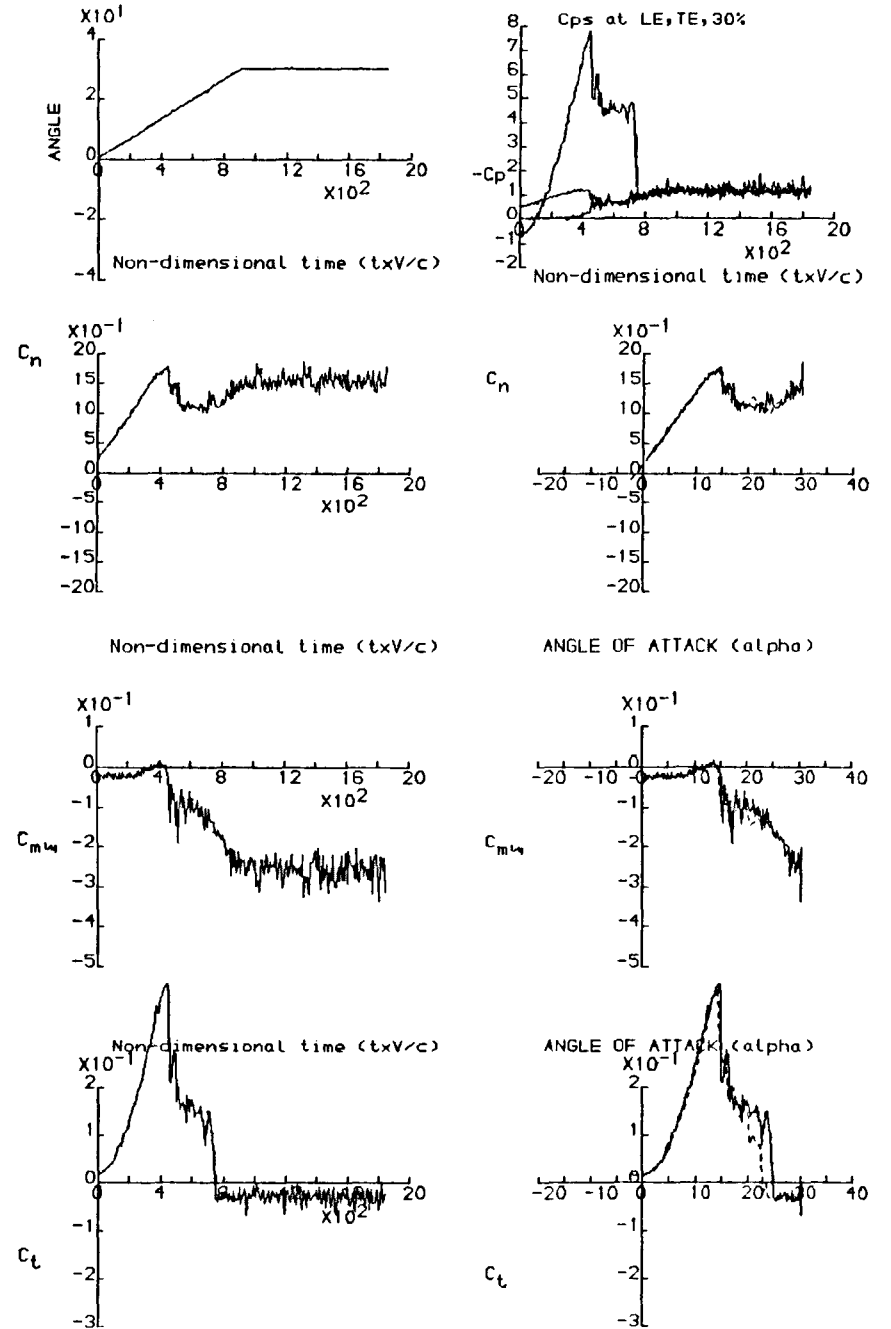


FIGURE 7.2(a) Ramp Data obtained for the NACA 23012.



DYNAMIC CHARACTERISTICS FOR THE NACA 23012 MODEL 01

RUN REFERENCE NUMBER: 20371

REYNOLDS NUMBER = 1537479.

DYNAMIC PRESSURE = 1020.41 Nm⁻²

NUMBER OF CYCLES = 5

MOTION TYPE: RAMP UP

START ANGLE = -1.00°

RAMP ARC = 40.000°

AVERAGED DATA OF 5 CYCLES

DATE OF TEST: 24/5/84

MACH NUMBER = 0.115

AIR TEMPERATURE = 29.0°C

SAMPLING FREQUENCY = 97.84 Hz.

REDUCED PITCH RATE = 0.00378

LINEAR PITCH RATE = 31.52°s⁻¹

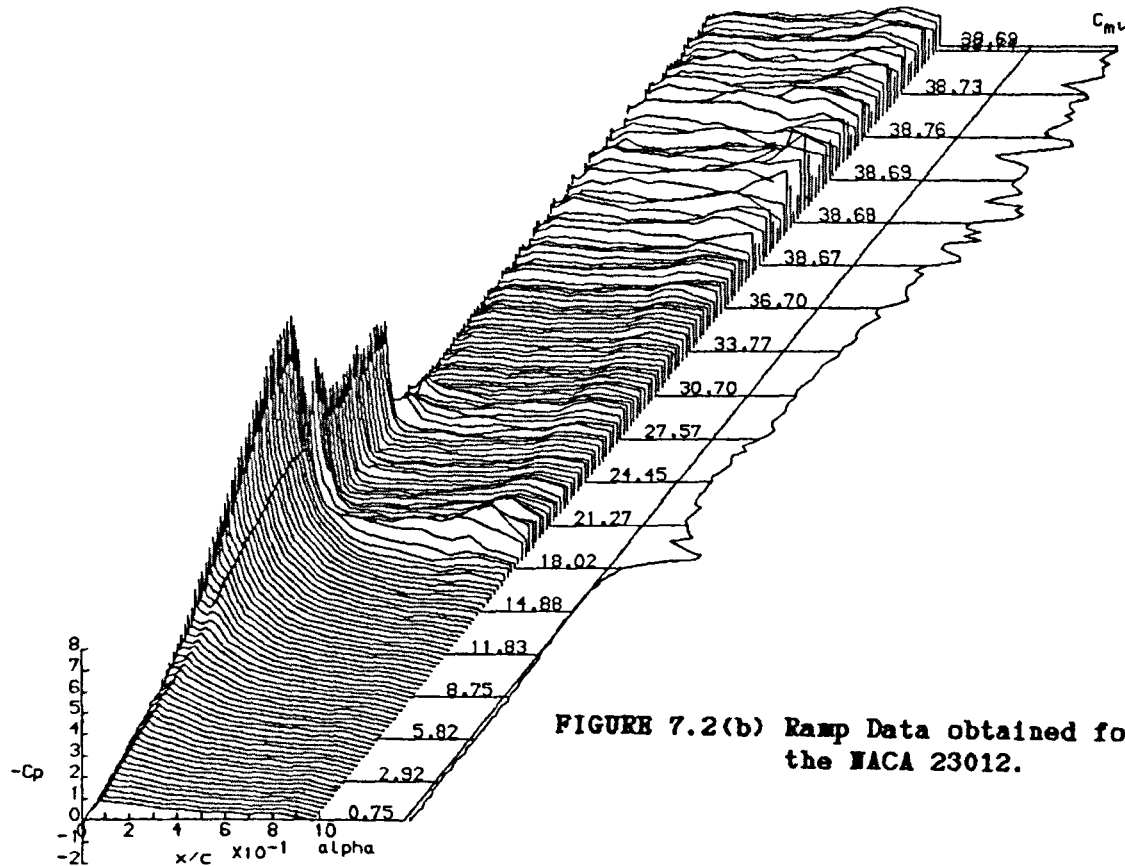
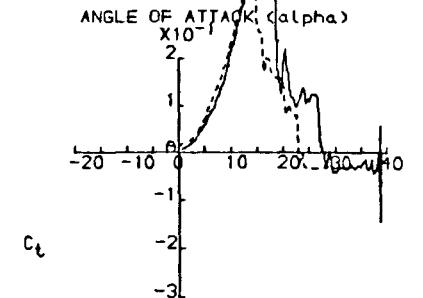
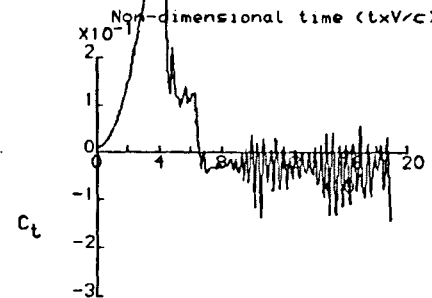
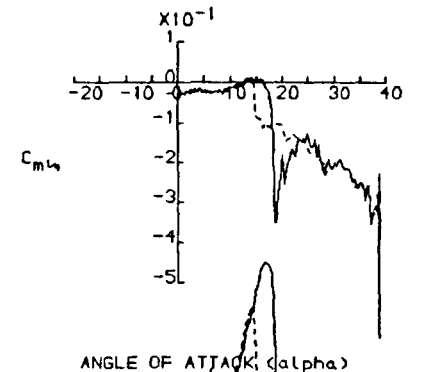
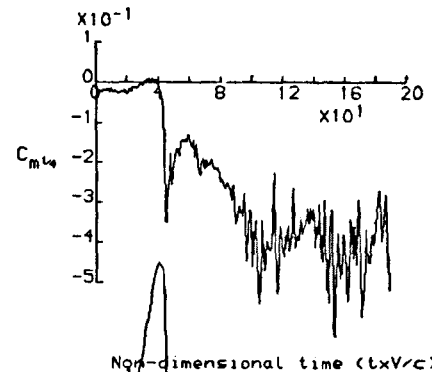
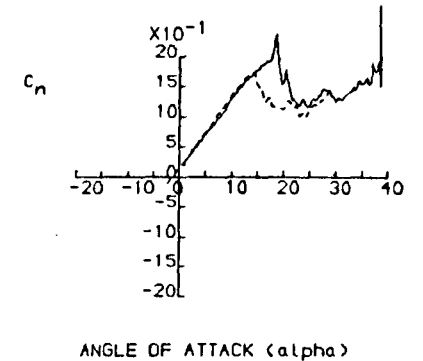
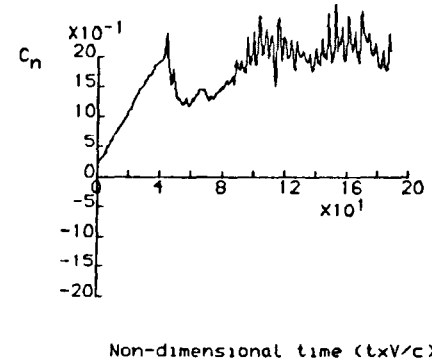
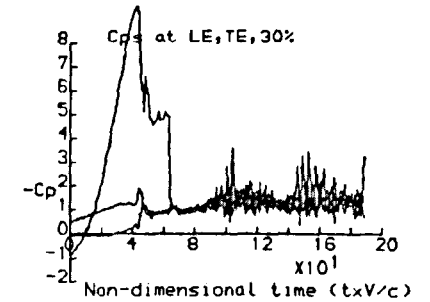
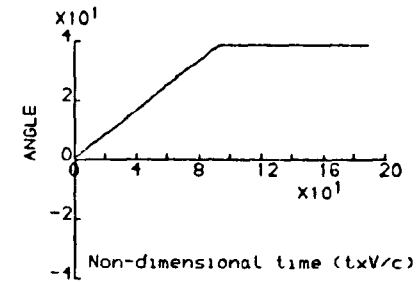


FIGURE 7.2(b) Ramp Data obtained for the NACA 23012.



DYNAMIC CHARACTERISTICS FOR THE NACA 23012 MODEL01

RUN REFERENCE NUMBER: 20451

DATE OF TEST: 24/5/84

REYNOLDS NUMBER = 1510862.

MACH NUMBER = 0.113

DYNAMIC PRESSURE = 985.38 Nm⁻²

AIR TEMPERATURE = 29.0°C

NUMBER OF CYCLES = 5

SAMPLING FREQUENCY = 489.24 Hz.

MOTION TYPE: RAMP UP

REDUCED PITCH RATE = 0.01842

START ANGLE = -1.00°

LINEAR PITCH RATE = 151.01°S⁻¹

RAMP ARC = 40.000°

AVERAGED DATA OF 5 CYCLES

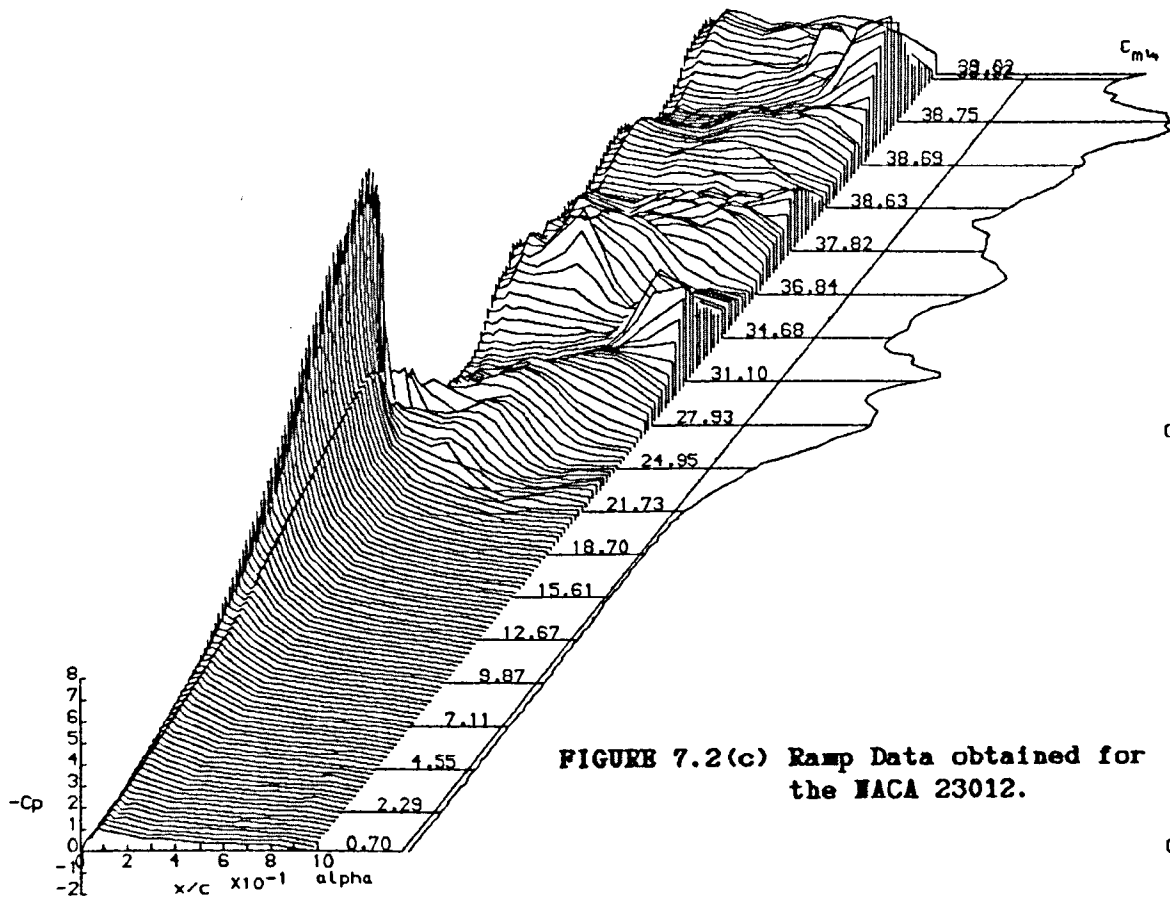
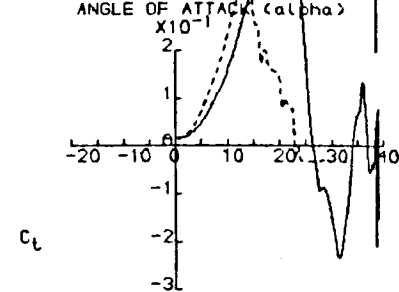
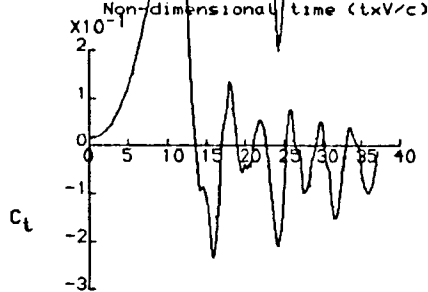
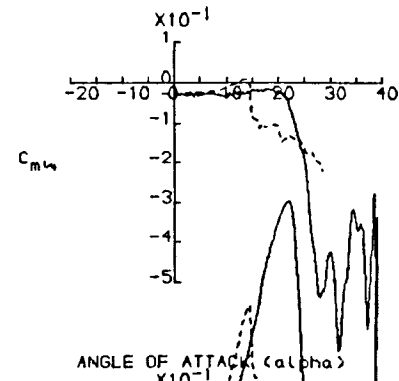
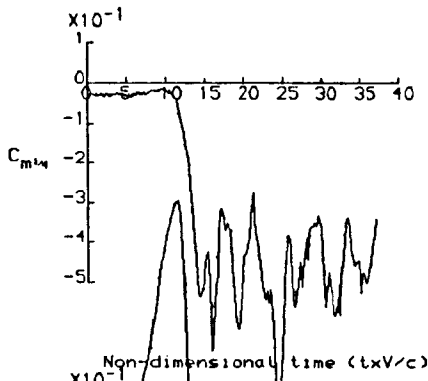
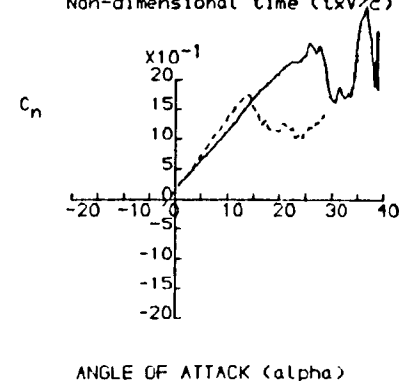
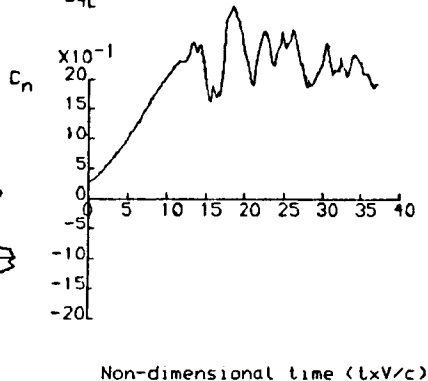
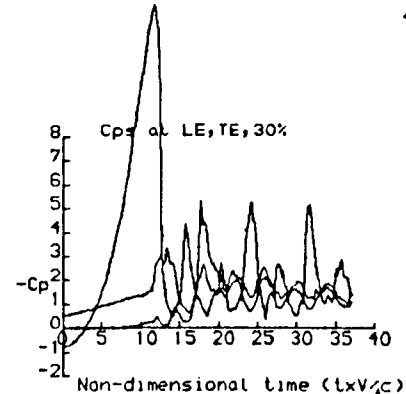
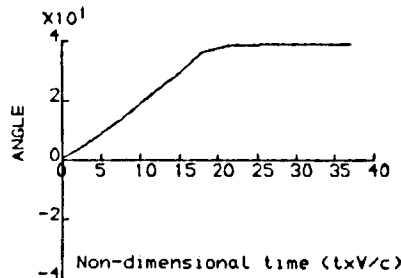


FIGURE 7.2(c) Ramp Data obtained for the NACA 23012.



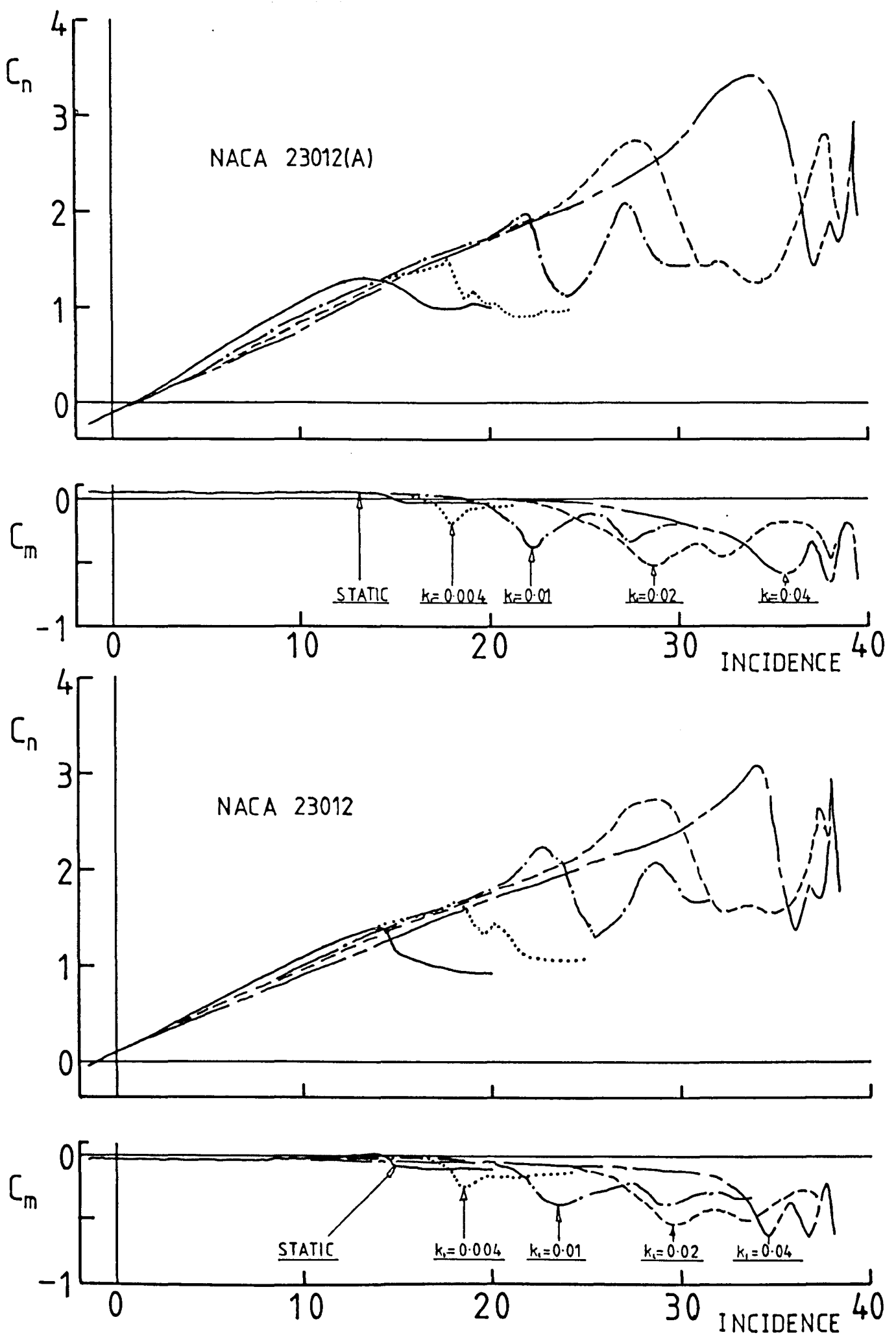


FIGURE 7.3 Effect of Pitch Rate on the Normal Force and Pitching Moment Coefficient obtained at 1.5×10^6 Reynolds number.

UNSTEADY PRESSURE/TIME DISTRIBUTION - UPPER SURFACE

RUN REFERENCE NUMBER: 20161
 REYNOLDS NUMBER = 1514126.
 DYNAMIC PRESSURE = 978.44 N/sq. M
 NUMBER OF CYCLES = 5
 MOTION TYPE: RAMP UP

DATE OF TEST: 28/ 2/86
 MACH NUMBER = 0.111
 AIR TEMPERATURE = 30.0
 SAMPLING FREQUENCY = 366.84 Hz.
 REDUCED PITCH RATE = 0.02
 LINEAR PITCH RATE = 146.43 DEG./SEC.

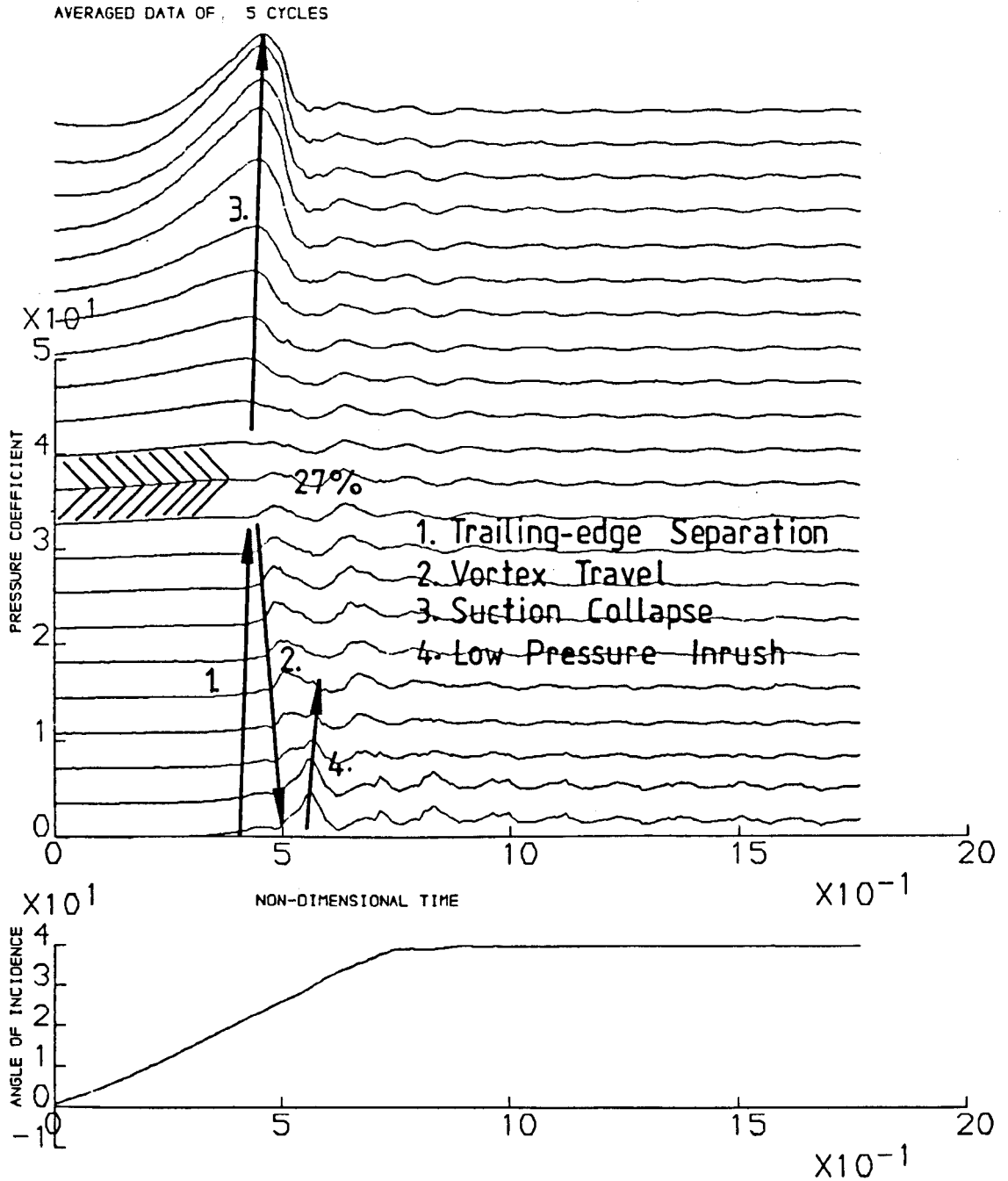


FIGURE 7.4 Unsteady Stall Categorisation of the NACA 23012(A) via Pressure Time Histories.

UNSTEADY PRESSURE/TIME DISTRIBUTION - UPPER SURFACE

RUN REFERENCE NUMBER: 20451

DATE OF TEST: 24/ 5/84

REYNOLDS NUMBER = 1510862.

MACH NUMBER = 0.113

DYNAMIC PRESSURE = 985.38 N/sq. M

AIR TEMPERATURE = 29.0

NUMBER OF CYCLES = 5

SAMPLING FREQUENCY = 489.24 Hz.

MOTION TYPE: RAMP UP

REDUCED PITCH RATE = 0.02

LINEAR PITCH RATE = 151.01 DEG./SEC.

AVERAGED DATA OF 5 CYCLES

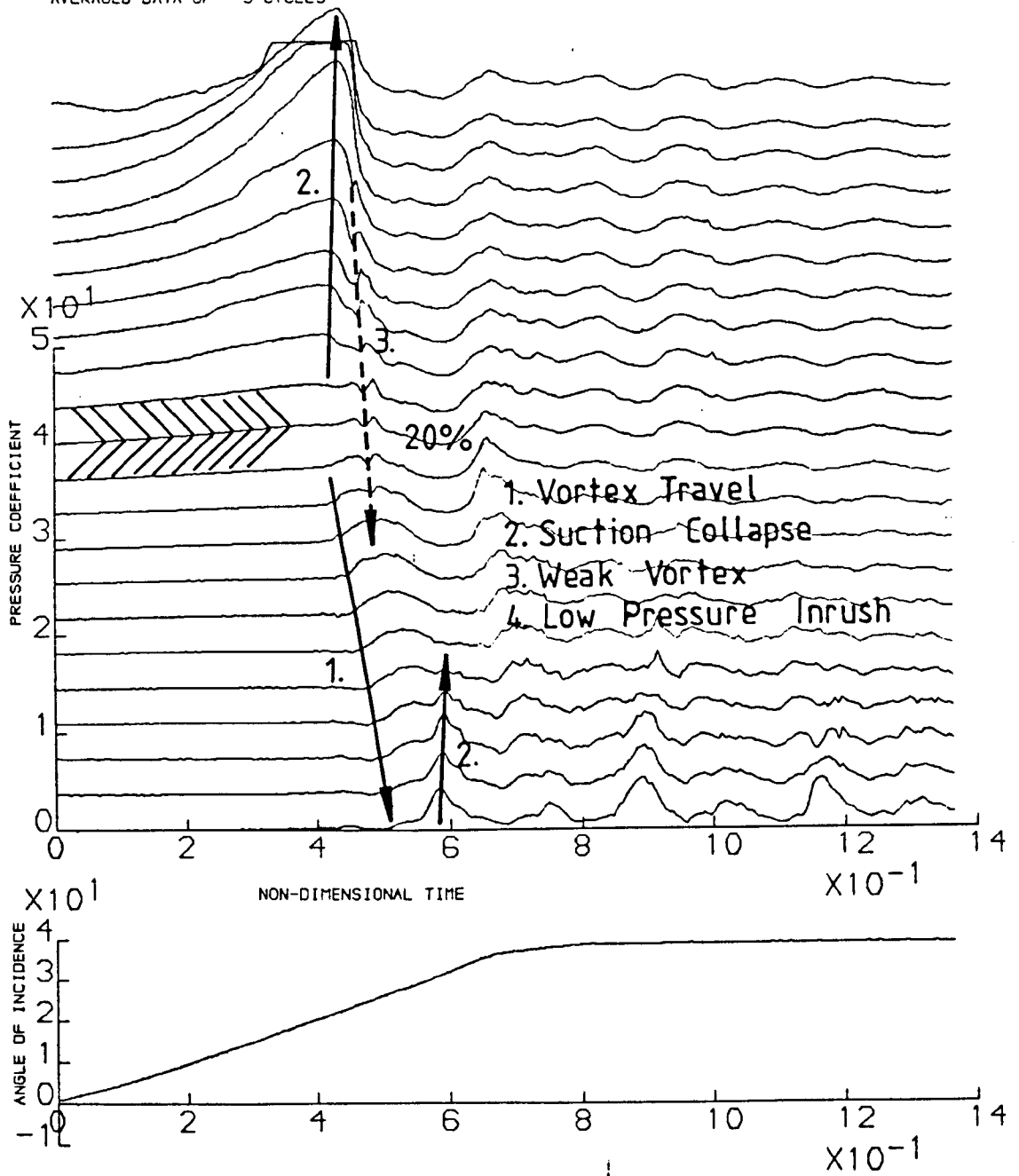


FIGURE 7.5 Unsteady Stall Categorisation of the NACA 23012 via Pressure Time Histories.

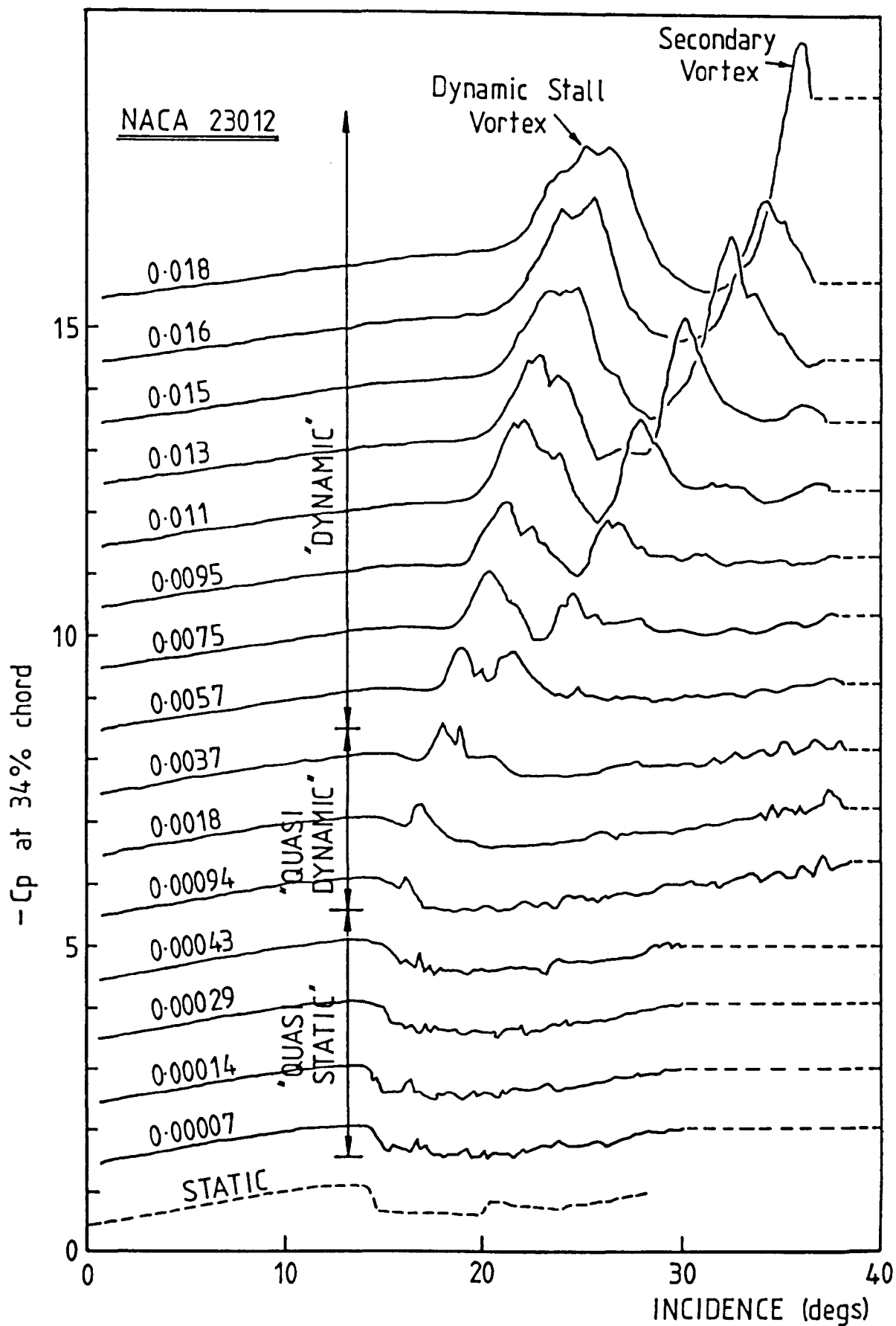


FIGURE 7.6 NACA 23012 Pressure Coefficient at 34% chord for Various Reduced Pitch Rates.

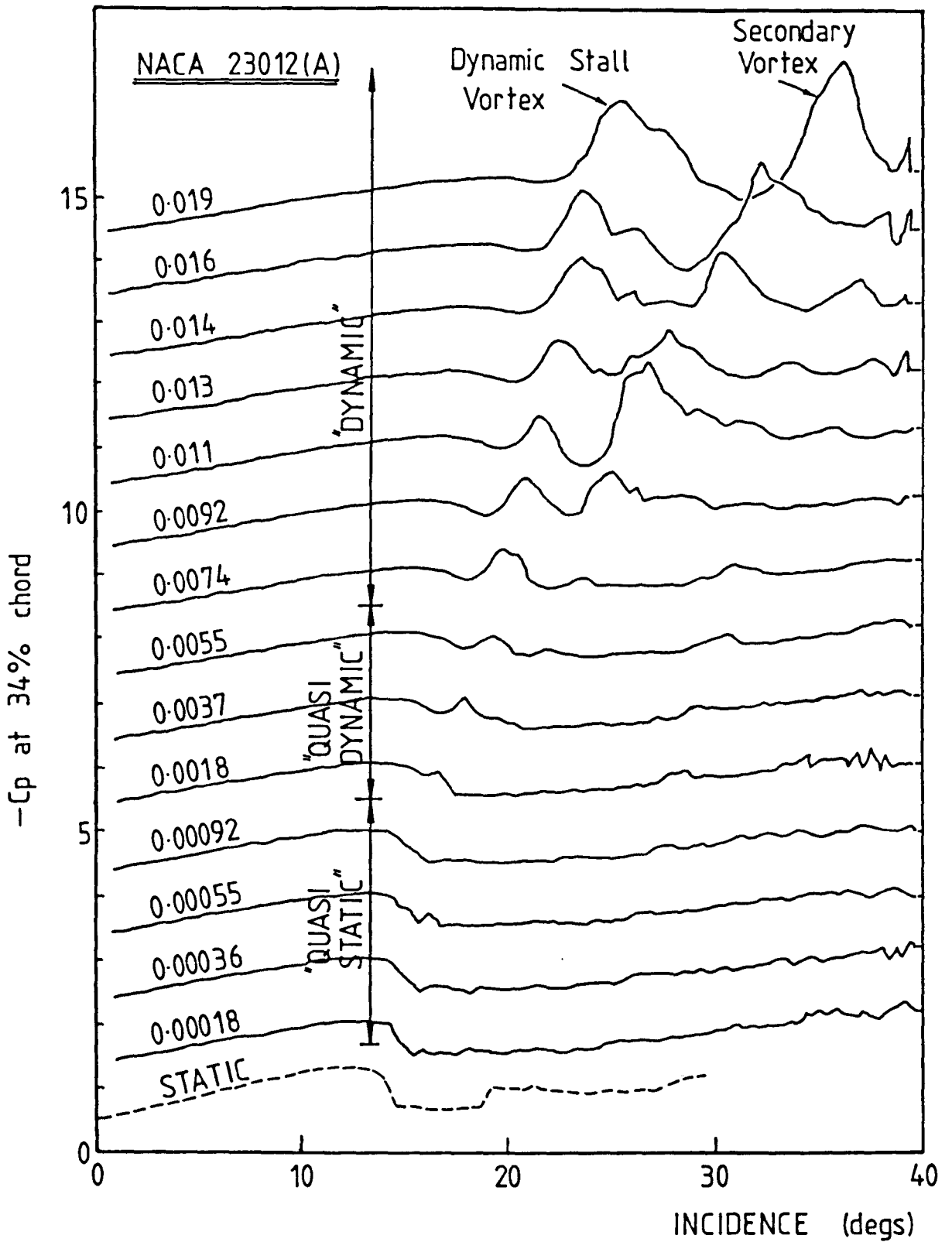


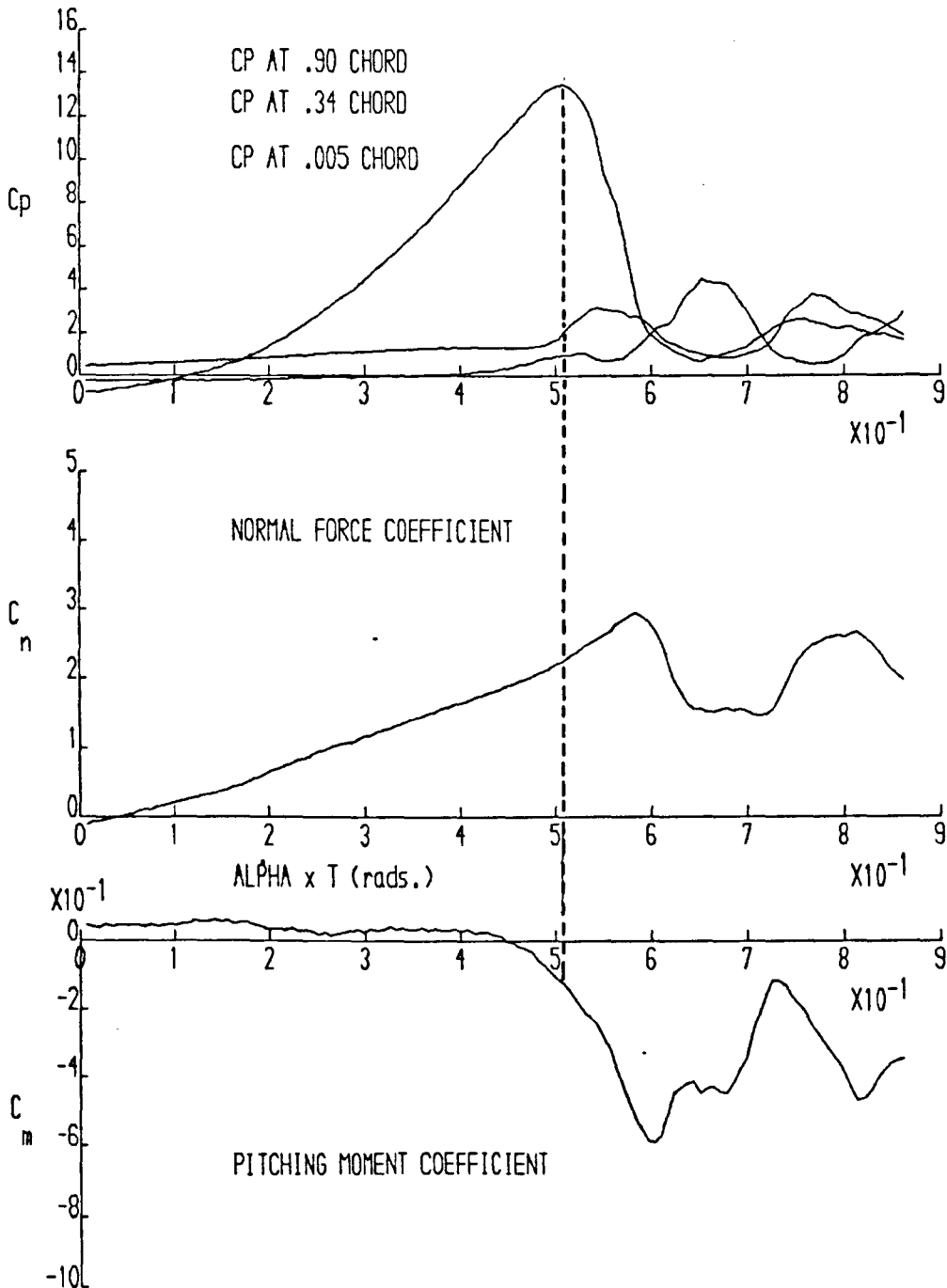
FIGURE 7.7 NACA 23012(A) Pressure Coefficient at 34% chord for Various Reduced Pitch Rates.

DYNAMIC LIFT AND MOMENT CHARACTERISTICS FOR THE NACA 23012 MOD. A

RUN REFERENCE NUMBER: 20201
 REYNOLDS NUMBER = 1531150.
 DYNAMIC PRESSURE = 1000.57 N/sq. m
 NUMBER OF CYCLES = 5
 MOTION TYPE: RAMP

DATE OF TEST: 28/ 2/86
 MACH NUMBER = 0.112
 AIR TEMPERATURE = 30.0
 SAMPLING FREQUENCY = 513.61 Hz.
 REDUCED PITCH RATE = 0.02440

AVERAGED DATA OF 5 CYCLES



2-FEB-88

Run No. 20201

FIGURE 7.8 Relative Phasing of Various Local Upper Surface Pressure Coefficient and Aerodynamic Loading Events for the NACA 23012(A).

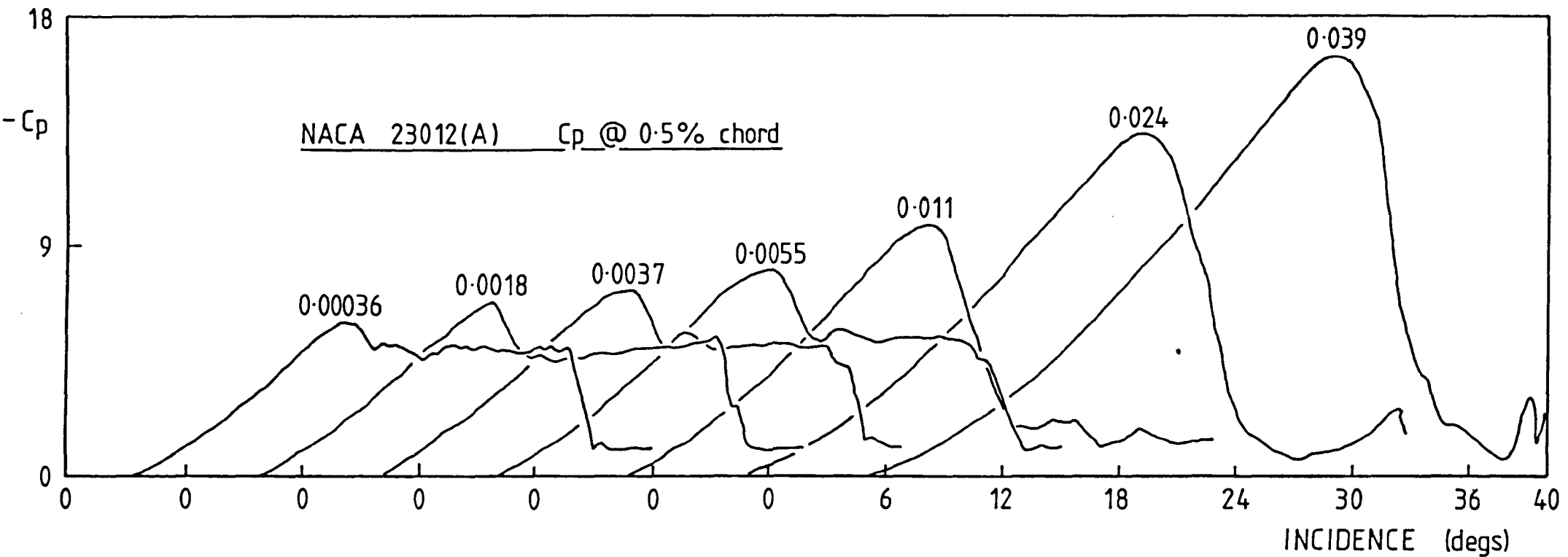


FIGURE 7.9 NACA 23012(A) Pressure Coefficient at 0.5% chord for Various Reduced Pitch Rates.

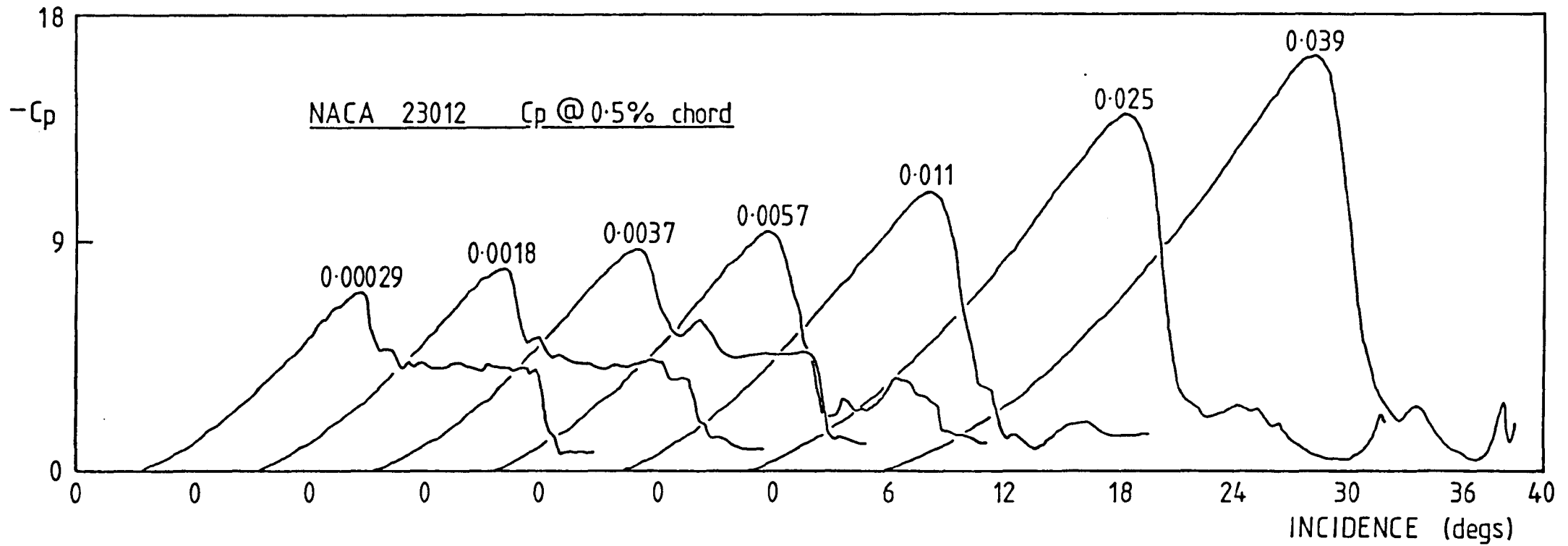


FIGURE 7.10 NACA 23012 Pressure Coefficient at 0.54% chord for Various Reduced Pitch Rates.

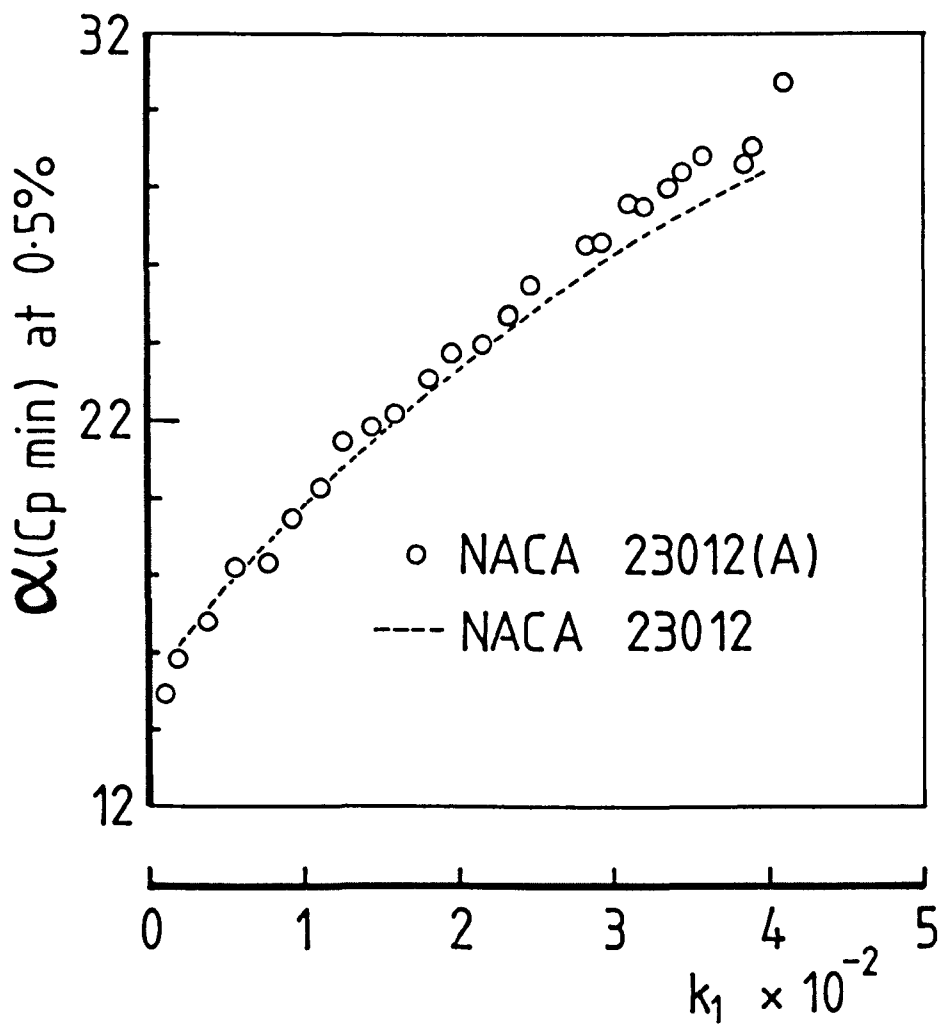
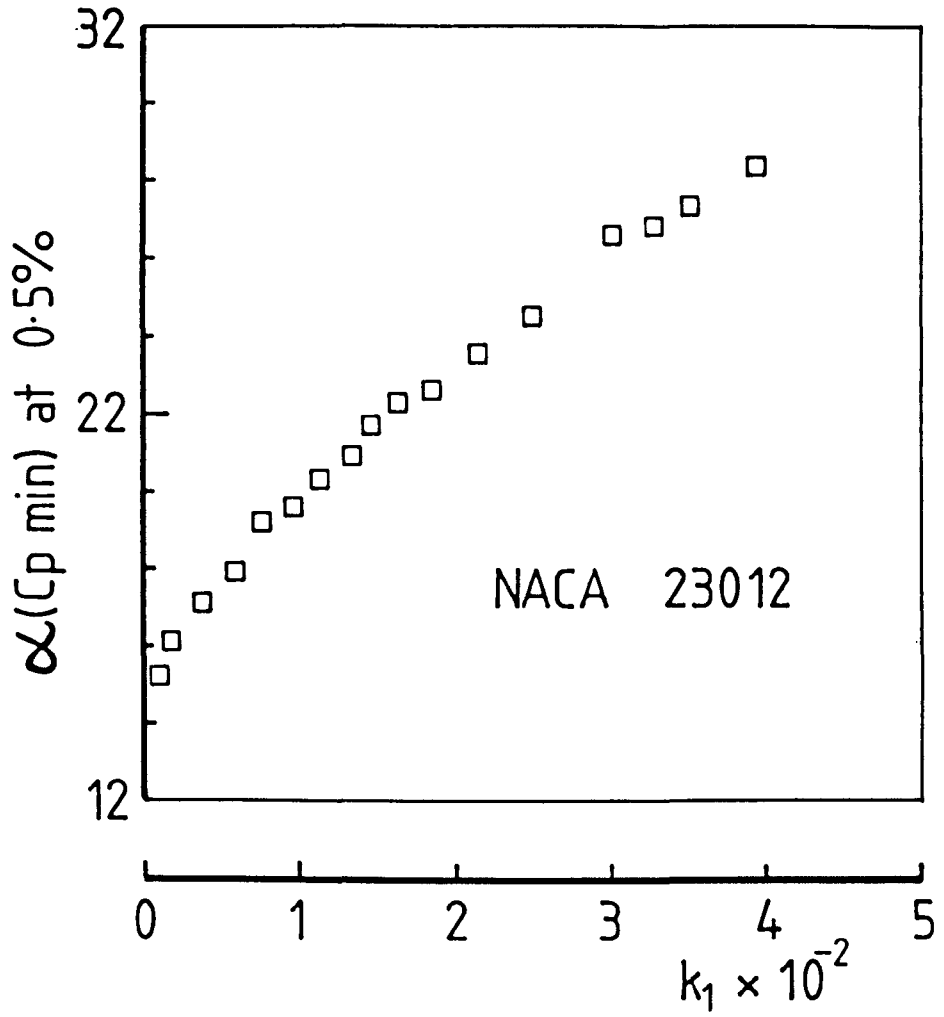
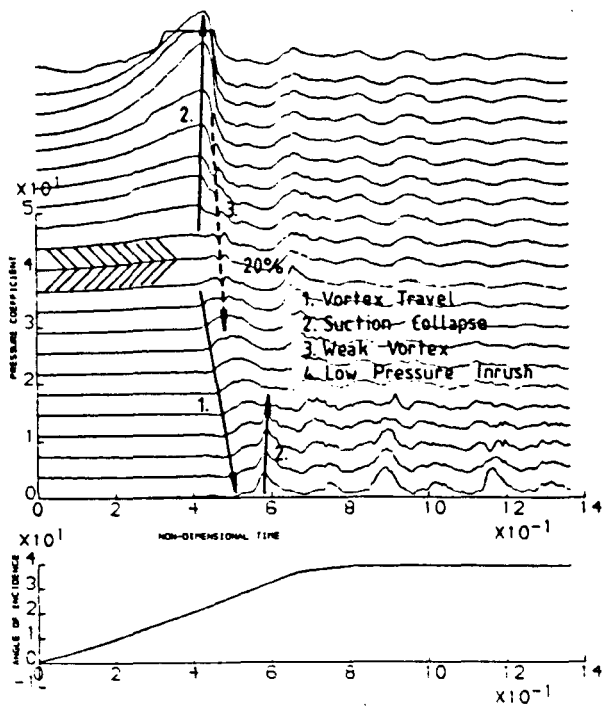
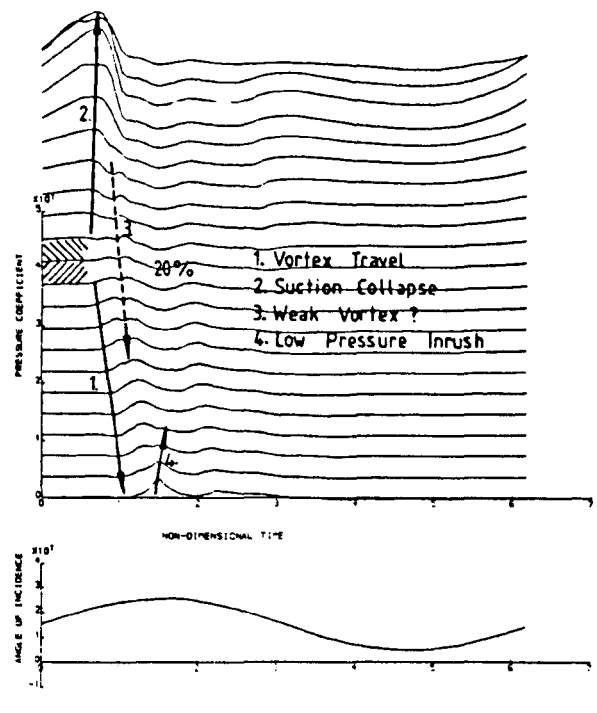


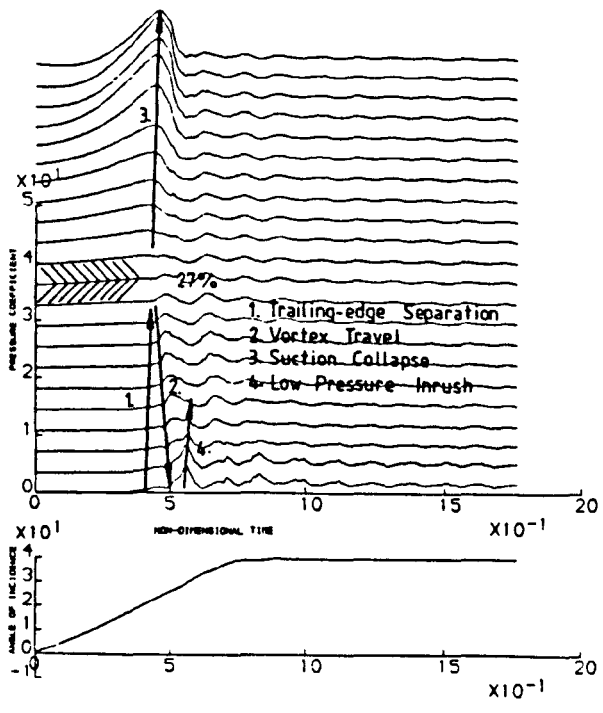
FIGURE 7.11 Minimum Pressure Coefficient Incidence at 0.5% chord for Various Reduced Pitch Rates.



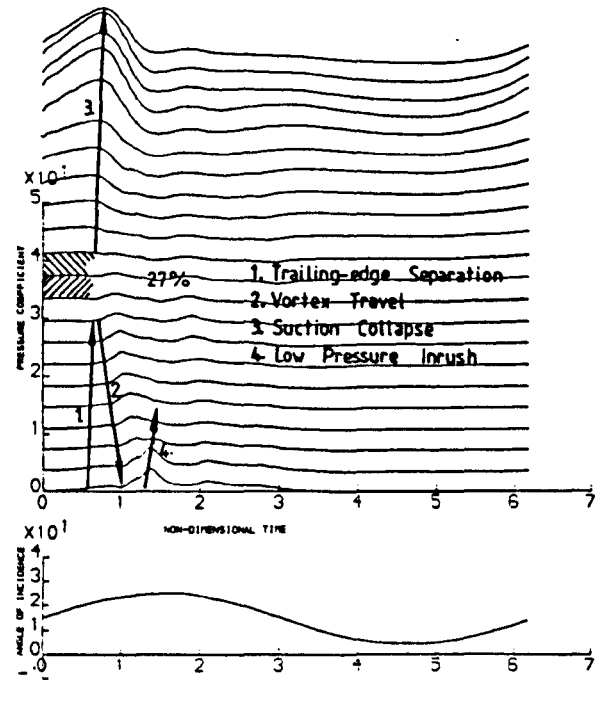
(a) NACA 23012
 $\dot{\alpha} = 150 \text{ }^\circ/\text{s}$



(b) NACA 23012
 $\alpha = 15 + 10 \text{ Sin } \omega t$
 $k = 0.10$



(c) NACA 23012(A)
 $\dot{\alpha} = 146 \text{ }^\circ/\text{s}$



(d) NACA 23012(A)
 $\alpha = 15 + 10 \text{ Sin } \omega t$
 $k = 0.10$

FIGURE 7.12 Comparison of Unsteady Separation Characteristics obtained during Oscillatory and Ramp Motions for the NACA 23012 and 23012(A) Aerofoils at 1.5×10^6 Reynolds number.

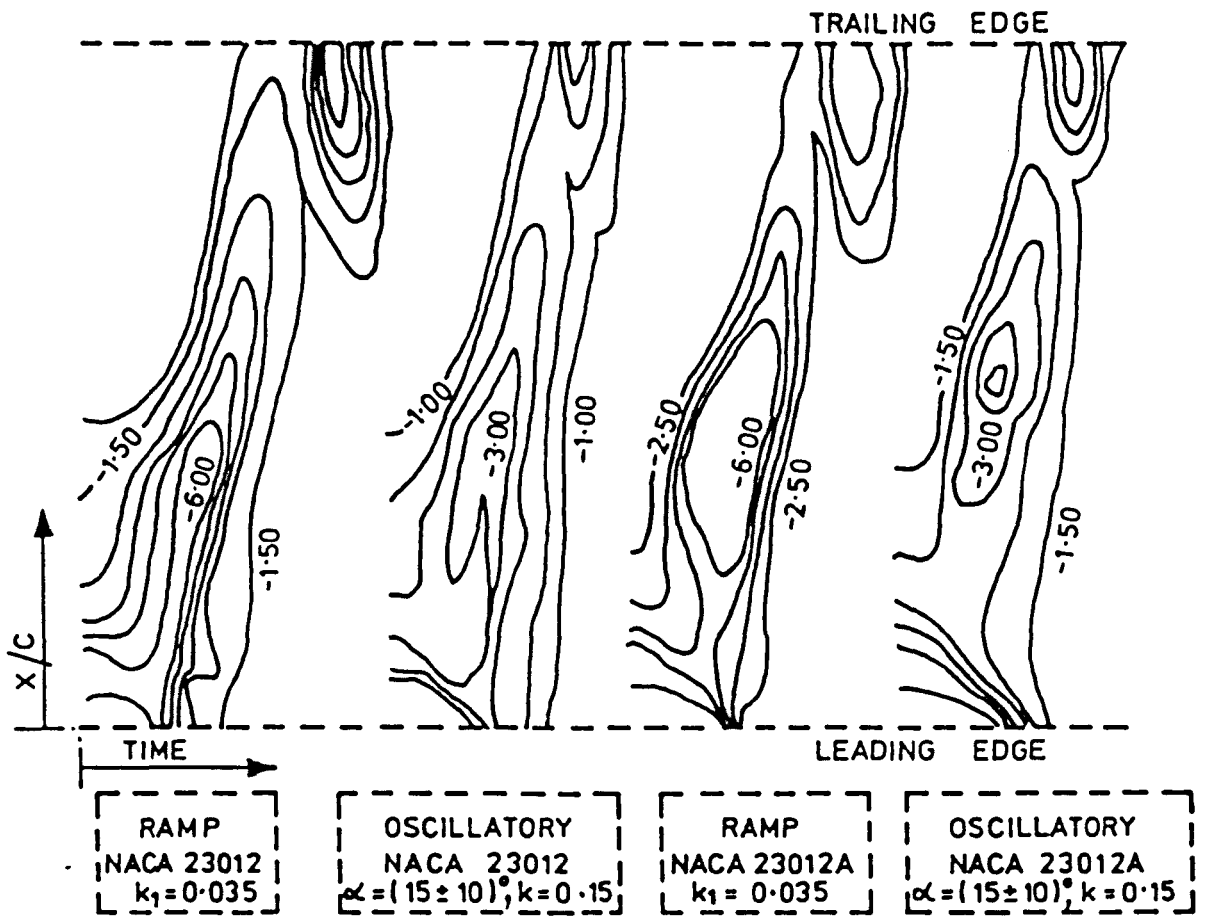


FIGURE 7.13 Comparison of Pressure Wave associated with Vortex Movement during Oscillatory and Ramp Motions for the NACA 23012 and 23012(A) Aerofoils at 1.5×10^6 Reynolds number.

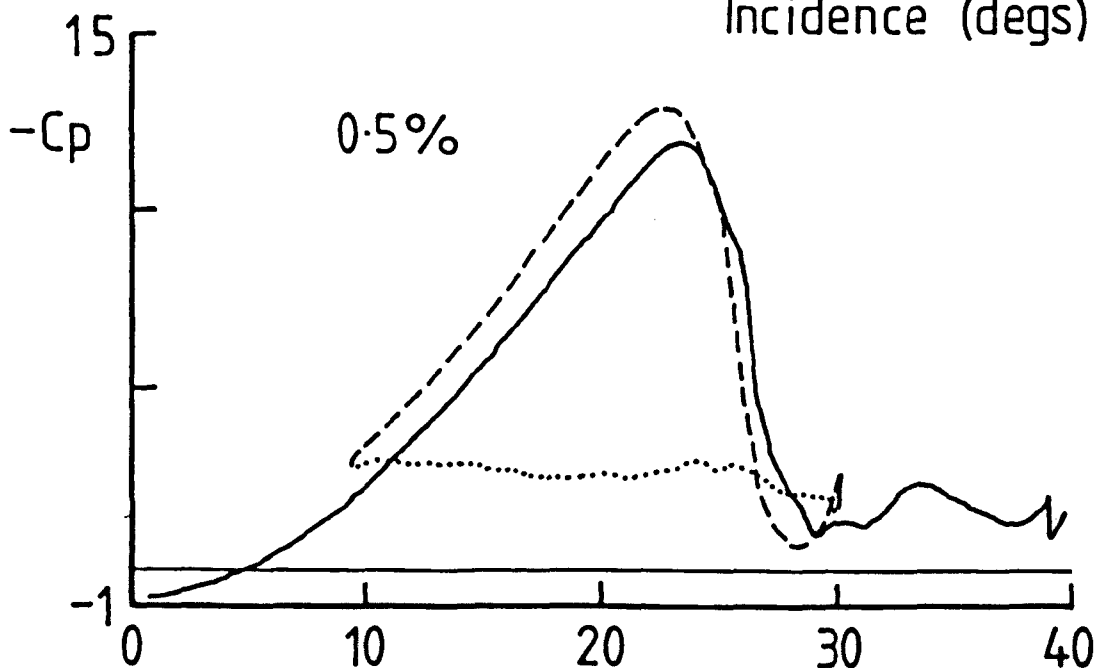
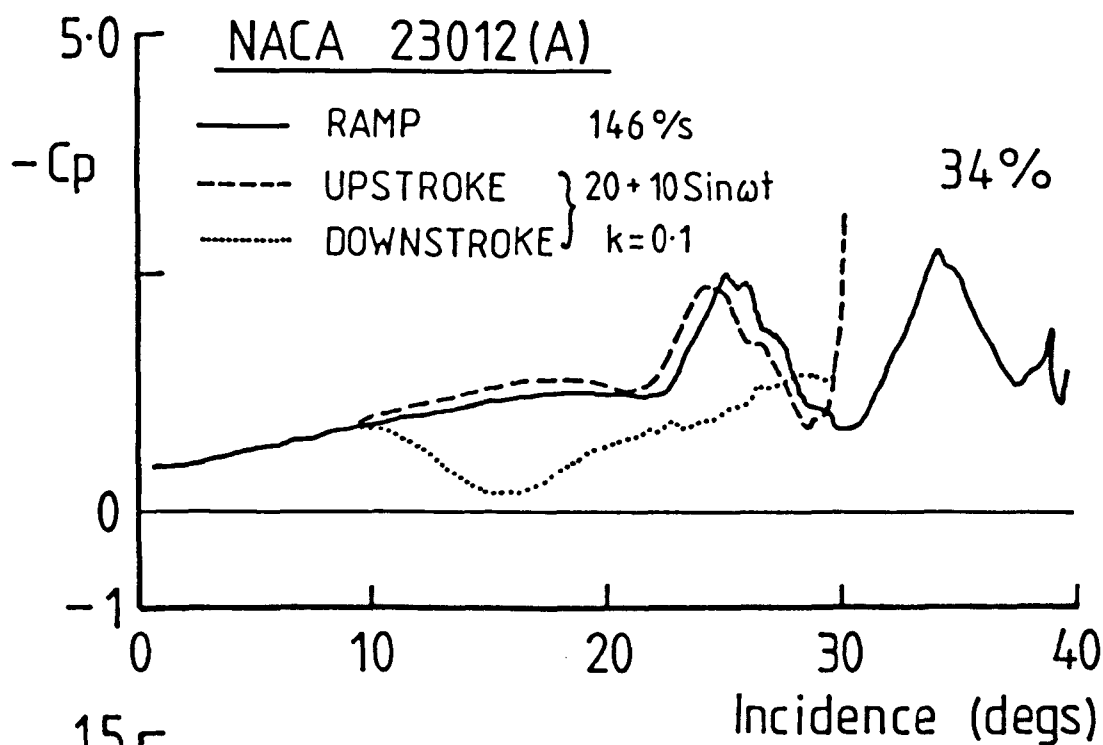
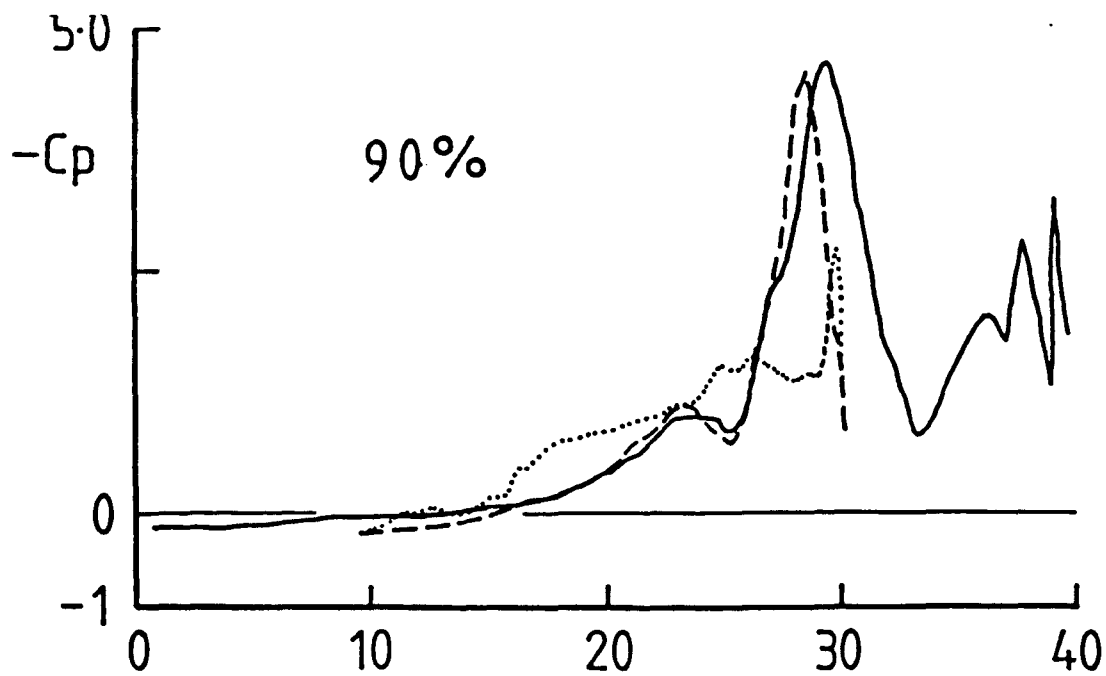


FIGURE 7.14 Comparison of Local Pressure Coefficient Response obtained for the NACA 23012(A) during Oscillatory and Ramp Motions at 1.5×10^6 Reynolds number.

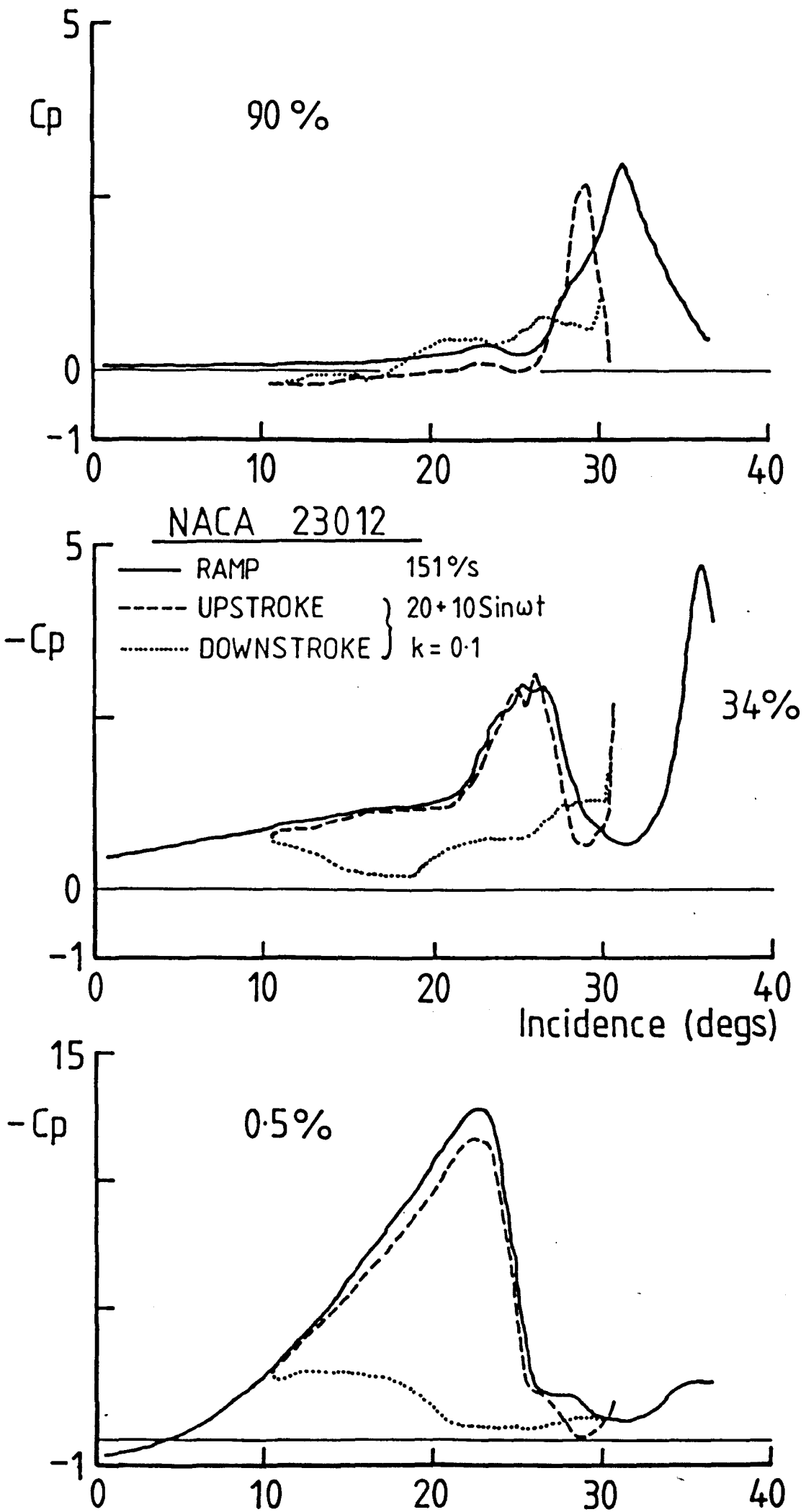


FIGURE 7.15 Comparison of Local Pressure Coefficient Response obtained for the NACA 23012 during Oscillatory and Ramp Motions at 1.5×10^6 Reynolds number.

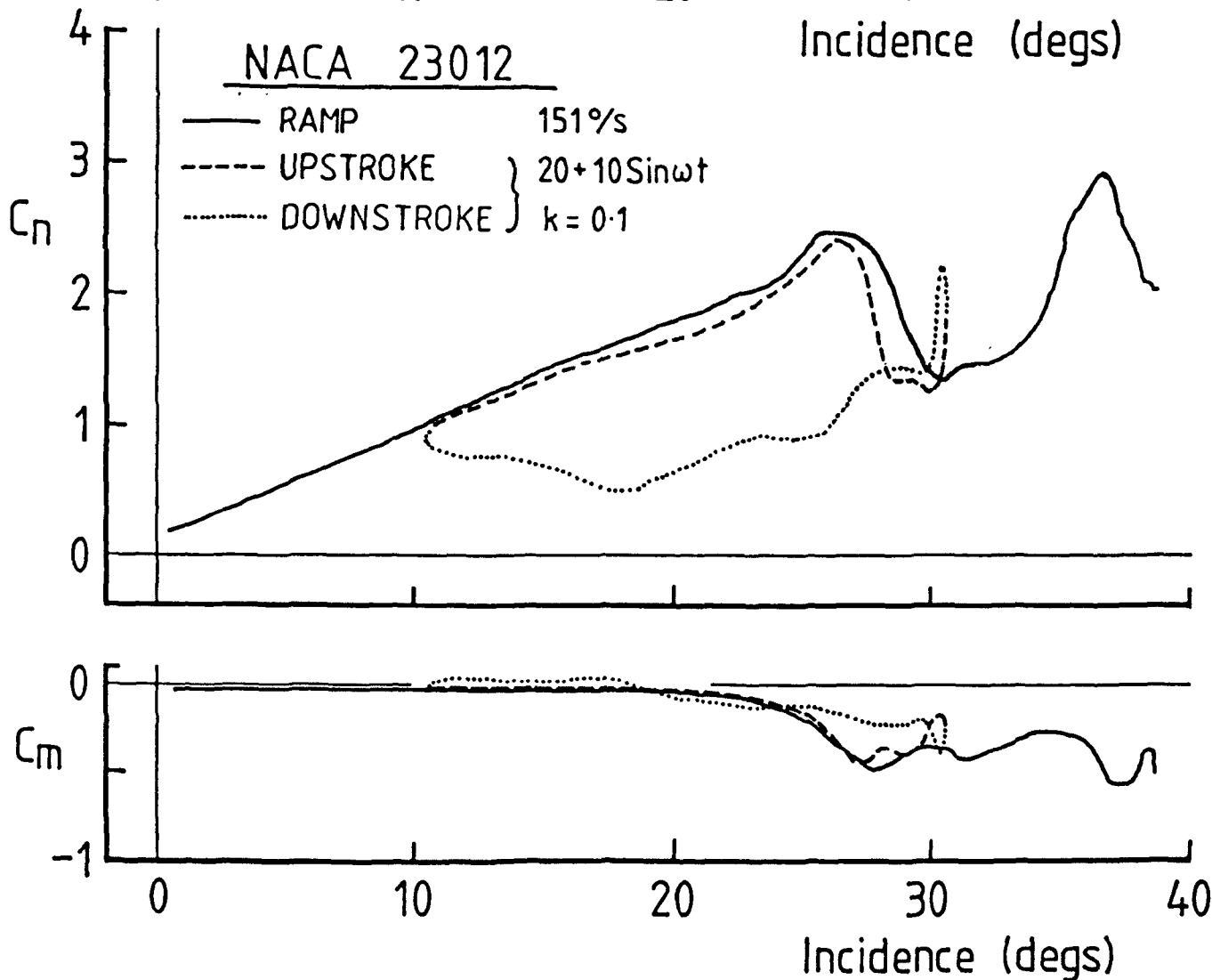
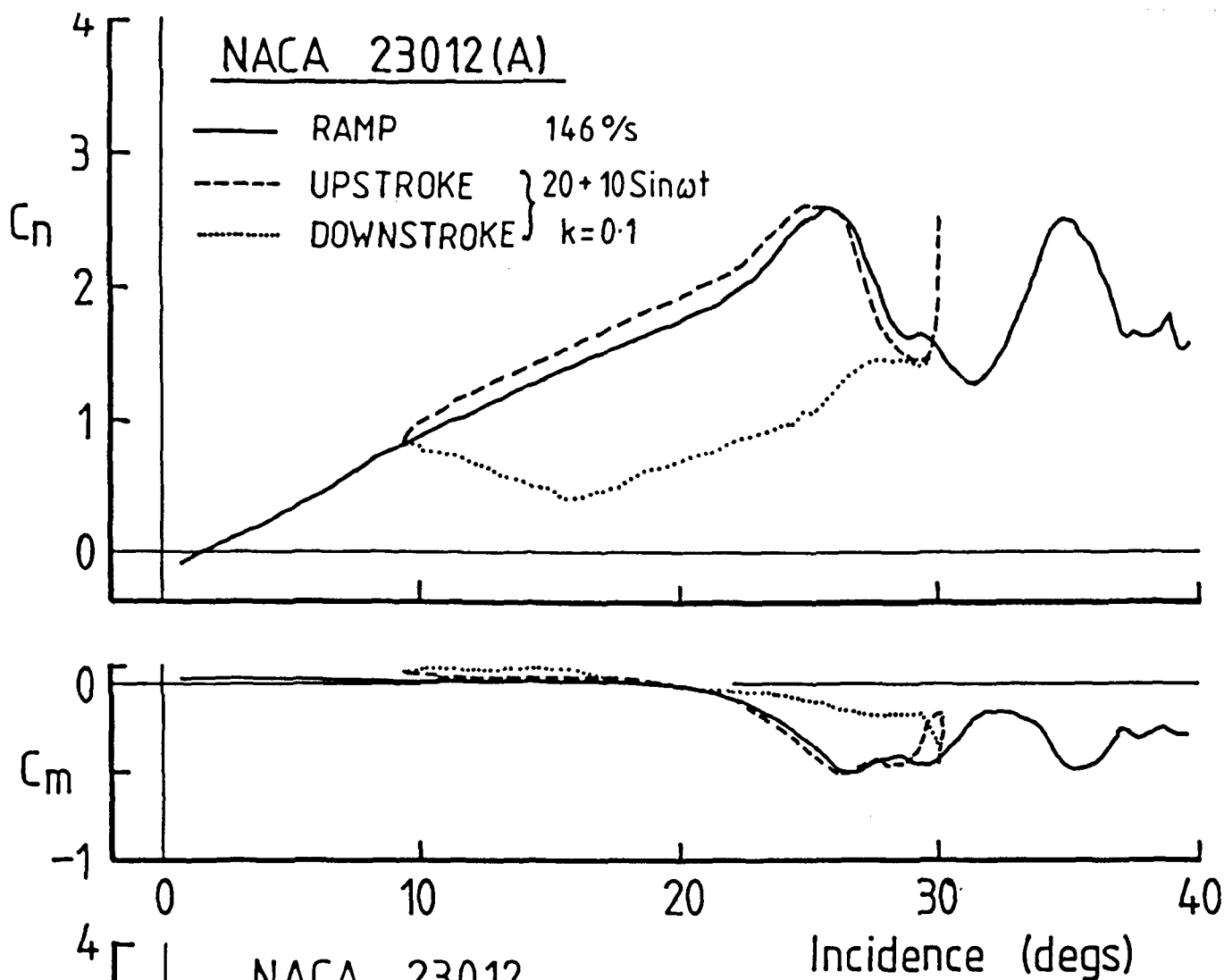


FIGURE 7.16 Comparison of Aerodynamic Loadings obtained during Oscillatory and Ramp Motions at 1.5×10^6 Reynolds number.

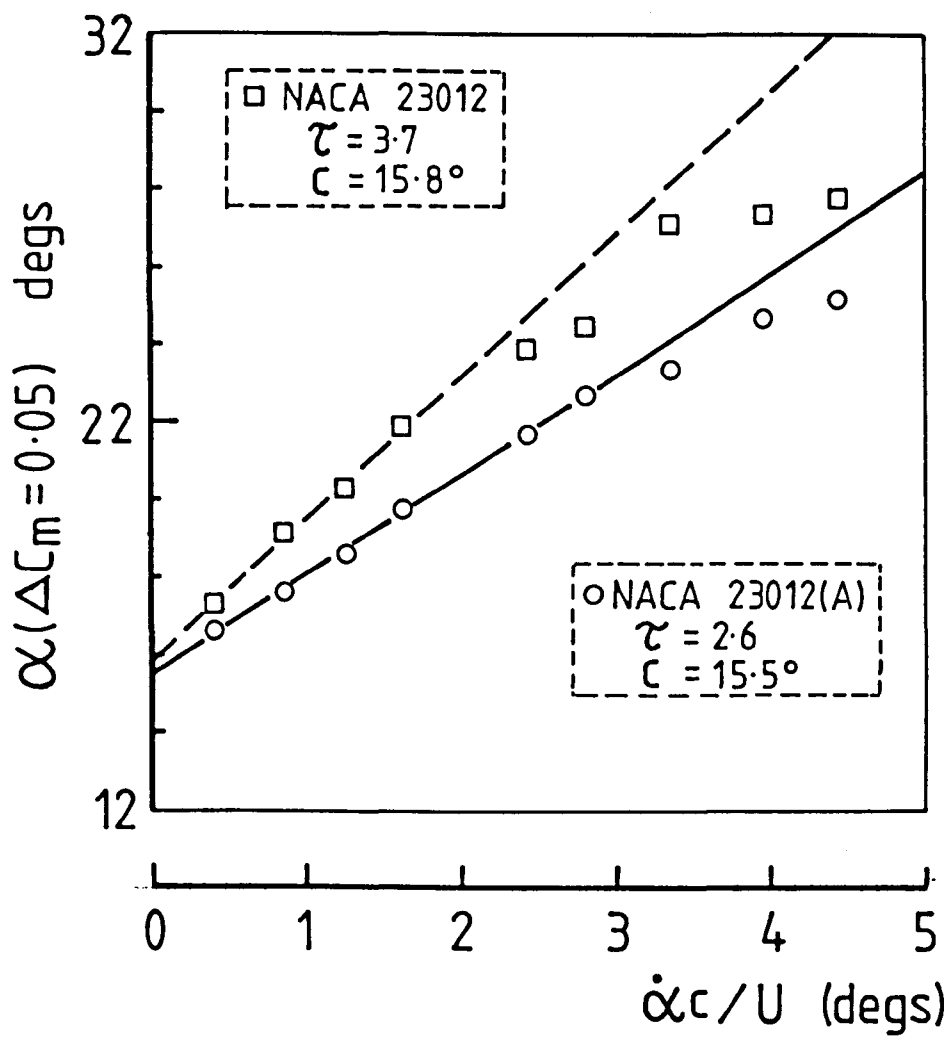


FIGURE 7.17 Non-Dimensional Vortex Inception Time Delay Calculation based on Pitching-Moment Response.

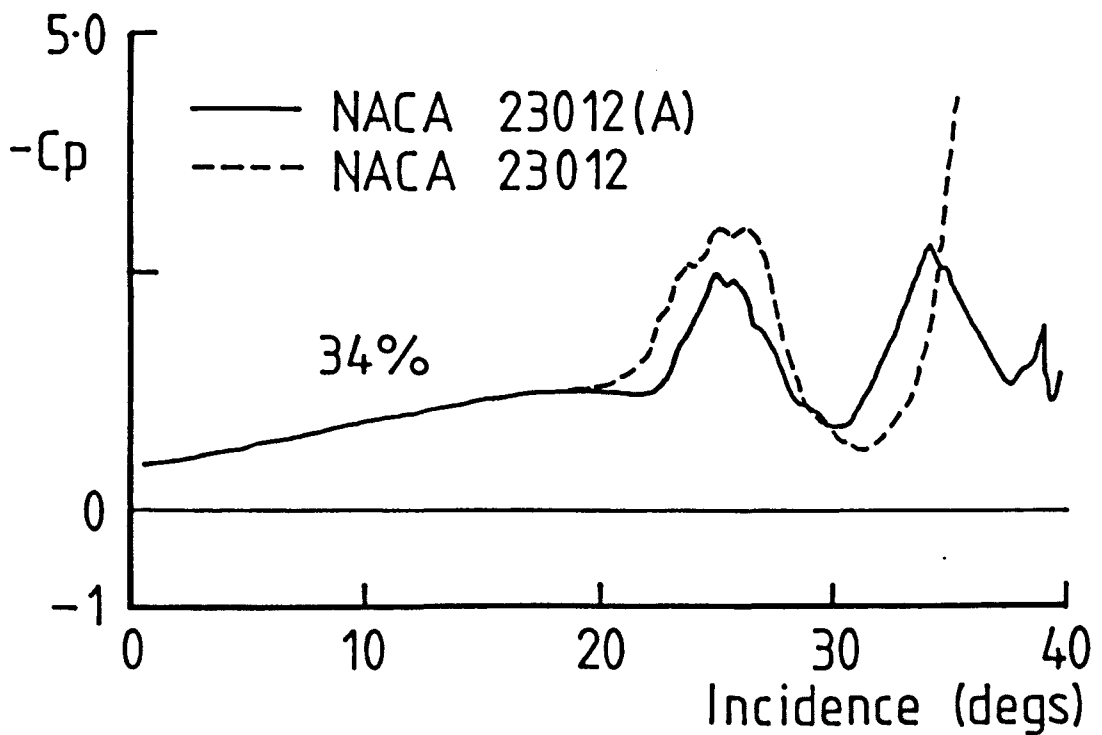


FIGURE 7.18 Pressure Coefficient Response at 34% chord obtained during Ramp tests of Pitch Rate = 150 °/s.

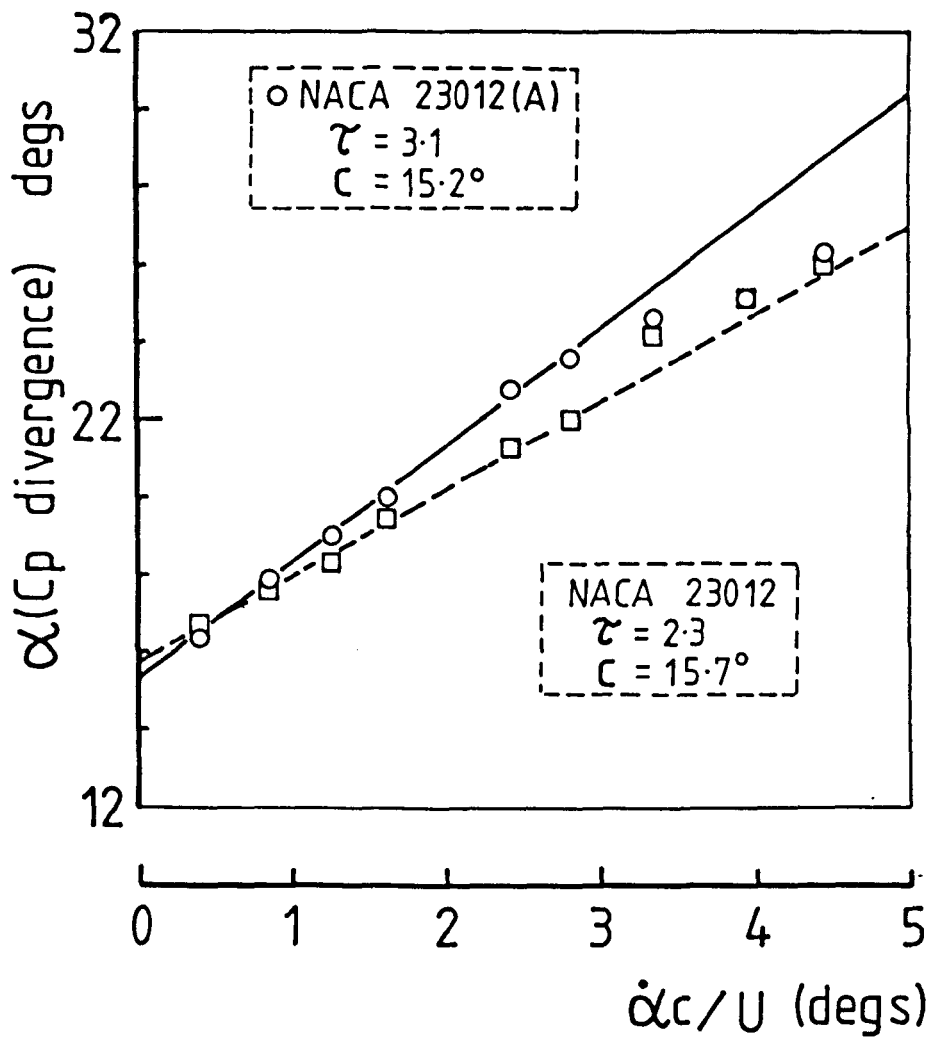


FIGURE 7.19 Non-Dimensional Vortex Inception Time Delay Calculation based on Local Pressure Coefficient Response.

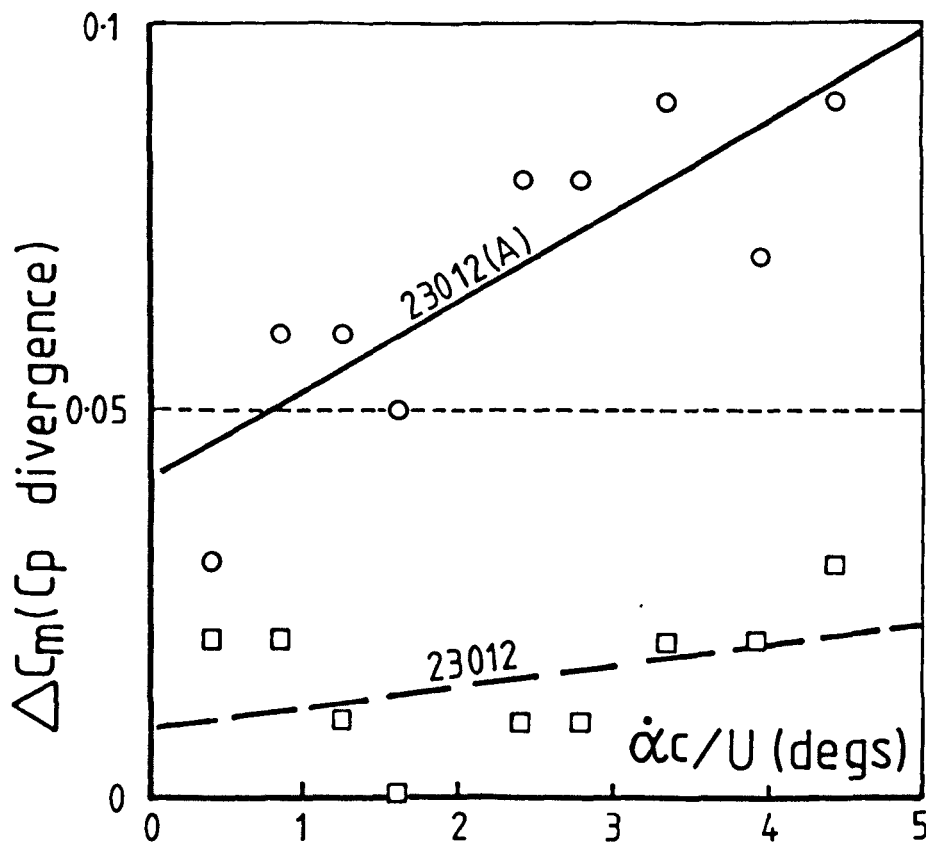


FIGURE 7.20 Pitching-Moment Drop at Vortex Inception Incidence (as defined in Figure 7.19).

DYNAMIC CHARACTERISTICS FOR THE NACA 23012 MODEL 2

RUN REFERENCE NUMBER: 20271

DATE OF TEST: 4/3/86

REYNOLDS NUMBER = 1478949.

MACH NUMBER = 0.114

DYNAMIC PRESSURE = 977.96 N/sq. m

AIR TEMPERATURE = 30.0

NUMBER OF CYCLES = 5

SAMPLING FREQUENCY = 550.05 Hz.

MOTION TYPE: RAMP UP

REDUCED PITCH RATE = 0.03

LINEAR PITCH RATE = 286.60 DEG./SEC.

AVERAGED DATA OF 5 CYCLES

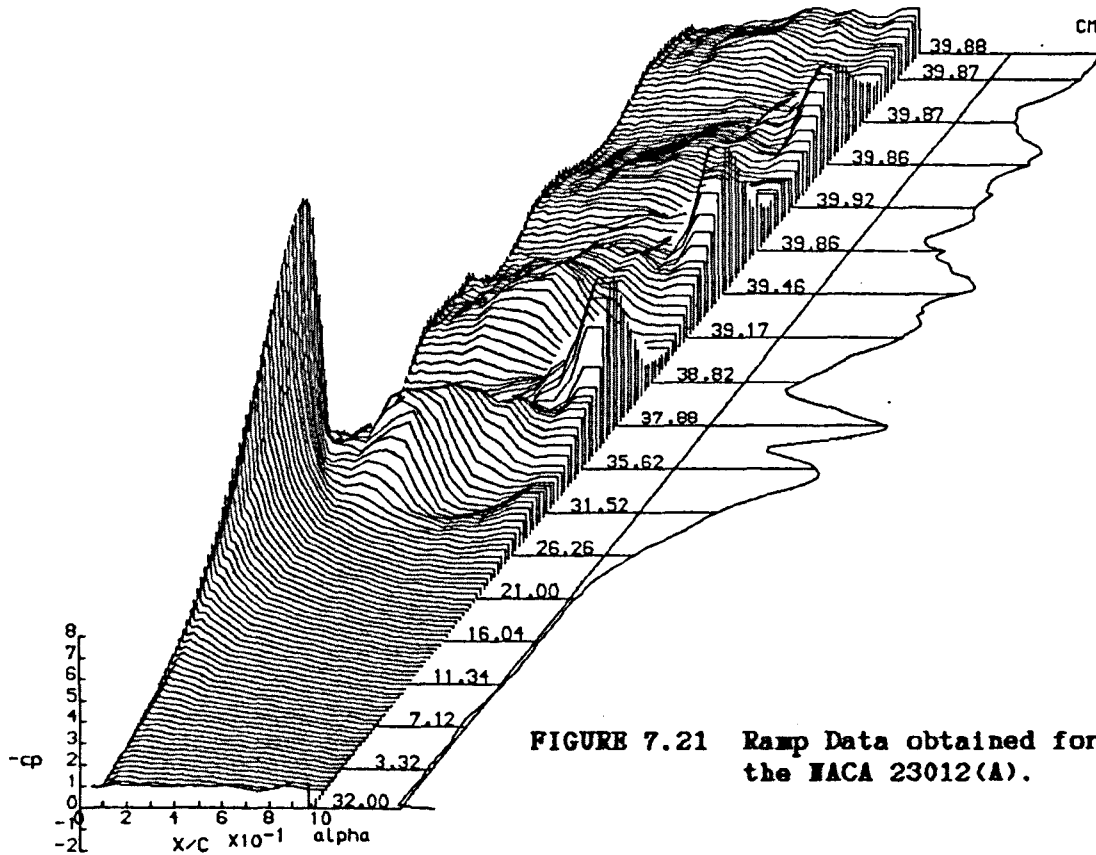
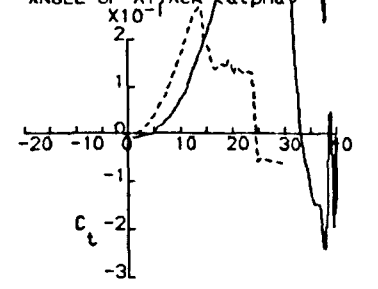
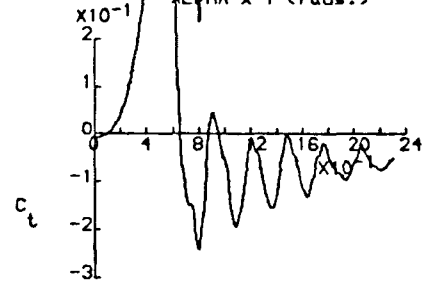
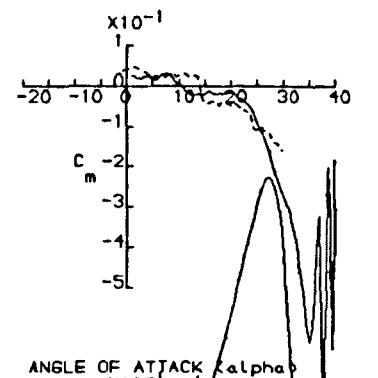
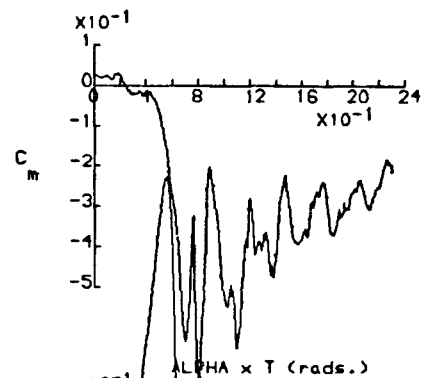
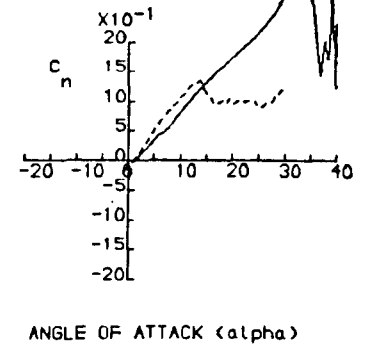
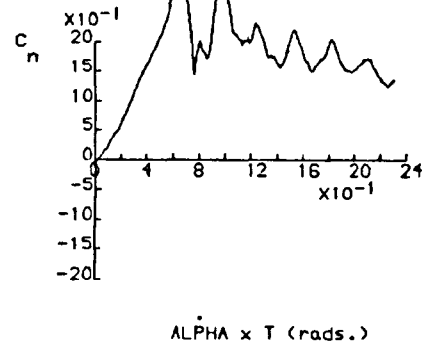
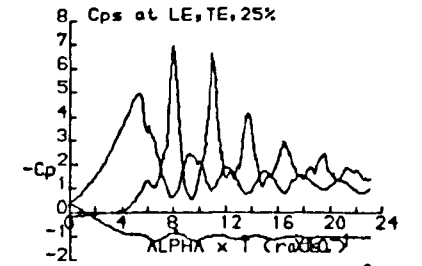
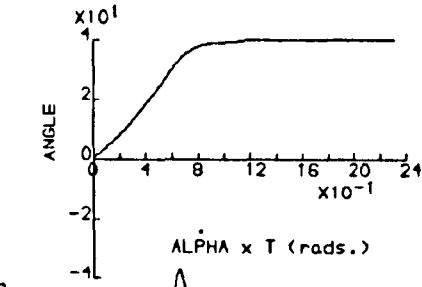


FIGURE 7.21 Ramp Data obtained for the NACA 23012(A).



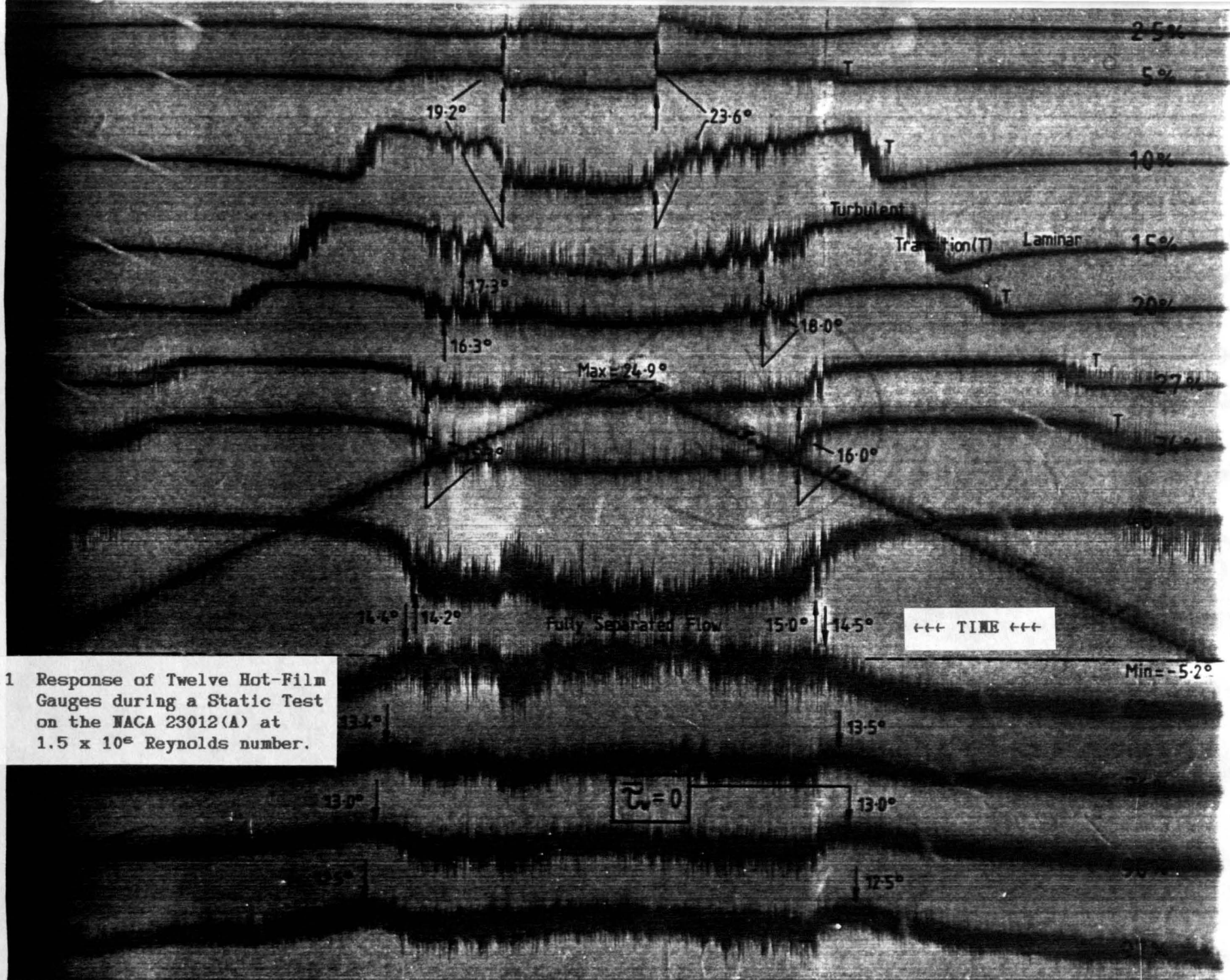


FIGURE 8.1 Response of Twelve Hot-Film Gauges during a Static Test on the NACA 23012(A) at 1.5×10^6 Reynolds number.

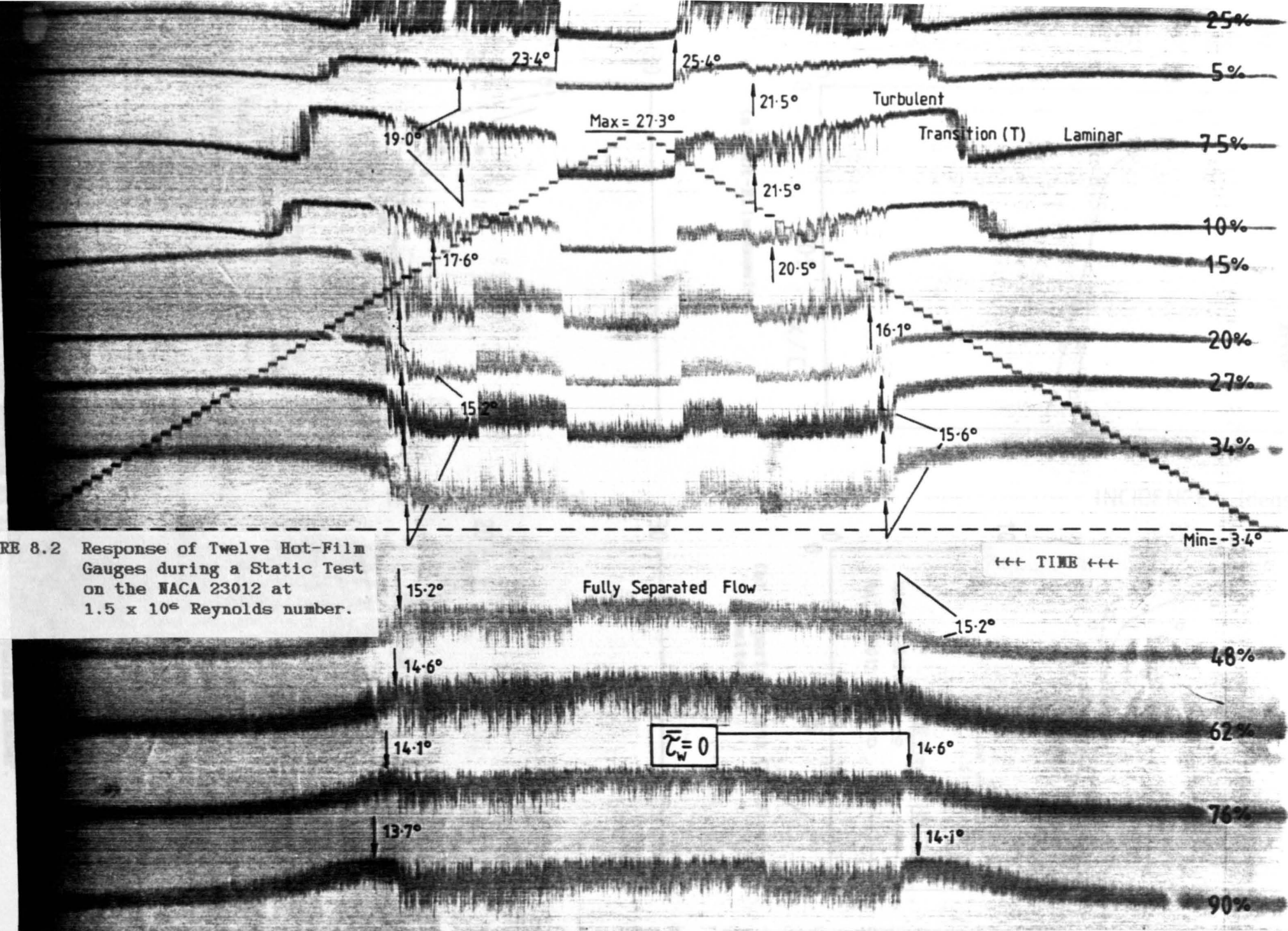
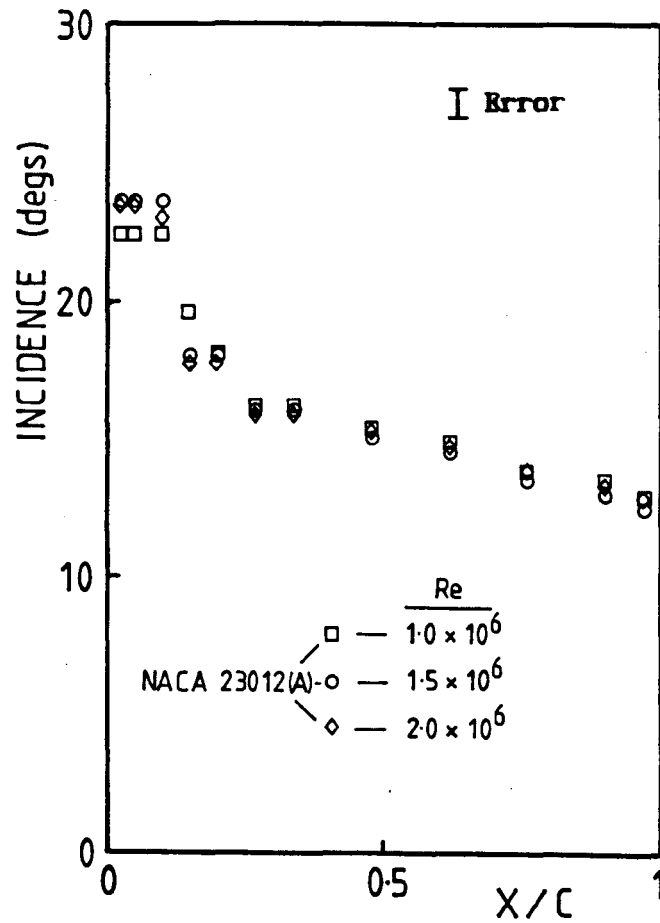
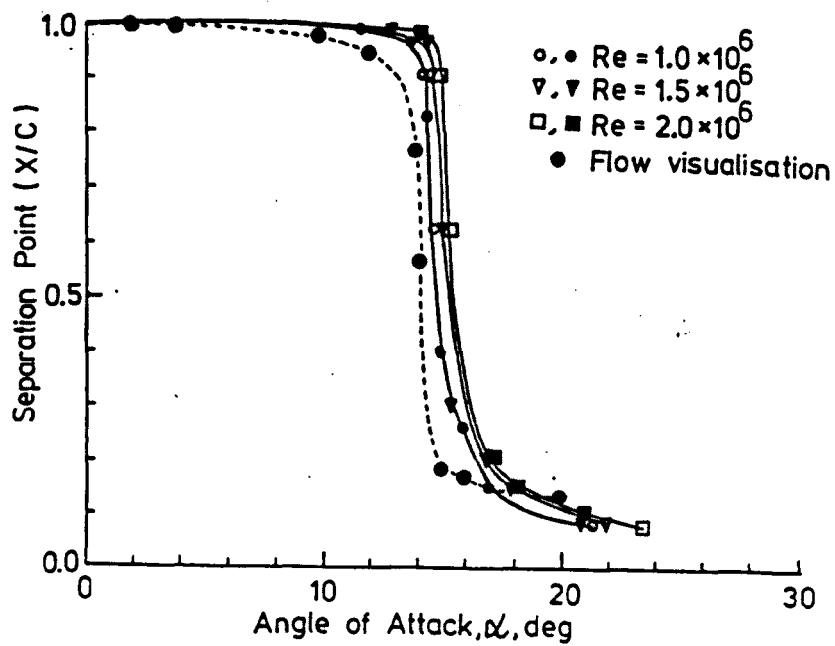


FIGURE 8.2 Response of Twelve Hot-Film Gauges during a Static Test on the NACA 23012 at 1.5×10^6 Reynolds number.



(a) NACA 23012(A).



(b) NACA 23012 (from Leishman, 1984).

FIGURE 8.4 Variation in Separation Characteristics with Reynolds number.

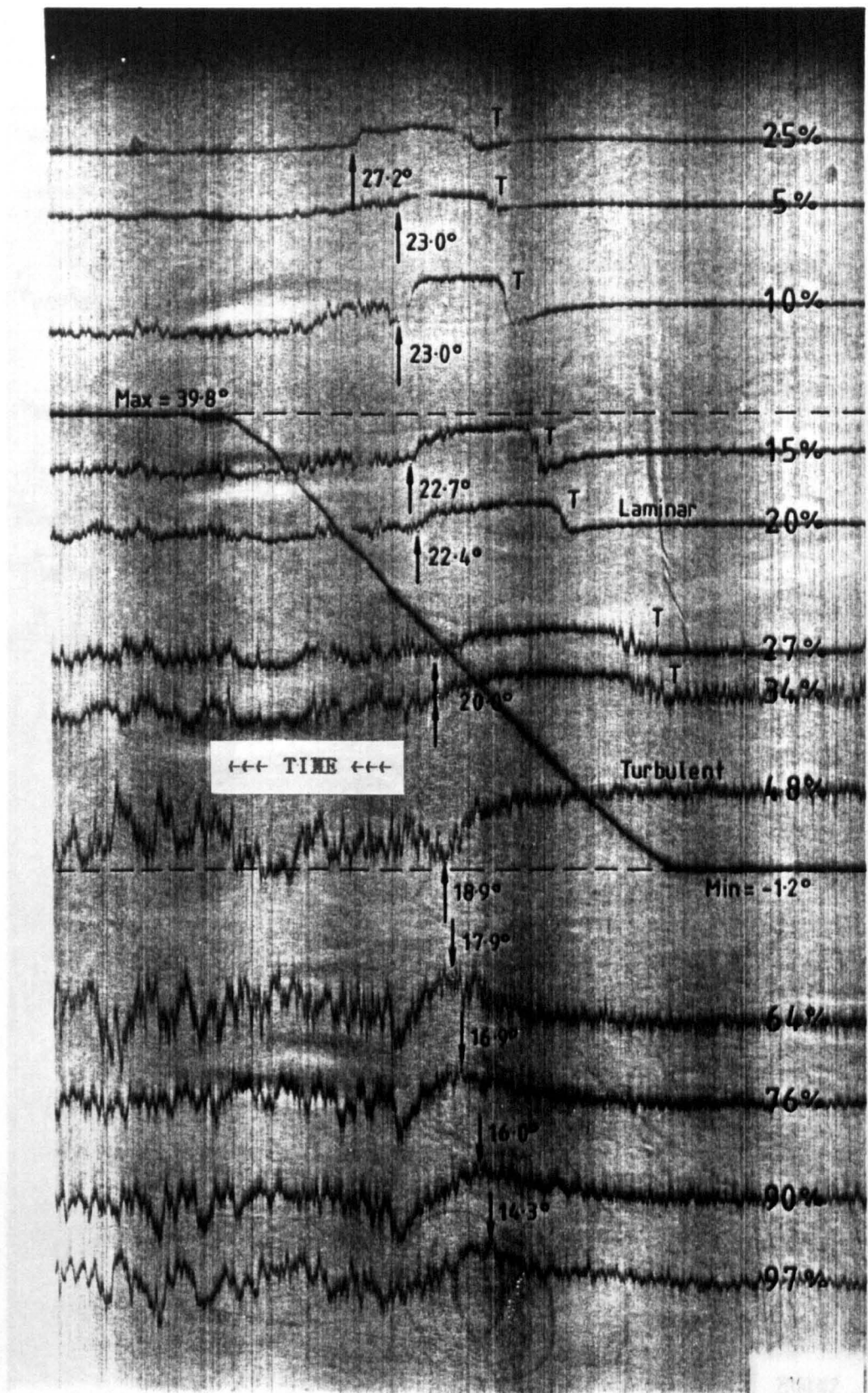


FIGURE 8.5 Response of Twelve Hot-Film Gauges during a Ramp Test of 100 °/s Pitch Rate on the NACA 23012(A) at 1.5×10^6 Reynolds number.

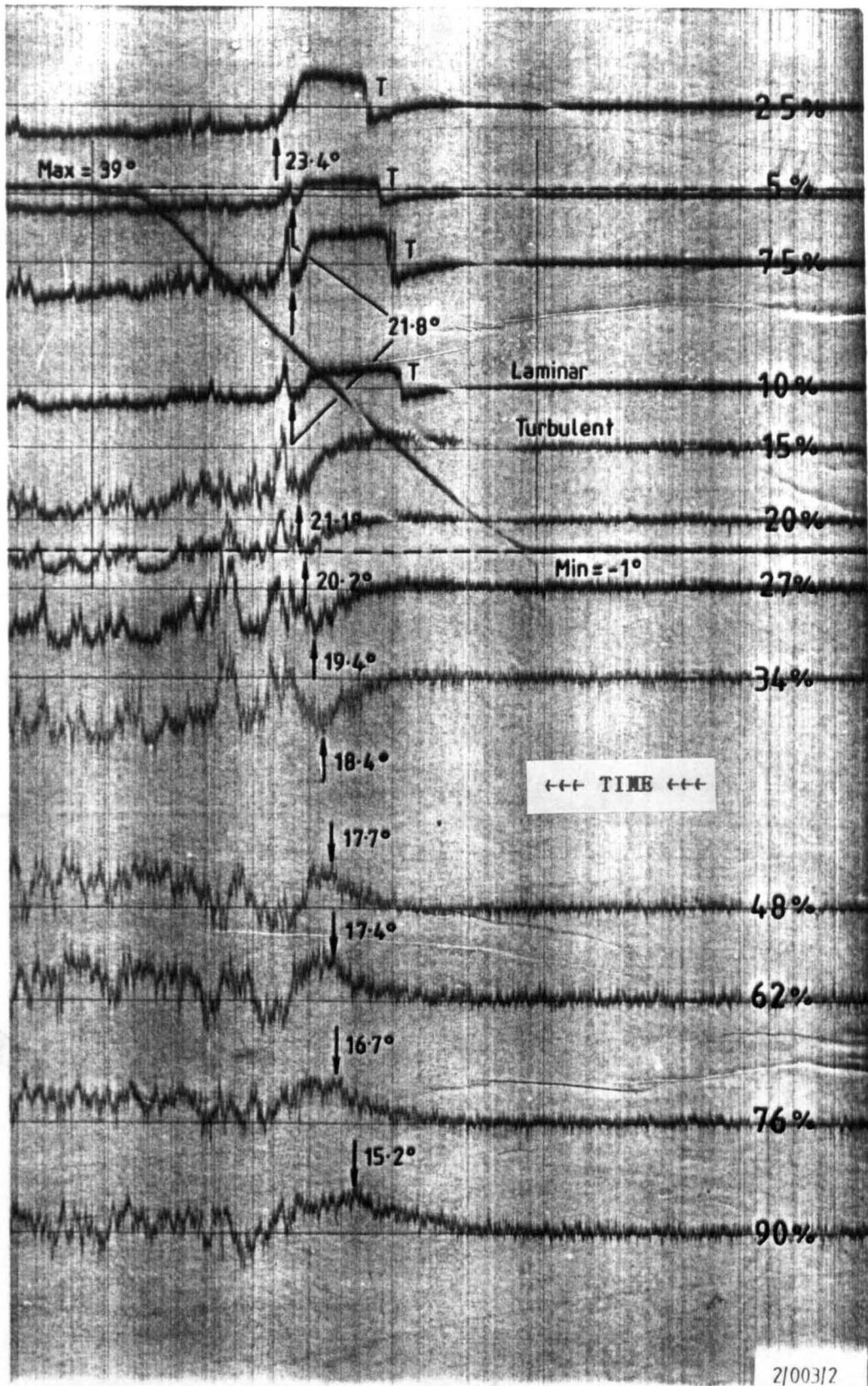
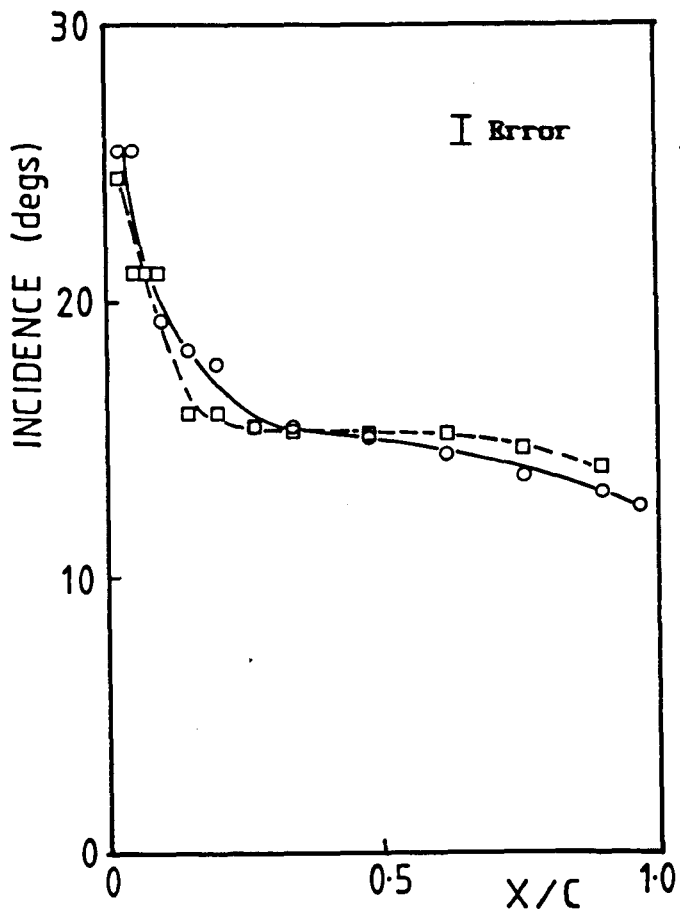
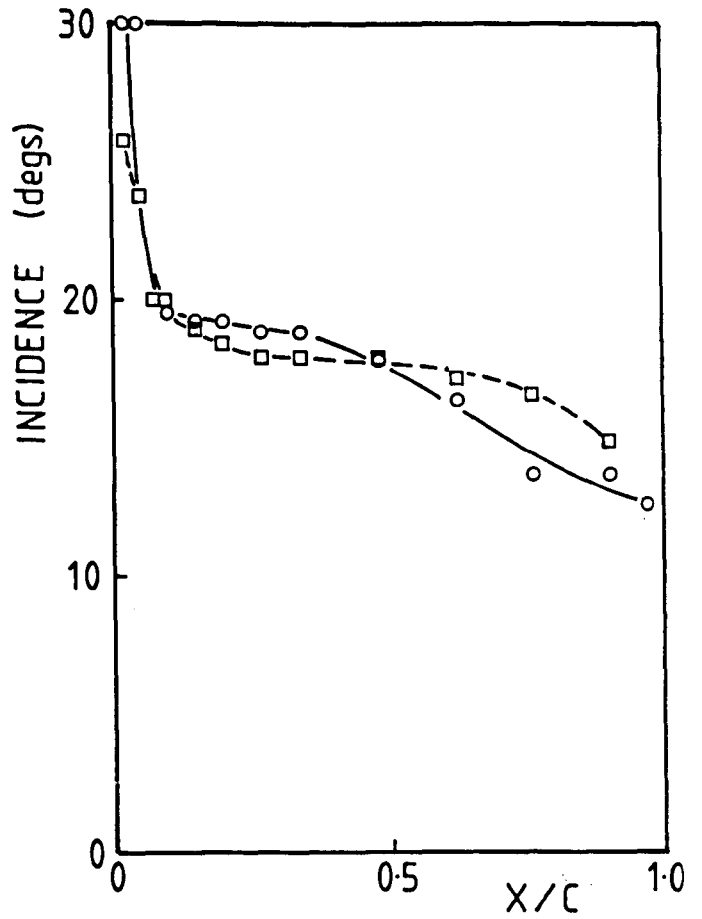


FIGURE 8.6 Response of Twelve Hot-Film Gauges during a Ramp Test of 100 °/s Pitch Rate on the NACA 23012 at 1.5×10^6 Reynolds number.

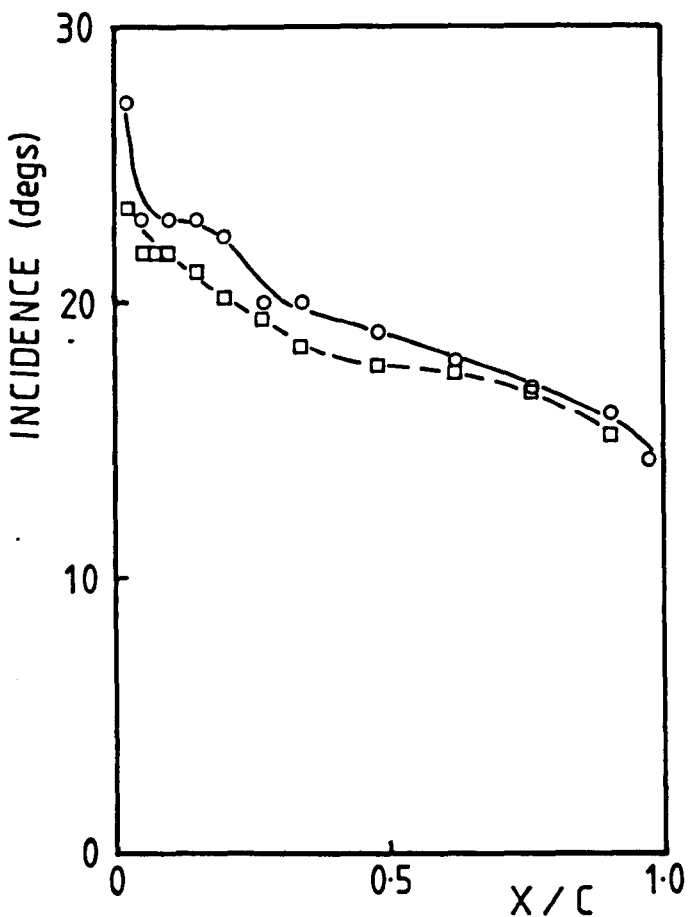
FIGURE 8.7 Effect of Pitch Rate on the Flow Reversal Characteristics at 1.5×10^6 Reynolds number.



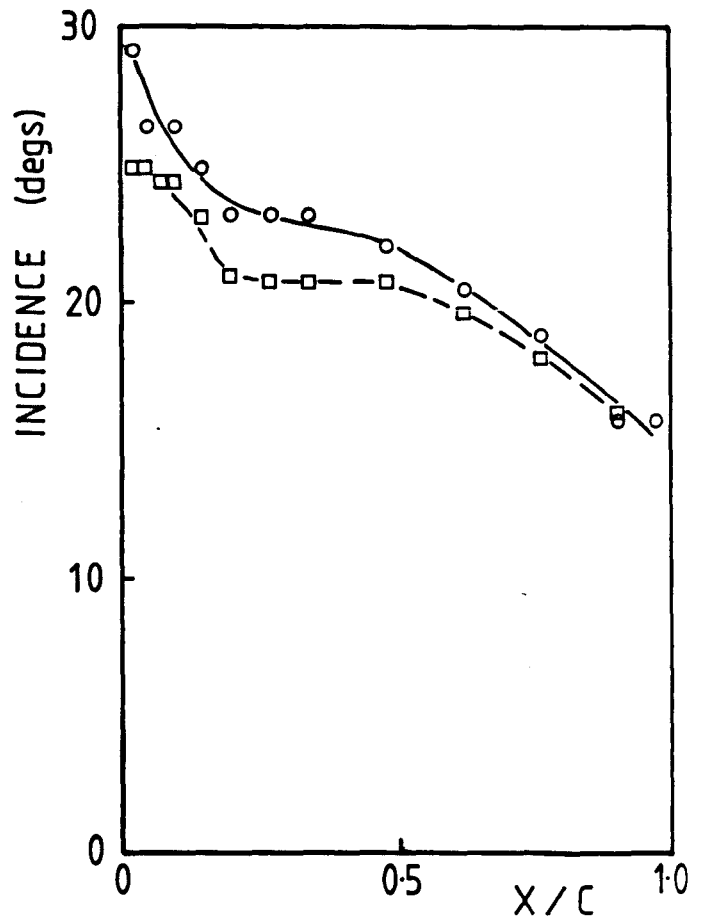
(a) $\dot{\alpha} = 4.8 \text{ }^\circ/\text{s}$



(b) $\dot{\alpha} = 45 \text{ }^\circ/\text{s}$



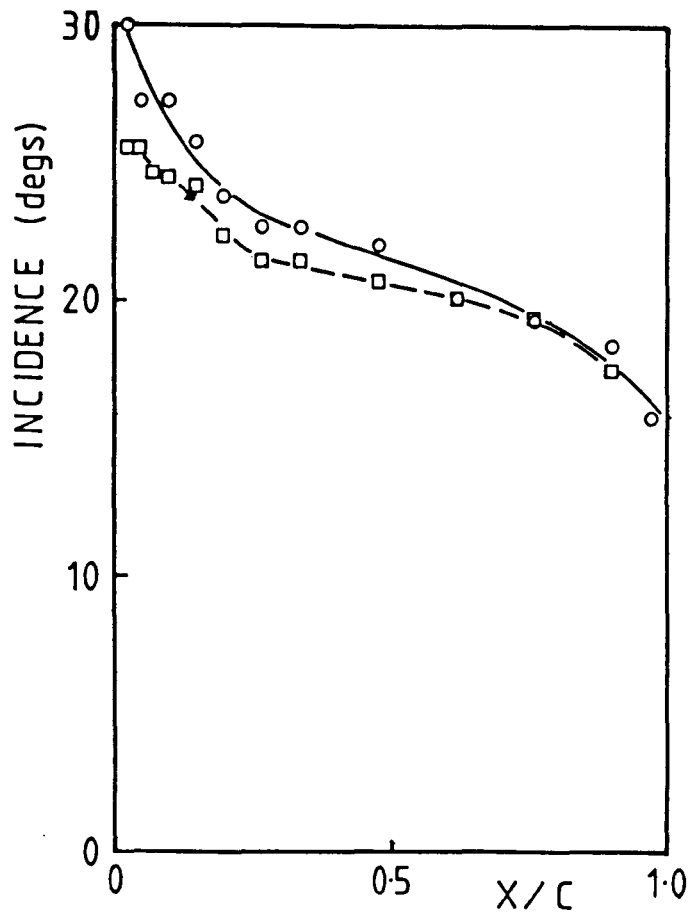
(c) $\dot{\alpha} = 100 \text{ }^\circ/\text{s}$



(d) $\dot{\alpha} = 163 \text{ }^\circ/\text{s}$

FIGURE 8.7 Effect of Pitch Rate on the Flow Reversal Characteristics at 1.5×10^6 Reynolds number.

○ - NACA 23012(A)
 □ - NACA 23012



(e) $\dot{\alpha} = 217 \text{ }^\circ/\text{s}$

FIGURE 8.7 Completed.

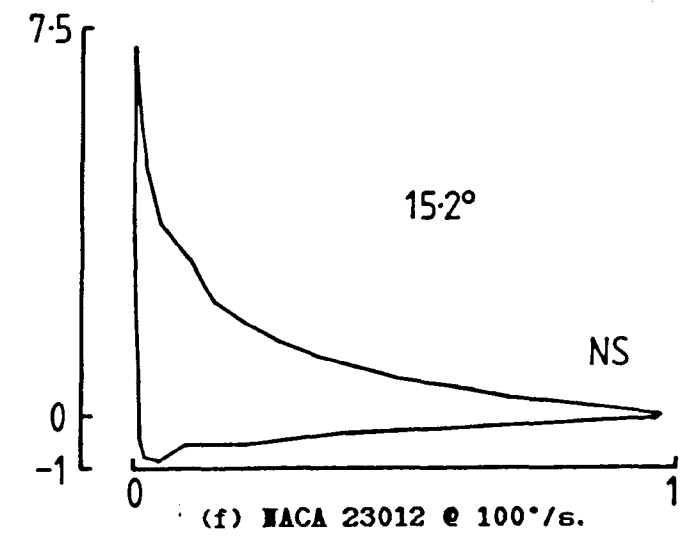
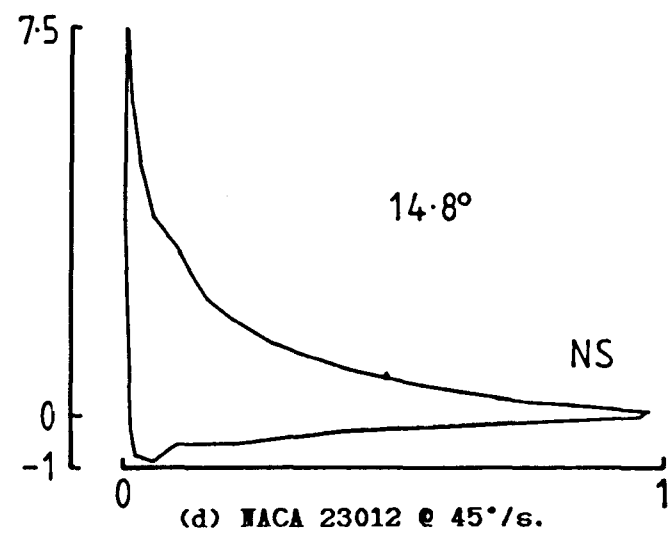
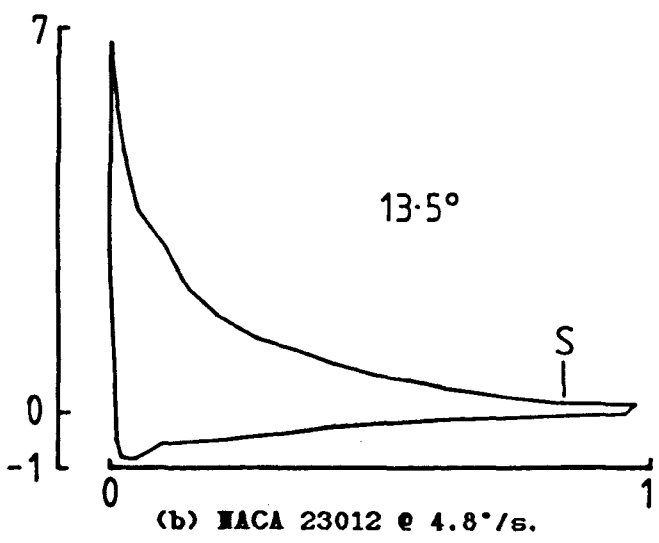
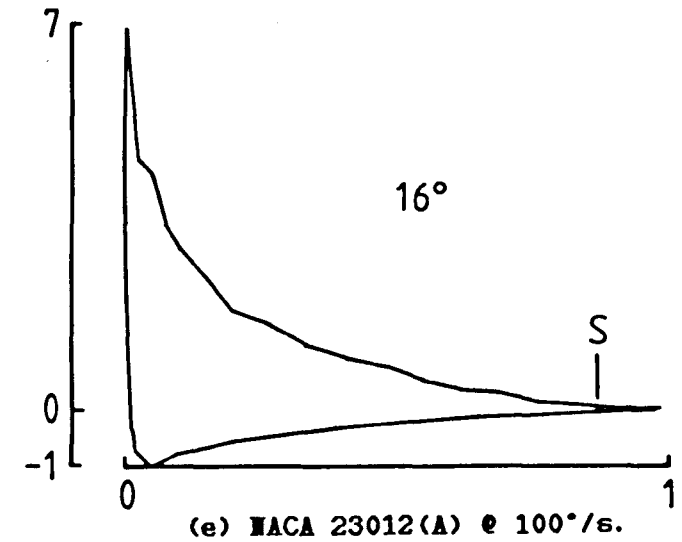
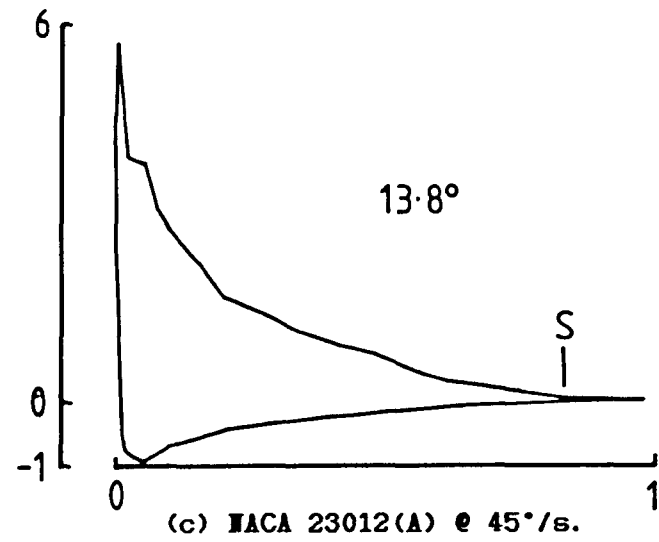
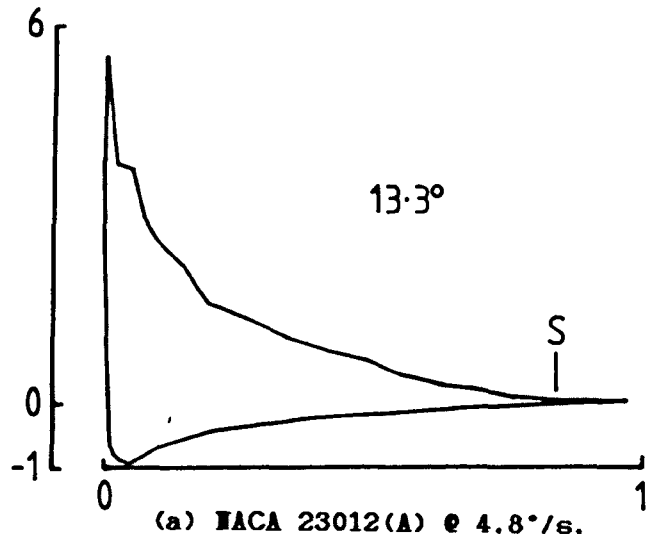


FIGURE 8.8 Discrete Chordwise Pressure Distributions obtained during Various Ramp Tests for the NACA 23012 and 23012(A) Aerofoils at 1.5×10^6 Reynolds number.

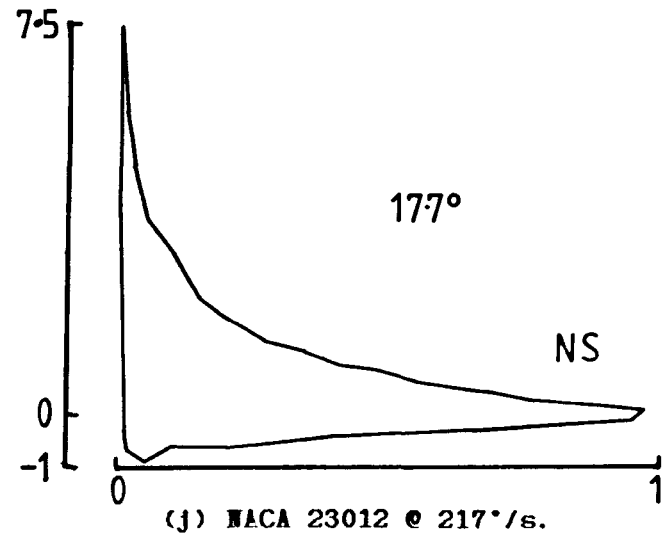
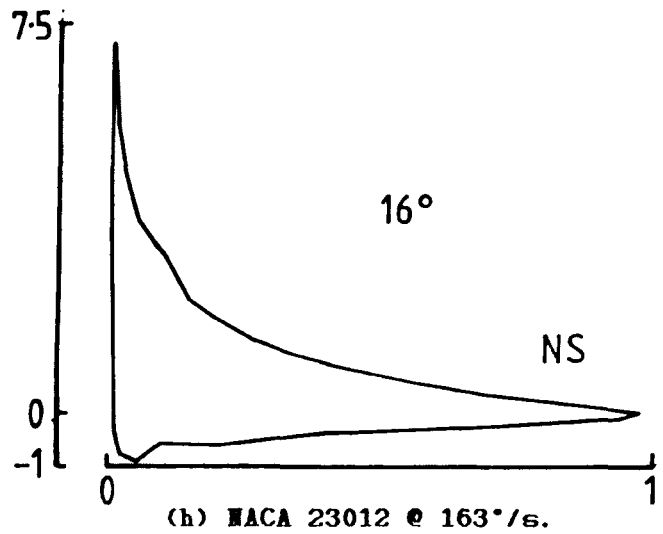
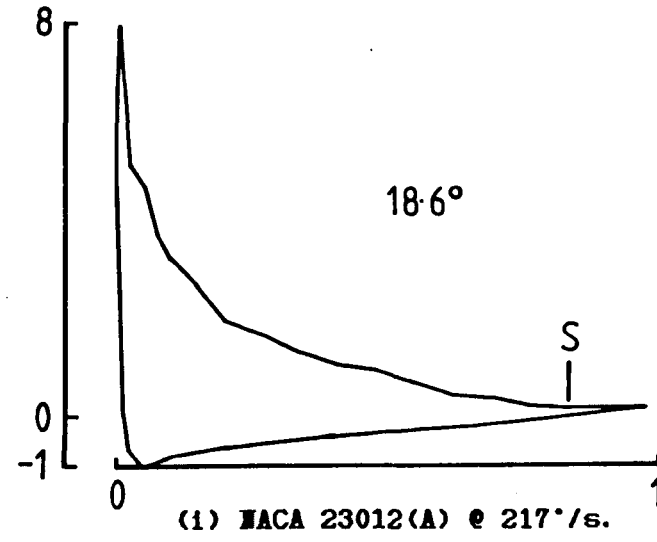
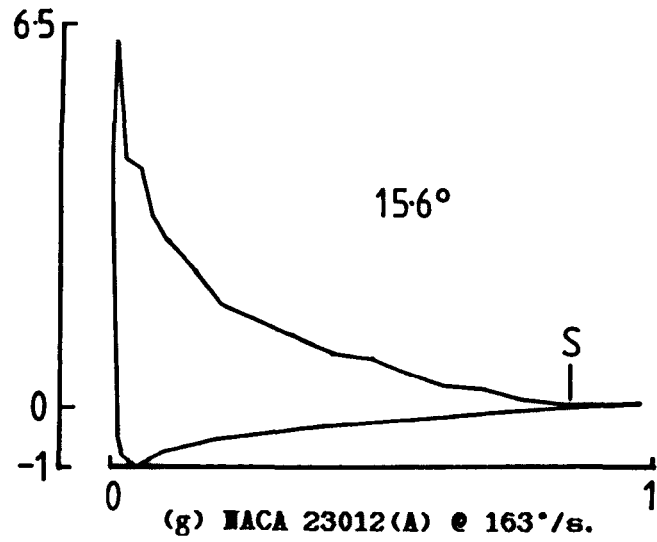
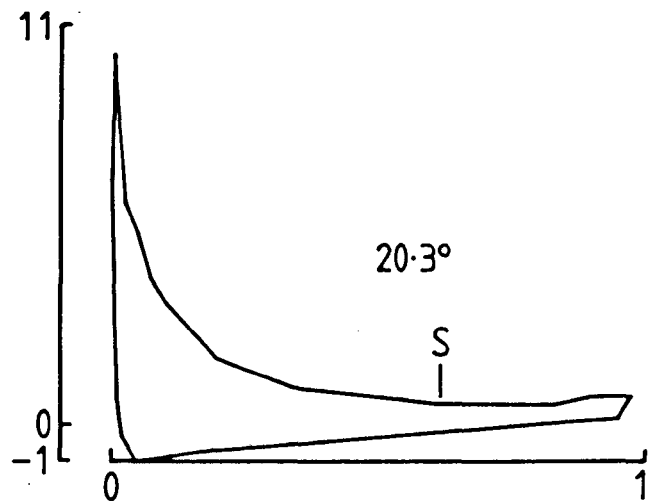
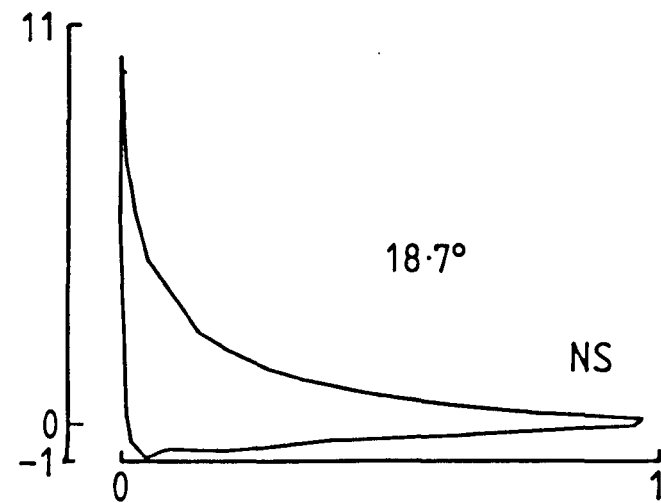


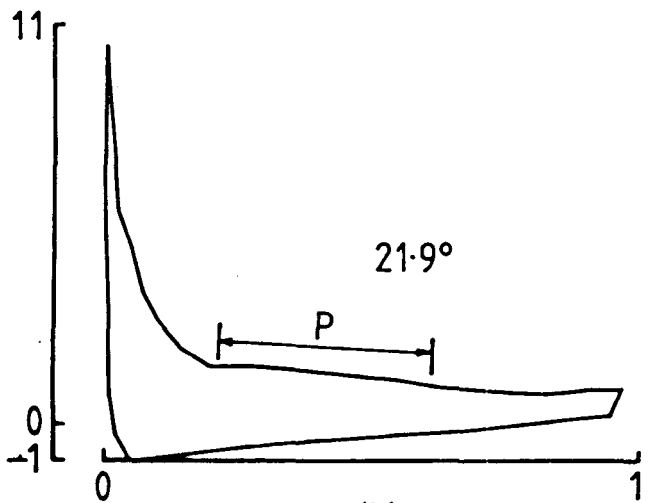
FIGURE 8.8 Completed.



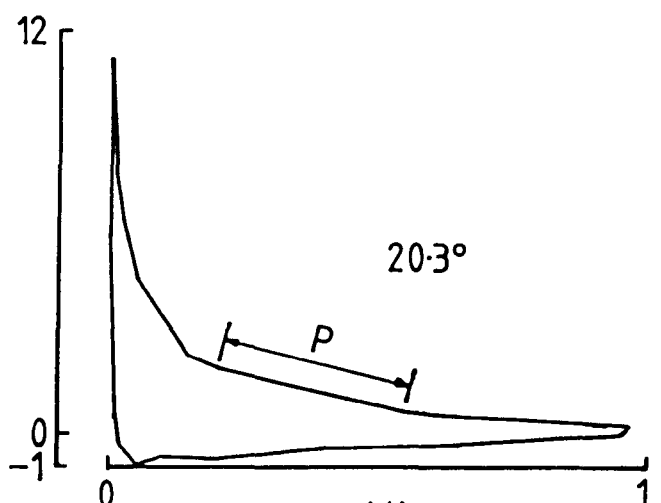
(a) NACA 23012(A)



(c) NACA 23012



(b) NACA 23012(A)



(d) NACA 23012

FIGURE 8.9 Discrete Chordwise Pressure Distributions obtained during a Ramp Tests of $100^\circ/\text{s}$ for the NACA 23012 and 23012(A) Aerofoils at 1.5×10^6 Reynolds number.

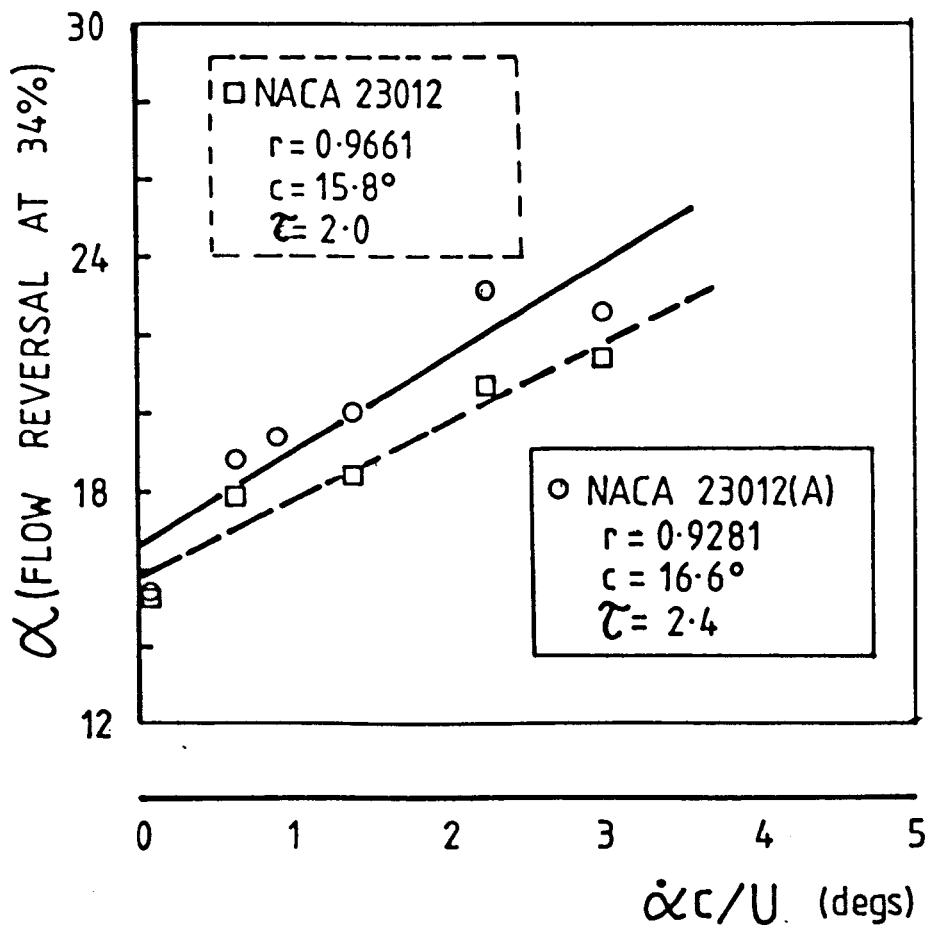
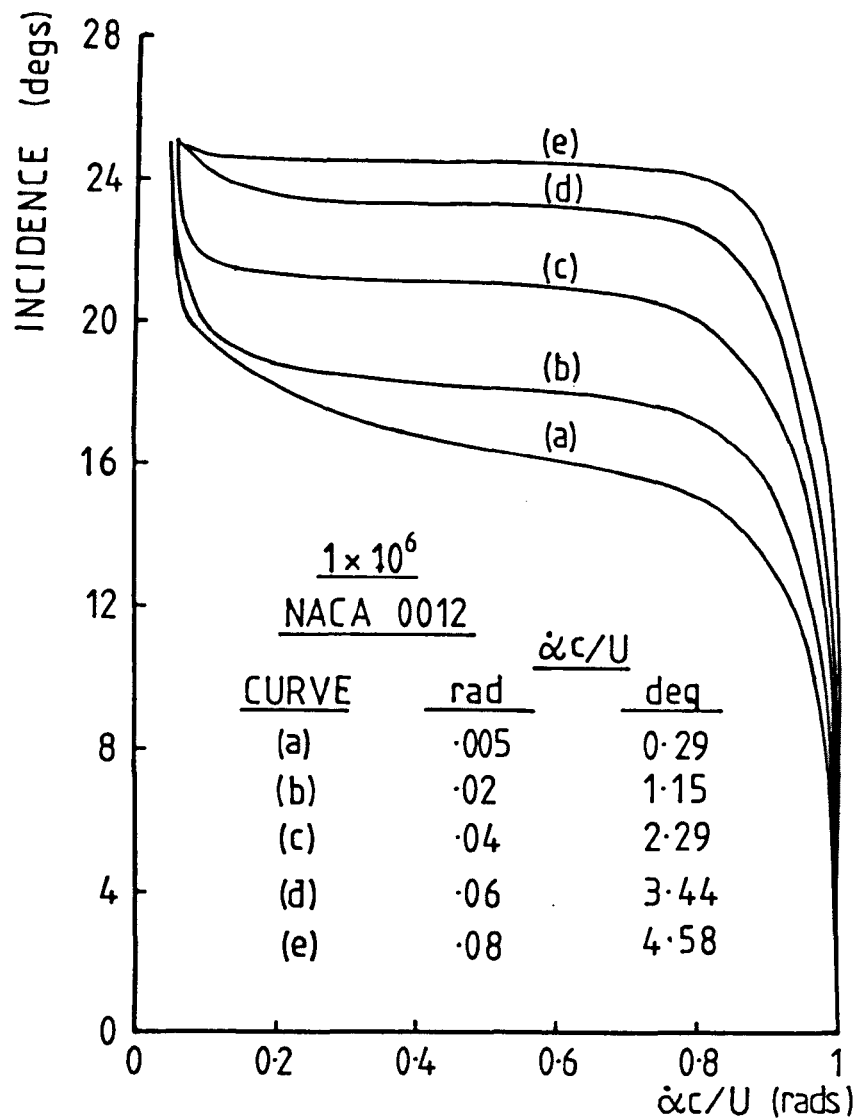


FIGURE 8.10 Non-Dimensional Vortex Inception Time Delay Calculation based on Flow Reversal Characteristics obtained during Ramp Tests at 1.5×10^6 Reynolds number.



(a) Variation with Pitch Rate.

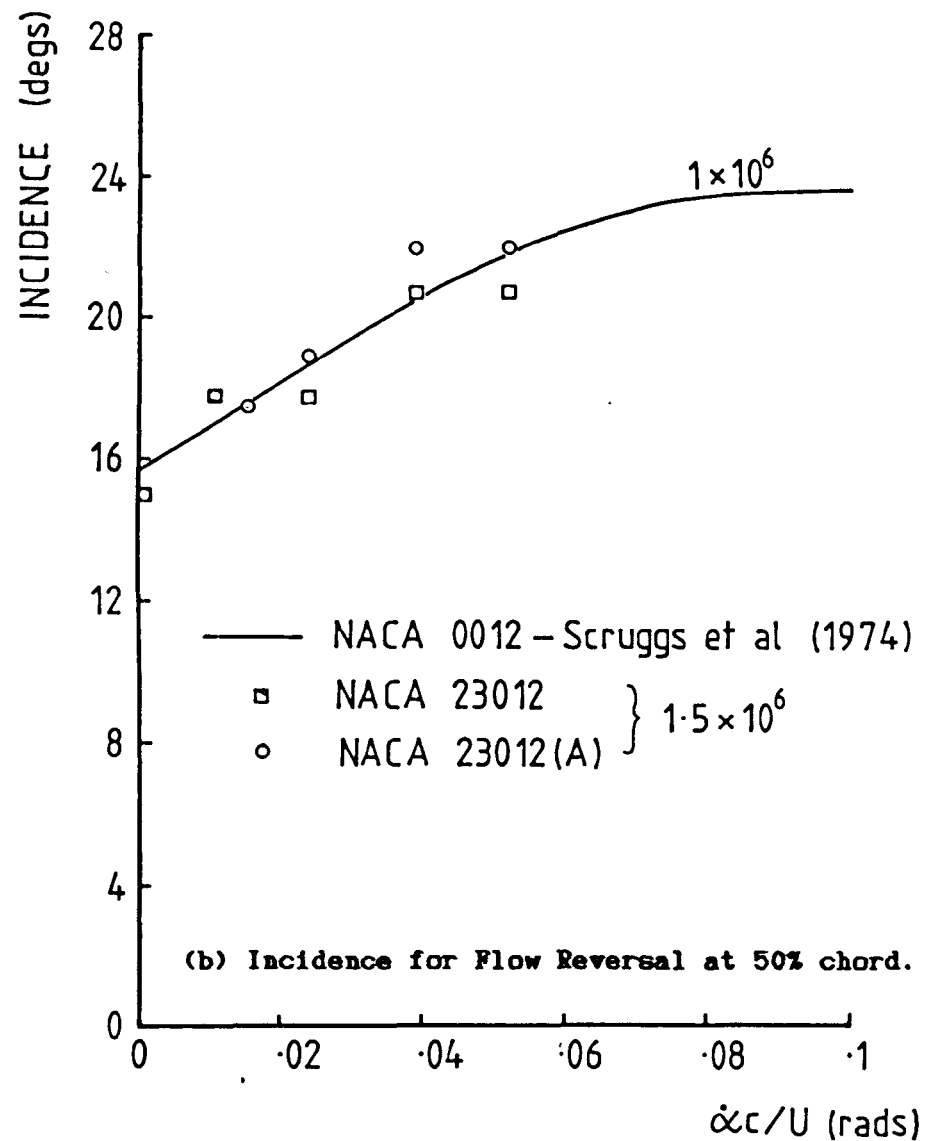


FIGURE 8.11 Predicted Loci of Turbulent Flow Reversal from an Unsteady Potential Flow / Unsteady Boundary Layer Computation (adapted from Scruggs et al, 1974).

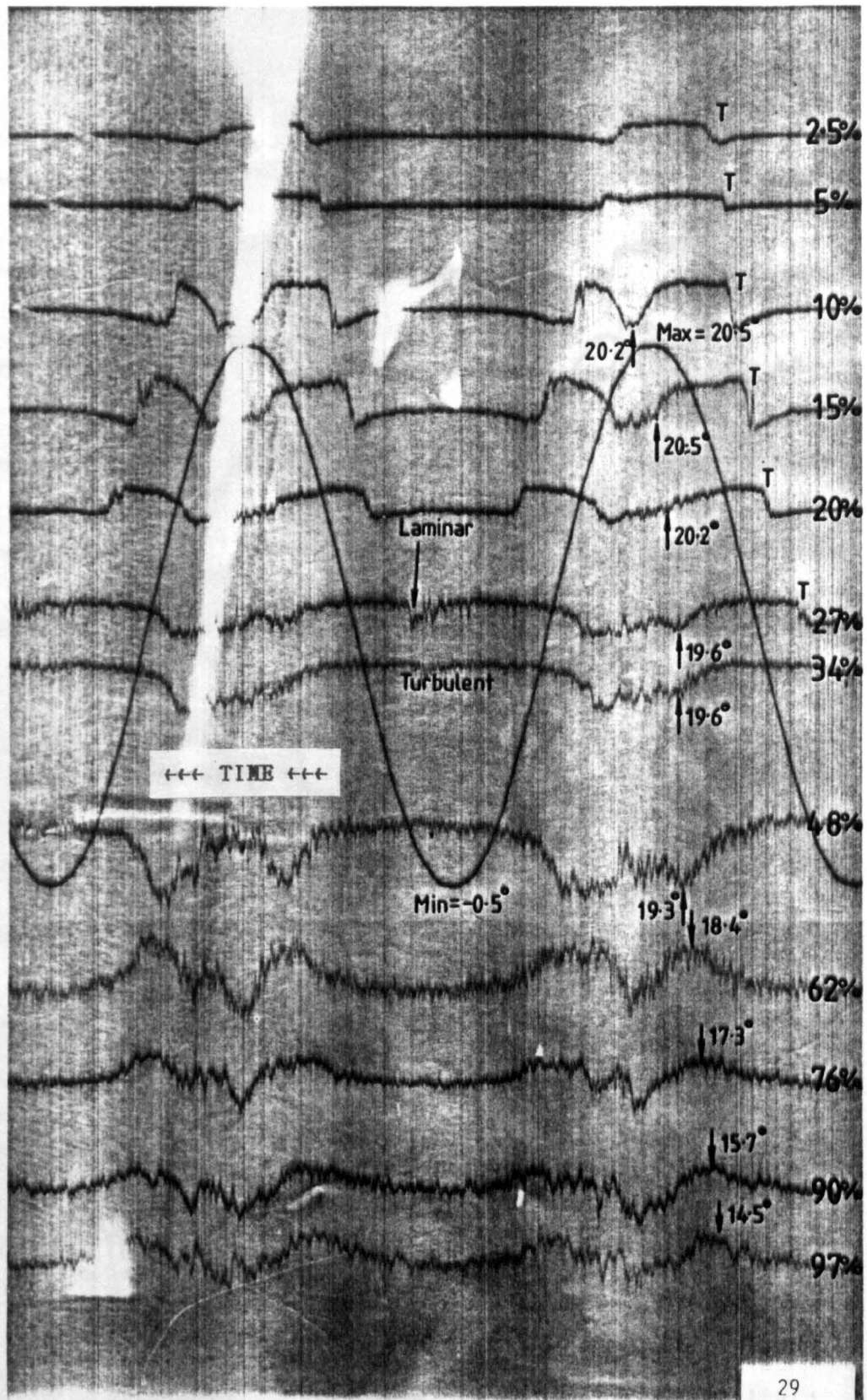


FIGURE 8.12 Response of Twelve Hot-Film Gauges during an Oscillatory Test of $\alpha = 10 + 10 \sin \omega t$ @ $k = 0.10$ on the NACA 23012(A) at 1.5×10^6 Reynolds number.

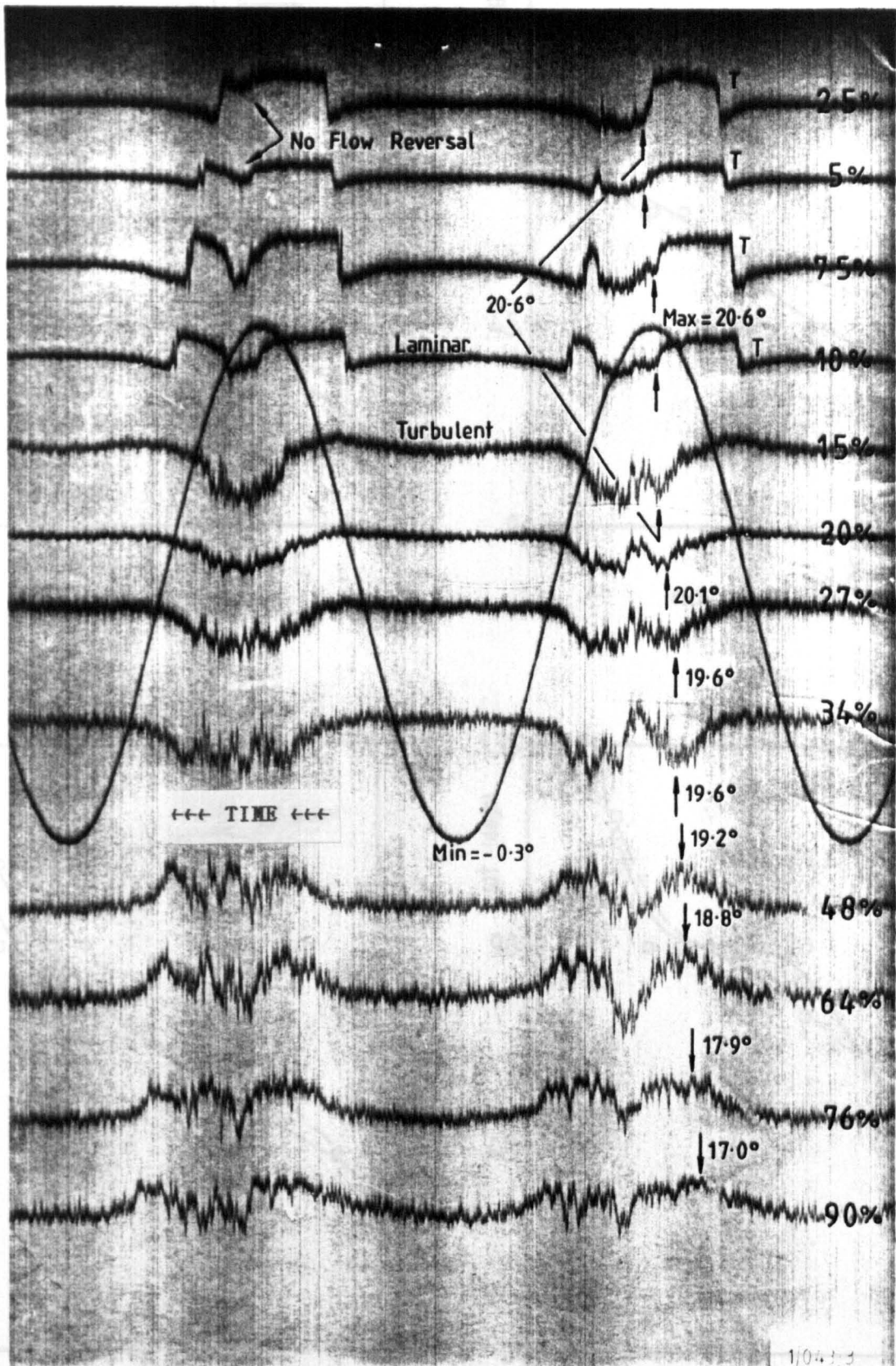


FIGURE 8.13 Response of Twelve Hot-Film Gauges during an Oscillatory Test of $\alpha = 10 + 10 \sin \omega t$ @ $k = 0.10$ on the NACA 23012 at 1.5×10^6 Reynolds number.

FIGURE 8.14 Effect of Reduced Frequency on Flow Reversal Time Angle during $\alpha = 10 + 5 \sin \omega t$.

○ — NACA 23012(11)
 □ — NACA 23012

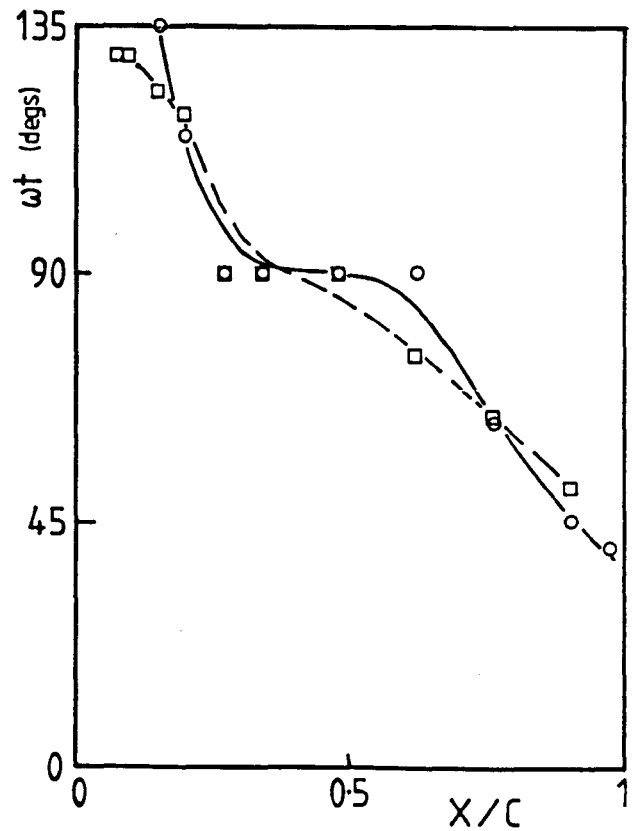
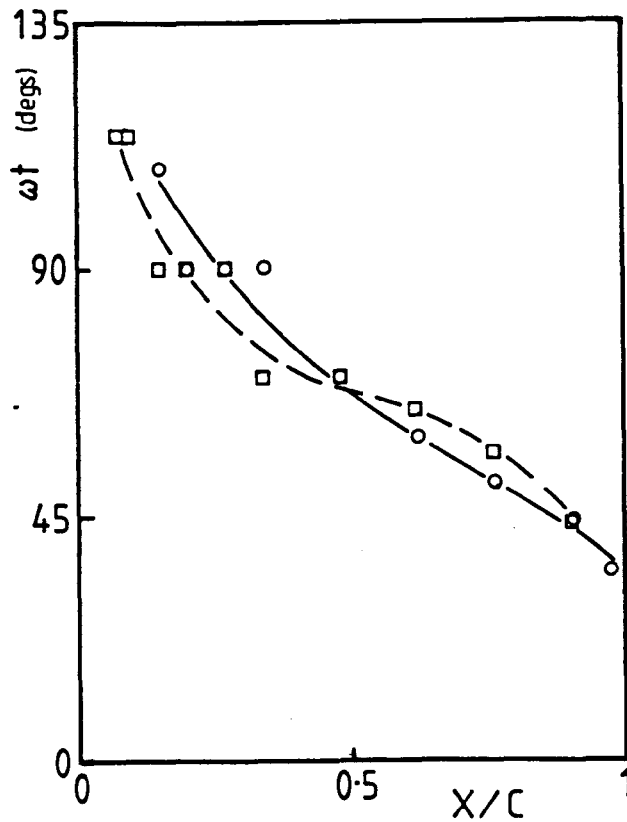
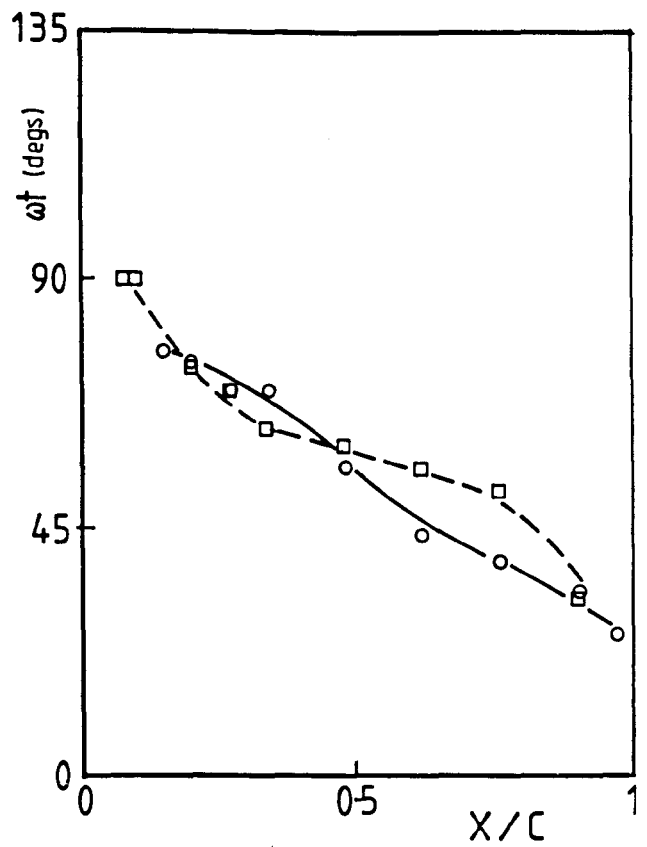
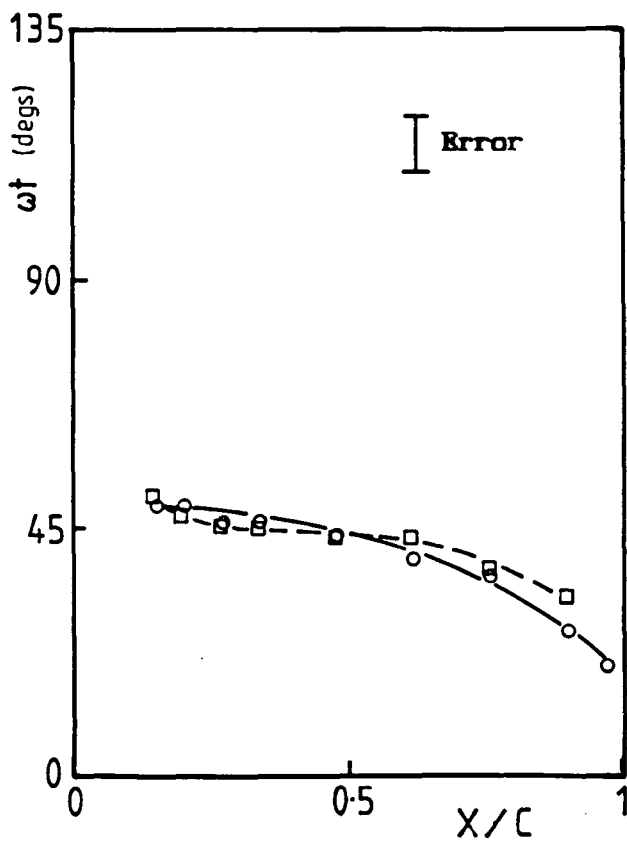


FIGURE 8.14 Effect of Reduced Frequency on Flow Reversal Phase Angle during $\alpha = 10 + 8 \sin \omega t$.

○ — NACA 23012(A)
 □ — NACA 23012

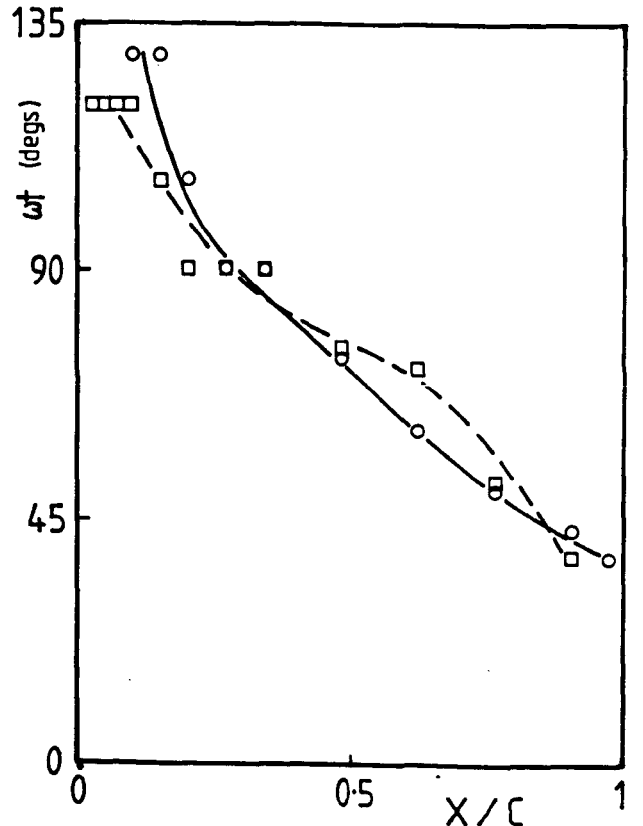
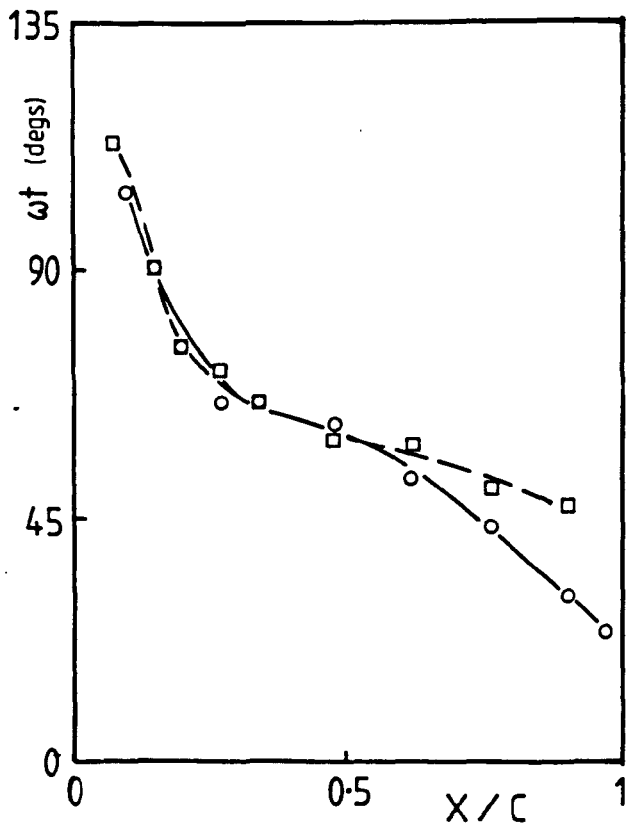
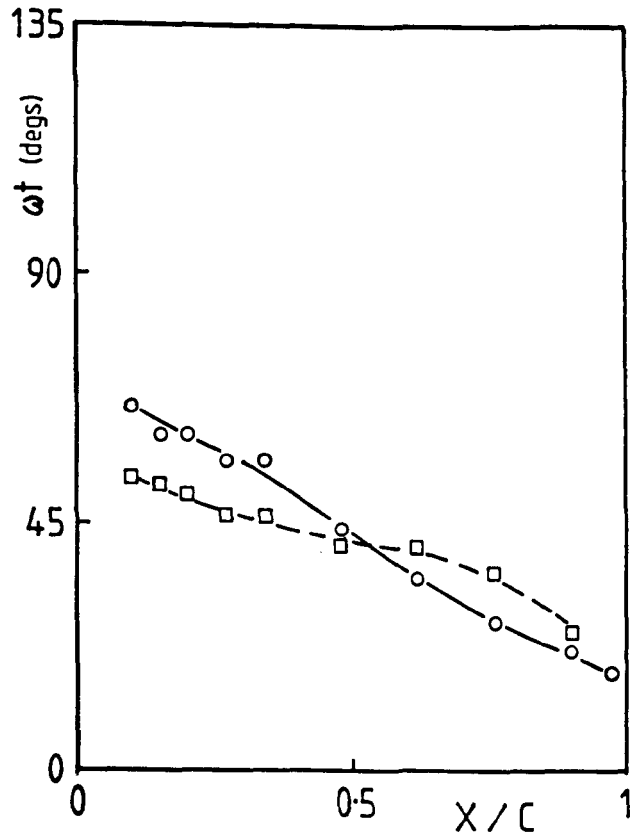
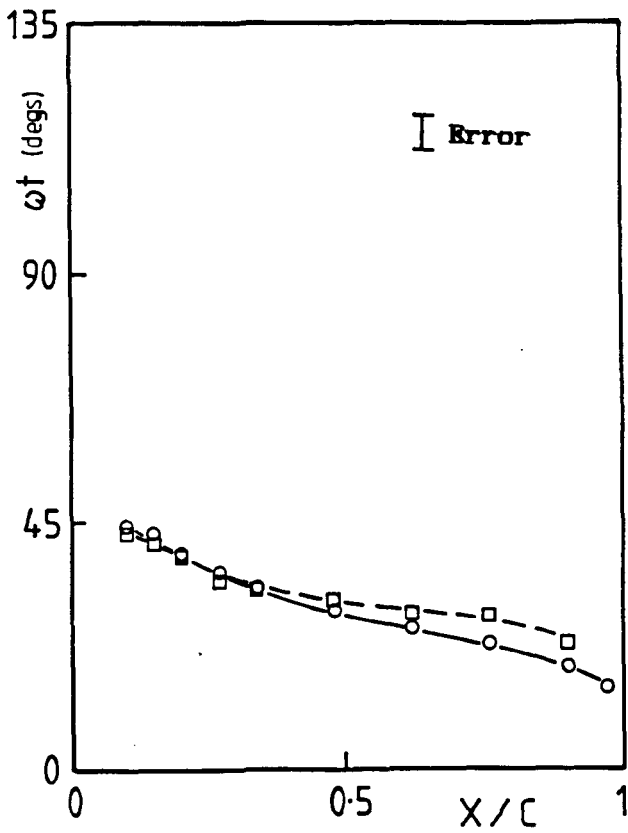


FIGURE 8.15 Effect of Reduced Frequency on Flow Reversal Phase Angle during $\alpha = 10 + 10 \sin \omega t$.

○ — NACA 23012(A)
 □ — NACA 23012

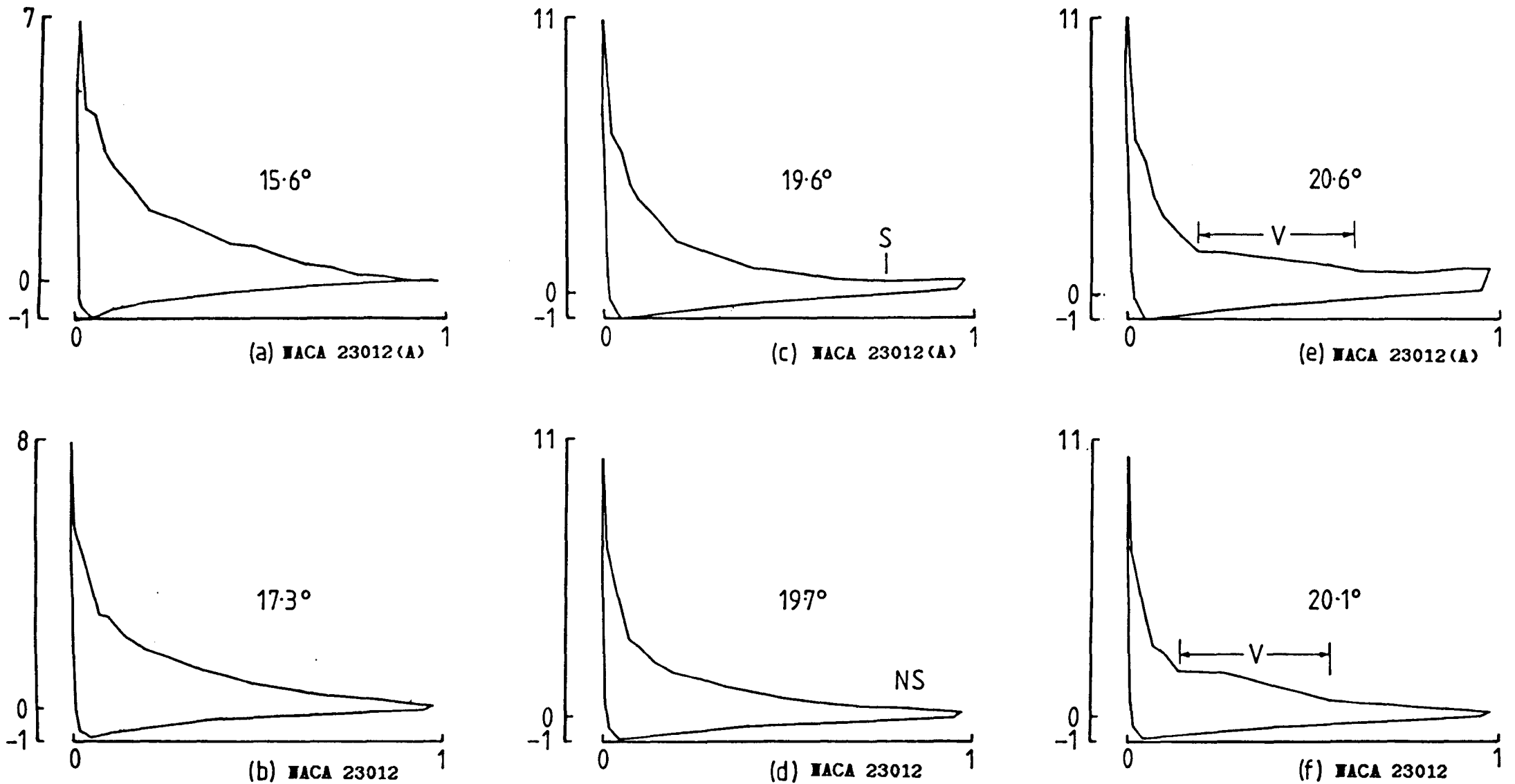


FIGURE 8.16 Discrete Chordwise Pressure Distributions obtained during an Oscillatory Tests of $\alpha = 10 + 10 \sin \omega t$ @ $k = 0.10$ for the NACA 23012 and 23012(A) Aerofoils at 1.5×10^6 Reynolds number.

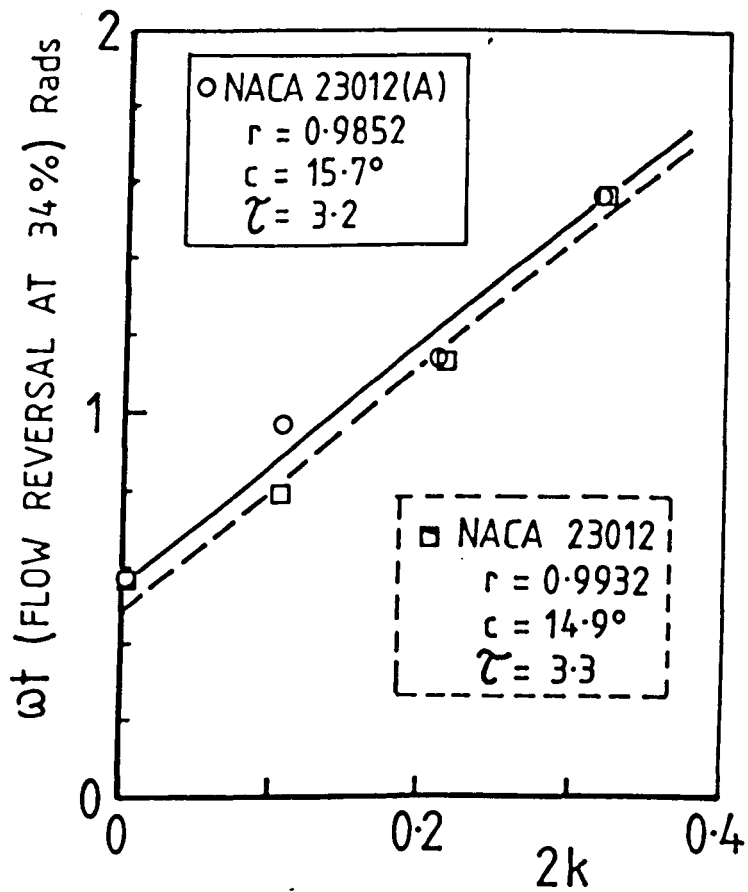


FIGURE 8.17 Non-Dimensional Vortex Inception Time Delay Calculation based on Flow Reversal Characteristics obtained during $\alpha = 10 + 10 \sin \omega t$ at various Reduced Frequencies (1.5×10^6 Reynolds number).

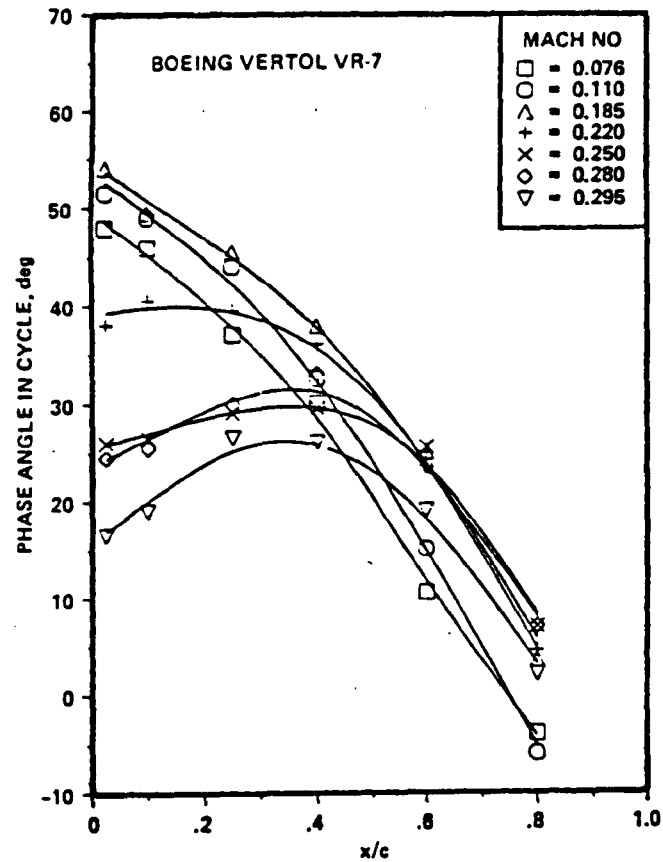
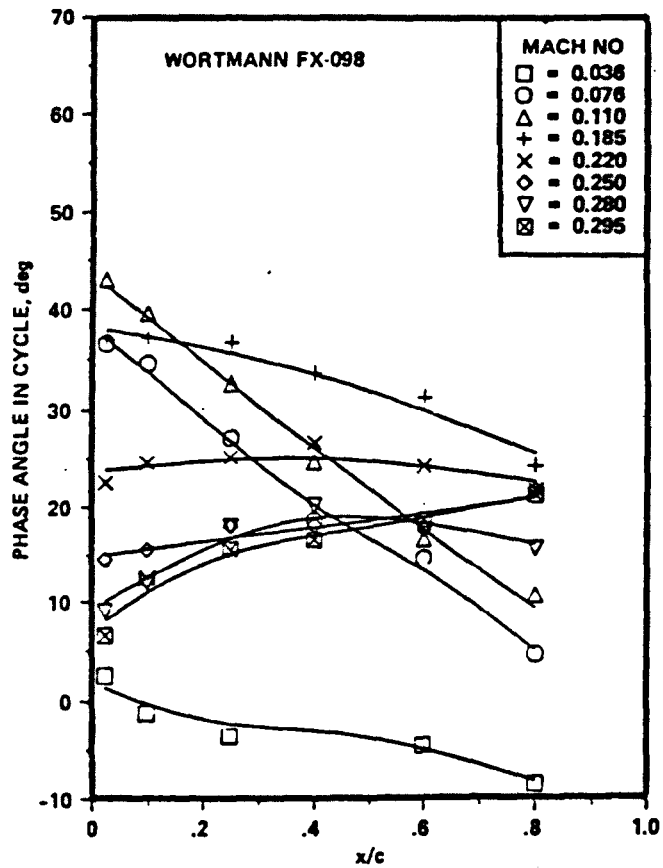
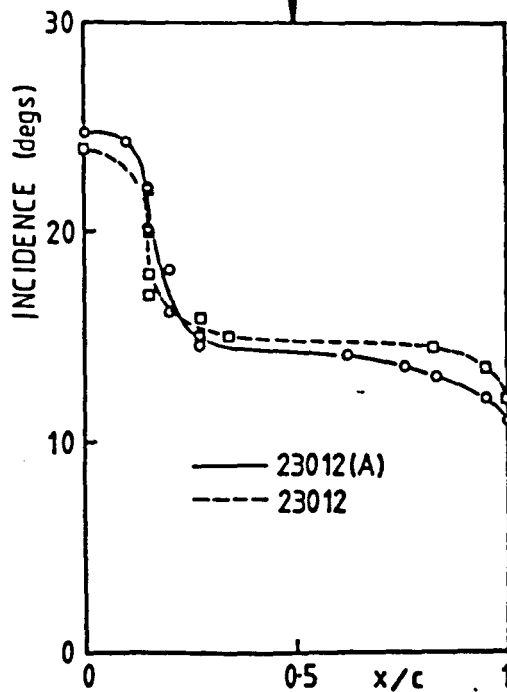
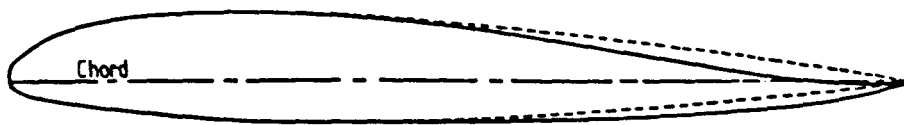
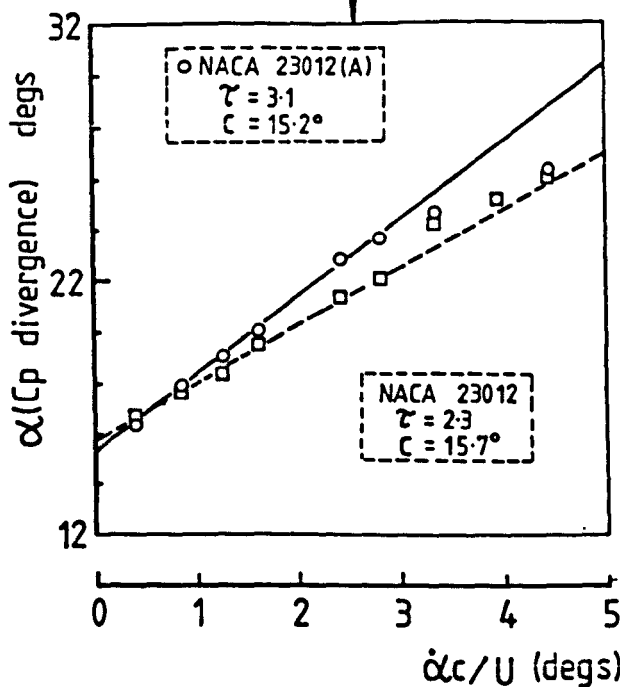


FIGURE 8.18 Phase Angle, ωt , of Flow Reversal for Range of Mach numbers at $\alpha = 15 + 10 \sin \omega t$ @ $k = 0.10$ (from McCroskey)



(a) Steady-State Separation Loci (Figure 5.5).



(b) Dynamic Stall Onset (Figure 7.19)

FIGURE 9.1 Effect of Steady-State Separation Characteristics on the Timing of Dynamic Stall Onset at 1.5×10^6 Reynolds number and 0.11 Mach number.

STALL PARAMETER	EFFECT
Aerofoil geometry	Large in some cases
Mach number	Small below $M_\infty \approx 0.2$ Large above $M_\infty \approx 0.2$
Reynolds number	Small at low Mach number Unknown at high Mach number
Reduced frequency	Large
Mean angle, amplitude	Large
Type of motion	Virtually unknown
Three-dimensional effects	Virtually unknown
Tunnel interference effects	Virtually unknown

TABLE 1.1 Importance of the Dynamic Stall Parameters
(from McCroskey *et al*, 1980).

NACA 23012(A)

(Stations and ordinates given in per cent of aerofoil chord)

Upper Surface		Lower Surface	
Station	Ordinate	Station	Ordinate
-0.044	0.802	0.000	0.000
0.000	0.000	0.436	-0.681
0.337	1.694	1.229	-1.226
1.166	2.657	2.354	-1.658
2.454	3.651	3.791	-2.008
4.207	4.626	5.529	-2.308
6.413	5.523	7.564	-2.588
9.048	6.286	9.910	-2.874
12.069	6.876	12.588	-3.180
15.421	7.276	15.631	-3.508
19.042	7.503	19.077	-3.838
22.902	7.603	22.925	-4.123
27.060	7.597	27.083	-4.333
31.507	7.479	31.530	-4.471
36.224	7.241	36.247	-4.540
41.195	6.872	41.216	-4.547
46.399	6.365	46.418	-4.498
51.816	5.725	51.831	-4.401
57.424	4.964	57.436	-4.261
63.202	4.103	63.209	-4.077
69.125	3.169	69.128	-3.843
75.169	2.202	75.169	-3.544
81.310	1.257	81.306	-3.147
87.521	0.422	87.515	-2.587
93.773	-0.125	93.768	-1.701
100.000	0.051	100.000	-0.050

TABLE 3.1 Coordinates of the NACA 23012(A) Aerofoil.

		MATERIAL	CONSTRUCTION	SPECIFICATION			
				PROPERTY	VALUE	±ERROR	ANALYSIS
S K I N		Glass-fibre ±45° woven roven Resin/gel-coat	3mm skin backed with balsa wood. 2 halves joined together with resin.	Weight (Kg)	18.0	0.5	Direct measurement
				Moment of Inertia (Kgm ²)	0.50	0.24	Physical pendulum experiment
				GJ (Nm ²)	36000	2000	Torsion rig experiment
				EI (Nm ²)	25000	?	Thin wall tube analysis Composite data sheets
S P A R		Aluminun	2 halves bolted together to form hollow tube.	Weight (Kg)	20.0	0.5	Direct measurement
				Moment of Inertia (Kgm ²)	0.14	?	Thin wall tube analysis
				GJ (Nm ²)	93000	?	as above
				EI (Nm ²)	18000	?	as above
F I N A L	M O D E L	<u>Natural Frequencies</u>		<u>Centre span deflections</u>			
		Torsion = 60 Hz Bending = 27 Hz		Twist = 0.26° Bending = 1.7 mm			

TABLE 3.2 Summary of the Structural Design of the NACA 23012(A) Aerofoil.